ACOUSTIC EXCITATION
AND TRANSMISSION OF
LIGHTWEIGHT STRUCTURES

JONAS BRUNSKOG

ACOUSTIC EXCITATION
AND TRANSMISSION OF
LIGHTWEIGHT STRUCTURES

JONAS BRUNSKOG

Abstract

In order to increase our knowledge of the sound transmission and radiation processes of lightweight wall and floor structures, theoretical models are needed. Detailed models may form a valuable tool. In lightweight floor structures, impact sound insulation is perhaps the most important property to consider. This thesis presents an overview of various solution strategies that may be useful in finding a theoretical model for impact sound insulation. Expressions for the point mobility of infinite plates driven by a rigid indenter are derived. These expressions are needed when determining the deformation close to the excitation area, which is important when studying impact noise to properly describe the interaction between the source and the floor. A detailed three-dimensional thick-plate analysis is used. The excitating pressure is found by means of a variational formulation. The point mobility is calculated by means of numerical integration. The excitation force provided by the ISO tapping machine is examined, partly in relation to the three-dimensional deformation analysis. Results found in the literature are reviewed and reconsidered. Low-frequency asymptotes are derived. A more general impact force description is derived, suited for arbitrary frequency-dependent mobilities of the floor structure. The frequency-dependency of the mobility can be due to local effects, investigated by means of thick-plate theory, and/or global effects, investigated by means of a spatial Fourier transform method. A theoretical model for a point-excited simple lightweight floor is presented. The model is used for the prediction of impact noise level. A comparison between numerical computations and measurements found in the literature is performed. A relatively good correspondence between measurements and calculations can be achieved. Lightweight walls (and floors) are often designed as a framework of studs with plates on each side. The studs can be seen as walls in the cavity, thus introducing finiteness. A prediction model for airborne sound insulation including these effects is presented. Due to variabilities, no structure can be perfectly periodic. The effects of near-periodicity are studied by means of transform technique and the expectation operator. The near-periodicity leads to an increase of the damping (if material damping is present). Resilient devices are commonly used in lightweight structures to decrease the sound transmission in a broad frequency band. Applications of such devices may be found, for example, in resiliently mounted ceilings in aeroplanes, ships and buildings. A measurement method to characterise the two-port acoustic properties of resilient devices is presented.

Key words

Building acoustics, impact noise, airborne noise, ISO tapping machine, lightweight, periodic, prediction model, resilient device, spatial Fourier transform, structural acoustics, timber, sound insulation, nearly periodic, near-periodicity, cavities, plate excitation, point mobility, Lamb waves, wood.

Preface

This thesis is a product of 'The Building and Its Indoor Environment' research school at Lund University. The research school is financed through the KK-Foundation (the Swedish Foundation for Knowledge and Competence Development). SBUF and Skanska Teknik AB have also contributed to the finalisation of the project leading to the thesis.

I would like to thank all my colleagues and friends at the division of Engineering Acoustics, LTH, Lund University, especially my supervisor Prof. Per Hammer, and also Dr. Erling Nilsson and Prof. Sven Lindblad, for all their valuable discussions and support. Dag Holmberg, Dr. Karl-Ola Lundberg, Per Hiselius, Ann-Charlotte Johansson, Lars-Göran Sjökvist, Mark Kartos, Klas Hagberg and Jan Frennberg have all contributed to the lively, spontaneous discussions in front of the whiteboard and in the classroom. These discussions have been a real education and the place where ideas have been shown as either worthless or meriting continuing attention. I wish to apologise for my temper. I would also like to thank Dr. Tamas Pritz who inspired me during his scientific visit at the division. Robert Månsson, Eva Dilton, Clary Nyquist-Persson and Bo Zadig have all been helpful with such practical things as measurements, travel booking, copying and drawing figures, etc. My colleagues at the divisions of Structural Mechanics, Structural Engineering, Building Materials and Engineering Geology at LTH have also been a great support (nobody mentioned, nobody forgotten).

I would also like to thank all my colleagues and friends at Skanska Teknik AB, Malmö, especially Ulf Persson, Jesper Bengtsson, Sigurd Karlsson, Dr. Tord Isaksson and Dr. Kyösti Tuutti. I have spent twenty percent of my time for Skanska Teknik as an acoustic consultant. This part of the work has *forced* me to focus on the important real world of building design instead of only theory and mathematics.

Finally, I wish to express my gratitude to friends and family, and especially to Elisabet for all her love and support during the course of this work.

Dissertation

Part I: Overview of field of research

Part II: The included papers

Paper A Prediction models of impact sound insulation on timber floor structures; a literature survey. *J. Building Acoustics* **7** (2000) 89–112

Paper B Rigid indenter excitation of plates. *Acustica / acta acustica* **submitted**

Paper C The interaction between the ISO tapping machine and lightweight floors. *Acustica / acta acustica* **accepted**

Paper D Prediction model for the impact sound level of lightweight floors. *Acustica / acta acustica* **accepted**

Paper E The influence of finite cavities in sound insulation of double-plate structures. Report TVBA 3119

Paper F Near-periodicity in acoustically excited stiffened plates and its influence on vibration, radiation and sound insulation. Report TVBA 3120

Paper G Measurement of the acoustic properties of resilient, statically tensile loaded devices in lightweight structures. *J. Building Acoustics* **9** (2002) 99–137

Contents of the thesis

The focus of the present thesis is on sound transmission through lightweight building elements. This includes both airborne sound insulation and impact sound insulation. Not included is the flanking transmission, which however is an important path of sound transmission in lightweight building structures.

It should be mentioned that when the project started, the focus was only on impact sound insulation, this being the most important problem. However, as airborne sound insulation problem is simpler in some ways, it can be used to show some special aspects more clearly.

Description of Part I: Overview of field of research

An introduction

The overview starts with an introduction that describes in a general discussion which parameters and aspects are important when studying the acoustics of lightweight structures. Both theoretical and empirical results are discussed, and the papers included in the thesis are introduced in this context.

More about periodicity

Periodicity is one of the typical features of a lightweight building structure. Different approaches to take the periodicity into account are presented, as well as some theorems and formulas required.

Moment reaction and coupling

The effects of moment reactions between the beams and the plates are not included in the papers, but are for the sake of completeness included in this chapter.

Power and sound radiation

Radiated power is an important measure of the sound radiation of a structure. Different approaches are presented and discussed. The chapter shows that the Cremer and Heckl formula for radiated power can be derived in different ways. This chapter is considered to be only an overview.

Which are the important parameters?

A parameter study is included in order to investigate which parameters in a lightweight structure are the most important in terms

of the impact noise level. The largest positive effects (that is, in decreasing the impact sound level) are gained if the construction depth is increased (when mineral wool is present in the cavity).

Summary and concluding remarks of the thesis

Part I ends with a summary of the entire thesis, and some of the conclusions drawn are presented.

Description of Part II: The included papers

Paper A: Prediction models of impact sound insulation on timber floor structures; a literature survey [1]

To develop new types of lightweight wall and floor structures it is important to increase the knowledge of the transmission and radiation processes for such structures. To do so, detailed models based on deterministic and statistical assumptions may form a valuable tool. In lightweight floor structures, impact sound insulation is perhaps the most important factor to consider. This paper gives an overview of various solution strategies that may be useful in finding a prediction model for impact sound insulation.

Paper B: Rigid indenter excitation of plates [2]

The paper presents expressions for the point mobility of infinite plates driven by a completely rigid indenter. The problem is of general interest in connection with the excitation and transmission of structure-borne sound. The indenter is assumed to be circular, weightless, and stiff compared with the plate. A rigid indenter is assumed to provide a better approximation of the actual situation than a soft indenter would, e.g when a hammer acts on a wooden plate. A detailed three-dimensional analysis is performed. Traditionally, the problem is solved in approximate terms by assuming a pressure distribution at the interface between the indenter and the plate. In the present study, a pressure distribution is also assumed, an optimal choice of the pressure amplitude being found by means of a variational formulation. Numerical results are presented and discussed, the discrepancy between the results obtained and the perfectly rigid indenter being examined.

Paper C: The interaction between the ISO tapping machine and lightweight floors [3]

The ISO standard tapping machine, used as an excitation source in rating the impact-sound level of a floor structure, interacts with the floor structure during the hammer impact. Expressions for the force spectrum due to the impact are presented. The 6 dB differ-

ence at low frequencies of the force spectrum, evident in measurements, and reasons for it, are discussed. The interaction is investigated by use both of simplified lumped models and arbitrary frequency-dependent models. Local effects due to indentation near the point of impact and to global effects due to stiffeners are included in the description of the mobility involved. Numerical results are presented, where it is concluded that both the local and the global effects of the driving point mobility are important in describing the force spectrum caused by the interaction between the tapping machine and the complex floor structure.

Paper D: Prediction model for the impact sound level of lightweight floors [4]

Lightweight floors are often troubled by poor impact-sound insulation. In order to develop and explain structures with acceptable insulation, a deterministic prediction model was developed. The paper considers transmission through the system and the response of the model. Excitation (as caused by the ISO-tapping machine) is considered in a separate paper [3]. The system description employs a spatial transform technique, making use of the periodicity of the floor structure with the aid of Poisson's sum rule. The radiated power is calculated using numerical integration in the wave-number domain, the radiated power enabling the impact sound level to be calculated. Comparisons are made between measurements found in the literature and the pro-

posed prediction model, the effects of different excitation models being discussed. A relatively close agreement is achieved, especially if an elaborate excitation model is employed.

Paper E: The influence of finite cavities in sound insulation of double-plate structures [5]

Lightweight walls are often designed as frameworks of studs with plates on each side – a double-plate structure. The studs constitute boundaries for the cavities, thereby both affecting the sound transmission directly by short-cutting the plates, and indirectly by disturbing the sound field between the plates. The paper presents a deterministic prediction model for airborne sound insulation including both effects of the studs. A spatial transform technique is used, taking advantage of the periodicity. The acoustic field inside the cavities is expanded by means of cosine-series. The transmission coefficient (angle-dependent and diffuse) and transmission loss are studied. Numerical examples are presented and comparisons with measurement are performed. The result indicates that a reasonably good agreement between theory and measurement can be achieved.

Paper F: Near-periodicity in acoustically excited stiffened plates and its influence on vibration, radiation and sound insulation [6]

Due to variabilities in the material, the geometrical configuration, or the manufacturing properties, a structure that is designed to be spatially periodic cannot be exactly periodic. The presence of small irregularities in a nearly periodic structure may influence the propagation of the vibration field, the field being localised. A number of papers have addressed such localisation phenomena. This paper will instead focus on the mean vibration field and its influence on sound radiation and sound insulation in a plate stiffened by supports or beams. The approach is to seek a formal solution with the aid of spatial transform technique (similar to the perfect periodic case) and then apply the expected value operator to the solution. Two assumptions must then be introduced: I) The reaction forces are statistically independent of a phase-term that is due to the irregularity, and II) the mean field is periodic. The approach is presented in general terms, the specific configuration (a stiffened plate) being presented as an example. Numerical results are presented and discussed, and it can be seen that the small irregularities cause an increase in stiffness and damping (when material damping is present).

Paper G: Measurement of the acoustic properties of resilient, statically tensile loaded devices in lightweight structures [7]

Resilient devices are commonly used in lightweight structures to decrease sound transmission in a broad frequency band. Applications of such devices may be found, e.g., in resilient mounted ceilings in aeroplanes, ships and buildings. A measurement method to characterise the frequency dependency of the transfer stiffness and the input stiffness of the resilient device is presented. The mechanical characteristics of the measurement method are investigated. In addition, some resilient devices used in buildings are analysed with respect to acoustic properties. Parameters such as static load and mountings for the devices are considered and handled by means of statistical analysis.

Part I

Overview of field of research

Chapter 1

An introduction

The development of new building systems has intensified. Such building systems are often lightweight, and developed to be used in load-bearing structures and dwellings. Although systems of this sort have many advantages, particularly that of low weight, they often fail to provide adequate sound insulation.

The term 'lightweight building systems' has no restriction in material choices, and the same is true for the theoretical models developed in this thesis. However, the examples in this thesis are mainly focused on timber structures.

For a major part of the last century, fire regulations have restricted builders in Scandinavia from using timber in the load-bearing structures in buildings more than two storeys high. However, the introduction of performance-based building codes in the 1990s has created new opportunities for timber constructions, and in recent years a number of residential housing projects with timber frames have been launched in Scandinavia [8].

The building codes in the Nordic countries give limit values for airborne noise and for impact noise. Airborne noise is seldom a problem in lightweight building constructions. However, the performance of lightweight floors regarding structure-borne noise is often insufficient in relation to the requirements from the tenants. Previous design solutions have led to complaints regarding footsteps and similar noise sources. Such sources give, for lightweight floors, high sound levels at low frequencies. Therefore, it is important to find design solutions that suppress the transmission at low frequencies [9].

In order to develop the sound insulation in lightweight buildings, a comprehensive description of the structure is needed on all levels: material descriptions, element descriptions, descriptions of the connections, and global descriptions including the acoustic response.

Existing theoretical models all rely on simplified assumptions and are often developed for heavy, homogenous structures such as concrete. The main purpose of the research project in which this thesis is included is to develop new theoretical models with a high level of complexity. It would then be pos-

sible to describe the substantial changes in the sound insulation caused by details in the lightweight structure. This is important in the development of new, simplified lightweight structures with good sound insulation.

The present chapter will consider the behaviour of lightweight walls and floor-structures and how this behaviour differs from that of heavy and homogeneous building components. To provide a thorough understanding of the problems, they are considered from four different perspectives: 1) various approaches used in dealing with acoustical problems and how applicable these are to lightweight building construction systems, 2) characteristics of various building materials, 3) the systems-effects of different types of building construction systems, and 4) factors that lead to sound being experienced as disturbing. By the term *systems-effects* is meant the extra effects that occur when joining different materials or elements in a system.

1.1 Different approaches

Two different approaches to describe and compute the acoustics of a building can be distinguished. The one involves determining the average flow of acoustical energy between separate components, often in combination with the use of empirically based knowledge or data. The other approach involves a detailed analysis of the problems from a deterministic point of view, using analytical and/or numerical methods utilising physical field variables such as sound pressure

and vibration velocity. The term *deterministic* means that one assumes that the laws of nature imply that no processes are considered as random (an idealisation of the actual situation).

The first approach includes Statistical Energy Analysis (SEA), other power-flow methods – such as those associated with the European standards for computing building acoustics (EN 12354 [10]) – and of various semi-empirical methods. Such an approach is often successfully used when details of a standard type of construction are considered, as for example when well-known building elements are combined in EN 12354, or when large variations in the material or geometrical data have little effect on the result. An approach of this type is basically pragmatic, emphasis being stressed on achieving reasonable results quickly. The amount of information used to account for the physics involved is minimal, as each building element is described by a single number (for each frequency). The number in question is the mean of the sound energy, obtained for each part or component of the structure separately. The fact that a minimal amount of information is used represents both an advantage and a disadvantage. This approach is particularly appropriate for dealing with homogeneous and clearly distinguishable building elements, such as is used in traditional building construction systems in which the elements are heavy, homogeneous and loosely coupled. Such an approach is not likely to be successful, however, if one's interest is in discovering new types of solutions to the problems, since the lack of information makes it impossible to describe the physics of

the situation adequately. Examples of SEA applied to sound insulation with double wall systems are Craik [11] and Craik and Smith [12]. Gerretsen has used a power flow approach [13, 14, 15] mainly dealing with flanking transmission and using the sound transmission loss and vibration level differences as parameters. When the direct path is studied, very simplified models only applied to homogeneous slabs are used. These papers were the basis for EN 12354 [10]. The power flow approach can also be described as first order SEA as no back coupling is taken into account. As an example of semi-empirical prediction models, the model described by Sharp [16] should be mentioned. These references are just a few examples, for there are many other papers that also could have been mentioned.

Since the other deterministic approach is generally more complicated and theoretically complex, the computations can easily fail due to the uncertainty in the input data; the complexity often leads to a high sensitivity to variations in the input data. Although the numerical methods employed (such as FEM) are often time-consuming, the use of a deterministic model often provides highly useful information and clear insight into a problem, as well as proving good opportunities for achieving optimal solutions. Also, one can always introduce statistics afterwards (such as through repeated simulations of the problem).

This thesis is mainly concerned with use of the latter, more detailed approach, especially in the papers [2, 3, 4, 5, 6]. A more detailed account of the theoretical approach is provided in [1], included in the thesis. Many of the results reported in this introduction, as well as in [7] (included in the thesis), are based on measurements.

1.2 Characteristics of different materials

The materials used in a lightweight construction differ in their characteristics from those used in traditional constructions. Traditional constructions often consist of concrete, steel (as reinforcement) and brick. In contrast, lightweight constructions often contain wood, mineral wool, plasterboard, chipboard, plywood and thin-walled steel as elements. Whereas sawdust or cinders were frequently used as filling materials in wooden constructions earlier, these have been largely replaced by mineral wool (which provides better sound insulation and is lower in weight). The air between the different components can also be viewed as a material that has interesting characteristics of its own, due to its viscosity. The specific characteristics for these various materials will be considered shortly.

Wood is inhomogeneous and orthotropic, in contrast to concrete (even if slightly orthotropic when steel-reinforced concrete is used). This implies that the structure-borne waves travel with different speeds, depending upon their direction. In beams and studs, pure wood is often used. However, the bending stiffness along the beam then dominates, implying that directionality is not particularly important in wooden structures

5

of this sort. Thus, methods for computing acoustical behaviour generally do not need to be specially adapted to the orthotopic nature of these constructions. The methods we have developed [4] are largely based on principles conceived in connection with shipbuilding [17]. In the case of massive wooden floor structures, orthotropic considerations can nevertheless be important.

Mineral wool can be described as having both a structural phase and a gas phase. However, in most material descriptions one ignores this, the material being described as a gas in which there is an extra damping effect. The simplest way of presenting the damping is by direct use of the flow resistance of the product. This is not entirely true, however, since structural movement and heat conduction in the structure also play a role. The next step in the direction of greater detail is to utilize an empirical model of the material that at least indirectly takes account of these various phenomena [18]. Such a model, which is employed in [4], is easy to use. More advanced models in which waves are seen as being propagated in both phases are also available [19, 20]. The role of mineral wool in lightweight constructions is important. Experiments have shown the density and thickness of it to be important parameters, e.g., as shown in [21]. Some of the conclusions in [21] are briefly recollected below: The effect of the density of mineral wool is exemplified in Figure 1.1. As can be seen, for glass wool a density of 26 kg/m^3 is the best choice of the three samples, stone wool with a density of 35 kg/m^3 also functioning well, whereas glass wool with a density of 15 kg/m^3 functions less
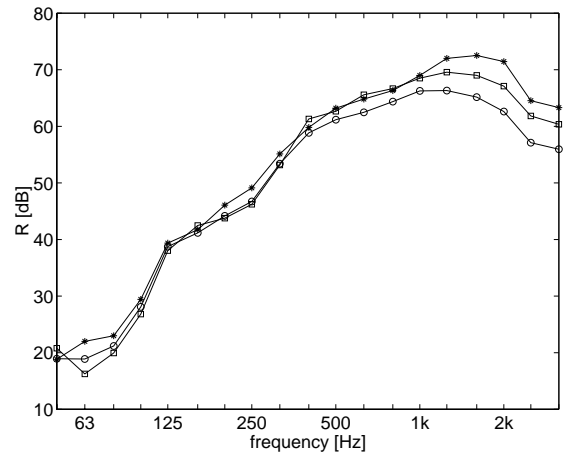
Figure 1.1: Effect of the density of the mineral wool on the transmission loss: glass wool 15 kg/m^3 (-∘-), glass wool 26 kg/m^3 (-∗-) and stone wool 35 kg/m^3 (-□-). 95 mm studs + 70 mm studs, 95 mm mineral wool, 2×13 mm plasterboard. After [21].

well. The largest differences are for frequencies greater than 250 Hz, although differences are also clearly evident for the lowest frequencies. Figure 1.2 shows the dependence of the transmission loss on the thickness of the mineral wool. If a wall with a total thickness of 165 mm is filled with mineral wool only 30 mm thick, the results are inferior to those obtained when mineral wool 95 mm thick is employed. If instead the mineral wool is 120 mm thick, the results are better yet for frequencies above 500 Hz and below 125 Hz. It should, however, be noted that the low frequency results are associated with measurement difficulties, making these results more uncertain.

Plasterboard consists of an inner core of plaster reinforced on both sides by an outer
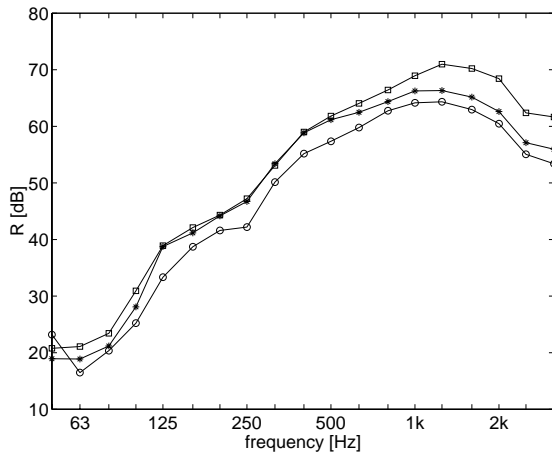
Figure 1.2: Effect of the degree of filling by mineral wool on the transmission loss: for a fiber thickness of 30 mm (-○-), of 95 mm (-∗-) and of 120 mm (-□-). 95 mm studs+70 mm studs, glass wool 15 kg/m^3, 2×13 mm plasterboard. After [21].

1.3 The systems-effects of building constructions

It is important to attend not simply to what happens within a given material or component (such as a plate or a beam), but also to what happens when different parts are coupled together. This is particularly true for lightweight constructions, since these consist of many different components, often joined together in a rather complicated way. In addition, a very broad frequency range is of interest, at least 50–5000 Hz, and in most cases still broader. The range is determined in part by the codes and classification standards that apply, and in part by what is important for a subjective evaluation of the construction. A broad frequency interval creates problems for the acoustician, as the wavelengths varying from several meters to only a few centimeters in length. This in turn affects what is important to consider when describing a construction; for example, the large-scale boundary conditions of the building structures or the anchoring of a single screw.

One of the most important assumptions when dealing with a given structure by use of the first approach mentioned above (e.g., SEA-like approaches), is that the field variables within each component (wall or room) are homogeneous. This means that, for any given frequency, the field (i.e., the sound pressure or vibration velocity) can be described by a single number. Nightingale [23], however, showed the fields to be far from constant over the area involved by measuring vi-

layer of cardboard, resulting in a sandwich structure. The characteristics of the plaster material itself are not so well known; it is relatively stiff, heavy and undamped (although it is more elastic and lighter in weight than concrete); it is probably isotropic. Of greater interest, however, is its behaviour as a component. The cardboard layers are important not for acoustical reasons but for facilitating production of the plasterboard, as well as for static and mechanical reasons. The reinforcement that the cardboard provides increases the shear deformations of the plaster layer, making it an important aspect already at low frequencies. When thus reinforced, plasterboards shows behaviour similar to that of thick plates, despite being quite thin [22].

Figure 1.3: A lightweight wall and a lightweight floor construction adjoining it were built in the sound-transmission laboratory at LTH, Lund. Photo: Lars-Göran Sjökvist.

bration velocities in lightweight wooden constructions. The measurements obtained suggest the vibrational energy to decrease with increasing distance from the source (or from the junction in question). This is to be expected from a structure that repeats itself in a nearly periodic way [24] – which is just what a lightweight structure reinforced with joists does. The joists and studs are located at some basic spacing, but there is always some degree of variation. In this thesis, this situation is more closely examined in [6]. Experiments in this area have been carried out by Sjökvist, as described in part (the experimental setup) in [25] and more thorough in [26]. The results and experimental setup found in [26] are briefly described below. As shown in Figure 1.3, a lightweight wall flanked by a lightweight floor construction was built in an air-transmission laboratory. Various flank-transmission measurements were performed.

The measurements of interest involved placing an ISO tapping machine at 6 different positions in the sending room, and at each of these positions the vibration velocity was measured at 10 randomly chosen positions in the recipient room. For each set of measurements, a linear regression was computed, where the distance from the separating wall served as the parameter. The aim was to determine whether the vibration velocity decreased with distance from the source. The results indicate a decrease by 2–6 dB/m, see Figure 1.4. This agrees with Nightingale's findings and shows the first approach referred to above – the simpler one – not to be appropriate for a construction of this type. A further observation of interest in Nightingale's [23] measurements is that the plates (in this case the OSB plates[1]) being finite in size and smaller than the floor structure as a whole is important for the manner in which vibrational energy is spread through them. One can clearly see that when vibration passes over a plate junction, the level of vibration decreases.

An important difference between building construction systems of the traditional and of the lightweight type is in the use of a simple slab or plate in the former case and of double plate in the latter. This is perhaps the most obvious difference between the two building construction systems and the one which has generated the greatest amount of research and contributed most to theory development [27, 28]. It also represents the area

---

[1]OSB means Oriented Strand Board and is a type of chipboard.
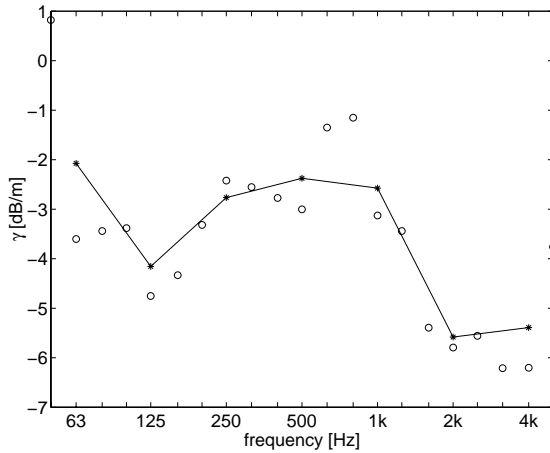
Figure 1.4: Sound transmission attenuation of a lightweight floor structure, γ. Each circle ○ represents the mean of 6 regressions over 10 measuring positions for each third octave band. The asterisk $*$ represent the corresponding octave bands. After [26].

in which the advantages of lightweight constructions are most obvious. The sound insulation a simple construction provides is as a first rough approximation determined by the mass law, i.e., the wall's weight alone being decisive for the sound insulation, and the transmission loss increases by 6 dB/octave[2]. A double construction, in contrast, can consist of two parallel plates separated by a cavity. The cavity can be filled either with air or with mineral wool. If one ignores the complications that can be introduced by the presence of mechanical connections by way of beams and studs (which, however, is the main subject of the thesis), one can conceive a double construction as consisting of two

simple constructions located in series. This makes it easy to understand why double constructions are advantageous: In the ideal case there are simply two layers of mass, one after the other, increasing the transmission loss to 12 dB/octave. In reality the transmission loss is never that great, partly because of the behaviour of beams and studs, and partly because of a resonance phenomenon that typically occurs in the low frequency range. This phenomenon, which can be described in terms of the inertia at the outer surface as well as the stiffness of the enclosed space (even air has stiffness), is referred to as the construction's basic resonance frequency. It is perhaps the most important design parameter in a double construction. In principle, the resonance frequency should always be as low as possible [29]. The cavity can be filled (partly or completely) with mineral wool. This has a positive effect in two different ways, partly that of the resonance being reduced by damping, and partly that of a fictive increase in the volume of the cavity being produced through the transition from adiabatic to isotherm compression – leading to a decrease in the resonance frequency. The studs or joists in the wall or floor structure are very important for the acoustic behaviour of the structure. If a double plate structure consists of a framework of studs, the studs will not only influence the vibration field directly, i.e., short-cutting the plates as sound bridges [30, pp. 462–474], but also affect the acoustic field in the cavities. The studs can be seen as walls within the cavities, thus introducing finiteness, which leads to resonances. Moreover, the studs are typi-

---

[2]An octave represents a doubling of the frequency.

cally given equal spacing, making the structure periodic (or at least nearly periodic, as discussed above). The periodicity not only causes the physics to involve some certain aspects – as passbands, stopbands and localisation [1] – it also makes it possible to reduce information in the prediction models, as in [4, 5, 6]. Recent measurements on wood stud walls, made by Bradley and Birta [31], show that the Lin and Garrelick theory [28] explains the most important low-frequency features of sound transmission through these wood stud walls. This fact can be seen as a confirmation that the approach taken in this thesis, i.e., a spatial transform approach taking into account the periodicity, is appropriate.

A floating floor is a type of double construction which, although frequently serving as a complement to massive constructions, can also be used in connection with a system of lightweight joists. Such a floor has many positive acoustic characteristics, particularly as regards high frequencies, whereas it is less effective in the case of low frequencies. It is also less well suited than other types of floors in terms of springiness and deformability. Having a strongly damped material located between the two surfaces is always advantageous here. If the layer between the two plates, instead of being a material that is deformed locally (as a resiliency effect, such as in the case of a foam or of mineral wool), is a layer that shears, such as a rubber mat, one obtains an extra damping effect without the negative effects that a floating floor would otherwise produce. Another solution is to let the two plates slide over each other more or

less friction-free.

When the distance between two plates becomes small, viscosity and other effects in the air gap between them become noticeable. One can distinguish between two separate (but closely related) phenomena: resonance and damping. The resonance phenomenon was first reported by Warnock [32] in a large series of measurements on wooden beam structures. In the sound level difference curve, the difference taken between the transmission loss for a construction with a single plate and one with two plates, a small but clear dip was found around 1 kHz. When two plasterboard plates are put together, there is always a small air gap between them, one which can be expected to be somewhat larger if they are attached suspended to a floor structure. Warnock estimated the air gap to be 1 mm in size. To determine whether a phenomenon of this sort could be observed in other measurements, the data reported in [21] were analyzed. The results are shown in Figure 1.5 (also being reported in [33]). A dip in the curve was found at 1.5 kHz, which basically corresponds to resonance from an air gap of 0.5 mm (the plates being masses). The damping phenomenon was discovered earlier, see for example [34], where the damping of steel plates is caused by the layer of air in between the plates. This phenomenon is due primarily to the viscosity of air, which has strongest effect when the gap is small, as is the case in the structures considered here (perhaps 0.01–1 mm), whereby thermic effects and friction may also have an effect [22]. In experiments, [35], involving freely hanging coupled plasterboards in which the distance

between the two plates varied from 0–1 mm, the damping was found to be optimal at distances of 0.3–0.5 mm. The damping achieved was then approximately $\eta = 0.025$ for 63 Hz and 0.02 for 1000 Hz; without the air gap, the damping was approximately $\eta = 0.013$ and 0.012, respectively, for the same frequencies. To this phenomena is then also added the screw connections between the two plates, which is a (nearly) periodic pointwise connection with possibly some resilient behaviour due to local deformation. A complete mechanical model of this situation – including viscous, thermic and mechanical effects – has not yet been achieved (even though attempts were made in [22, 33][3]). Thus, in all examples in this theses only single plates are considered.

It is quite common to use small resilient elements in a lightweight double construction so as to recapture some of the weakness lost through the presence of beams and studs. Resilient channels are frequently employed, for example, as elements in wooden floor structures. These are beams that can be deformed in their cross-section. The behaviour of the resilient channel is examined experimentally in [7], included in the thesis. The resilient channel is also studied by Bradley and Brita [36], containing both experimental results as well as simplified models of the effects the channel has on a lightweight wall. Another example is the use of either wooden or thin-walled steel studs in lightweight walls, where the latter can also be seen as being
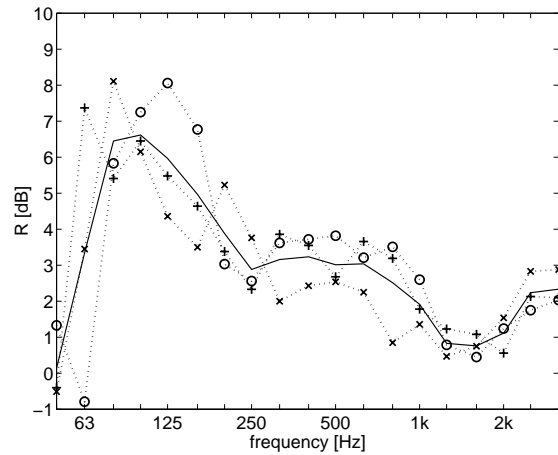
Figure 1.5: Difference between use of a single and of a double layer of plasterboard. The continuous line (—) represents the mean. Data taken from [21].

beams that can be deformed in their cross-section. The mechanical description of this phenomenon is not yet adequate, although much can be learned from experiments that have been carried out. The type of studs chosen has been shown to be an important parameter [21]. In walls containing 45 mm studs the transmission loss R_w is increased from 42 dB to 47 dB (R_w being the weighted single number transmission loss according to ISO 717-1 [37]), when a change from wooden studs to thin-walled metal studs was preformed (with use of mineral wool 30 mm thick at 15 kg/m^3, 2×13 mm plasterboard)(see Figure 1.6). One can readily see that the difference is considerable and that thin-walled steel studs are 5–15 dB better at frequencies above 250 Hz. For frequencies below 100 Hz the relation is the opposite. This could be a random result, however, since for low frequencies the

---

[3]This subject could have been included in the thesis if my computer had not been stolen.
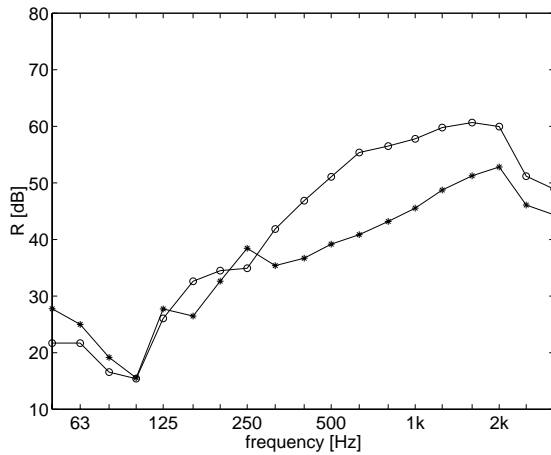
Figure 1.6: Difference between use of wooden (-∗-) and of steel studs (-∘-): 45 mm studs, 30 mm thick mineral wool 15 kg/m³, 2×13 mm plasterboard. After [21].
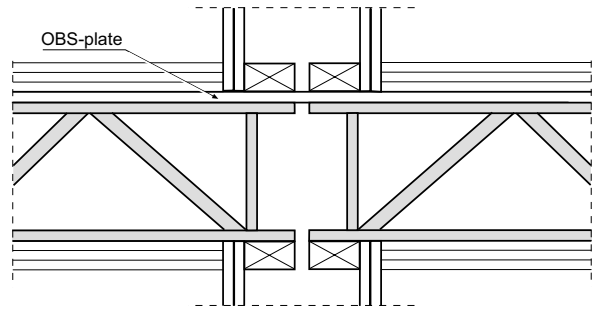
Figure 1.7: Junction between party wall and floor structure. Note that the OSB-plate is continuous across the wall. The floor construction is as follows: Carpet or parquet, 25 mm anhydrite, resilient layer, OSB, 400 mm wooden joist and 400 mm mineral wool 26 kg/m³, resilient channels, 2×13 mm plasterboards. Orgelbänken, Linköping [9].

measurement error is large, but is more likely due to the extra weight of the wooden studs compared to the thin-walled steel studs.

In order to build successfully using lightweight building techniques, one also needs to deal successfully with flanking transmission problems. The junction between walls separating adjoining apartments and floor structures is constructed in a manner aimed at reducing the transmission of flanking sounds. In principle, this can be accomplished by means of completely separating the construction frameworks of the adjoining apartments from each other. Although separation, if it can be accomplished, is always a safe solution, it is often not a practicable one, since the framework need to be stabilised in order to manage e.g. horizontal wind loads. Although adequate theoretical models for the flanking transmission have not yet been de-

veloped, practical solutions can be found in [38, 9]. Although one approach is to only stabilize the structure at its stiffest points, there are also more unconventional solutions that if adequately worked out, can yield satisfactory results. Orgelbänken, for example, achieved excellent results with use of a board of OSB (a sort of chipboard) that was continuous through the junction as shown in Figure 1.7 and described more closely in [38, 9].

For lightweight floor structures, footsteps represent the primary source of disturbances. At low frequencies, the sound level is determined primarily by the person's body weight, foot weight, and number of steps per second. At high frequencies, the type of footwear is relevant [39]. An important difference between the sound of footsteps and other sources of noise is that, even at low frequencies, footsteps produce a high degree of noise

disturbance. In most countries, assessments of the level of noise produced by footsteps involve use of a standardised tapping machine as a source of sound (whereas in Japan use is made of a machine on which rubber tires are mounted, the idea being that the excitation more closely resembles that of a walking person). The tapping machine consists of five steel cylinders. These are made to strike the beam structure being tested at an overall repetition frequency of 10 Hz. For massive floor structures, regardless of whether bare or covered, the characteristics of the force spectrum of this process have long been known [30, 40, 41]. This force spectrum cannot necessarily be assumed to apply, however, to a lightweight floor structure. The force spectrum that the tapping machine produces on such a structure is therefore analysed in this thesis [3]. The difference can be described briefly as being that for a massive floor structure with a resilient layer in terms of floor covering, with a deformation of the floor covering. A loss of energy will then only occur at that deformation zone. In contrast, in a lightweight floor structure, loss of energy also takes place through the propagation of waves within the plate, a local deformation occurring primarily in the plate's cross-section (where the degree of local deformation can be determined according to the reference [2], included in this thesis). In determining the force spectrum of a lightweight floor structure, one needs in principle to take account of the entire structure (individual beams and the like included). The force spectrum plays an important role, since it can vary in a quite large span; for low frequencies

it can vary as much as 6 dB, and for high frequencies the span is still greater. The 6 dB variation can be found by considering the extreme cases of the cylinder leaving the plate or not [3, 41].

It should also be noted that even though the excitation situation is quite different in the case of impact noise compared to airborne noise, there are some similarities: In the latter case, a diffuse sound field is assumed meaning that all angles of incidence have the same probability, each angle giving rise to one set of wavenumber. Thus, the transmission loss is found by integrating over all possible incident angles. In the former case, all wavenumbers are excited at once, but the radiated power (that is the quantity of interest) is found by means of integrating over the angles that can be radiated to. Thus, in both cases the same amount of (possibly numerical) integration is required.

1.4 How sound is experienced

Acoustics is mostly of importance from the standpoint of hearing and of how sound and vibrations are perceived and experienced. In building acoustics and sound isolation, the major aim in setting building codes is to see to it that the sound disturbances that are experienced do not exceed some reasonable limit, based on what is generally accepted. This is the intention of the official regulations in Sweden contained in BBR [42] and in SS 025267 / -68 [43, 44], a matter which

should be borne in mind in discussions between building contractors and those commissioning building projects. The requirements for sound insulation that have long existed were formulated with homogeneous simple constructions in mind. It has been found that these requirements do not function as they should in regard to lightweight constructions, which behave quite differently in the case of low frequencies than massive constructions do, low frequencies also being dominant in connection with footsteps. Another quite important aspect of the problem is that of the source of noise adjusting to the structure involved; it is more pleasant to come down hard on one's heels when walking on a wooden floor structure than when walking on a concrete floor. Thus, children might be more inclined to run around more wildly on a lightweight floor structure than on a concrete floor (although this is simply an hypothesis). Matters such as these make it important to formulate other criteria and building codes than the traditional ones. Working out the details of such building codes calls for widespread and systematic interviews with those living in such buildings. The results can then be examined further with the help of statistical methods in order to relate different objectively measurable results with subjective ratings. A measure that in an optimal way correlates the subjective ratings with the objective sound insulation measurement can then be chosen. Pioneering work in this area in regard to the impact sound in lightweight floor structures was carried out by Fasold [45] and Bodlund [46]. A very useful side-effect of the latter work was the finding that the

number of residents in an apartment house who are disturbed by the sound of footsteps can be estimated from the impact-noise frequency curve of the floor structure involved. This finding was made use of in the design of the floor structures of the wooden buildings erected in Sweden within the framework of the Nordic Wood Project (in the building projects Wälludden and Orgelbänken [9]). The assessments of interviews with the tenants carried out some time after the houses were finished confirmed the subjective predictions made. The methods employed are described in [9] and to some extent in [38]. Lately, laboratory tests of footstep noise and subjective evaluation have been carried out [47, 48]. Listening tests showed that using loudness to evaluate the impact sound yields a high correlation with listeners' preference values, also when the tapping machine is used as the source.

1.5 Summary of the introduction

In conclusion, one can state that to understand the acoustics of lightweight building constructions it is not enough to simply take account of results obtained for massive constructions. A more detailed approach is needed, involving deep knowledge and understanding of the material contained in such constructions and of different methods of relevance, together with insight of how different materials and components can be employed in conjunction with each other in a way al-

lowing the system phenomena that are typical of lightweight constructions to be adequately exploited. It is also important to gain a greater understanding of how the acoustic characteristics of lightweight buildings affect how sound is perceived by the inhabitants.

The present thesis presents papers addressing most of these aspects, except for the subjective experience.

Chapter 2

More about periodicity

As was stated in the preceding chapter, periodicity is one of the typical features of a lightweight structure. In this chapter various approaches to take account of the periodicity in a Fourier transform solution of the governing equations is dealt with, as this is the main idea behind the prediction models presented in this thesis. This chapter is a complement to the literature survey in [1]; the approach here is more theoretical. Moreover, even though the number of references herein is not as large as in [1], some additional references of relevance have been found and thus included [49, 50, 51]. Moreover, compared to the discussion in [1] the paper by Rumerman [52] is put forward herein. The approach used by Mace in [53, 54, 55, 56] is basically the one used by Rumerman. The fact that the use of Floquét's principle is used in the Rumerman's approach but not in the approach following Evseev is described now, as this may be a key difference.

Three approaches are presented: The first is used by Evseev [57], Lin and Garelik [28], Mace [17] and Takahashi [58], and by the present author in [3, 4]. This approach will be denoted *Evseev's approach*. The second approach is used by Rumerman [52], Mace [53, 54, 55, 56], Skelton [49] and by the present author in [6, 5], and will be denoted *Rumerman's approach*. Nordborg [51] uses the third approach, and will be denoted *Nordborg's approach*.

Urusovskii [50], dealing with double plate systems, uses a space harmonic approach, similar, for example to Mead and Pujara [59] (cf. [1, 60]). This type of approach will not be discussed further here.

It should also be noted that periodically supported systems are treated in Morse and Ingard [61, pp. 662–679, 695], where the situation of a thin plate periodically loaded with line impedances is given as a student problem.

2.1 The basic problem

The basic problem, which in this chapter is taken to be a plate reinforced by beam stiffeners with equal spacing, can be described as a differential equation with a periodic array of reaction forces. The problem in question

can be with or without excitation (the later problem referred to as free wave motion), and the excitation can be periodic or non-periodic in space. That gives in total three cases, roughly corresponding to the three approaches above, as will be evident. (See also the discussion in [1].)

The governing differential equation describing the problem can symbolically be written

$$\mathcal{S}[w] = p_e - \sum_{n=-\infty}^{\infty} F_n \delta(x - nl), \qquad (2.1)$$

where $w(x, y)$ is the displacement of the plate, $p_e(x, y)$ is the excitation pressure and $F_n(y)$ is a reaction line force (from the beam stiffeners), and where $\mathcal{S}$ is the differential operator, typically the Kirchhoff plate operator (other forms of the operator can thus also apply)

$$\mathcal{S} = B' \left(\frac{\partial^2}{\partial x^2} + \frac{\partial^2}{\partial y^2} \right)^2 - \omega^2 m'', \qquad (2.2)$$

where $B' = EI'/(1 - \nu^2)$ is the bending stiffness per unit width, E is Young's modulus, $I' = h^3/12$ is the moment of inertia per unit width, ν is the Poisson ratio, h is the plate thickness and m'' is the mass per unit area, see for example [30, pp. 95–109]. A Fourier transform of (2.2) in the x-y-coordinates, using (2.8), becomes

$$S = B' \left(\alpha^2 + \beta^2 \right)^2 - \omega m'', \qquad (2.3)$$

which is an algebraic expression.

The beams reinforcing the plate can be described by a similar differential equation,

$$\mathcal{G}[w_n] = F_n, \qquad (2.4)$$

where $w_n(y) = w(nl, y)$ is the displacement of the n'th beam, and also the displacement of the plate at that position (and thus a boundary condition assuring equal displacement in the intersection). The differential operator $\mathcal{G}$ is typically a Euler beam operator

$$\mathcal{G} = B_f \frac{\partial^4}{\partial y^4} - \omega^2 m'_f, \qquad (2.5)$$

where $B_f = E_f I_f$ is the bending stiffness of the beam, E_f is the Young's modulus of the beams, I_f is the moment of inertia of the beams and m'_f is the mass per unit length of the beams. A Fourier transform of (2.5) in the y-coordinate, using (2.10), becomes

$$G = B_f \beta^4 - \omega^2 m'_f. \qquad (2.6)$$

In this description the beams affect the plate only as line forces, and no moment coupling is included. This is also the case in the papers in this thesis [4, 5, 6]. However, in chapter 3 the moment coupling is introduced.

2.2 Fourier, Floquet, Bloch and Poisson

Before we proceed with the three approaches, some general theorems and formulas must first be presented, so that these can be employed in the succeeding sections.

The main approach to solve differential equations in the thesis is to make use of the Fourier transform, applied to the spatial coordinates. Those not familiar with the Fourier transform technique may wish to refer to the standard textbooks in mathematics

for theoretical physics [62, 63]. However, the actual transform pair used has to be defined: The Fourier transform pair used in this thesis is, in the two-dimensional case

$$u(x,y) = \frac{1}{4\pi^2} \iint\limits_{-\infty}^{\infty} \tilde{u}(\alpha, \beta) \mathrm{e}^{-\mathrm{i}(\alpha x + \beta y)} \mathrm{d}\alpha \mathrm{d}\beta \quad (2.7)$$

for the inverse transform (u being an arbitrary function), and

$$\tilde{u}(\alpha, \beta) = \iint\limits_{-\infty}^{\infty} u(x,y) \mathrm{e}^{\mathrm{i}(\alpha x + \beta y)} \mathrm{d}x \mathrm{d}y \qquad (2.8)$$

for the forward transform, where α and β are the transform wavenumbers. In the one-dimensional case the transform pair is

$$u(x) = \frac{1}{2\pi} \int\limits_{-\infty}^{\infty} \tilde{u}(\alpha) \mathrm{e}^{-\mathrm{i}\alpha x} \mathrm{d}\alpha \qquad (2.9)$$

and

$$\tilde{u}(\alpha) = \int\limits_{-\infty}^{\infty} u(x) \mathrm{e}^{\mathrm{i}\alpha x} \mathrm{d}x, \qquad (2.10)$$

where x and α can be exchanged by y and β. If both the one- and the two-dimensional transform pairs are used, then the symbol $\breve{}$ is employed instead of $\tilde{}$ in the one-dimensional case.

Floquet's principle concerning wavemotion in periodic structures is a useful tool employed frequently in the thesis. A discussion of the principle is included below. As no really adequate proof of the principle has been found, it is also made probable. Originally the principle was restricted to solutions of

Mathieu's equation; proof and discussions of this case can be found, for example, in [62, pp. 555–557] or [64, 65].

The principle is made most probable if one consider a simple periodic structure consisting of a cascade of identical substructures, e.g., a chain of masses and springs [30, pp. 405–415]. It is then found that the ratio of the value of a field variable at the input point of a substructure to that at the output point of the substructure is the same for all elements:

$$u_{n+1} = u_n e^g,$$

or by repeated use

$$u_0 = u_n e^{-ng}, \qquad (2.11)$$

where u is an arbitrary field variable. However, the principle is only made probable by means of an example. A more elaborate investigation would be appropriate.

Since the assumed form of the solution indicated in equation (2.11) places no restriction on the exponent g, one may take this exponent to be complex,

$$g = a + \mathrm{i}b.$$

In the simplest cases (as the one discussed in this chapter), the exponent is either the 'attenuation coefficient' satisfying $a = 0$, or the 'phase coefficient' satisfying $b = n\pi$, where $n = 0, 1, 2, \cdots$. The first of this cases is referred to as a pass band, the second as a stop band.

Brillouin, in his book on wave propagation in periodic structures [65] discusses Floquet's and Bloch's principles. Floquet's theorem (or

principle) can be expressed as follows: A one-dimensional homogenous Helmholtz equation with periodic wave-speed can be written

$$\frac{\partial^2 u}{\partial x^2} + J(x)u = 0 \qquad (2.12)$$

where $J(x) = \omega^2/c^2(x)$ is l-periodic (ω is the angular frequency and c is the wave speed). According to Brillouin, an equation of the type (2.12) is called a Hill's equation, and has the solution

$$u(x) = A(x)e^{\mu x} \qquad (2.13)$$

where $A(x)$ has a period l. This means, for instance,

$$u(x) = e^{\mu l}u(x-l)$$

and

$$u(0) = u(nl)e^{-\mu n l}$$

which is the same result as (2.11) if $g = \mu l$. The general solution is then built up by two solutions of the form, (2.13)

$$u(x) = A_1(x)e^{\mu x} + A_2(x)e^{-\mu x}.$$

Bloch's theorem is simply the extension of Floquet's theorem to a three-dimensional periodicity, according to Brillouin. A three-dimensional periodicity is of interest, for example, in wavemotion through crystal lattices. In the 'Dictionary of acoustics' [66] only the term *Bloch wave* is used:

> Bloch wave – *in a medium or waveguide whose structure is periodic in the propagation direction* a propagating single-frequency wave

in which the same pattern is repeated within each cell or period of the structure, with a fixed phase shift from one cell to the next (F Bloch 1928). [...]

This definition or description corresponds to equation (2.13). In the present thesis only the term *Floquet's principle* (or *theorem*) will be used, and only one-dimensional periodicity is considered.

The case of a periodically driven inhomogeneous Hill's differential equations is not considered by Brillouin. However, it is quite simple to show that a version of Floquet's principle holds also for this case. The inhomogeneous Hill's differential equation can be written

$$\frac{\partial^2 u}{\partial x^2} + J(x)u = \mathrm{e}^{-\mathrm{i}k_x x}, \qquad (2.14)$$

where once again $J(x)$ is l-periodic, $J(x) = J(x-l)$. We are only interested in the steady state solution, so the solution will be of the form

$$u(x) = A(x)\mathrm{e}^{-\mathrm{i}k_x x}, \qquad (2.15)$$

where $A(x)$ is still undetermined. Insert this assumption in equation (2.14), which yields

$$J(x) = A^{-1}(x)\left(1 - \mathcal{L}[A(x)]\right), \qquad (2.16)$$

where the operator $\mathcal{L}$ is due to the double derivation of (2.15), and is defined as

$$\mathcal{L}[A] = \frac{\partial^2 A}{\partial x^2} - \mathrm{i}2k_x\frac{\partial A}{\partial x} - k_x^2 A.$$

It should here be noted that $\mathcal{L}$ operating on A do not affect any possible periodicity; if A is periodic so is $\mathcal{L}[A]$. By inspection of

equation (2.16) it can be seen that the left hand side of the equation is l-periodic, which means that also the right hand side of the equation is l-periodic. This result is fulfilled only if $A(x - l) = A(x)$ as this is the only parameter with a x-dependency. $A(x)$ is therefore also l-periodic. Thus, equation (2.15) is the Floquet's principle in this case, where μ is exchanged by $-\mathrm{i}k_x$ if we compare with (2.13). It should also be mentioned that the same type of argument can be used in the free wave case. The solution is then assumed to be of the form

$$u(x) = A(x)e^{\mu x},$$

which after some manipulation leads to

$$J(x) = -\mathcal{L}[A(x)]/A(x),$$

where both the left and the right side has to be l-periodic.

The situation so far is that we know that Floquet's principle holds for free and forced wave propagation in the Hill-type of differential equations, and we have a similar relation (2.11) for simplified structures (however only shown in examples). We do not have a Floquet theorem that holds for more general types of differential equations or waveguides, such as a plate reinforced by beams at a periodic distance. In [1] the present author uses simple geometrical arguments to show that Floquet's theorem holds also in this case. However, also this type of situation can be brought back to the Hill equation, as will be shown in a simple example: Consider a periodically stiffened plate as described by equation (2.1–2.2). The excitation is of the form

$p_e = \mathrm{e}^{-\mathrm{i}k_x x - \mathrm{i}k_y y}$. Thus, the governing equation can be written

$$B'\left(\frac{\partial^2}{\partial x^2} - k_y^2\right)^2 w - \omega^2 m'' w$$

$$= \mathrm{e}^{-\mathrm{i}k_x x} - \sum_{n=-\infty}^{\infty} F_n \delta(x - nl), \quad (2.17)$$

where the y-dependency is suppressed. The reaction forces F_n are described by equations (2.4–2.5). If these equations are introduced in (2.17), we can after some rearrangements write

$$B'\left(\frac{\partial^2}{\partial x^2} - k_y^2\right)^2 w - J(x)w = \mathrm{e}^{-\mathrm{i}k_x x}, \quad (2.18)$$

where

$$J(x) = \omega^2 m'' - G \sum_{n=-\infty}^{\infty} \delta(x - nl)$$

which is l-periodic and fulfills $J(x) = J(x-l)$. G is found in equation (2.6) with β exchanged by k_y. Equation (2.18) is thus of Hill-type, but of order four instead of two. However, as was seen in the discussion of the forced Hill equation and especially in equation (2.16), the order of the differential equation has no significant importance for Floquet's principle. Thus, the principle holds also in this case. For the general driven waveguide Floquet's principle is written

$$w(x - nl) = w(x)\mathrm{e}^{-\mathrm{i}k_x nl}, \quad (2.19)$$

where k_x is the forced wavenumber, caused by the excitation of the form $p_e = \hat{p}_e \exp(-\mathrm{i}k_x x)$.

A very useful tool in the analysis of infinite sums is the Poisson sum formula. It relates one infinite sum with another, that in some cases can then be written in a closed form by means of the geometric series. The Poisson sum can be derived by contour integration and Fourier transformation (cf. Morse and Feshbach [62]) and can be written

$$\sum_{n=-\infty}^{\infty} g(an) = \frac{2\pi}{a} \sum_{n=-\infty}^{\infty} \tilde{g}(2n\pi/a) \quad (2.20)$$

where $\tilde{g}$ is the Fourier transform of g. One useful example of the Poisson sum formula is that it can be used to show that

$$\sum_{n=-\infty}^{\infty} e^{i\alpha nl} = \frac{2\pi}{l} \sum_{n=-\infty}^{\infty} \delta(\alpha - 2n\pi/l), \quad (2.21)$$

which states that a sum of harmonics equal a sum of Dirac functions.

2.3 Evseev's approach

The problem is described by an inhomogeneous differential equation, described in equation (2.1), and a boundary condition (equal for al n), described in equation (2.4). In Evseev's approach the driving pressure does not need to be periodic; it can especially be a point force $p_e = \hat{p}_e \delta(x - x_0)$. Thus, Floquet's principle is not applicable in this case. However, the Poisson sum formula is still possible to use.

The Fourier transform in x and y can be applied so that (2.1) becomes

$$S\tilde{w} = \tilde{p}_e - \sum_{n=-\infty}^{\infty} F_n e^{i\alpha nl} \quad (2.22)$$

where $\tilde{p}_e = \hat{p}_e \exp(i\alpha x_0 + i\beta y_0)$ for a point force located at (x_0, y_0). Applying the Fourier transform to (2.4) yields

$$G\breve{w}_n = F_n \quad (2.23)$$

where

$$\breve{w}_n(\beta) = \int_{-\infty}^{\infty} w(nl, y)e^{i\beta y}dy$$

is the Fourier transform in the y-direction (2.10). However, it can also by definition be written

$$\breve{w}_n(\beta) = \frac{1}{2\pi} \int_{-\infty}^{\infty} \tilde{w}(\alpha^*, \beta)e^{-i\alpha^* nl}d\alpha^*, \quad (2.24)$$

where α^* is used in order to distinguish the new integration variable from the old (thus, it does not mean a complex conjugate in this case). The force array becomes, by using (2.23)

$$\sum_{n=-\infty}^{\infty} F_n e^{i\alpha nl} = G \sum_{n=-\infty}^{\infty} \breve{w}(nl, \beta)e^{i\alpha nl}. \quad (2.25)$$

By also making use of (2.24)

$$\sum_{n=-\infty}^{\infty} F_n e^{i\alpha nl} \quad (2.26)$$

$$= \frac{G}{2\pi} \sum_{n=-\infty}^{\infty} \int_{-\infty}^{\infty} \tilde{w}(\alpha^*, \beta)e^{-i\alpha^* nl}d\alpha^* e^{i\alpha nl}.$$

The Poisson sum formula is now to be used. Thus, using the result (2.21), and then inter-

changing the order of summation and integration in (2.26) yields

$$\sum_{n=-\infty}^{\infty} F_n \mathrm{e}^{\mathrm{i}\alpha n l} \qquad (2.27)$$

$$= G \int_{-\infty}^{\infty} \tilde{w}(\alpha^*, \beta) \sum_{n=-\infty}^{\infty} \delta((\alpha - \alpha^*)l - 2\pi n) \mathrm{d}\alpha^*$$

$$= \frac{G}{l} \sum_{n=-\infty}^{\infty} \tilde{w}(\alpha - 2n\pi/l, \beta).$$

The transformed displacement can be solved for, using (2.22) and (2.27)

$$\tilde{w}(\alpha) = \frac{\tilde{p}_e(\alpha)}{S(\alpha)} - \frac{G}{lS(\alpha)} \sum_{n=-\infty}^{\infty} \tilde{w}(\alpha - 2n\pi/l).$$
$$(2.28)$$

However, a $\tilde{w}$ term is still present in the right hand side of equation (2.28). Substitute $\alpha \to \alpha - 2m\pi/l$ and sum over all m, making use of the fact that

$$\sum_{n=-\infty}^{\infty} \tilde{w}(\alpha - 2n\pi/l - 2m\pi/l) = \sum_{n=-\infty}^{\infty} \tilde{w}(\alpha - 2n\pi/l),$$

for integer m, then yields

$$\sum_{m=-\infty}^{\infty} \tilde{w}(\alpha - 2m\pi/l) = \sum_{m=-\infty}^{\infty} \frac{\tilde{p}_e(\alpha - 2m\pi/l)}{S(\alpha - 2m\pi/l)}$$

$$- \sum_{m=-\infty}^{\infty} \frac{G}{lS(\alpha - 2m\pi/l)} \sum_{n=-\infty}^{\infty} \tilde{w}(\alpha - 2n\pi/l),$$

or after some rearrangements

$$\sum_{m=-\infty}^{\infty} \tilde{w}(\alpha - 2m\pi/l) = P(\alpha)l / (l + GT_0(\alpha)),$$
$$(2.29)$$

where the following notations have been introduced

$$T_0(\alpha) = \sum_{m=-\infty}^{\infty} \frac{1}{S(\alpha - 2m\pi/l)}, \qquad (2.30)$$

$$P(\alpha) = \sum_{m=-\infty}^{\infty} \frac{\tilde{p}_e(\alpha - 2m\pi/l)}{S(\alpha - 2m\pi/l)}. \qquad (2.31)$$

The transformed displacement is then found to be

$$\tilde{w}(\alpha) = \frac{\tilde{p}_e(\alpha)}{S(\alpha)} - \frac{GP(\alpha)}{S(\alpha)\,(l + GT_0(\alpha))}. \quad (2.32)$$

The displacement $w(x)$ can be found by means of applying the inverse Fourier transform (2.7). This operation is not trivial to perform analytically. This is a drawback of Evseev's approach compared to other approaches. However, it is not always necessary to perform this operation, as discussed below and in chapter 4, due to the fact that the transformed displacement is the basis for calculating the radiated power. In the appendix of [3] is a procedure to perform a numerical integration, based on [54].

Evseev's approach is appropriate when the exciting pressure is non-periodic, or when Heckl's formulas for power radiation [30, pp. 526–537] are to be used (repeated in chapter 4) or when the far-field pressure is to be calculated, as in both the later cases the transformed version of the field variables is used as a start point.

23

2.4 Rumerman's approach

In Rumerman's approach both the structure and the excitation is periodic, so Floquet's principle can be employed. Once again the problem is described by an inhomogeneous differential equation described in equation (2.1), and a boundary condition (equal for all n) described in equation (2.4). In this case the excitation pressure needs to be periodic, and more specifically of the form

$$p_e = \hat{p}_e \mathrm{e}^{-\mathrm{i}k_x x}$$

Floquet's principle (2.19) is then valid, which in the present case takes the form

$$F_n = F_0 \mathrm{e}^{-\mathrm{i}k_x nl} \tag{2.33}$$

and thus, equation (2.1) can be written

$$\mathcal{S}[w] = \hat{p}_e \mathrm{e}^{-\mathrm{i}k_x x} - F_0 \sum_{n=-\infty}^{\infty} \mathrm{e}^{-\mathrm{i}k_x nl} \delta\left(x - nl\right),$$

implying that only the 0'th boundary condition has to be used. By use of Fourier transformation this equation becomes

$$S\tilde{w} = 2\pi\hat{p}_e \delta(x - k_x) - F_0 \sum_{n=-\infty}^{\infty} \mathrm{e}^{-\mathrm{i}k_x nl}\mathrm{e}^{\mathrm{i}\alpha nl} \tag{2.34}$$

The Poisson sum formula is used to show that

$$\sum_{n=-\infty}^{\infty} \mathrm{e}^{-\mathrm{i}k_x nl}\mathrm{e}^{\mathrm{i}\alpha nl} = \frac{2\pi}{l} \sum_{n=-\infty}^{\infty} \delta(\alpha - k_x - 2n\pi/l),$$

compare with (2.21). Thus, equation (2.34) can be written

$$\begin{aligned} S\tilde{w} &= 2\pi\hat{p}_e \delta(x - k_x) \\ &- F_0 \frac{2\pi}{l} \sum_{n=-\infty}^{\infty} \delta(\alpha - k_x - 2n\pi/l) \end{aligned}$$

which is easily inverse transformed (due to the Diracs)

$$w = \frac{\hat{p}_e}{S(k_x)}\mathrm{e}^{-\mathrm{i}k_x x} - \frac{F_0}{l} \sum_{n=-\infty}^{\infty} \frac{\mathrm{e}^{-\mathrm{i}(k_x + 2n\pi/l)x}}{S(k_x + 2n\pi/l)} \tag{2.35}$$

or

$$w(x) = w_\infty(x) - F_0 T(x) \tag{2.36}$$

where the meaning of the notations can be identified in (2.35). Two alternative forms of writing the solution will be presented. The first alternative form is

$$w(x) = A(x)\mathrm{e}^{-\mathrm{i}k_x x}, \tag{2.37}$$

where

$$A(x) = \frac{\hat{p}_e}{S(k_x)} - \frac{F_0}{l} \sum_{n=-\infty}^{\infty} \frac{\mathrm{e}^{-\mathrm{i}2n\pi x/l}}{S(k_x + 2n\pi/l)} \tag{2.38}$$

is l-periodic, compare with equation (2.15). The second alternative form is

$$w(x) = \sum_{n=-\infty}^{\infty} W_n \mathrm{e}^{-\mathrm{i}(k_x + 2n\pi/l)x}, \tag{2.39}$$

where

$$W_n = \frac{\hat{p}_e}{S(k_x)}\delta_{0n} - \frac{F_0}{l}\frac{1}{S(k_x + 2n\pi/l)}$$

24

and where δ_{0n} is the Kronecker delta. This form of the solution equals the space harmonic form used, for example, by Mead and Pujara [59], see also Mead [60].

The reaction force F_0 is now to be determined from equation (2.5) and (2.36), letting $x \to 0$

$$F_0 = \frac{\mathcal{G}[w_\infty(0)]}{1 + \mathcal{G}[T(0)]}$$

where $\mathcal{G} \to G$ if a $\exp(-\mathrm{i}k_y y)$ dependency is assumed in the y-direction parallel with the beams (which is assumed henceforth in this section).

Free waves are found if $w_\infty \to 0$

$$w(0) = -F_0 T(0).$$

By applying the beam operator $\mathcal{G}$ and use equation (2.5)

$$Gw(0) = -F_0 GT(0) = F_0,$$

simplified to

$$1 + GT(0) = 0. \qquad (2.40)$$

Equation 2.40 is the dispersion equation that has to be solved in order to get the appropriate wavenumbers. Every pair (f, k_y) then yields a number of solutions μ (or k_x).

If the response of a point force is of interest, equations (2.7) and (2.37) can be combined as

$$w(x,y) = \frac{1}{4\pi^2} \iint_{-\infty}^{\infty} A(x_0) \mathrm{e}^{-\mathrm{i}(k_x x + k_y y)} \mathrm{d}k_x \mathrm{d}k_y, \qquad (2.41)$$

where in the present case $\hat{p}_e = F \exp(\mathrm{i}k_x x_0)$ (assuming $y_0 = 0$), and thus equation (2.38)

becomes (if also incorporating F_0)

$$\begin{aligned} A(x_0) \;=\; & \frac{F\mathrm{e}^{\mathrm{i}k_x x_0}}{S(k_x)} \\ & - \frac{GP(k_x)}{S(k_x)(l + GlT(0))} \end{aligned}$$

which should be compared with equation (2.32) in Evseev's approach (where $T(0) = T_0/l$), and where

$$P(k_x) = \sum_{n=-\infty}^{\infty} \frac{F e^{\mathrm{i}(k_x - 2n\pi/l)x_0}}{S(k_x + 2n\pi/l)}.$$

Equation (2.41) is thus identical with the inverse transform of equation (2.32) in Evseevs approach. The integral is examined by Mace in [54]. In the presence of fluid loading, numerical integration has to be applied (but the integrals can be simplified due to the periodicity). If neglecting the fluid loading, the numerical integration is simplified.

Rumerman's approach is thus an elegant way to get the displacement due to a convected harmonic pressure. However, when the response to a point force is of interest, then the both approaches yield the same integral to be solved.

2.5 Nordborg's approach

Nordborg's approach is very similar to Rumerman's approach; the difference is basically the order in which the operations are applied. However, Nordborg in his paper is interested in the free wave propagation, which then is used to form the response of a point force. This strategy is also used herein.

The homogenous version of the governing equation (2.1) is,

$$\mathcal{S}[w] = -\mathcal{G}[w] \sum_{n=-\infty}^{\infty} \delta\left(x - nl\right)$$

where the boundary conditions (2.4) has been included directly into the equation. The Fourier transform of this equation is given by

$$S\tilde{w} = -G \sum_{n=-\infty}^{\infty} w(nl)e^{i\alpha nl}$$

The Floquets principle can be applied then, in the present case

$$w(nl) = w(0)e^{\mu ln}$$

and thus

$$\tilde{w} = -\frac{Gw(0)}{S} \sum_{n=-\infty}^{\infty} e^{\mu ln}e^{i\alpha nl} \qquad (2.42)$$

Inverse transform equation (2.42), formally written

$$w(x) = -w(0) \sum_{n=-\infty}^{\infty} e^{\mu ln} I_n(x), (2.43)$$

$$I_n(x) = \mathcal{F}_x^{-1}\left\{G/S\right\}$$

(where the y-dependency is assumed to be of the form $e^{-ik_y y}$). The integral I_n can usually be evaluated by means of contour integration and residue calculus, whereafter the sum can be evaluated to give a closed formulation. If this is not possible, as the case when fluid loading is present, Rumermans approach is an alternative.

Putting $x = 0$ in equation (2.43) gives the dispersion relation to determine the possible μ

$$1 + \sum_{n=-\infty}^{\infty} e^{\mu ln} I_n(0) = 0 \qquad (2.44)$$

which is identical to equation (2.40), the difference in the representation of the sum being exactly the Poisson formula. Every pair (f, k_y) then yields a number of solutions μ (or k_x). The differential equation (2.1–2.2) is of order four, and there should therefore be four solutions to (2.44). These can be denoted $\pm\mu_a$ and $\pm\mu_b$. The general solution can be written

$$w(x) \qquad\qquad\qquad (2.45)$$
$$= c_{+a}A(x,\mu_a)e^{\mu_a x} + c_{-a}A(x,-\mu_a)e^{-\mu_a x}$$
$$+ c_{+b}A(x,\mu_b)e^{\mu_b x} + c_{-b}A(x,-\mu_b)e^{-\mu_b x}$$

where $c_{\pm a}$ and $c_{\pm b}$ are constants to be determined by boundary conditions, and where

$$A(x,\mu) = \sum_{n=-\infty}^{\infty} e^{\mu ln} I_n(x) \qquad (2.46)$$

is l-periodic, cf. section 2.2.

When the response of a point force is wanted, which is the Green's function $G(x|x_0)$ to the problem, Nordborg uses the free waves to build the field. The approach is suited for the case of a periodic beam (Nordborg studied rail vibrations), or the response of a line force on a plate. Since the solution must remain finite as $x \to \pm\infty$, only two solutions (out of four) are possible on each side of the force. Thus, inside the first bay,

$0 \leq x \leq l$, Green's function can be found as

$$G^r(x|x_0) \tag{2.47}$$
$$= c_{-a}A(x,-\mu_a)e^{-\mu_a x} + c_{-b}A(x,-\mu_b)e^{-\mu_b x}$$

where $G(x|x_0) = G^r(x|x_0)$ if the observation point is to the right of the excitation point, $x_0 \leq x \leq l$, and

$$G^l(x|x_0) \tag{2.48}$$
$$= c_{+a}A(x,\mu_a)e^{\mu_a x} + c_{+b}A(x,\mu_b)e^{\mu_b x}$$

and where $G(x|x_0) = G^l(x|x_0)$ if the observation point is to the left of the excitation point, $0 \leq x \leq x_0$. Outside the first bay, $0 \geq x$ or $x \geq l$, Floquet's theorem is to be used. The four constants $c_{\pm a}$ and $c_{\pm b}$ are chosen to match the boundary conditions in the source region, which are [51]

$$G^r(x_0) - G^l(x_0) = 0,$$
$$\left.\frac{\partial G^r}{\partial x}\right|_{x=x_0} - \left.\frac{\partial G^l}{\partial x}\right|_{x=x_0} = 0,$$
$$\left.\frac{\partial^2 G^r}{\partial x^2}\right|_{x=x_0} - \left.\frac{\partial^2 G^l}{\partial x^2}\right|_{x=x_0} = 0,$$
$$\left.\frac{\partial^3 G^r}{\partial x^3}\right|_{x=x_0} - \left.\frac{\partial^3 G^l}{\partial x^3}\right|_{x=x_0} = 1/B'.$$

Solving this system of four linear equations yields the four constants. Thus, Green's function can be determined.

Compared to Rumerman's approach, Norborg's approach have advantages when the sum involved (2.43) *can* be evaluated by means of contour integration and geometric series. Nordborg's free wave approach to gain the response of a point force is elegant, and can be applied to other problems such as flanking transmission.

2.6   Double plates

An approach useful in dealing with lightweight wall and floor structures must be able to handle a double-plate system. Lin and Garelik [28], Takahashi [58], Skelton [49] and Urusovskii [50] have all treated periodically stiffened double-plate structures. This is also the case in [4, 5].

Instead of one plate equation, as in (2.1), two equations are here present, coupled to each other through a cavity field and through the beams,

$$\mathcal{S}_1[w_1] = p_e - p_c^{(1)} - \sum_{n=-\infty}^{\infty} F_n^{(1)}\delta(x-nl), \tag{2.49}$$

$$\mathcal{S}_2[w_2] = p_c^{(2)} + \sum_{n=-\infty}^{\infty} F_n^{(2)}\delta(x-nl), \tag{2.50}$$

where p_c is the pressure reaction from the cavity between the plates, and where the suffix $\cdot^{(1)}$ and $\cdot^{(2)}$ refer to the first and the second plate respectively. This system of equations can be written, using matrix notations (matrices being bold-faced)

$$\boldsymbol{\mathcal{S}}[\mathbf{w}] = \mathbf{p}_e - \mathbf{p}_c - \sum_{n=-\infty}^{\infty} \mathbf{F}_n\delta(x-nl), \tag{2.51}$$

and the three approaches previously described can be applied (holding in mind the order of the matrix multiplications).

In the case of a double-plate system, one set of reaction forces acts on each plate. The reaction forces are related to each other via the beam equation

$$F_n^{(1)} - F_n^{(2)} = \mathcal{G}w_n^{(f)}, \tag{2.52}$$

27

where $\cdot^{(f)}$ refers to the beam, and via a boundary condition. A resilient device can be added here, for example, a ideal spring between the beam and the second plate,

$$F_n^{(2)} = K \left(w_n^{(f)} - w_n^{(2)} \right),\qquad (2.53)$$

where K is the spring constant. This is one choice of boundary condition. An alternative is to set the displacement of the beams equal to the displacement of the both plates, $w_n^{(1)} = w_n^{(f)} = w_n^{(2)}$, as is the case in [4, 28].

Extra consideration concerning the cavity field p_c must be made. The simplest model of the cavity is to use a locally reacting spring (as in [30, pp. 450–462]). A more elaborate description is to describe the field in the cavity as a wave field, but neglecting the influence of the beams. The description of the cavity field is the same as London [27] used. This has been the case for all mentioned papers, except for [5] where also the influence of the beams as walls inside the cavity is taken into account.

Some comments regarding Urusovskii's paper [50] will here be discussed. Urusovskii states that, concerning the paper by Lin and Garelick [28]:

> However, the basic equations do not include the phase factor associated with the force exerted on the plates by the beam as a result of oblique incidence of plane wave on the plate, nor do they take the mass reactance of the beams into account. Also, the acoustical influence of medium between the plates is disregarded

prematurely in the intermediate expressions, and the final equations do not contain explicit expressions for the amplitudes of the spatial spectrum of diffracted waves, including those transmitted through the plate.

None of these statements is entirely correct. First of all, it should be noted that Lin and Garelick use Evseev's approach even though the excitation is periodic (an incident sound wave). This means that Floquet's principle is not needed in the solution, and therefore is the phase factor associated with the reaction force not explicitly introduced. The beams are modelled as locally reacting mechanical line impedances. In the numerical examples, these impedances are specified as mass reactances. What, however, is not included in either [28] nor in [50] is the bending of the beams, (cf. equations (2.4–2.5)). Concerning the influence of the medium between the plates and of the diffracted waves; the reason that Urusovskii in his reading cannot find them is that Evseev's approach is used, and thus, the equations are solved in the wavenumber domain where only one wavenumber is present at the time. However, the transformed result includes all components, and in the last figure of the numerical section in [28] the effect of the scattered waves, i.e., the components not radiating in the incidence direction, is examined.

28

Chapter 3

Moment reaction and coupling

In the prediction model presented in papers [4, 5], the beam-stiffeners do not cause any moment reaction to the plate. In [4] it is argued that this is the main reason for the disagreement between measurement and prediction model. Thus, it is important to see in what degree the moment reaction does affect the result. Moment reaction on periodically stiffened plates has been treated, for example, by Rumerman [52], Mace [53, 54], and Takahashi [58].

3.1 A single plate

The moment reaction is introduced as a reaction pressure p_t (t for torsion), in the same way as the force reactions

$$p_f(x, y) = \sum_{n=-\infty}^{\infty} F_n(y)\delta(x - nl) \quad (3.1)$$

$$p_t(x, y) = \sum_{n=-\infty}^{\infty} M_n(y)\delta'(x - nl) \quad (3.2)$$

where $\delta'(x) = \partial\delta/\partial x$ is the derivative of the Dirac delta function. The governing equation for a one-plate system is thus equation (2.1)

with an extra reaction pressure p_t from the moment reaction,

$$\mathcal{S}[w] = p_e - p_f - p_t$$

where the operator $\mathcal{S}$ is found in equation (2.2), being the Kirchhoff plate bending operator. Each reaction force and moment are

$$
\begin{aligned}
F_n(y) &= \mathcal{G}w(nl, y) & (3.3) \\
M_n(y) &= \mathcal{H}\theta(nl, y) & (3.4)
\end{aligned}
$$

where

$$\theta(x) = \partial w/\partial x$$

The bending operator for the beam is given in equation (2.5), and the torsion operator for the beam is

$$\mathcal{H}\theta_n = T\partial^2\theta_n/\partial y^2 + \Theta\omega^2\theta_n \quad (3.5)$$

where $\theta_n = \theta(nl, y)$, cf. [30].

3.2 Using Rumerman's approach

In this case the driving pressure needs to be periodic, and thereby of the form

$$p_e = \hat{p}_e e^{-\mathrm{i}k_x x}$$

It is now assumed that the exciting pressure is of the form $p_d = \hat{p}_e e^{-ik_x x} \leftrightarrow \tilde{p}_e = \hat{p}_e 2\pi\delta(\alpha - k_x)$ if omitting the y-dependency, whereby Floquet's principle is valid. The pressure caused by the reaction forces is, together with its Fourier transform,

$$p_f(x,y) \;=\; F_0(y)\sum_{n=-\infty}^{\infty} e^{-ik_x nl}\delta(x-nl) \quad (3.6)$$

$$\tilde{p}_f(\alpha,y) \;=\; F_0(y)\sum_{n=-\infty}^{\infty} e^{-i(k_x-\alpha)nl} \qquad (3.7)$$

The Fourier transform of δ' is

$$\mathcal{F}_x\left[\delta'(x-nl)\right] = -i\alpha e^{i\alpha nl}$$

and thereby, the pressure caused by the reaction moments is, together with its Fourier transform,

$$p_t(x,y) \;=\; M_0(y)\sum_{n=-\infty}^{\infty} e^{-ik_x nl}\delta'(x-nl)$$

$$\tilde{p}_t(\alpha,y) \;=\; -i\alpha M_0(y)\sum_{n=-\infty}^{\infty} e^{-i(k_x-\alpha)nl}$$

The Poisson sum (2.21) is used, which yields

$$\tilde{p}_f \;=\; \frac{2\pi}{l}F_0\sum_{n=-\infty}^{\infty}\delta(\alpha - k_x - 2n\pi/l)$$

$$\tilde{p}_t \;=\; -\frac{2\pi}{l}i\alpha M_0\sum_{n=-\infty}^{\infty}\delta(\alpha - k_x - 2n\pi/l)$$

where $\tilde{p}_f = \tilde{p}_f(\alpha,x)$ et cetera. The transformed solution is then found as

$$\tilde{w} = \tilde{p}_e/S - \tilde{p}_f/S - \tilde{p}_t/S$$

and the displacement, applying the inverse Fourier transform (2.9), and the solution can be written

$$w(x) = w_\infty(x) - F_0 T^{(0)}(x) - M_0 T^{(1)}(x) \quad (3.8)$$

where the following notation has been introduced:

$$T^{(1)}(x) = -\frac{i}{l}\sum_{n=-\infty}^{\infty}\frac{(k_x + 2n\pi/l)\,e^{-i(k_x+2n\pi/l)x}}{S(k_x + 2n\pi/l)}$$

and $T^{(0)}(x)$ is the same as $T(x)$ in equations (2.35–2.36). One may observe that $T^{(1)}(x)$ simply is the first derivative of $T^{(0)}(x)$. The rotation θ is found by means of derivation of equation (3.8), which yields

$$\theta(x) = \theta_\infty(x) - F_0 T^{(1)}(x) - M_0 T^{(2)}(x) \quad (3.9)$$

where

$$\theta_\infty(x) = -ik_x w_\infty(x) = -ik_x\hat{p}_e\frac{e^{-ik_x x}}{S(k_x)}$$

and

$$T^{(2)}(x) = -\frac{1}{l}\sum_{n=-\infty}^{\infty}\frac{(k_x+2n\pi/l)^2\,e^{-i(k_x+2n\pi/l)x}}{S(k_x + 2n\pi/l)}$$

is the derivative of $T^{(1)}(x)$ and the second derivative of $T^{(0)}(x)$. Applying the boundary conditions (3.3–3.4) to equations (3.8) and (3.9) yields, if also assuming a $y-$dependency of the form $\exp(-ik_y y)$ so that $\mathcal{G} \to G$ and $\mathcal{H} \to H$,

$$Gw_\infty(0) - F_0 G T_0^{(0)} - M_0 G T_0^{(1)} = F_0$$

and

$$H\theta_\infty(0) - F_0 H T_0^{(1)} - M_0 H T_0^{(2)} = M_0.$$

Thus, the system of equations can be expressed in terms of matrixes,

$$
\begin{bmatrix} 1 + GT_0^{(0)} & GT_0^{(1)} \\ HT_0^{(1)} & 1 + HT_0^{(2)} \end{bmatrix} \begin{bmatrix} F_0 \\ M_0 \end{bmatrix}
$$
$$
= \begin{bmatrix} Gw_\infty(0) \\ H\theta_\infty(0) \end{bmatrix}, \quad (3.10)
$$

from which the force F_0 and the moment M_0 is determined. The dispersion relation for free waves is found when the determinant of the matrix in (3.10) is put to zero.

3.3 Double plates

In the case of a double-plate system one set of reaction forces and one set of reaction moments act on each plate. Takahashi [58], dealing with double plate systems connected both with point connector and beam in two orthogonal directions, included the moment reaction for both the point connectors and the beams.

As described in section 2.6, the governing equation for the double-plate system can be described in term of systems of equations, in this case

$$
\boldsymbol{\mathcal{S}}[\mathbf{w}] = \mathbf{p}_e - \mathbf{p}_c - \mathbf{p}_f - \mathbf{p}_t, \quad (3.11)
$$

where the three approaches in chapter 2 can be applied.

The reaction forces are related through the beam equation as in equation (2.52). As in section 3.1, what is added in the case of moment coupling is the torsion equation (3.5), in this case

$$
M_n^{(1)} - M_n^{(2)} = \mathcal{H}\theta_n^{(f)}, \quad (3.12)
$$

A resilient device can be added here, e.g., a ideal spring between the beam and the second plate, as in equation (2.53), and/or an ideal rotational spring between the beam and the second plate,

$$
M_n^{(2)} = C\left(\theta_n^{(f)} - \theta_n^{(2)}\right), \quad (3.13)
$$

where C is the rotational spring constant. As an alternative, the boundary condition can be rigid; that is equal displacement $w_n^{(1)} = w_n^{(f)} = w_n^{(2)}$ and rotation $\theta_n^{(1)} = \theta_n^{(f)} = \theta_n^{(2)}$ is used instead.

31

Chapter 4

Power and sound radiation

In many situations of sound radiation, the sound pressure in the radiated field is not a good measure of the radiation; it is a field variable and has therefore to be integrated to yield a single real number that one could compare with other situations. Energy measures as radiated power and sound intensity are better alternatives. One example is the transmission coefficient τ (and transmission loss R dB). The transmission coefficient is defined as

$$\tau = \Pi_t / \Pi_i \qquad (4.1)$$

where Π_t is the transmitted power and Π_i is the incident power. Also, the impact noise level can be determined from the power radiating from the structure that is excited by an ISO tapping machine, as is used in [4].

In the present chapter, power radiation is considered and discussed in connection to the papers in this thesis. The purpose of the chapter is to give an overview of the available theory. However, the chapter has no intention to give a complete survey; the list of reference is (unfortunate) incomplete. It will be shown that the Cremer and Heckl formula for radiated power can be derived in different ways.

4.1 Radiated power from wavenumber domain

Cremer and Heckl [30, pp. 526–534] present a very useful formula to calculate the power radiating from a structure. The formula uses the transformed velocity (or, in our case, the transformed displacement). As the transformed field variable is used, the inverse transform is not required in the solution.

The Fourier transform pair for the infinite case is found in equations (2.7–2.8). In order to also include the finite case, the transform (2.7) can also be written

$$\tilde{w}(\mathbf{k}) = \int_\Omega w(\mathbf{r}) e^{i\mathbf{k}\cdot\mathbf{r}} d\mathbf{r} \qquad (4.2)$$

where $\mathbf{k} = (\alpha, \beta)$, $\mathbf{r} = (x, y)$ and $\mathbf{k} \cdot \mathbf{r} = \alpha x + \beta y$. The integration domain Ω can be both the infinite domain and the finite (rectangular) domain. The inverse transform (2.8) is with the same notations

$$w(\mathbf{r}) = \frac{1}{4\pi^2} \int_{-\infty}^{\infty} \tilde{w}(\mathbf{k}) e^{-i\mathbf{k}\cdot\mathbf{r}} d\mathbf{k}. \qquad (4.3)$$

The boundary condition connecting the acoustic pressure field to the plate displacement is

$$\left.\frac{\partial p}{\partial z}\right|_{z=0} = \omega^2 \rho w \qquad (4.4)$$

Assuming outgoing waves $\propto \mathrm{e}^{-\gamma z}$ – with propagation constant $\gamma = \sqrt{\alpha^2 + \beta^2 - k^2}$ in the z-direction – the transformed pressure is then related to the transformed displacement according to

$$\tilde{p}(\mathbf{k}) = -\omega^2 \rho \tilde{w}(\mathbf{k})/\gamma(\mathbf{k}) \qquad (4.5)$$

Using equations (4.3) and (4.5), the total sound-pressure is thus given by

$$p(\mathbf{r}, z) = \frac{-1}{4\pi^2} \qquad (4.6)$$
$$\times \int_{-\infty}^{\infty} \frac{\omega^2 \rho \tilde{w}(\mathbf{k})}{\gamma(\mathbf{k})} \mathrm{e}^{-\gamma(\mathbf{k})z} \mathrm{e}^{-\mathrm{i}\mathbf{k}\cdot\mathbf{r}} \mathrm{d}\mathbf{k}.$$

The radiated power can be defined as

$$\Pi_{rad} = \frac{1}{2}\Re\left\{\int_\Omega p(\mathbf{r},0)v^*(\mathbf{r})\mathrm{d}\mathbf{r}\right\} \qquad (4.7)$$

where $v = \mathrm{i}\omega w$ is the velocity and $\cdot^*$ is the complex conjugate. Inserting equation (4.6) in (4.7) yields

$$\Pi_{rad} = \frac{1}{8\pi^2}$$
$$\times \Re\left\{\iint_\Omega \int_{-\infty}^{\infty} \frac{\mathrm{i}\omega^3 \rho \tilde{w}(\mathbf{k})}{\gamma(\mathbf{k})} w^*(\mathbf{r})\mathrm{e}^{-\mathrm{i}\mathbf{k}\cdot\mathbf{r}} \mathrm{d}\mathbf{k}\mathrm{d}\mathbf{r}\right\}$$

or if (4.3) also is used for $w^*(\mathbf{r})$

$$\Pi_{rad} = \frac{\omega^3 \rho}{32\pi^4}\Re\Bigg\{ \qquad (4.8)$$
$$\mathrm{i}\iint_\Omega \int_{-\infty}^{\infty}\int_{-\infty}^{\infty} \frac{\tilde{w}(\mathbf{k})\tilde{w}^*(\mathbf{k}')}{\gamma(\mathbf{k})}\mathrm{e}^{\mathrm{i}\mathbf{k}'\cdot\mathbf{r}}\mathrm{e}^{-\mathrm{i}\mathbf{k}\cdot\mathbf{r}}\mathrm{d}\mathbf{k}'\mathrm{d}\mathbf{k}\mathrm{d}\mathbf{r}\Bigg\}.$$

One may evaluate this integral by observing that substitution of equation (4.3) in (4.2):

$$\tilde{w}(\mathbf{k}) = \frac{1}{4\pi^2}\int_\Omega \int_{-\infty}^{\infty} \tilde{w}(\mathbf{k}')\mathrm{e}^{-\mathrm{i}\mathbf{k}'\cdot\mathbf{r}}\mathrm{e}^{\mathrm{i}\mathbf{k}\cdot\mathbf{r}}\mathrm{d}\mathbf{k}'\mathrm{d}\mathbf{r}. \qquad (4.9)$$

With some rearrangements of the order of integration and identification of the result in (4.9), the radiated power can be written

$$\Pi_{rad} = \frac{\omega^3 \rho}{8\pi^2}\Re\left\{\mathrm{i}\int_{-\infty}^{\infty} \frac{\tilde{w}(\mathbf{k})\tilde{w}^*(\mathbf{k})}{\gamma(\mathbf{k})}\mathrm{d}\mathbf{k}\right\}, \qquad (4.10)$$

or if real value operator $\Re$ is applied and the integrals are written out

$$\Pi_{rad} = \frac{\omega^3 \rho}{8\pi^2}\iint_{\alpha^2+\beta^2\leq k^2} \frac{|\tilde{w}(\mathbf{k})|^2}{\sqrt{k^2 - \alpha^2 - \beta^2}}\mathrm{d}\alpha\mathrm{d}\beta. \qquad (4.11)$$

Make use of the substitution $\alpha = k\cos\varphi$, $\beta = k\sin\varphi$ (so that $\mathrm{d}\mathbf{k} = \mathrm{d}\alpha\mathrm{d}\beta = k_r\mathrm{d}k_r\mathrm{d}\varphi$),

$$\Pi_{rad} = \frac{\omega^3 \rho}{8\pi^2}\int_0^{2\pi}\int_0^k \frac{|\tilde{w}(\mathbf{k})|^2}{\sqrt{k^2 - k_r^2}}k_r\mathrm{d}k_r\mathrm{d}\varphi. \qquad (4.12)$$

One more substitution can be made; $k_r = k\cos\theta$, where $k = \omega/c$ is constant and the angle θ is the parameter. Thus, $\mathrm{d}k_r = -k\sin\theta\mathrm{d}\theta$ and equation (4.12) is written

$$\Pi_{rad} = \frac{-\omega^3 \rho k}{8\pi^2}\int_0^{2\pi}\int_{-\pi/2}^0 |\tilde{w}(\mathbf{k})|^2\cos\theta\mathrm{d}\theta\mathrm{d}\varphi. \qquad (4.13)$$

which equals equation (4.30) if the substitution $\theta' = \pi/2 + \theta$ is employed.

In order to see the difference between radiation from finite and infinite structures, the following notations for the finite transform

(where it is assumed that the region Ω is rectangular with edge length $2a$ and $2b$ respectively) can be used

$$\tilde{w}^f(\mathbf{k}) = \int_\Omega w(\mathbf{r})\mathrm{e}^{\mathrm{i}\mathbf{k}\cdot\mathbf{r}}\mathrm{d}\mathbf{r}$$

and the following notations for the infinite transform

$$\tilde{w}^i(\mathbf{k}) = \int_{-\infty}^{\infty} w(\mathbf{r})\mathrm{e}^{\mathrm{i}\mathbf{k}\cdot\mathbf{r}}\mathrm{d}\mathbf{r}.$$

With the aid of the inverse transform, the finite transform can be expressed in terms of the infinite version,

$$\tilde{w}^f(\mathbf{k}) = \frac{1}{4\pi^2}\int_\Omega\int_{-\infty}^{\infty} \tilde{w}^i(\mathbf{k}')\mathrm{e}^{\mathrm{i}(\mathbf{k}-\mathbf{k}')\cdot\mathbf{r}}\mathrm{d}\mathbf{k}'\mathrm{d}\mathbf{r}$$
(4.14)

The Fourier relation

$$\mathrm{e}^{\mathrm{i}(\mathbf{k}-\mathbf{k}')\cdot\mathbf{r}} = \int_{-\infty}^{\infty}\delta(s-\Delta\alpha)\delta(t-\Delta\beta)\mathrm{e}^{\mathrm{i}(xs+yt)}\mathrm{d}s\mathrm{d}t$$

can be used, where $\Delta\alpha = \alpha - \alpha'$ and $\Delta\beta = \beta - \beta'$, insert in (4.14) and interchange the order of integration so that $\mathbf{r} = (x, y)$ is integrated under the integration sign. Make use of the integral

$$\int_\Omega \mathrm{e}^{\mathrm{i}(xs+yt)}\mathrm{d}x\mathrm{d}y = 4\,ab\,\mathrm{sinc}(as)\,\mathrm{sinc}(bt),$$
(4.15)

where $\mathrm{sinc}(s) = \sin(s)/s$, so that (4.14) can be written, if the Dirac function is taken into account

$$\tilde{w}^f(\mathbf{k}) = \frac{ab}{\pi^2}\int_{-\infty}^{\infty} \tilde{w}^i(\mathbf{k}')\mathrm{sinc}(a\Delta\alpha)\mathrm{sinc}(b\Delta\beta)\mathrm{d}\mathbf{k}'.$$
(4.16)

Using the limes representation of the Dirac delta function

$$\delta(x) = \lim_{a\to\infty}\sin(ax)/\pi x = \lim_{a\to\infty}\frac{a}{\pi}\mathrm{sinc}(ax),$$

it can be seen that $\tilde{w}^f(\mathbf{k}) = \tilde{w}^i(\mathbf{k})$ in the limit where $a, b \to \infty$, as it should.

4.2 Radiated power from Green's function

The Helmholtz integral equation can be written (see, for example, [67, pp. 79–84])

$$p(\mathbf{r}) = -\varepsilon\int_{\Omega_0}\left(p\frac{\partial G}{\partial n_0} - \omega^2\rho Gw\right)\mathrm{d}\mathbf{r}_0.$$
(4.17)

where $\varepsilon = 1$ if $\mathbf{r}$ is inside the volume of integration, $\varepsilon = 2$ if $\mathbf{r}$ is on the boundary of the volume of integration, and $\varepsilon = 0$ elsewhere. When every point in Ω_0 is located in the same plane, as is the case for a plane surface vibration an a wall, the Helmholtz integral equation is reduced to Rayleigh's integral,

$$p(\mathbf{r}) = \omega^2\rho\varepsilon\int_{\Omega_0} G(\mathbf{r}|\mathbf{r}_0)w(\mathbf{r}_0)\mathrm{d}\mathbf{r}_0. \quad (4.18)$$

The radiated power, given by equation (4.7), becomes (if radiation to only one side of the structure is considered)

$$\Pi_{rad} = \frac{-\omega}{2}\Re\left\{\mathrm{i}\int_\Omega p(\mathbf{r})w^*(\mathbf{r})\mathrm{d}\mathbf{r}\right\} \quad (4.19)$$

$$= \frac{-\omega^3\rho}{2}\Re\left\{\mathrm{i}\int_\Omega\int_{\Omega_0} G(\mathbf{r}|\mathbf{r}_0)w(\mathbf{r}_0)w^*(\mathbf{r})\mathrm{d}\mathbf{r}_0\mathrm{d}\mathbf{r}\right\}.$$

It should here be noted two double integrals is used to calculate the power, and if the displacement is given in transform space even

one more double integration is needed (the inverse transform). If equation (4.12) were used instead, only one double integration has to be employed. Green's function is [67])

$$G(\mathbf{r}|\mathbf{r}_0) = -\frac{e^{-ikr}}{4\pi r}$$

where

$$r = \sqrt{(x - x_0)^2 + (y - y_0)^2}.$$

If the displacements $w(\mathbf{r}_0)$ and $w^*(\mathbf{r})$ are expressed in their Fourier transforms, as in section 4.1, the integrals in equation (4.19) can be written

$$\int_\Omega \int_{\Omega_0} G(\mathbf{r}|\mathbf{r}_0)w(\mathbf{r}_0)w^*(\mathbf{r})\mathrm{d}\mathbf{r}_0\mathrm{d}\mathbf{r} \quad (4.20)$$

$$= \frac{1}{8\pi^4} \int_{-\infty}^\infty \int_{-\infty}^\infty \tilde{w}(\mathbf{k})\tilde{w}^*(\mathbf{k}')I_G(\mathbf{k},\mathbf{k}')\mathrm{d}\mathbf{k}'\mathrm{d}\mathbf{k}$$

where

$$I_G(\mathbf{k},\mathbf{k}') \equiv \int_\Omega \int_{\Omega_0} G(\mathbf{r}|\mathbf{r}_0)e^{i\mathbf{k}'\cdot\mathbf{r} - i\mathbf{k}\cdot\mathbf{r}_0}\mathrm{d}\mathbf{r}_0\mathrm{d}\mathbf{r}.$$

$$(4.21)$$

This type of integral can be simplified following the procedure, for example, in Thomasson [68]. The idea is to express the Green's function by its Fourier transform and then integrate in $\mathbf{r}$ and $\mathbf{r}_0$ under the integral sign. Thus, the Fourier transform of Green's function must be found. The following Hankel transform can be found in mathematics tables (e.g. [69]),

$$G = -\frac{e^{-ikr}}{4\pi r} = -\int_0^\infty \frac{\kappa \mathrm{J}_0(\kappa r)}{2\pi\sqrt{\kappa^2 - k^2}}\mathrm{d}\kappa. \quad (4.22)$$

Expressing the Bessel function in one of its integral representations [69]

$$\mathrm{J}_0(\kappa r) = \frac{1}{2\pi}\int_{-\pi}^\pi e^{i\kappa r \sin\varphi}\mathrm{d}\varphi$$

and inserting it in (4.22), yields

$$G = \frac{-1}{8\pi^2}\int_{-\pi}^\pi \int_0^\infty \frac{\kappa e^{i\kappa r \sin\varphi}}{\sqrt{\kappa^2 - k^2}}\mathrm{d}\kappa\mathrm{d}\varphi. \quad (4.23)$$

Finally, with the suitable substitution $\alpha'' = \kappa\cos\varphi$ and $\beta'' = \kappa\sin\varphi$ Green's function can be written

$$G(\mathbf{r}|\mathbf{r}_0) = \frac{-1}{8\pi^2}\int_{-\infty}^\infty \frac{e^{i\mathbf{k}''\cdot(\mathbf{r}-\mathbf{r}_0)}}{\sqrt{\alpha''^2 + \beta''^2 - k^2}}\mathrm{d}\mathbf{k}''.$$

$$(4.24)$$

The integral (4.21) can thus be written, if interchanging the order of integration,

$$I_G(\mathbf{k},\mathbf{k}') = \frac{-1}{8\pi^2}\int_{-\infty}^\infty \frac{1}{\sqrt{\alpha''^2 + \beta''^2 - k^2}}$$

$$\times \int_\Omega \int_{\Omega_0} e^{i\mathbf{k}''\cdot(\mathbf{r}-\mathbf{r}_0)}e^{i\mathbf{k}'\cdot\mathbf{r} - i\mathbf{k}\cdot\mathbf{r}_0}\mathrm{d}\mathbf{r}_0\mathrm{d}\mathbf{r}\,\mathrm{d}\mathbf{k}''. \quad (4.25)$$

The two inner integrals can be evaluated using equation (4.15). The result in (4.16), that is the transformation from an infinite to an finite Fourier transform, can then be identified if inserting $I_G(\mathbf{k},\mathbf{k}')$ in equation (4.20) and once again interchanging the order of integration. Thus, the radiated power is

$$\Pi_{rad} = \quad\quad\quad\quad\quad\quad\quad (4.26)$$

$$= \frac{\omega^3\rho}{8\pi^2}\Re\left\{\int_{-\infty}^\infty \frac{|\tilde{w}^f(\mathbf{k}'')|^2\,\mathrm{d}\mathbf{k}''}{\sqrt{k^2 - \alpha''^2 - \beta''^2}}\right\}$$

which equals the result in section 4.1, equation (4.10).

4.3 Radiated power from the far-field pressure

A far-field approximation of the pressure field was used by Mace [17] and Takahashi [58]. It is derived by means of a stationary phase asymptotic approximation in Junger and Feith [67]. The method determines the wavenumber that affects the result the most, which then is used in the solution. The result reads

$$p(r, \theta, \varphi) = -\rho\omega^2 \tilde{w}(\alpha_0, \beta_0) \frac{\mathrm{e}^{-\mathrm{i}kr}}{2\pi r} \qquad (4.27)$$

where $\alpha_0 = k\sin\theta\cos\varphi$, $\beta_0 = k\sin\theta\sin\varphi$ and $k = \omega/c$. In order to compare with the other results, the radiated power is calculated also in this case. In the spherical type of wave in (4.27) the intensity is

$$I = |p|^2/\rho c$$

in the wave direction, and therefore

$$\Pi_{rad} = \int\limits_{hemisphere} I\mathrm{d}S = \frac{1}{\rho c} \int\limits_{hemisphere} |p|^2 \mathrm{d}S \quad (4.28)$$

Using the fact that for a sphere of radius R the area element is $\mathrm{d}S = R^2\sin\theta\mathrm{d}\theta\mathrm{d}\varphi$,

$$\Pi_{rad} = \frac{1}{\rho c} \int_0^{2\pi} \int_0^{\pi/2} |p|^2 R^2 \sin\theta\mathrm{d}\theta\mathrm{d}\varphi \quad (4.29)$$

Taking the absolute value of equation (4.27) yields

$$|p(R, \theta, \varphi)| = \frac{\rho\omega^2}{2\pi R} |\tilde{w}(\alpha_0, \beta_0)|,$$

and thus equation (4.29) can be written

$$\Pi_{rad} = \frac{\rho\omega^4}{c4\pi^2} \int_0^{2\pi} \int_0^{\pi/2} |\tilde{w}(\alpha_0, \beta_0)|^2 \sin\theta\mathrm{d}\theta\mathrm{d}\varphi \qquad (4.30)$$

The dependency of the radii R herewith disperses. Equation (4.30) is equal to equation (4.13) derived from the Cremer and Heckl radiation formula. This derivation of the radiation formula was used by Takahashi in [58] and the present author in [70, 71].

4.4 Sound radiation of an infinite structure

An infinite structure will, if the wavefield is travelling (non-decaying), radiate an infinite amount of power. It is therefore not appropriate to use the power as a measure. Instead the sound intensity is used. It should therefore be noted that the following discussion is only valid for infinite (periodic) structures.

When a structure is periodic in space and force, Floquet's principle applies and both displacement and pressure field can be described in terms of space harmonics (periodicity in x). Thus, for the displacement a space harmonic series as in equation (2.39) can be assumed. The radiated pressure will be of the same form (as it is caused by the periodic structure),

$$p(x, y) = \sum_{n=-\infty}^{\infty} P_n \mathrm{e}^{-\mathrm{i}(k_x + 2n\pi/l)x - \mathrm{i}k_y y - \kappa_z z}. \qquad (4.31)$$

Thus, the radiated field will be built up by plane waves in discrete angles, in contrast to

37

an infinite homogenous structure where only one angle (the incident) is represented, or to a finite structure where the angle distribution is continuous.

The cases considered herein are driven by a convected pressure, that, for example, can be an incident pressure wave. The incident wave is generally described by two angles, θ and φ, together with the wavenumber in the fluid $k = \omega/c$,

$$
\begin{aligned}
k_x &= k \sin\theta \cos\varphi, \\
k_y &= k \sin\theta \sin\varphi, \\
k_z &= k \cos\theta.
\end{aligned} \tag{4.32}
$$

The angles fall in the regions

$$ 0 \le \theta < 2\pi $$

and

$$ 0 \le \varphi < \pi/2. $$

The angle-dependent transmission efficiency can in the infinite periodic case be defined as

$$
\tau(\theta, \varphi) \equiv \frac{\mathbf{I}_t \cdot \mathbf{n}}{\mathbf{I}_i \cdot \mathbf{n}} = \frac{I_{n,t}(\theta, \varphi)}{I_{n,i}(\theta, \varphi)} \tag{4.33}
$$

where index n stands for normal direction, $\mathbf{I}_t$ and $\mathbf{I}_i$ is the intensity vector for the transmitted and incident field respectively, and $\mathbf{n}$ is the unit vector normal to the plate. Thus, in the definition of the angle-dependent transmission efficiency only power flow through the structure is accounted for. For a simple homogenous and infinite structure this angle dependency is not a problem as the radiated wave has the same direction as the incident

wave, and therefore (suppressing the azimuth angle)

$$
\tau(\theta) = \frac{I_t(\theta) \cos\theta}{I_i(\theta) \cos\theta} = \frac{I_t(\theta)}{I_i(\theta)}.
$$

However, this is not generally the case, and the definition (4.33) is preferred.

The statistical transmission efficiency is then found by means of considering the mean intensity (both incident and transmitted), the mean taken as a arithmetic mean over all solid angles of incidence of a halfsphere. The following definitions is thus introduced: For the incident wave field, the mean intensity is

$$
I_{i,s} = \langle I_{i,n}(\theta, \varphi) \rangle = I_i \langle \cos\theta \rangle, \tag{4.34}
$$

where the brackets $\langle \cdot \rangle$ denote the mean taken over the incident angles, and where the last equality is due to the diffuse field definition, where all directions have the same intensity and probability. For the transmitted wave field, the mean intensity is

$$
I_{t,s} = \langle I_{t,n}(\theta, \varphi) \rangle = I_i \langle \tau(\theta, \varphi) \cos\theta(\theta, \varphi) \rangle, \tag{4.35}
$$

where the last equality is due to equation (4.33).

The average over all solid angles of incidence of a halfsphere, is

$$
\langle I_n(\theta, \varphi) \rangle = \left. \int_{hemisphere} I_n(\theta, \varphi) \mathrm{d}\Omega \middle/ \int_{hemisphere} \mathrm{d}\Omega \right. . \tag{4.36}
$$

The infinitial solid angle is found to be

$$
\mathrm{d}\Omega = \sin\theta \, \mathrm{d}\theta \, \mathrm{d}\varphi,
$$

so the integrals become

$$\int\limits_{hemisphere} I_n(\theta, \varphi) \mathrm{d}\Omega = \int\limits_0^{2\pi} \int\limits_0^{\pi/2} I_n(\theta, \varphi) \sin\theta \, \mathrm{d}\theta \, \mathrm{d}\varphi \tag{4.37}$$

and

$$\int\limits_0^{2\pi} \int\limits_0^{\pi/2} \sin\theta \, \mathrm{d}\theta \, \mathrm{d}\varphi = 2\pi.$$

The statistical transmission efficiency is then found to be

$$\tau_s \equiv \frac{I_{t,s}}{I_{i,s}} = \frac{\langle \tau(\theta, \varphi) \cos\theta \rangle}{\langle \cos\theta \rangle} \tag{4.38}$$

which, if using (4.36–4.37) becomes

$$\tau_s = \frac{\int\limits_0^{2\pi} \int\limits_0^{\pi/2} \tau(\theta, \varphi) \cos\theta \sin\theta \, \mathrm{d}\theta \, \mathrm{d}\varphi}{\int\limits_0^{2\pi} \int\limits_0^{\pi/2} \cos\theta \sin\theta \, \mathrm{d}\theta \, \mathrm{d}\varphi}. \tag{4.39}$$

Evaluating the integral in the denominator results in

$$\tau_s = \frac{1}{\pi} \int\limits_0^{2\pi} \int\limits_0^{\pi/2} \tau(\theta, \varphi) \sin\theta \cos\theta \, \mathrm{d}\theta \, \mathrm{d}\varphi \tag{4.40}$$

or when no azimuth angle φ dependency is present

$$\tau_s = 2 \int\limits_0^{\pi/2} \tau(\theta) \sin\theta \cos\theta \, \mathrm{d}\theta \tag{4.41}$$

which is found in many textbooks, for example, [66, pp. 369].

39

Chapter 5

Which are the important parameters?

In order to find out which of the parameters of a lightweight floor are important and how to change them in order to achieve better results, the prediction model in [4] (and the simple mass-resistance excitation model in [3]) is used in a parameter study. It should therefore be noted that the parameter study only applies for the type of floor structure included there; i.e., a structure consisting of two plates rigidly connected to the reinforcing beams ($w_1(nl) = w_f = w_2(nl)$). The floor structure can be seen in Figure 5.1. Thus, the results found here cannot necessarily be applied to another type of floor structure, such as a floor with resilient channels. The variations are based on a original set of input data (in what is called the base floor). One (or sometimes two) parameter is varied at the time. The variation is performed with a factor taking the values $\{0.25\ 0.5\ 1\ 2\ 4\}$ applied to the varied parameter, keeping the rest of the parameters constant. The result is presented as the increase in impact sound level compared to the base floor.

$$\Delta L_n = L_n - L_n|_0$$

where the notation $\cdot|_0$ henceforth denotes the
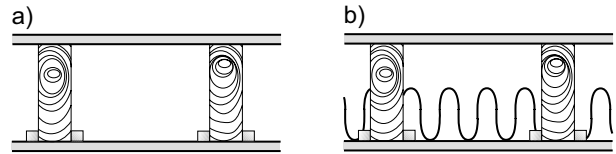
Figure 5.1: A sketch of the base floor structure. Case a) without mineral wool, case b) with mineral wool.

base floor and the original set of data. In the figures this variation will be represented by five curves of ΔL_n (including the zero line). The curves are denoted, in order of increasing factor: $\circ$, $\times$, then the zero line without any marker, then $\square$ and $\triangledown$.

A sketch of the floor structure can be seen in Figure 5.1 (the same figure is also used in [4]), and the results for the calculations of the base floor are shown in Figure 5.2, where the case without mineral wool in the cavity is denoted $(-\circ-)$, and the case with mineral wool of a depth of half the cavity depth is denoted $(-\times-)$. The base floor without mineral wool is used except where the opposite is noted. Some of the variations will just change the positions of the peaks and dips, but other variations will cause a broad band increase or

41
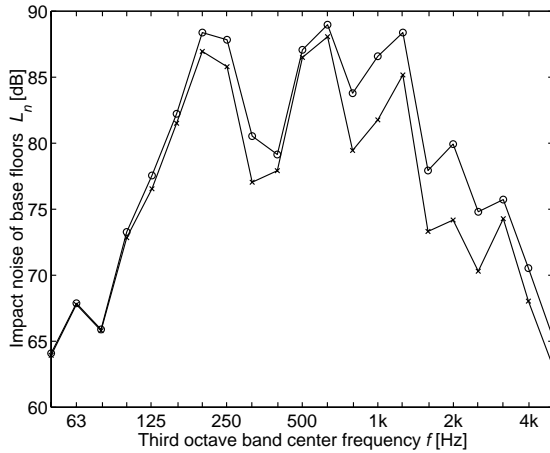
Figure 5.2: Impact noise level of the base floors, case a) without mineral wool (-o-), case b) with mineral wool (-×-).

decrease of the impact sound level.

The material and geometrical data of the original configuration are: 'plate' modulus for the wood in the plates $E/(1 - \nu^2) = 6 \cdot 10^9$ N/m^2, thickness of the (solid wood) plates $22 \cdot 10^{-3}$ m, yielding $B_1' = B_2' = EI'/(1 - \nu^2) = 5.32 \cdot 10^3$. The masses per unit area of the plates are $m_1'' = m_2'' = 10$ kg/m^2. The beams have Young's modulus $E_f = 11 \cdot 10^9$ N/m^2 and density $\rho_f = 455$ kg/m^3 and cross section 67×220 mm, giving an area of $A_f = 14.7 \cdot 10^{-3}$ m^2 and a moment of inertia of $I_f = 5.95 \cdot 10^{-5}$ m^4. The material damping for wood is $\eta = 0.03$, added to the Young's modulus in the plates and beams. The depth of the cavity $d = 220 \cdot 10^{-3}$ m is the same as the height of the beams. When mineral wool is present, the flow resistivity is $R = 11770$ Ns/m^4. The density of the air is $\rho = 1.29$ kg/m^3 and the speed of sound in air is $c = 340$ m/s. Material damping for the air is taken to
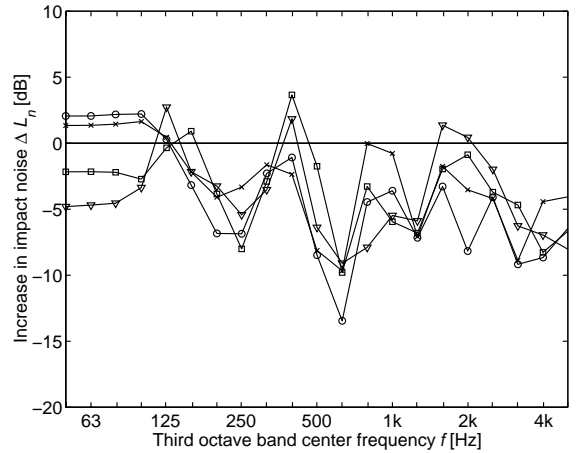
Figure 5.3: Increase in impact noise level when varying the weight of the first plate. The weight is varied as $m_1'' = \{0.25\ 0.5\ 1\ 2\ 4\} \cdot m_1''|_0$, with the line order $\circ$, $\times$, the zero line without marker, $\square$ and $\triangledown$.

be $\eta_{air} = 10^{-8}$, added to the speed of sound. Only one excitation position is used: $x_0 = 0.43$ m.

First, the weight of the plates is varied. Thus, in Figure 5.3 m_1'' is varied, in Figure 5.4 m_2'' is varied, and in Figure 5.5 both of them are varied. It can be seen that increasing the weight of the second plate decreases the impact sound more than the increase for the first plate. It should be remembered here that changes in the first plate affect both the system (that is the wave transmission through the floor structure) and the excitation force as the excitation model in [3] is used.

The stiffnesses of the plates are then varied. In Figure 5.6 B_1' is varied, in Figure 5.7 B_2' is varied, and in Figure 5.8 the stiffness of both of the plates is varied together. In this case, a decrease the stiffness of the first

42
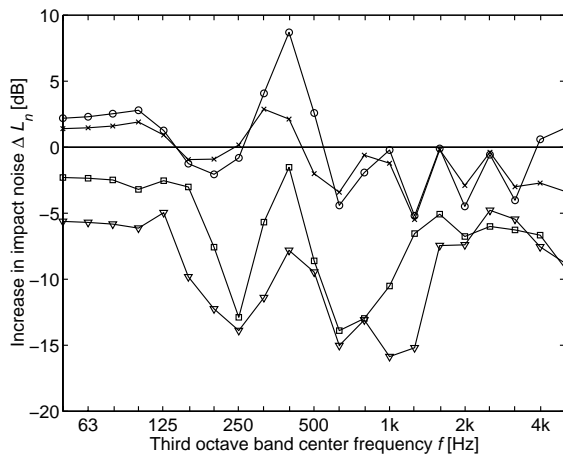
Figure 5.4: Increase in impact noise level when varying the weight of the second plate. The weight is varied as $m_2'' = \{0.25\ 0.5\ 1\ 2\ 4\} \cdot m_2''|_0$, with the line order $\circ$, $\times$, the zero line without marker, $\square$ and $\triangledown$.

Figure 5.5: Increase in impact noise level when varying the weight of the first and second plate. The weight is varied as $m_1'' = \{0.25\ 0.5\ 1\ 2\ 4\} \cdot m_1''|_0$ and $m_2'' = \{0.25\ 0.5\ 1\ 2\ 4\} \cdot m_2''|_0$, with the line order $\circ$, $\times$, the zero line without marker, $\square$ and $\triangledown$.

plate is advantageous. The reason for this is that a softer excitation point will influence the excitation force in a favourable manner, extending the contact time.

The influence of the beams is then analysed. In Figure 5.9 the influence of the stiffness of the beams is analysed, and in Figure 5.10 the influence of the weight of the beams is analysed. No big changes can be seen, but at lower frequencies (below 250 Hz) positive effects can be gained. The beams should be weaker and heavier in order to decrease the impact sound in this frequency range.

The influence of mineral wool was also studied. In Figure 5.11 the flow resistance of the mineral wool is varied (the case b in Figures 5.1 and 5.2), and in Figure 5.12 the fraction of mineral wool occupying the cavity is varied (that is $d_{min} = \{0\ 0.25\ 0.5\ 0.75\ 1\} \cdot d$).

Figure 5.6: Increase in impact noise level when varying the stiffness of the first plate. The stiffness is varied as $B_1' = \{0.25\ 0.5\ 1\ 2\ 4\} \cdot B_1'|_0$, with the line order $\circ$, $\times$, the zero line without marker, $\square$ and $\triangledown$.
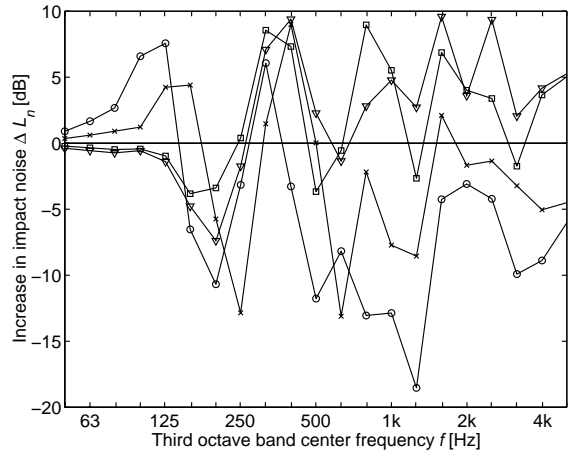
Figure 5.8: Increase in impact noise level when varying the stiffness of the first and second plate. The stiffness is varied as $B_1' = \{0.25\ 0.5\ 1\ 2\ 4\} \cdot B_1'|_0$ and $B_2' = \{0.25\ 0.5\ 1\ 2\ 4\} \cdot B_2'|_0$, with line order $\circ$, $\times$, the zero line without marker, $\square$ and $\triangledown$.

Figure 5.7: Increase in impact noise level when varying the stiffness of the second plate. The stiffness is varied as $B_2' = \{0.25\ 0.5\ 1\ 2\ 4\} \cdot B_2'|_0$, with the line order $\circ$, $\times$, the zero line without marker, $\square$ and $\triangledown$.
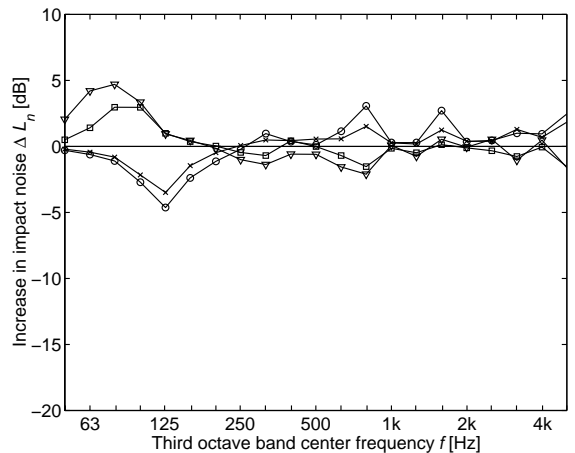
Figure 5.9: Increase in impact noise level when varying the stiffness of the beams. The stiffness is varied as $E_f = \{0.25\ 0.5\ 1\ 2\ 4\} \cdot E_f|_0$, with the line order $\circ$, $\times$, the zero line without marker, $\square$ and $\triangledown$.

44
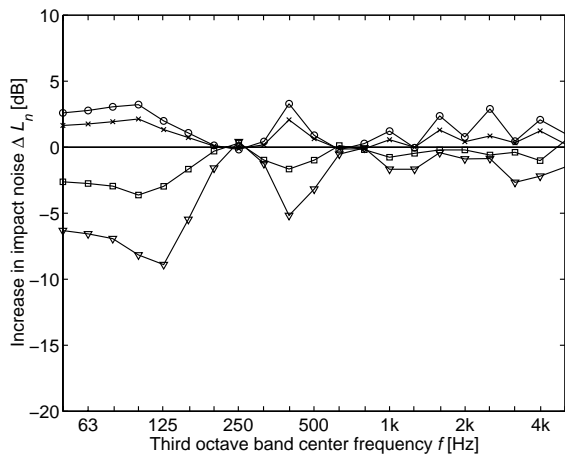
Figure 5.10: Increase in impact noise level when varying the weight of the beams. The weight is varied as $\rho_f = \{0.25\ 0.5\ 1\ 2\ 4\} \cdot \rho_f|_0$, with the line order $\circ$, $\times$, the zero line without marker, $\square$ and $\triangledown$.

Changing the flow resistance does not affect the result much, but the result is clear. The result of the variation can especially be noticed in the frequency region 100–316 Hz, and increasing the flow resistance decreases the impact noise in this region. However, this result is probably in part due to the limitation of the description of the mineral wool in the prediction model. The mineral wool is described by a version of the Delaney and Bazely model [18], in which the structural phase of the medium is included only as second order effects, as the empirical model only has a fluid phase. However, with increasing flow resistance the structural phase will eventually be increasingly important, implying that in reality there should be an optimal value for the flow resistance. This was noted in Figure 1.1, where mineral wool with density 26 kg/m^3 is better than wool with density 15 kg/m^3 and 35 kg/m^3 (assuming a simple one-to-one relationship between density and flow resistance). In order to improve the model, the mineral wool should be modelled as a Biot material [19, 20], that includes both structural and fluid phases. In the case of varying the fraction of mineral wool, Figure 5.12, it can first of all be said that it makes a big difference whether mineral wool is present or not. When mineral wool is present, increasing the fraction will not make any major difference, but in the frequency region 100–316 Hz it can be seen that increasing the fraction decreases the impact noise. This result can be compared with the result presented in Figure 1.2, where the fraction of mineral wool also is varied, experimentally but for a wall with separated studs. There is a decrease gained in the entire frequency range when increasing the fraction. The difference between the two cases is probably that the structural connection is more predominant in the numerical example in Figure 5.12.

The periodic distance between the beams is varied in Figure 5.13. The influence seen is mainly due to frequency shifts of the peaks and dips. However, at low frequencies, below 125 Hz, the results indicate that increasing the periodic distance increases the impact noise level. The main reason for this is probably the decrease in weight associated with the increase of periodic distance. The tendency in these results is confirmed by measurements found in [72] (also reported and discussed in [73]), where the spacing is changed from 400 mm to 600 mm in a floor structure similar to the one studied herein. For low frequen-
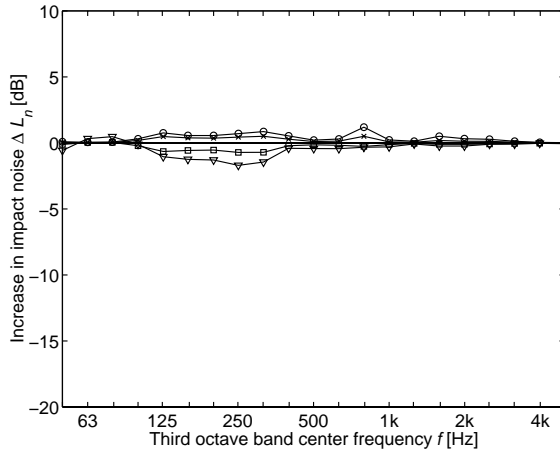
Figure 5.11: Increase in impact noise level when varying the flow resistance of the mineral wool. The case b) in Figures 5.1 and 5.2 is used as base floor. The flow resistance is varied as $R = \{0.25 \ 0.5 \ 1 \ 2 \ 4\} \cdot R|_0$, with the line order ○, ×, the zero line without marker, □ and ▽.
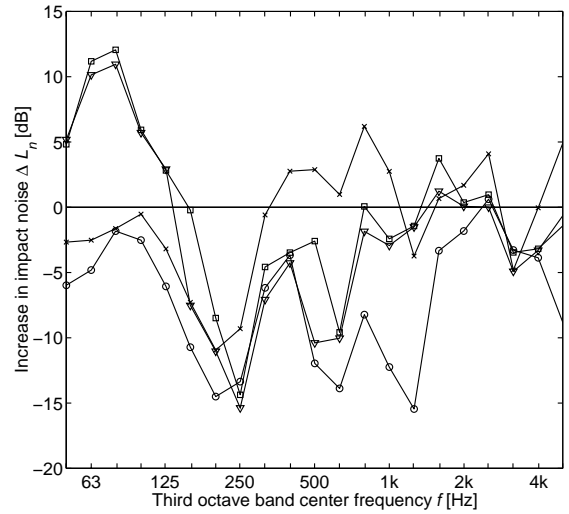
Figure 5.13: Increase in impact noise level when varying the distance between the beams. The distance is varied as $L = \{0.25 \ 0.5 \ 1 \ 2 \ 4\} \cdot L|_0$, with the line order ○, ×, the zero line without marker, □ and ▽.
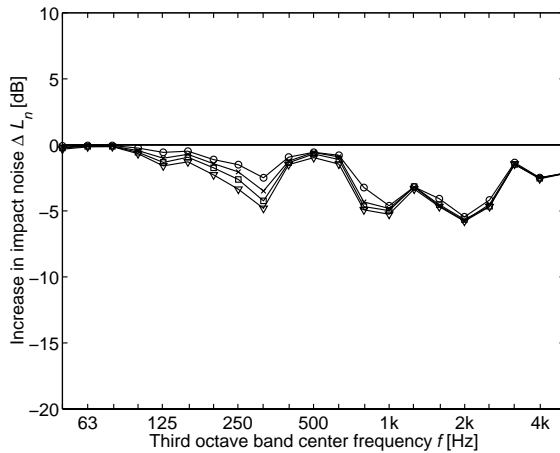
Figure 5.12: Increase in impact noise level when varying the fraction of mineral wool in the cavity. The fraction is varied as $d_{min} = \{0 \ 0.25 \ 0.5 \ 0.75 \ 1\} \cdot d$, where the line order starts with the zero line, and then ○, ×, □ and ▽.

cies, the floor with a 400 mm spacing had lower impact noise level than the floor with 600 mm spacing. However, for other frequencies the results shift. In connection with this, it may be interesting to note that for another floor structure studied in [73, pp. 40–43], a floor structure with a resilient channel, a clear trend could be seen in the measurement; the floor with 400 mm spacing had lower impact noise level than the floor with 600 mm spacing in the entire frequency range.

In Figures 5.14 and 5.15 is the variation of the construction depth studied. Both the depth of the cavity and the beams are varied. In Figure 5.14 no mineral wool is included in the cavity (case a in Figures 5.1 and 5.2), whereas in Figure 5.15 mineral wool is in-
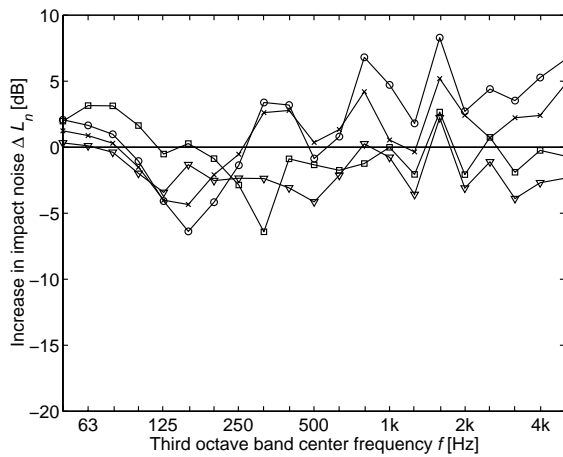
Figure 5.14: Increase in impact noise level when varying the depth of the construction, including both cavity and beams. The depth is varied as $d = \{0.25\ 0.5\ 1\ 2\ 4\} \cdot d|_0$, with the line order ○, ×, the zero line without marker, □ and ▽.

cluded in the cavity (case b). In this case it makes a major difference if mineral wool is present or not; without mineral wool, increasing the construction depth do decrease the impact noise, but if mineral wool is present the decrees can be up to 10–15 dB larger than if mineral wool is not present. The difference is more predominant for higher frequencies than for lower frequencies.

In summary, it can be said that the largest positive effects (that is, decreasing the impact sound level) are gained by: increasing the construction depth (when mineral wool is present), increasing the mass of the second plate (without changing the stiffness, which can be achieved if adding an extra plate loosely to the first one), or for low frequencies increasing the mass and decreasing the stiffness of the beams. Other variations also
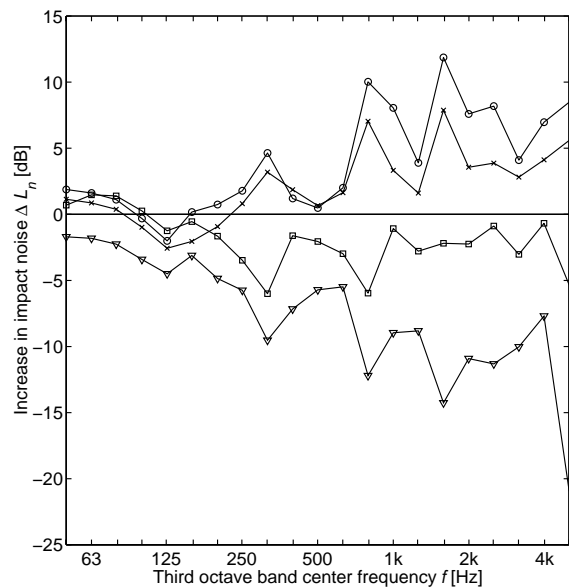
Figure 5.15: Increase in impact noise level when varying the depth of the construction, including both cavity and beams. The cavity contains mineral wool of a hight of 11 cm, case b) in Figures 5.1 and 5.2. The depth is varied as $d = \{0.25\ 0.5\ 1\ 2\ 4\} \cdot d|_0$, with the line order ○, ×, the zero line without marker, □ and ▽.

47

have a large influence in a limited frequency range, but this influence is mainly due to frequency shifts of the peaks and dips in the impact noise frequency curve.

Chapter 6

Summary and concluding remarks of the thesis

In chapter 1 different aspects typical for a lightweight building system were considered and discussed, so that the acoustics of such constructions can be understood. It was there concluded that it is not enough to simply take account of results obtained for heavy and homogenous constructions and apply them to lightweight structures. Nor does it seem possible to gain insight using SEA and similar approaches. A more detailed and elaborate approach is required. The approach has to be able to involve an elaborate description of the material and components comprising such constructions. Moreover, an inclusion of conjunctions between various components allowing the system-phenomena that are typical of lightweight constructions to be adequately described, should be possible.

Periodicity and the phenomena that this causes (which are typical system-phenomena) are important characteristics of lightweight structures. The periodicity is exploited in chapter 2 and in [1]. A literature survey over theoretical approaches that can be used for point excited periodic structures is presented

in [1]. The findings are that an approach using the spatial Fourier transform can handle point forces, radiation and periodicity, and is thus suited in the present situation. The spatial Fourier transform approach is therefore frequently employed in this thesis, with the aid of Floquet's principle and Poisson's sum. It can be concluded that the approach is a successful one, as seen in the papers [4, 5]; the predicted response/transmission loss have a reasonable agreement compared with measurements, and the troughs and peaks correspond well with those being found in the experimental curve.

Due to different variabilities in real constructions, the situation is actually nearly – rather than perfectly – periodic. The effects of small irregularities in a nearly periodic spatially excited structure have been studied in [6]. A novel statistical approach was used, suited for sound insulation problems. The irregularities cause extra damping and stiffness in the mean vibration field if material damping is present. A conclusion addressed to shipyards and the building industry is that

it may be a good idea to maintain and increase the amount of irregularities and imperfections in built up structures such as walls and floors.

In order to predict sound transmission of lightweight structures, excitation has to be dealt with properly. In the case of air-borne sound insulation the exitation is caused by a diffuse field, represented by incoming (and reflected) plane waves. The only difference compared to an infinite homogeneous slab is that there is a finite number of radiating components. However, in the case of impact noise insulation the excitation is achieved by means of the ISO tapping machine, the situation is more complicated as the source interacts with the system involved [3]. It was there found that the force spectrum produced by the tapping machine when acting on a heavy and homogeneous floor structure can not be applied to a lightweight structure – the excitation is not invariant with respect to the system. At low frequencies there is a spread in the force spectrum of 6 dB, depending on whether the hammer leaves the excited structure or not. In order to adequately describe what occurs, the global and the local driving-point mobility have to be combined. The results indicate that it is important to use an accurate and detailed system description in order to predict the impact force spectrum appropriate.

When assessing the force spectrum, the point mobility of the structure must be known. The local effects of the point mobility are due to the deformation near the excitation point, as studied in [2]. A variational technique was used to determine the pressure distribution under the indenter (and thereby also the mobility) when a rigid indenter acts on a plate of finite thickness. The functional that was used in the variational formulation was identified as the complex input power. Two types of pressure distributions were analysed, a distribution with one constant, and a distribution with two constants, the latter yielding an improved solution compared to the solutions found in the literature.

Radiation and response were discussed in chapter 4, and also to some extent in [4, 5, 6]. The power radiated from a structure can be calculated in the wavenumber domain using the formula of Cremer and Heckl. This formula was derived in different ways in chapter 4.

The cavity between the plates in a double construction is of importance to achieve a reasonable result. In chapter 5 it was found that increasing the construction depth (when mineral wool is present) is the most effective way to gain decreased impact noise level. The cavity field was more closely studied in [5]. It was shown there that at frequencies below the first resonance the two plates have displacements that are out of phase with each other (if the displacement relative to the beams is considered). This is due to the reaction field caused by the beam connection. A comparison between measured and calculated results shows satisfactory agreement.

Resilient devices are often present in lightweight structures. The purpose of these devises is to provide a loose coupling between the two plates. The resilient device was studied experimentally [7] and to some extent theoretically [5]. A tensile loaded resilient device

is often used in lightweight floor structures, mounted in the ceiling (e.g., a resilient channel). In [7] the frequency dependence of the transfer and input stiffness of such devices is investigated experimentally, using a test rig consisting of two known masses. Internal resonances were found for higher frequencies, which affect the performance of the device in the lightweight structure.

Finally, some important numerical results can be found in chapter 5, where a parameter study is performed on the basis of the impact noise prediction model in [4]. It was shown there (not surprisingly) that the most positive broad-band effects (i.e., decreasing the impact sound level) are gained when the construction depth is increased – when mineral wool is present. Alternatively, the mass of the lower plate can be increased .

Bibliography

[1] J. Brunskog, P. Hammer: Prediction models of impact sound insulation on timber floor structures; A literature survey. J. Building Acoustics **7** (2000) 89–112.

[2] J. Brunskog, P. Hammer: Rigid indenter excitation of plates. Acustica / acta acustica **submitted**.

[3] J. Brunskog, P. Hammer: The interaction between the ISO tapping machine and lightweight floors. Acustica / acta acustica **accepted**.

[4] J. Brunskog, P. Hammer: Prediction model for the impact sound level of lightweight floors. Acustica / acta acustica **accepted**.

[5] J. Brunskog: Including the influence of finite cavities in sound insulation of double-plate structures. TVBA 3119, Engineering Acoustics, LTH, Lund University, Box 118, SE-221 00 Lund, Sweden, 2002.

[6] J. Brunskog: Near-periodicity in acoustically excited stiffened plates and its influence on vibration, radiation and sound insulation. TVBA 3120, Engineering Acoustics, LTH, Lund University, Box 118, SE-221 00 Lund, Sweden, 2002.

[7] J. Brunskog, P. Hammer: Measurement of the acoustic properties of resilient, statically tensile loaded devices in lightweight structures. J. Building Acoustics **9** (2002) 99–137.

[8] S. Thelandersson: Multi-story timber housing in the Nordic countries. Proceedings, 5th World Conference on Timber Engineering, Montreux, Switzerland, Eds. J. Natterer and J. L. Sandoz, 1998.

[9] P. Hammer: Sound insulation in a multi-storey wooden house, Wälluden and Orgelbänken. TVBA 3084 A-B, Engineering Acoustics, LTH, Lund University, Box 118, SE-221 00 Lund, Sweden, 1996.

[10] EN 12354: Building acoustics – estimation of acoustic performance of buildings from the performace of products. part I: Airborne sound insulation between rooms. EN 12354-1. part II: Impact sound insulation between rooms. EN 12354-2. European Standard, 1996.

[11] R. J. M. Craik: Sound transmission through buildings. Gower, Aldershot, Hampshire GU11 3HR, England, 1996.

[12] R. J. M. Craik, R. S. Smith: Sound transmission through double leaf lightweight partitions, Part I: airborne sound. Applied Acoustics **61** (2000) 223–245.

[13] E. Gerretsen: Calculation of the sound transmission between dwellings by partions and flanking structures. Applied Acoustics **12** (1979) 413–433.

[14] E. Gerretsen: Calculation of airborne and impact sound insulation between dwellings. Applied Acoustics **19** (1986) 245–264.

[15] E. Gerretsen: European devlopments in prediction models for building acoustics. Acta acustica **2** (1994) 205–214.

[16] B. H. Sharp: Prediction methods for the sound transmission of building elements. Noise Control Engineering **11** (1978) 53–63.

[17] B. R. Mace: Sound radiate from a plate reinforced by two sets of parallel stiffeners. J. of Sound and Vibration **71** (1980) 435–441.

[18] M. E. Delaney, E. N. Bazely: Acoustical properties of fibrous absorbent materials. Applied Acoustics **3** (1970) 105–116.

[19] M. A. Biot. – In: Acoustics, elasticity, and thermodynamics of porous media – Twenty-one papers by M.A. Biot. I. Tolstoy (ed.). Acoustical Society of America, 1992.

[20] J. F. Allard: Propagation of sound in porous media: Modeling sound absorbing materials. Elsevier Applied Science, 1993.

[21] P. Hammer, E. Nilsson: Light weight partition walls and floors – the influence of mineral wool on sound insulation. TVBA 3095, Engineering Acoustics, LTH, Lund University, Box 118, SE-221 00 Lund, Sweden, 1997.

[22] J. Brunskog, P. Hammer: On the mechanics of gypsum plate systems. Proceeding ICA-01, Rom, 2001.

[23] T. R. T. Nightingale, I. Bosmans: Vibration response of lightweight wood frame building elements. J. Building Acoustics **6** (1999) 269–288.

[24] J. Hodges, C. H. och Woodhouse: Vibration isolation from irregularity in a nearly periodic structure: Theory and measurement. J. Acoustical Society of America **74** (1983) 894–905.

[25] L.-G. Sjökvist, P. Hammer: Flanking transmission in lightweight buildings. Proceeding ICA-01, Rom, 2001.

[26] L.-G. Sjökvist: — (in preparation). TVBA 3118, Engineering Acoustics, LTH, Lund University, Box 118, SE-221 00 Lund, Sweden, 2002.

[27] A. London: Transmission of reverberant sound through double walls. J. Acoustical Society of America **22** (1950) 270–279.

[28] G. F. Lin, J. M. Garrelick: Sound transmission through periodically framed parallel plates. J. Acoust. Soc. Am. **61** (1977) 1014–1018.

[29] P. Hammer, J. Brunskog: Subjektiv bedömning och ljudisolerings-index; en designvägledning för lätta konstruktioner. TVBA 3085, Engineering Acoustics, LTH, Lund University, Box 118, SE-221 00 Lund, Sweden, 1996.

[30] L. Cremer, M. Heckl, E. E. Ungar: Structure-borne sound. Springer-Verlag, Berlin, 1988.

[31] J. S. Bradley, J. A. Birta: On the sound insulation of wood stud exterior walls. J. Acoust. Soc. Am. **110** (2001) 3086–3096.

[32] A. Warnock: Airborne and impact sound insulation of joist floor systems: A collection of data. NRCC 44210, National Research Council Canada, Monteral, 2000.

[33] S. G. Lindblad, J. Brunskog: On the airgap between narrow plates. Proceeding ICA-01, Rom, 2001.

[34] A. Trochidis: Köperschalldämpfung mittels gas- oder flüssigkeitsschichten. Acustica **51** (1982) 201–211.

[35] D. Bergmans: Damping of gypsumplates with variable narrow air-gaps. TVBA 3112, Engineering Acoustics, LTH, Lund University, Box 118, SE-221 00 Lund, Sweden, 2001.

[36] J. S. Bradley, J. A. Birta: A simple model of the sound insulation of gypsum board on resilient supports. Noise Control Eng. **49** (2001) 216–223.

[37] EN ISO 717-1:1996: Acoustics – Rating of sound insulation in buildings and building elements – Part 1: Airborne sound insulation. European standard, 1996.

[38] P. Hammer: Ljud. – In: Flervånings trähus. Nordic Wood, Träinformation, 1997, 19– 26.

[39] B. G. Watters: Impact-noise characteristics of female hard-heeld foot traffic. J. Acoust. Soc. Am. **37** (1965) 619–630.

[40] Vér: Impact noise isolation of composite floors. Journal of the Acoustical Society of America **50** (1971) 1043–1050.

[41] S. Lindblad: Impact sound characteristics of resilient floor coverings. a study on linear and nonlinear dissipative compliance. Dissertation. Division of Building Technology, Lund Institute of Technology, Lund, Sweden, 1968.

[42] Boverkets byggregler, BBR. Boverket, Box 534, 371 23 Karlskrona, Sweden, 1999.

[43] SS 02 52 67: Acoustics – Sound classification of spaces in buildings – Dwellings. Svensk Standard, 1998.

[44] SS 02 52 68: Acoustics – Sound classification of spaces in buildings – Institutional premises, rooms for education, day centers and after school centres, rooms for office work, and hotels. Svensk Standard, 2000.

[45] W. Fasold: Untersuchungen über den verlauf der sollkurve für den trittschallschutz im wohnungsbau. Acustica 15 (272–284) 1965.

[46] K. Bodlund: Alternative reference curves for evaluation of the impact sound insulation between dwellings. J. Sound and Vibration 102 (1985) 381–402.

[47] P. Hammer, E. Nilsson: On subjective impact sound insulation classes. TVBA 3102, Engineering Acoustics, LTH, Lund University, Box 118, SE-221 00 Lund, Sweden, 1999.

[48] E. Nilsson, P. Hammer: Subjective evaluation of impact sound transmission through floor structures. TVBA 3103, Engineering Acoustics, LTH, Lund University, Box 118, SE-221 00 Lund, Sweden, 1999.

[49] E. A. Skelton: Acoustic scattering by parallel plates with periodic connectors. Proc. R. Soc. Lond. A 427 (1990) 419–444.

[50] I. A. Urusovskii: Sound transmission through two periodically framed parallel plates. Sov. Phys. Acoust. 38 (1992) 411–413.

[51] A. Nordborg: Vertical rail vibrations: Pointforce excitation. ACUSTICA / acta acustica 84 (1998) 280–288.

[52] M. L. Rumerman: Vibration and wave propagation in ribbed plates. J. Acoust. Soc. Am. 57 (1975) 370–373.

[53] B. R. Mace: Periodically stiffened fluid-loaded plates, I: Response to convected harmonic pressure and free wave propagation. J. Sound and Vibration 73 (1980) 473–486.

[54] B. R. Mace: Periodically stiffened fluid-loaded plates, II: Response to line and point forces. J. Sound and Vibration 73 (1980) 487–504.

[55] B. R. Mace: Sound radiation from fluid loaded orthogonally stiffened plates. J. Sound and Vibration 79 (1981) 439–452.

[56] B. R. Mace: The vibration of plates on two-dimensionally periodic point supports. J. Sound and Vibration 192 (1996) 629–643.

[57] V. N. Evseev: Sound radiation from an infinite plate with periodic inhomogeneities. Soviet physics – Acoustics 19 (1973) 345–351.

[58] D. Takahashi: Sound radiated from periodically connected double-plate structures. J. Sound and Vibration 90 (1983) 541–557.

[59] D. J. Mead, K. K. Pujara: Space-harmonic analysis of periodically supported beams: response to convected

random loading. J. Sound and Vibration **14** (1971) 525–541.

[60] D. J. Mead: Wave propagation in continous periodic structures: research contributions from Southampton, 1964–1995. J. Sound and Vibration **190** (1996) 495–524.

[61] P. M. Morse, K. U. Ingard: Theoretical acoustics. Prinston university press, Prinston, New Jersey, 1968.

[62] P. M. Morse, H. Feshbach: Methods of theoretical physics, part I. McGraw-Hill Book Company, Inc., New York, 1953.

[63] G. B. Arfken, H. J. Weber: Mathematical methods for physicists. Academic Press, San Diego, 1995.

[64] G. Blanch: Mathieu functions. – In: Handbook of mathematical functions. M. Abramowitz, I. A. Stegun (eds.). Dover, New York, 1964, 721–750.

[65] L. Brillouin: Wave propagation in periodic structures. Dover Publications, Inc., New York, 1953.

[66] C. L. Morfey: Dictionary of acoustics. Academic press, 2001.

[67] M. Junger, D. Feit: Sound, structures, and their interaction. Acoustical Society of America through the American Institute of Physics, 1972.

[68] S.-I. Thomasson: Theory and experiments on the sound absorption as function of the area. TRITA-TAK 8201, Dep.

Technical Acoustics, KTH, Stockholm, Sweden, 1982.

[69] L. Råde, B. Westergren: Mathematics handbook for science and engineering. Studentlitteratur, Lund, Sweden, 1995.

[70] J. Brunskog, P. Hammer: Prediction of impact sound on light weight floor structures. Proceedings of Inter-Noise 97, Budapest, Hungary, 1997. 751–754.

[71] J. Brunskog, P. Hammer: On sound transmission trough point excited light weight periodic structures. Proceedings of Inter-Noise 98, Christchurch, New Zealand, 1998.

[72] L. C. Fothergill, P. Royle: Sound insulation of timber platform floating floors. Applied Acoustics **33** (1991) 249–261.

[73] P. Hammer: Impact sound transmission of wooden-joist floor. TVBA 3077, Engineering Acoustics, LTH, Lund University, Box 118, SE-221 00 Lund, Sweden, 1994.

Part II

The included papers

Rigid indenter excitation of plates

Jonas Brunskog and Per Hammer

Division of Engineering Acoustics, LTH, Lund University, P.O. Box 118, SE-221 00 Lund, Sweden
E-mail: jonas.brunskog@acoustics.lth.se, per.hammer@acoustics.lth.se

Summary

The paper presents expressions for the point mobility of infinite plates driven by a completely rigid indenter. The problem is of general interest in connection with the excitation and transmission of structure-borne sound. The indenter is assumed to be circular, weightless, and stiff compared with the plate. A rigid indenter is assumed to provide a better approximation of the actual situation than a soft indenter would, e.g when a hammer acts on a wooden plate. A detailed three-dimensional analysis is performed. Traditionally, the problem is solved in approximate terms by assuming a pressure distribution at the interface between the indenter and the plate. In the present study, a pressure distribution is also assumed, an optimal choice of the pressure amplitude being found by means of a variational formulation. Numerical results are presented and discussed, the discrepancy between the results obtained and the perfectly rigid indenter being examined.

PACS no. 43.40.Dx

1. Introduction

The aim of the present paper is to derive an expression for the point mobility of infinite plates driven by a weightless, circular and completely rigid indenter. The problem is of general interest in the generation and transmission of structure-borne sound. The work reported here has been prompted, however, by a special need; that of obtaining an accurate description of the imaginary part of the point mobility, such as in an impact situation in which a 'spring' makes the impacting body rebound [1] (the impact being of the type where the contact area is constant during the impact). The hypothesis considered is that in the expressions derived earlier and reported in the literature the imaginary part of the mobility is not entirely correct. The findings in the present paper indicates this hypothesis to sometimes be correct, such as when the radius of the indenter is of the same size or larger than the thickness of the plate, or in case of high frequencies. It is assumed that a rigid indenter provides a better description of the actual situation than a soft indenter does, e.g. when a metal hammer acts on a wooden or a gypsum plate. Use of a rigid indenter is also more reasonable than use of a soft one (assuming the pressure distribution to be uniform), as it allows the pressure distribution under the indenter to change as the frequency increases.

A situation closely connected to the present problem is that of an indenter acting on a semi-infinite elastic half-sphere. The static version of this problem was first solved by Bousinesq [2]. Bycroft [3] solved the dynamic problem of an rigid indenter by means of assuming the pressure distribution to be that archived by Bousinesq [2]. This attack to the problem will soon be discussed. Robertson [4] analysed the same problem by means of an approximate series solution. Hryniewicz [5, 6] analysed bodies, especially a rigid strip, vibrating on a semi-infinite elastic half-sphere

by making use of numerical methods. One conclusion that can be drawn from his study is that the distribution of the contact pressure is sensitive to the variation of the frequency. For low frequencies the pressure distribution is similar to Bousinesq's results, but not for higher frequencies. Krenk and Schmidt [7, 8] treated a circular indenter acting on a semi-infinite elastic half-sphere, but they let the indenter to be elastic. Both vertical and rocking vibrations were considered. They conclude that for a rigid indenter and low frequencies their analysis do not deviate much from those of Bycroft [3], but when the frequency is increased or if the indenter is elastic the pressure distribution is radically changed and a complete analysis is necessary.

The mobility is defined as the complex ratio of velocity to force at the intersection between the indenter and the plate. It has been shown by means of the classical Kirchhoff thin plate equations [2, 9] that the point mobility Y of an infinite plate can be written as

$$Y \equiv \frac{v}{F} = \frac{1}{8\sqrt{m''B}} \qquad (1)$$

where v is the vibration velocity in the direction normal to the plate, F is the driving force normal to the plate, m'' is the mass per unit area and B is the bending stiffness. In [10] Ljunggren discusses the accuracy of equation (1) and compares it with Mindlin theory and with a three-dimensional theory in which only the poles corresponding to the bending waves are taken into account. He shows that an extra imaginary part appears due to the slight difference in magnitude between the real and the imaginary bending-wave poles.

In all analyses describing the motion of 'thin' structures, such as in the Kirchoff and Mindlin theories, it is assumed that the two sides of the structure have exactly the same displacement at each point. This is an approxi-

mation and, when excitation is concentrated to an area of the same size or smaller than the structural thickness, additional weakness effects can occur. Moreover, when the radius of the indenter is of the same size or larger than the thickness, additional inertia effects can occur due to the mass under the indenter vibrating in phase.

More detailed three-dimensional analyses have been carried out, by Paul [11] and by Ljunggren [12] for a rigid indenter and by Heckl [13] for a soft indenter. Petersson and Heckl [14] have investigated the influence of different choices of pressure distribution. The boundary value problem is simpler for a soft indenter than for a rigid one since the pressure distribution under a soft indenter is given by the problem itself and is constant in space, and thus Neumann boundary conditions, i.e. prescribed pressures, are found both outside and under the indenter. In contrast, for a rigid indenter the displacement under the indenter and the pressure distribution outside the indenter are prescribed, so that mixed Neumann and Dirichlet conditions are present. This is a more complicated mathematical problem than that for a Neumann condition alone.

Paul [11] investigated plates resting on rigid bases and those free on the back side. Only the latter are of interest here. The problem was solved in approximate terms by a method applied earlier to a semi-infinite elastic solid [4]. However, Paul's solution does not seem to be correct, partly since reference is made to "the root" of the Rayleigh-Lamb equations without any hint of there being an infinite number of roots, and partly since the low-frequency asymptote of the solution approaches the value of a semi-infinite medium irrespective of the thickness of the plate [12].

By assuming a pressure distribution under the indenter, Ljunggren [12], and Petersson and Heckl [14] (when dealing with the rigid indenter) avoided the problem of needing to solve integral equations. The pressure distribution taken was that of a rigid indenter statically loading an elastic semi-infinity. Since there is no guarantee that this assumption actually results in a uniform displacement under the indenter, such a case can be designated as quasi-rigid. In obtaining a solution Ljunggren [12] first found expressions for the outer field, $r \geq R$, and then examined the displacement at the boundary circle of the indenter, $r = R$. Finally, the solution was found by means of contour integration on the basis of the dispersion relation, although the position of the poles was solved numerically or by approximation. Since Heckl [13] was considering a soft indenter, he used a constant pressure distribution. The mobility was determined by means of numeric calculation of the displacement at the center of the indenter. A comparison of the results obtained can be found in [12] (see Figure 9 in the reference). Calculated values for the local reaction, all based on the same numerical input data, are presented for the solutions in [13] and in [12]. There is virtually no agreement at all between the results of the two studies. As Ljunggren [12] points out, this is scarcely astonishing in view of the differences in the assumptions made. Petersson and Heckl [14] achieved their solution by numerical integration and used the mean displacement

under the indenter as the input for the mobility calculations, employing the complex input power to obtain the mean. The pressure distributions considered in [14] were: the constant (i.e. the soft) distribution, the quasi-rigid, and the parabolic.

In the present paper the pressure distribution at the interface between the indenter and the plate is found by use of a variational formulation. The expressions obtained are approximations, although the choice of these made is an optimal one. It will be shown that for the quasi-rigid case the results obtained according to [14] and according to the approach taken in the present paper are identical. This is not surprising, since the variational technique is closely related to the complex input power. What is special for the present paper is the use of a variational technique for solving the problem and the improved solution this provides. The latter can be verified by comparing the results obtained with those reported in the literature, which indicates that the boundary condition are much close to being fulfilled in the present case (see Figure 9 and 10). The organisation of the paper is as follows: the problem under investigation is described in section 2, the variational formulation is presented in section 3, and is used in section 4 to provide a solution, the results of various earlier works are expressed in terms of the present notations in section 5 allowing comparisons to be made, the numerical approach taken is examined in section 6, the numerical results obtained are presented in section 7, the overall results are discussed in section 8, and in section 9 the conclusions drawn are summarized.

2. Formulation of the problem

The situation to be analysed is that of an indenter acting on a plate of finite thickness, shown in Figure 1. It is assumed that the indenter is circular, weightless and stiff compared with the plate, that the plate is isotropic and that the frequencies are within the audible range. The theory is to be a linear one. What is sought is the point mobility Y of the excitation situation, and thus the force acting on the interface between the indenter and the plate, when the indenter is displaced the distance $w_i \mathrm{e}^{\mathrm{i}\omega t}$, where the time dependence $\mathrm{e}^{\mathrm{i}\omega t}$ is henceforth suppressed, and where $\mathrm{i} = \sqrt{-1}$ is the imaginary unit, $\omega = 2\pi f$ is the angular frequency and t is time. The loading of the surrounding medium is not included in the analysis. Only forces in the direction normal to the plate are considered. Thus, no friction forces between the indenter and the plate is included. The term 'admittance' is in the present analysis used to denote the ratio of spatially harmonic velocity to spatially harmonic pressure, whereas 'mobility' is used for point or field ratios of velocity to force.
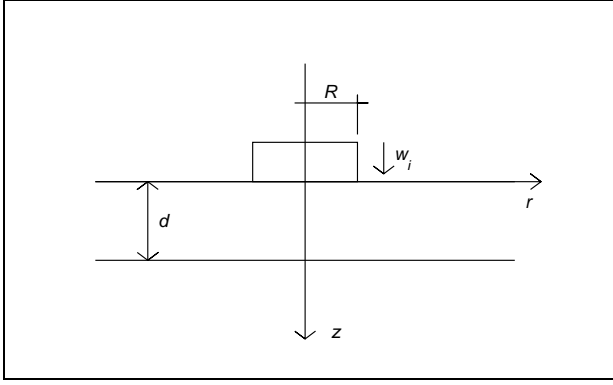
Figure 1. A rigid indenter of radius R acting on a plate of thickness d. The indenter is displaced the distance w_i.
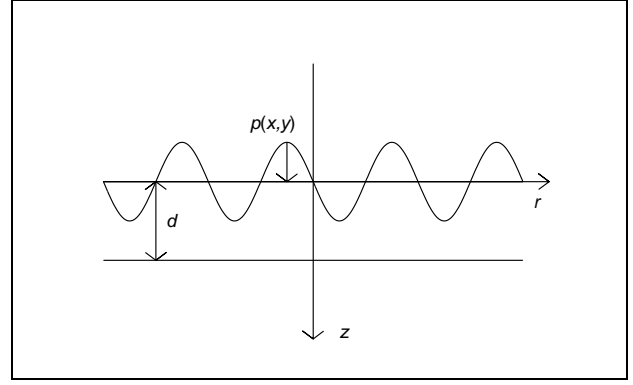
Figure 2. A spatially harmonic excited plate.

2.1. Boundary conditions

For a stiff indenter, the boundary conditions on the upper surface are

$$
\begin{cases}
w(x,y,0) = w_\mathrm{i} & \text{for } r \leq R \text{ and } z = 0 \\
p(x,y,0) = \sigma_z = 0 & \text{for } r > R \text{ and } z = 0
\end{cases}
\tag{2}
$$

where $r = \sqrt{x^2 + y^2}$ is the distance from the center of the indenter, $p(x,y,0)$ is the pressure acting on the upper surface of the plate and $w(x,y,z)$ is the displacement of the plate. For the bottom side of the plate, the boundary conditions are

$$
p(x,y,d) = \sigma_z = 0 \text{ for } z = d,
\tag{3}
$$

The tangential shear stresses in the x-y-plane at the surfaces $z = 0$ and $z = d$ are set to be zero for $0 \leq r \leq \infty$, and thus also under the indenter. Note that the displacement of the indenter w_i is a real constant (provided the time dependence e^{iwt} is suppressed), and that the pressure p and the displacement w are generally complex. The force is found as the integral of the pressure field under the indenter,

$$
F = \int_\Omega p(r)\mathrm{d}A = 2\pi \int_0^R p(r)r\mathrm{d}r.
\tag{4}
$$

The point mobility is then found as

$$
Y = \frac{v}{F} = \frac{\mathrm{i}\omega w_\mathrm{i}}{2\pi \int_0^R p(r)r dr}.
\tag{5}
$$

Thus, when the actual pressure distribution has been obtained, then the problem is solved.

2.2. A spatially harmonic excited plate

The boundary conditions at $z = 0$, equation (2), is not a prescribed pressure. In order to solve the problem nevertheless, consider first a plate excited by a time- and space-harmonic pressure, Figure 2. These pressure components

will be integrated in section 2.3 to form the actual displacement field. The formulation, similar to that in Ljunggren [10, 12], involves the plate being excited by a pressure in the form

$$
\tilde{p}(0)\mathrm{e}^{-\mathrm{i}k_x x - \mathrm{i}k_y y}
$$

where thereafter the argument $z = 0$ is suppressed. The vertical displacement $w(x,y,z)$ can then be written as

$$
\tilde{w}(z)\mathrm{e}^{-\mathrm{i}k_x x - \mathrm{i}k_y y}
$$

where k_x and k_y are the excitation wavenumbers in the x- and the y-direction, respectively. The pressure field needs now to be associated with the displacement field by way of admittances, the field being regarded as the superposition of an antisymmetric and a symmetric mode. In this way, the boundary conditions (3) at $z = d$ are automatically fulfilled when the two modes are combined.

Consider the displacement at $z = 0$ and $z = d$,

$$
\begin{aligned}
\tilde{w}(0) &= \left(A_A + A_S\right)\tilde{p}/\mathrm{i}\omega \\
\tilde{w}(d) &= \left(A_A - A_S\right)\tilde{p}/\mathrm{i}\omega
\end{aligned}
\tag{6}
$$

where the admittance for the antisymmetric and the symmetric mode, as used e.g. in [10, 12, 13, 14], is given as

$$
A_A = \frac{-\mathrm{i}\omega\alpha k_T^2/2\mu}{\left(k_r^2 + \beta^2\right)^2 \tanh(\alpha d/2) - 4\alpha\beta k_r^2 \tanh(\beta d/2)}
$$

$$
A_S = \frac{-\mathrm{i}\omega\alpha k_T^2/2\mu}{\left(k_r^2 + \beta^2\right)^2 \coth(\alpha d/2) - 4\alpha\beta k_r^2 \coth(\beta d/2)}
\tag{7}
$$

using the notations

$$
k_r^2 = k_x^2 + k_y^2
$$

and

$$
\begin{aligned}
\alpha^2 &= k_r^2 - k_L^2, & \beta^2 &= k_r^2 - k_T^2, \\
k_L^2 &= \rho\omega^2/(\lambda + 2\mu), & k_T^2 &= \rho\omega^2/\mu,
\end{aligned}
$$

the Lamé constants λ and μ being employed. The constants k_L and k_T are the longitudinal and the transverse

wavenumber respectively, and ρ is the density of the material in the plate. Since only the upper surface of the plate is of interest, where $z = 0$, the following abbreviation is used,

$$A = A_A + A_s.$$

The actual field for any given excitation can be found by means of the inverse Fourier transform, such that

$$w = \frac{1}{4\pi^2} \int_{-\infty}^{\infty} \int_{-\infty}^{\infty} \tilde{w} \mathrm{e}^{-\mathrm{i}k_x x - \mathrm{i}k_y y} \mathrm{d}k_x \mathrm{d}k_y \qquad (8)$$

which gives the displacement for a given spatial displacement component $\tilde{w}$. The corresponding Fourier transform is

$$\tilde{w} = \int_{-\infty}^{\infty} \int_{-\infty}^{\infty} w \mathrm{e}^{\mathrm{i}k_x x + \mathrm{i}k_y y} \mathrm{d}k_x \mathrm{d}k_y \qquad (9)$$

which represents a transform pair.

2.3. Plates excited by a rigid indenter

Consider now a plate excited by a rigid indenter, see Figure 1. When the excitation is of a pure force type, i.e. without moment or rotational excitation, the situation is polar symmetric. The two-dimensional Fourier transform then changes to a Hankel transform. Hence, change to polar coordinates,

$$k_x = k_r \cos\theta, \ k_y = k_r \sin\theta$$

and $dk_x dk_y = k_r dk_r d\theta$. Equation (8) can then be written as

$$w = \frac{1}{4\pi^2} \int_0^{2\pi} \int_{-\infty}^{\infty} \tilde{w} \mathrm{e}^{-\mathrm{i}k_r(\cos\theta x + \sin\theta y)} k_r \mathrm{d}k_r \mathrm{d}\theta \qquad (10)$$

Polar symmetry implies there to be no angular dependence in the displacement field. Thus,

$$w = \frac{1}{4\pi^2} \int_0^{\infty} \tilde{w} \int_0^{2\pi} \mathrm{e}^{-\mathrm{i}k_r(\cos\theta x + \sin\theta y)} k_r \mathrm{d}k_r \mathrm{d}\theta$$

The inner integral equals 2π times the Bessel function of zero order. Equation (10), where r denotes the radius from the origin, can be written as

$$w = \frac{1}{2\pi} \int_0^{\infty} \tilde{w} \mathrm{J}_0(k_r r) k_r \mathrm{d}k_r \qquad (11)$$

which is the 'ordinary' Hankel transform, except for the factor $1/2\pi$, see e.g. [15], due to the $4\pi^2$ in the definition above of the 2-dimensional inverse Fourier transform. Equation (11) will be used as the present definition of the Hankel transform.

The displacement of the upper surface of the plate, where $z = 0$, is

$$w(r) = \frac{1}{2\pi} \int_0^{\infty} \frac{\tilde{p}}{i\omega} A(k_r) \mathrm{J}_0(k_r r) k_r \mathrm{d}k_r \qquad (12)$$

where the admittances $A(k_r)$ are the same as in equation (7), where they are already written in polar coordinates.

The pressure distribution under the indenter is still unknown. The transformed pressures are found, using the Hankel transform and the same definition as in (11). The Hankel transform pair for the pressure is then

$$\tilde{p}(k_r) = 2\pi \int_0^{\infty} p(r) \mathrm{J}_0(k_r r) r \mathrm{d}r, \qquad (13)$$

$$p(r) = \frac{1}{2\pi} \int_0^{\infty} \tilde{p}(k_r) \mathrm{J}_0(k_r r) k_r \mathrm{d}k_r., \qquad (14)$$

allowing the boundary conditions in equation (2) to be written, by the use of (12) and (14), as

$$\begin{cases} \frac{1}{2\pi} \int_0^{\infty} \frac{\tilde{p}}{i\omega} A(k_r) \mathrm{J}_0(k_r r) k_r \mathrm{d}k_r = w_i \text{ for } r \leq R \\ \frac{1}{2\pi} \int_0^{\infty} \tilde{p}(k_r) \mathrm{J}_0(k_r r) k_r \mathrm{d}k_r = 0 \quad \text{ for } r \geq R \end{cases} \qquad (15)$$

The second condition in (15), applied to equation (13), can be expressed as

$$\tilde{p}(k_r) = 2\pi \int_0^R p(s) s \mathrm{J}_0(k_r s) \mathrm{d}s \qquad (16)$$

where s is a new integration variable. Insert (16) into the first expression in equation (15) and interchange the order of integration. The inner integral can be regarded then as a kernel. Hence, a kernel K can be defined as

$$K(r, s) = \int_0^{\infty} \mathrm{J}_0(k_r s) A(k_r) \mathrm{J}_0(k_r r) k_r \mathrm{d}k_r \quad (17)$$

The kernel K is symmetric in terms of r and s, $K(r, s) = K(s, r)$. The first expression in equation (15) can then be written as

$$\frac{1}{i\omega} \int_0^R p(s) s K(r, s) \mathrm{d}s = w_\mathrm{i} \text{ for } r \leq R \qquad (18)$$

This is a Fredholms integral equation of the first kind. In order for it to be symmetric, make the following substitutions

$$q(r) \equiv p(r)r, \ \ v \equiv \mathrm{i}\omega w_i, \qquad (19)$$

where v is the velocity of the indenter. This allows the integral equation (18) to be written as

$$\int_0^R q(s) K(r, s) \mathrm{d}s = v \text{ for } r \leq R \qquad (20)$$

The function q in (20) is to be determined.

3. Variational formulation

The integral equation (20) is to be approximately solved by use of a variational technique, described by Morse and Ingard [16]. This approach provides a close approximation of the pressure and a very close approximation of the integral of the pressure, i.e. of the force F. Since the components of the integral equation, including the kernel, are complex, an adjoint approach is employed. This involves

the physical situation being made symmetric in terms of the complex power. The correctness of the variational formulation is checked by calculating the displacement under the indenter and comparing it with the boundary conditions, see Figures 9 and 10.

Multiply equation (20) by the complex conjugate q^* and integrate the entire expression from 0 to R. The resulting equation can be written as

$$0 = \int_0^R q^*(r)v\mathrm{d}r$$
$$- \int_0^R q^*(r) \int_0^R q(s)K(r,s)\mathrm{d}s\mathrm{d}r. \qquad (21)$$

Define a functional now as

$$V \equiv \int_0^R q(r)v^*\mathrm{d}r. \qquad (22)$$

Adding equations (21) and (22) results then in the variational formulation of the problem,

$$V = \int_0^R q(r)v^*\mathrm{d}r + \int_0^R q^*(r)v\mathrm{d}r$$
$$- \int_0^R q^*(r) \int_0^R q(s)K(r,s)\mathrm{d}s\mathrm{d}r. \qquad (23)$$

The pressure field that gives the functional (21) a stationary point is the best choice in a variational sense. The physical meaning of the functional V is found by comparing definition (22) with the expression for the force (4), which can be written as

$$\Pi_{\mathrm{in}} = \pi V.$$

Thus, the functional V is proportional to the complex input power, denoted as Π_{in}. The force can be expressed in terms of the functional as

$$F = -2\pi V/v.$$

4. Variational solution

The variational formulation (23) will now be used to find an approximate solution. The result of using one constant is examined first, and then of using two constants.

4.1. One constant

Assume a pressure distribution that corresponds to the semi-infinite case, used by e.g. Ljunggren [12] and Petersson and Heckl [14] (in dealing with the quasi-rigid case),

$$p(r) = c/\sqrt{R^2 - r^2}, \qquad (24)$$

where c is the constant to be determined. With this pressure distribution, the variational formulation (23) becomes

$$V = (cv^* + c^*v) \int_0^R \frac{r}{\sqrt{R^2 - r^2}}\mathrm{d}r$$

$$- cc^* \int_0^R \frac{r}{\sqrt{R^2 - r^2}} \int_0^R \frac{sK(r,s)}{\sqrt{R^2 - s^2}}\mathrm{d}s\mathrm{d}r, (25)$$

where the identity

$$\int_0^R \frac{r}{\sqrt{R^2 - r^2}}\mathrm{d}r = R$$

can be used to simplify the expression. A stationary point is solved for by means of derivation

$$\frac{\partial V}{\partial c^*} = 0 = vR$$
$$- c \int_0^R \frac{r}{\sqrt{R^2 - r^2}} \int_0^R \frac{sK(r,s)}{\sqrt{R^2 - s^2}}\mathrm{d}s\mathrm{d}r \quad (26)$$

Thus, the constant c that best fits the variational formulation of the present pressure distribution is

$$c = vR / \int_0^R \frac{r}{\sqrt{R^2 - r^2}} \int_0^R \frac{sK(r,s)}{\sqrt{R^2 - s^2}}\mathrm{d}s\mathrm{d}r. \ (27)$$

The input mobility can then be determined from equations (4) and (27) as being

$$Y = \frac{1}{2\pi R^2} \int_0^R \frac{r}{\sqrt{R^2 - r^2}} \int_0^R \frac{sK(r,s)}{\sqrt{R^2 - s^2}}\mathrm{d}s\mathrm{d}r. \qquad (28)$$

Inserting the expression for the kernel, equation (17), interchanging the order of integration and utilizing the relation [15]

$$\int_0^R \frac{r\mathrm{J}_0(rk_r)\mathrm{d}r}{\sqrt{R^2 - r^2}} = \frac{\sin(Rk_r)}{k_r}$$

yields

$$Y = \frac{1}{2\pi R^2} \int_0^\infty \frac{\sin^2(Rk_r)}{k_r}A(k_r)\mathrm{d}k_r \qquad (29)$$

This result is equivalent to the result in [14] for a quasi-rigid pressure distribution. Although it does not appear to be possible to calculate this integral analytically, it can be calculated by use of numerical integration, see sections 6 and 7.

The pressure wave number spectrum (16) for the pressure distribution considered here is determined as being

$$\tilde{p}(k_r) = 2\pi c \sin(Rk_r)/k_r. \qquad (30)$$

The displacement at the upper surface is then calculated from equations (12) and (30)

$$w(r) = \frac{c}{\mathrm{i}\omega} \int_0^\infty \sin(Rk_r)\mathrm{J}_0(rk_r)A(k_r)\mathrm{d}k_r. \quad (31)$$

4.2. Two constants

Another pressure distribution is now assumed, one that combines the distribution in equation (24) with a constant pressure distribution,

$$p(r) = c_1/\sqrt{R^2 - r^2} + c_2. \qquad (32)$$

Using two constants allows the pressure field to form itself more freely since an additional degree of freedom is present. With this pressure distribution, the functional (23) becomes

$$
\begin{aligned}
V =\ & v^*(c_1 R + c_2 R^2/2) + v(c_1^* + c_2^* R^2/2) \\
& - c_1 c_1^* I_a - c_1 c_2^* R I_b - c_2 c_1^* R I_b - c_2 c_2^* R^2 I_c
\end{aligned} \tag{33}
$$

where

$$
\begin{aligned}
I_a &= \int_0^R r/\sqrt{R^2 - r^2} \int_0^R s K(r,s)/\sqrt{R^2 - s^2}\,ds\,dr, \\
R I_b &= \int_0^R r \int_0^R s K(r,s)/\sqrt{R^2 - s^2}\,ds\,dr, \\
R^2 I_c &= \int_0^R r \int_0^R s K(r,s)\,ds\,dr.
\end{aligned}
$$

A stationary point is solved for by means of derivation in c_1^* and c_2^*. This yields the system of equations

$$
\begin{bmatrix} I_a & R I_b \\ R I_b & R^2 I_c \end{bmatrix} \begin{bmatrix} c_1 \\ c_2 \end{bmatrix} = \begin{bmatrix} vR \\ vR^2/2 \end{bmatrix}. \tag{34}
$$

Solving (34) gives the two constants

$$
c_1 = (I_c - I_b/2)vR/\Delta \tag{35}
$$
$$
c_2 = (I_a/2 - I_b)v/\Delta \tag{36}
$$

where the determinant is

$$
\Delta = I_a I_c - I_b^2.
$$

Using (4) yields the mobility,

$$
Y = \frac{1}{2\pi R^2} \frac{\Delta}{I_c - I_b + I_a/4}. \tag{37}
$$

The integrals I_a, I_b and I_c are simplified by interchanging the order of integration. I_a is identified from equations (28) and (29)

$$
I_a = \int_0^\infty \frac{\sin^2(R k_r)}{k_r} A(k_r)\,dk_r. \tag{38}
$$

For the other two integrals the identity [15]

$$
\int_0^R J_0(k_r r) r\,dr = J_1(k_r R) R/k_r
$$

is employed. The integral I_b then reads

$$
I_b = \int_0^\infty \frac{J_1(k_r R)\sin(R k_r)}{k_r} A(k_r)\,dk_r, \tag{39}
$$

and I_c is

$$
I_c = \int_0^\infty \frac{J_1^2(k_r R)}{k_r} A(k_r)\,dk_r. \tag{40}
$$

These two integrals are not solved analytically but are integrated numerically, as dealt with in sections 6 and 7.

The pressure wave number spectrum (16) is determined as

$$
\tilde{p}(k_r) = \frac{2\pi}{k_r}(c_1 \sin(R k_r) + c_2 R J_1(R k_r)). \tag{41}
$$

The displacement is determined then from equations (12) and (41)

$$
\begin{aligned}
w(r) =\ & \frac{c_1}{i\omega} \int_0^\infty \sin(R k_r) J_0(r k_r) A(k_r)\,dk_r \\
& + \frac{c_2 R}{i\omega} \int_0^\infty J_1(R k_r) J_0(r k_r) A(k_r)\,dk_r \\
=\ & c_1 I_d(r)/i\omega + c_2 R I_e(r)/i\omega,
\end{aligned} \tag{42}
$$

in which the integrals $I_d(r)$ and $I_e(r)$ are defined.

5. Comparison with earlier works

Ljunggren's [12] conception of the mobility of a rigid indenter, expressed in terms of the present notations, is that

$$
Y = \frac{1}{2\pi R} \int_0^\infty \sin(k_r R) J_0(k_r r) A(k_r)\,dk_r, \tag{43}
$$

where $r \to R$, the integral being $I_d(R)$. Ljunggren solves this integral by means of contour integration, but uses numerical approximations for the poles.

The result for a soft indenter that Ljunggren [10] and Heckl [13], in terms of the present notations, can be expressed as

$$
Y = \frac{1}{\pi R} \int_0^\infty J_1(k_r R) J_0(k_r r) A(k_r)\,dk_r, \tag{44}
$$

where $r \to R$ in [12] and $r \to 0$ in [13], and the respective integrals are $I_e(R)$ and $I_e(0)$.

In Petersson and Heckl [14] the result for a rigid indenter is identical to equation (29), whereas the result for a soft indenter is

$$
Y = \frac{1}{2\pi R^2} \int_0^\infty \frac{J_1^2(k_r R)}{k_r} A(k_r)\,dk_r, \tag{45}
$$

the integral in this case being I_c.

6. Numerical evaluation

Special attention will be directed now at how the numerical integration of the integrals presented in the previous sections should be carried out. The main numerical integration method is that of adaptive gaussian quadrature. In order to shift the singularities contained in $A(k_r)$ off the real axis, and ensure numerical stability, a certain amount of hysteretic damping needs to be introduced ($\eta = 10^{-4}$ is used in the numerical examples in section 7). The real part and the imaginary part of the integrands are integrated separately in order to make fully use of the adaptive routine.

The tail of the integration needs to be dealt with. The integrals in equations (38) to (40) can be expressed as

$$I_i = R^2 \int_0^\infty E_i(k_r) A(k_r) k_r \mathrm{d}k_r, \ i = a, b, c \qquad (46)$$

where

$$E_i(k_r) = \begin{cases} \sin^2(k_r R)/(k_r R)^2 & \text{for } i = a \\ \sin(k_r R) \mathrm{J}_1(k_r R)/(k_r R)^2 & \text{for } i = b \\ \mathrm{J}_1^2(k_r R)/(k_r R)^2 & \text{for } i = c \end{cases}, \quad (47)$$

and for the integrals used for calculating the displacement

$$E_i(k_r) = \begin{cases} \sin(k_r R)/(k_r R^2) \mathrm{J}_0(k_r r) & \text{for } i = d \\ \mathrm{J}_1(k_r R)/(k_r R^2) \mathrm{J}_0(k_r r) & \text{for } i = e \end{cases}. \quad (48)$$

The integrals (46) can separated into two parts,

$$I_i = R^2 \int_0^M E_i(k_r) A(k_r) k_r \mathrm{d}k_r$$
$$+ R^2 \int_M^\infty E_i(k_r) A(k_r) k_r \mathrm{d}k_r = I_i^I + I_i^{II} \quad (49)$$

where a sufficiently large M is selected that $\tanh(\alpha d/2) \approx \tanh(\beta d/2) \approx 1$, provided that the imaginary part of α and β can be neglected. Accordingly, in the integrals I_i^{II} the admittance $A(k_r)$ reduces to

$$A(k_r) = -\frac{\mathrm{i}\omega \alpha k_T^2 / \mu}{(k_r^2 + \beta^2)^2 - 4\alpha\beta k_r^2}.$$

From the fact that here $k_r^2 >> 1$, and therefore

$$A(k_r) = \frac{\mathrm{i}\omega/\mu}{2k_r(1 - k_L^2/k_T^2)}, \qquad (50)$$

it follows that

$$I_i^{II} \approx \frac{\mathrm{i}\omega R^2}{4\mu} \int_M^\infty E_i \mathrm{d}k_r = \frac{\mathrm{i}\omega R^2}{2(1 - k_L^2/k_T^2)\mu}$$
$$\times \left(\int_0^\infty E_i \mathrm{d}k_r - \int_0^M E_i \mathrm{d}k_r \right) \quad (51)$$

in which the definite integral over the semi-infinite range is established analytically for all $E_i(k_r)$ contained in equation (47),

$$\int_0^\infty E_a \mathrm{d}k_r = \pi/2R$$
$$\int_0^\infty E_b \mathrm{d}k_r = \pi/4R$$
$$\int_0^\infty E_c \mathrm{d}k_r = 4/3\pi R \qquad (52)$$

and for the integrals used to calculate the displacement, as given in (48)

$$\int_0^\infty E_d \mathrm{d}k_r$$
$$= \begin{cases} \pi/2R^2 & \text{for } 0 < r < R \\ \mathrm{arccosec}(r/R)/R^2 & \text{for } r > R \end{cases}$$
$$\int_0^\infty E_e \mathrm{d}k_r$$
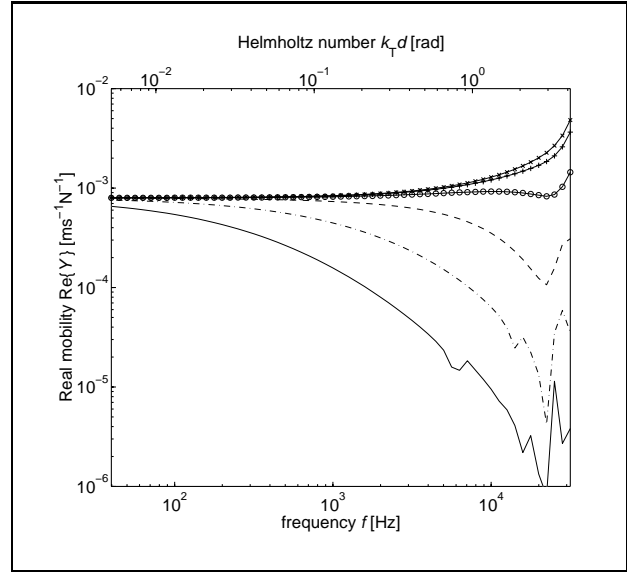
Figure 3. Mobility, real part. Geometric ratio $d/R = \{0.25\ 0.5\ 1\ 2\ 4\ 8\}$, thickness $d = 2 \cdot 10^{-2}$ m. Equation (37). The order of the lines is; —, − · —, - - -, –o–, –+– and –×–.

$$= \begin{cases} \frac{1}{R^2} F(\frac{1}{2}, -\frac{1}{2}; 1; (\frac{r}{R})^2) & \text{for } 0 < r < R \\ \frac{1}{2rR} F(\frac{1}{2}, \frac{1}{2}; 2; (\frac{R}{r})^2) & \text{for } r > R \end{cases} \quad (53)$$

where $F(a, b; c, z)$ is a hypergeometric function, see Appendix.

7. Numerical results

In this section numerical results will be presented. Unless specified otherwise, the following input data are involved: $\rho = 840 \,\mathrm{kg/m^3}$, $\lambda = 1.1538 \cdot 10^9$ Pa and $\mu = 7.6923 \cdot 10^9$ Pa (Young's modulus $E = 2 \cdot 10^9$ Pa and Poisson's ratio $\nu = 0.3$). The damping, introduced in the elastic constants, is set to $\eta = 10^{-4}$.

7.1. Mobility

In Figures 3 and 4 the radius of the indenter varied, such that $R = \{80\ 40\ 20\ 10\ 5\ 2.5\} \cdot 10^{-3}$ m whereas the plate thickness was held constant $d = 2 \cdot 10^{-2}$ m. Thus, the geometric ratio is changed as $d/R = \{0.25\ 0.5\ 1\ 2\ 4\ 8\}$. The mobility was calculated using equation (37).

In Figures 5 and 6 the radius of the indenter was held constant $R = 10^{-2}$ m, whereas the plate thickness was changed in accordance with $d = \{5\ 10\ 20\ 40\ 80\ 160\ 320\} \cdot 10^{-3}$ m . Thus, the geometric ratio is changed as $d/R = \{0.5\ 1\ 2\ 4\ 8\ 16\ 32\}$. The mobility was calculated using equation (37).

In Figures 7 and 8 the mobility is calculated using equation (29), which gives the same result as in [14], and equation (37). Whereas in Figure 7 the radius is $R = 80 \cdot 10^{-3}$ m, in Figure 8 it is $R = 5 \cdot 10^{-3}$ m. In both cases the thickness is $d = 2 \cdot 10^{-2}$ m, the other data is kept the same as before.
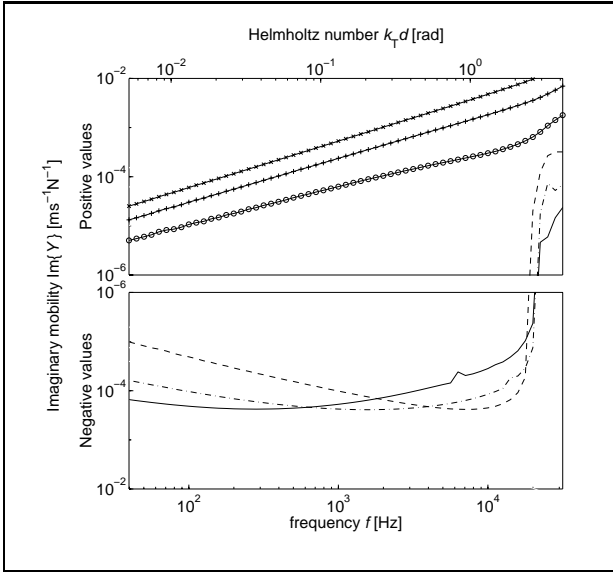
Figure 4. Mobility, imaginary part. Geometric ratio $d/R = \{0.25\ 0.5\ 1\ 2\ 4\ 8\}$, thickness $d = 2 \cdot 10^{-2}$ m. Equation (37). Note the reversed scale for the negative values. The order of the lines is; —, — · —, - - -, –○–, –+– and –×–.
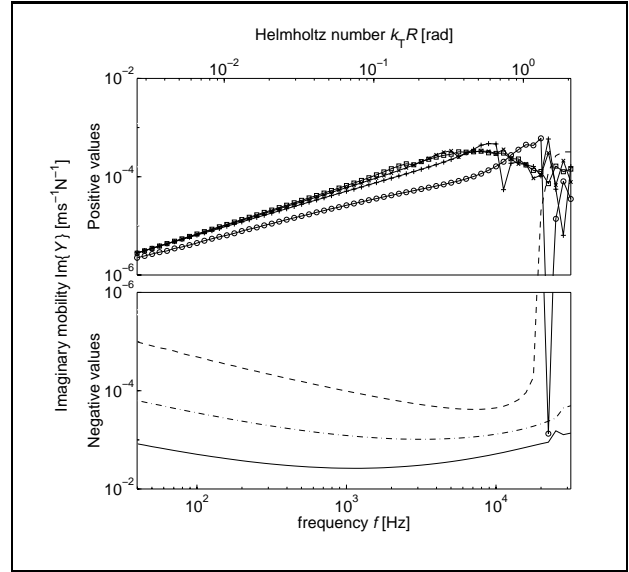
Figure 6. Mobility, imaginary part. Geometric ratio $d/R = \{0.5\ 1\ 2\ 4\ 8\ 16\ 32\}$, radius $R = 10^{-2}$ m. Equation (37). Note the reversed scale for the negative values. The order of the lines are; —, — · —, - - -, –○–, –+–, –×– and –□–.
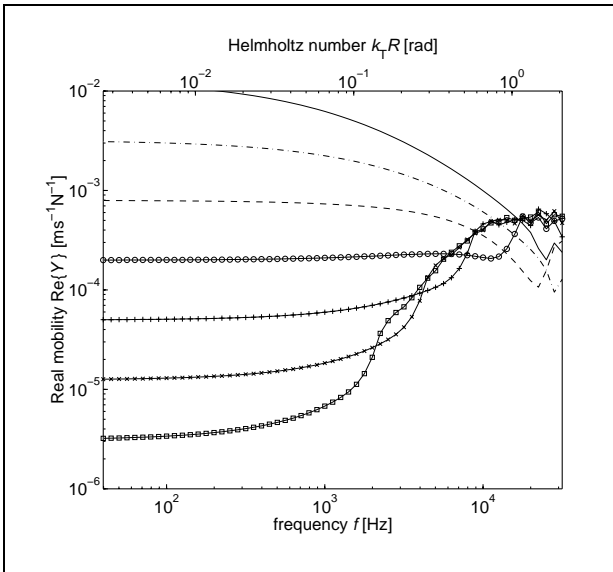
Figure 5. Mobility, real part. Geometric ratio $d/R = \{0.5\ 1\ 2\ 4\ 8\ 16\ 32\}$, radius $R = 10^{-2}$ m. Equation (37). The order of the lines is; —, — · —, - - -, –○–, –+–, –×– and –□–.
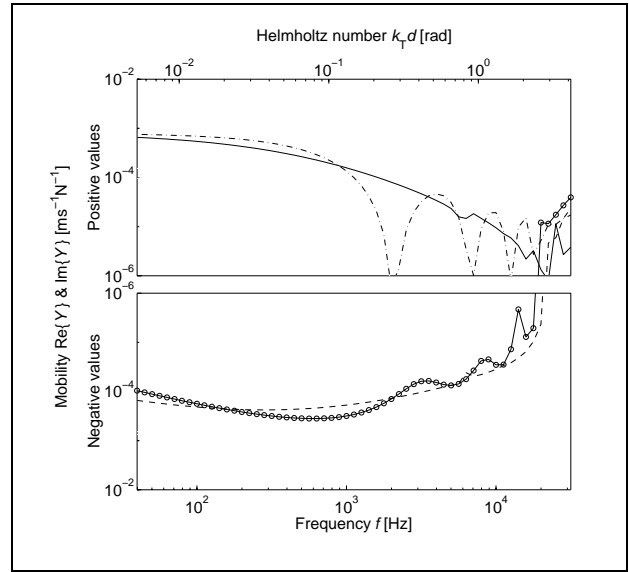
Figure 7. Mobility, real part equation (37) solid (—), real part equation (29) dotted (— · —), imaginary part equation (37) dash-dotted (- - -), and imaginary part equation (29) dashed (–○–). Note the reversed scale for the negative values.

7.2. Spatial dependency of displacement and pressure

Since the solution technique employed is an approximate one, it is important to examine the extent of disagreement between the resulting displacement (indentation) and the displacement of the completely rigid indenter in terms of the boundary conditions (2).

In Figures 9 and 10 show the displacement for $0 \leq r \leq 2R$, normalised to the boundary condition, $w(r)/w_i$. Note that the scale is reversed. The geometric parameters were

chosen as $R = d = 2 \cdot 10^{-2}$ m. The frequency is $f = 100$ Hz in Figure 9 and $f = 1000$ Hz in Figure 10.

In Figure 11 and 12 the pressure is shown as a function of the radius for the interval $0 \leq r \leq R$, both the one-constant ($\cdots$) and the two-constant case (—) being presented for comparison purpose. The geometric parameters were chosen once again as $R = d = 2 \cdot 10^{-2}$ m, the frequency being $f = 100$ Hz in Figure 11 and $f = 1000$ Hz in Figure 12.
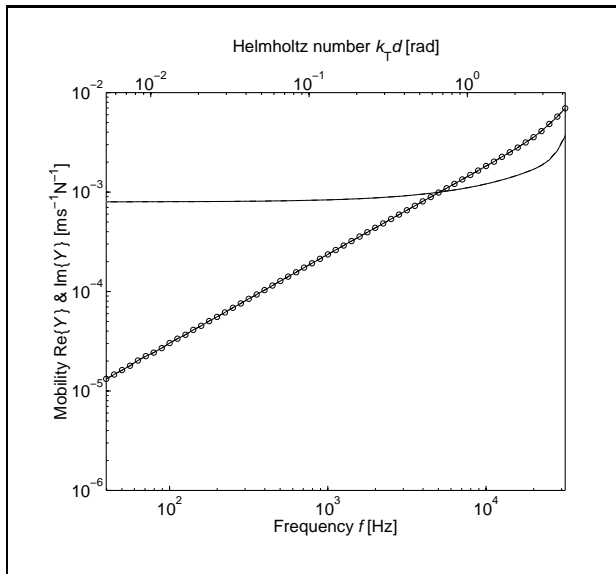
Figure 8. Mobility, real part equation (37) solid (—), real part equation (29) dotted (− · −), imaginary part equation (37) dash-dotted (- - -), and imaginary part equation (29) dashed (–○–).
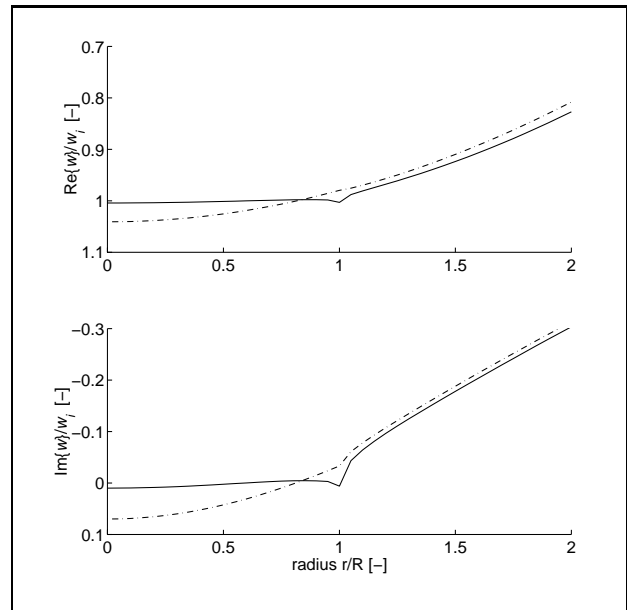
Figure 10. Indentation, real and imaginary part. Frequency $f = 1000$ Hz. Equation (31), one constant, dash-dotted line (− · −), and (42), two constants, solid line (—).
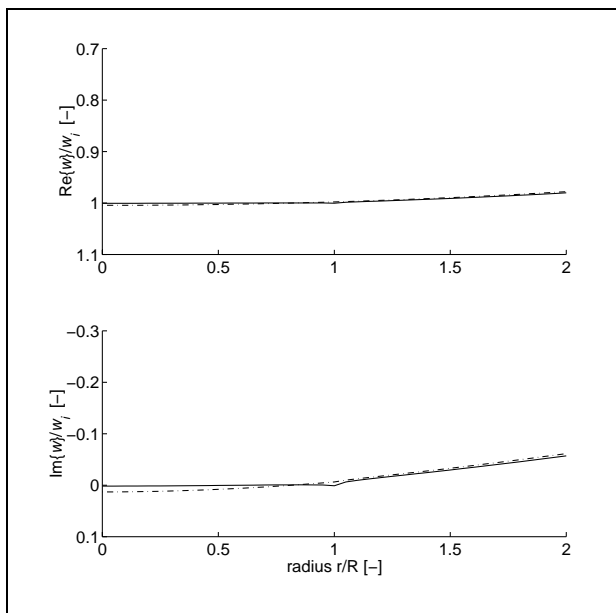
Figure 9. Indentation, real and imaginary part. Frequency $f = 100$ Hz. Equation (31), one constant, dash-dotted line (− · −), and (42), two constants, solid line (—).
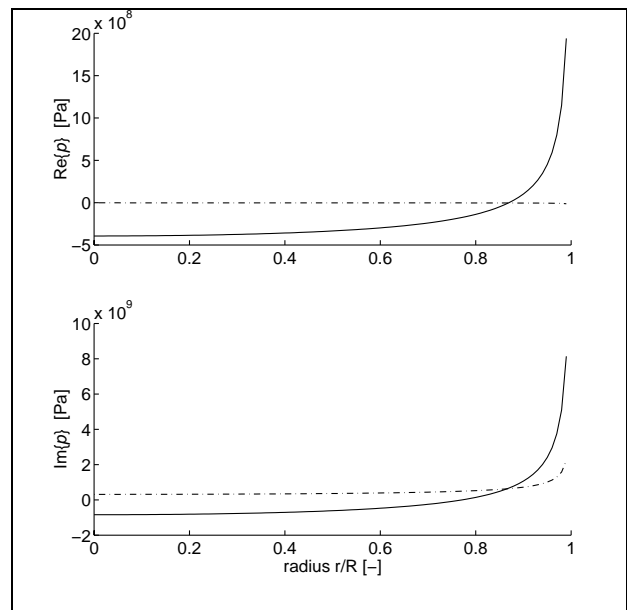
Figure 11. Pressure, real and imaginary part. Frequency $f = 100$ Hz. Equation (24), one constant, dash-dotted line (− · −), and (32), two constants, solid line (—).

8. Discussion

Unless indicated otherwise, the discussion concerns the two-constant cases according to section 4.2.

The frequency dependency of the mobility for different values of d and R is typically as follows: For low frequencies the real part of the mobility, $Y_\Re$, is equal to the result given by equation (1), $1/8\sqrt{m''B}$. When the geometrical ratios are approximately in the region $0 < d/R < 2$ the real part $Y_\Re$ decreases with an increase in frequency. For a geometrical ratio larger than approximately $d/R > 2$,

it is the real part $Y_\Re$ which instead increases with an increase in frequency, as can be seen in Figures 3 and 5. The imaginary part of the mobility, $Y_\Im$, is predominantly negative when the geometrical ratio is approximately $0 < d/R < 2$, and is positive when $d/R > 2$. A positive imaginary part $Y_\Im$ can be regarded as an elastic deformation near the indenter, whereas a negative imaginary part $Y_\Im$ can be regarded as representing inertia effects near the indenter. However, the sign of $Y_\Im$ can also be con-

Figure 12. Pressure, real and imaginary part. Frequency $f = 1000$ Hz. Equation (24), one constant, dash-dotted line ($- \cdot -$), and (32), two constants, solid line (—).

matching effect, analogous to the coincidence effect in airborne sound radiation, when the spatial dependency of the pressure field is unable to change. Note that the actual physical pressure is able to change its spatial dependency, and that the wave-trace-matching effect is thus not likely to occur in the actual situation. This argumentation holds for all theories with a fixed spatial dependency of the pressure. As indicated, Figures 7 and 8 gives an idea of how the present analysis is related to the analysis presented by Petersson and Heckl [14]. The other analysis, equations (43) and (44), can be analysed by considering the spatial dependency of the displacement in Figures 9 and 10, since the same integrals, $I_d(r)$ and $I_e(r)$, are involved. Equation (43) is to describe the mobility of a rigid indenter, the spatial dependency of $I_d(r)$ appearing as the dotted line ($\cdot \cdot$) in Figures 9 and 10, where $r = R$. Since the radius $r = R$ is a special case, as can be seen in the figures, the correctness can be questioned. The same argumentation holds for equation (44). The soft indenter in Petersson and Heckl [14], equation (45), is included for comparison purposes.

The spatial dependency of the displacement is examined in Figure 9 and is compared with the boundary condition, equation (2), are much better fulfilled in the two-constant case than in the one-constant case, equation (42). This result can be regarded as surprisingly good, in view of the solution technique being only approximate. The spatial dependency of the pressure field is shown in Figures 11 and 12. The pressure for the one-constant case is compared there with that for the two-constant case. The two-constant pressure typically changes sign as the radius r increases; the sign is negative for both the real and the imaginary parts at approximately $r/R < 0.8 - 0.9$, and is positive at $r/R > 0.8 - 0.9$. Since the one-constant pressure is fixed, it cannot change sign. Note that in both cases a singularity occurs at $r = R$, the figures there being truncated.

sidered as being a consequence of the causality principle. The main consequence of the causality here is well-known from linear system theory, through the principle that the real and the imaginary part of the frequency response function are interrelated. In the present situation the frequency response function is the mobility $Y = Y_\Re + iY_\Im$. The relations linking the real and the imaginary parts of the frequency response function are generally referred to as Kramers-Kronig dispersion relations. The local (and approximate) version of these dispersion relations can be written [17, 18] as

$$Y_\Im \approx \frac{\pi\omega}{2} \frac{\mathrm{d}Y_\Re}{\mathrm{d}\omega} \approx \frac{\pi}{4.6} \frac{\mathrm{d}Y_\Re(\omega)}{\mathrm{d}(\log\omega)} \tag{54}$$

Thus, when the real part $Y_\Re$ has a positive derivative, the imaginary part $Y_\Im$ is positive and 'spring-like', whereas when $Y_\Re$ has a negative derivative, $Y_\Im$ is negative and 'inertia-like'. This can be observed in Figures 3 to 6.

Some of the roughness for high frequencies in Figures 3 to 6 is due to numerical instability in the integration that is somewhat magnified in the evaluation as subtraction is present in equation (37).

In Figures 7 and 8, one-constant mobility, equation (29), and the result for [14], are compared with two-constant mobility, equation (37). Whereas in Figure 7 the two results disagree, in Figure 8 they are in principle identical. The difference between the results for the two calculations is that in Figure 7 the geometric ratio is $d/R = 0.25$, whereas in Figure 8 the geometric ratio is $d/R = 4$. Thus, consideration of the more elaborate two-constant case appears to be necessary in dealing with small geometric ratios. As can be seen, the real part $Y_\Re$ in the one-constant case involves zeros, whereas there are no zeros in the two-constants case. This can be interpreted as a wave-trace-

9.   Concluding remarks

A variational technique is used to determine the mobility of a rigid indenter that acts on a plate of finite thickness. In this approach, a particular spatial form of the pressure field under the indenter is assumed, the constant magnitude of this assumed field best satisfying the variational formulation is found by means of optimisation. The functional that is used in the variational formulation is identified as the complex input power. Two types of pressure distributions are analysed, a distribution with one constant $p(r) = c/\sqrt{(R^2 - r^2)}$, and a distribution with two constants $p(r) = c_1/\sqrt{(R^2 - r^2)} + c_2$. The latter yields a more elaborate result. Expressions for the mobility involving integrals that need to be calculated numerically are derived for both cases. Numerical results are presented, its being shown that the imaginary part of the mobility can have either a positive or a negative sign, depending on the derivative of the real part. It is also shown that, for small geometric ratios d/R in particular, the more elaborate two-constant case is needed for describing the mobil-

ity, especially of the imaginary part. Thus, the hypothesis that in the expressions in the literature, the imaginary part of the mobility is not entirely correct cannot be rejected. It is also shown that the two-constant analysis is close to fulfilling the boundary conditions, and is thus also close to being a correct analysis. The present analysis is thus an improvement on earlier analysis.

Acknowledgement

Appendix

The hypergeometric function $F(a, b; c, z)$ is implemented by use of the Gauss hypergeometric series [19]

$$F(a, b; c, z) = \frac{\Gamma(c)}{\Gamma(a)\Gamma(b)} \sum_{n=0}^{\infty} \frac{\Gamma(a+n)\Gamma(b+n)}{\Gamma(c+n)} \frac{z^n}{n!} \quad (A1)$$

which has a convergence circle of $|z| = 1$. When the sum is used in numerical calculations, it is truncated.

References

[1] J. Brunskog, P. Hammer: The interaction between the iso tapping machine and lightweight floors. Acustica / acta acustica **accepted**.

[2] J. Boussinesq: Applications des potentiels. Gauthier-Villars, Paris, 1885.

[3] G. Bycroft: Forced vibrations of a rigid circular plate on a semi-infinite elastic space and on an elastic stratum. Philosophical Transactions of the Royal Society **A248** (1956) 327–368.

[4] I. A. Robertson: Forced vertical vibration of a rigid circular disc on a semi-infinite elastic solid. Proc. Camb. Phil. Soc. **62** (1966) 547–553.

[5] Z. Hryniewicz: Vibration of a rigid body on an elastic half-plane. Computer methods in applied mechanics and engineering **24** (1980) 113–123.

[6] Z. Hryniewicz: Dynamic responce of a rigid strip on an elastic half-space. Computer methods in applied mechanics and engineering **25** (1981) 355–364.

[7] S. Krenk, H. Schmidt: Vibration of an elastic circular plate on an elastic half space. A direct approach. Journal of Applied Mechanics **48** (1981) 161–168.

[8] H. Schmidt, S. Krenk: Asymmetric vibrations of a circular elastic plate on an elastic space. Int. J. Solids Structures **18** (1982) 91–105.

[9] H. Cremer, L. Cremer: Theorie der entstehung des klopf-schalls. Frequenz **2** (1948) 61–71.

[10] S. Ljunggren: Mechanical excitation of plates at low frequencies: A discussion on the use of the bending wave equation. Acta acustica **3** (1995) 531–538.

[11] H. S. Paul: Vibration of a rigid circular disk on an infinite isotropic elastic plate. Journal of the Acoustical Society of America **42** (1967) 412–416.

[12] S. Ljunggren: Generation of waves in an elastic plate by a vertical force and by a moment in the vertical plane. Journal of Sound and Vibration **90** (1983) 559–584.

[13] M. Heckl: Körperschallübertragung bei homogenen platten beliebiger dicke. Acustica **49** (1981) 183–191.

[14] B. A. T. Petersson, M. Heckl: Concentrated excitation of structures. Journal of Sound and Vibration **196** (1996) 295–321.

[15] L. Råde, B. Westergren: Mathematics handbook for science and engineering. Studentlitteratur, Lund, Sweden, 1995.

[16] P. M. Morse, K. U. Ingard: Theoretical acoustics. Prinston university press, Prinston, New Jersey, 1968.

[17] M. O'Donnell, E. T. Jaynes, J. G. Miller: Kramers-Kronig relationship between ultrasonic attenuation and phase velocity. Journal of the Acoustical Society of America **69** (1981) 696–701.

[18] T. Pritz: Frequency dependences of complex moduli and complex poisson's ratio of real solid materials. Journal of Sound and Vibration **214** (1998) 83–104.

[19] F. Oberhettinger: Hypergeometric functions. – In: Handbook of mathematical functions. M. Abramowitz, I. A. Stegun (eds.). Dover, New York, 1965, 555–566.

The interaction between the ISO tapping machine and lightweight floors

Jonas Brunskog and Per Hammer
Division of Engineering Acoustics, LTH, Lund University, P.O. Box 118, SE-221 00 Lund, Sweden
E-mail: jonas.brunskog@acoustics.lth.se, per.hammer@acoustics.lth.se

Summary
The ISO standard tapping machine, used as an excitation source in rating the impact-sound level of a floor structure, interacts with the floor structure during the hammer impact. Expressions for the force spectrum due to the impact are presented. The 6 dB difference at low frequencies of the force spectrum, evident in measurements, and reasons for it, are discussed. The interaction is investigated by use both of simplified lumped models and arbitrary frequency-dependent models. Local effects due to indentation near the point of impact and to global effects due to stiffeners are included in the description of the mobility involved. Numerical results are presented, where it is concluded that both the local and the global effects of the driving-point mobility are important in describing the force spectrum caused by the interaction between the tapping machine and the complex floor structure.

PACS no. 43.40.Dx, 43.40.Kd, 43.55.Ti

1. Introduction

The use of lightweight building techniques has increased during the last few years. It is well-known, however, that structures of this type often have poor impact-sound insulation. A prediction model is an important tool in developing structures that have acceptable insulation characteristics and in explaining how they function. A model for predicting impact noise can be said to consist of three parts: the excitation, the system and the response. The present paper focuses on the excitation part. Point impact excitation can be caused by e.g. footsteps or the impact of dropped items. Excitation can also be produed by the ISO standard tapping machine [1], as dealt with in the present paper. Thus, the paper aims at deriving expressions for the force spectrum produced by the impact of a hammer on a lightweight floor.

The system, or more specifically the representation of the floor system in question, is important not only as a transfer part from excitation to response, but also of deriving the impact force. It is important, therefore, that attention be directed at the interaction between the hammer and the floor. The system and the response are examined in greater detail in [2], in which measurements are also compared with predictions derived from a model. A comprehensive survey of the literature on prediction model approaches is presented in [3].

The ISO standard tapping machine can be used as an excitation source for rating the impact-sound level of a floor structure. Although the machine provides no genuine simulation of real footsteps, the test results obtained yield valuable information concerning the dynamic behaviour of the floor. If the description of the tapping machine as a source is sufficiently thorough and precise, it may be possible sometime in the future to solve the problem of the correlation between sound disturbances by footsteps and the impact sound level produced by the machine.

Cremer has derived the impact noise level caused by a tapping machine for homogenous structures of high impedance, the results being summarised by Cremer and Heckl [4, pp. 269–271, 333–339]. In dealing with a bare slab Cremer makes use of momentum calculations that assume there to be a perfect elastic impact (described in section 2 of the present paper) the results are quit satisfactory. However, when taking into account the effects of a resilient floor covering, Cremer's description of the problem implies that the hammer becomes stuck to the floor after impact. This leads to resonant behaviour that is not to be found in measurements according to the ISO standard. In fact, the hammer rebounds after impact, there being only an initial positive force pulse present, a matter investigated by Lindblad [5]. Also, regarding linear excitation Lindblad considered the effect of an energy-consuming part of the deformation, conceived as a resistance in series with a spring to represent the resilient covering. The resistance can be due to local material damping or, as in the present study, to energy being transported within the plate away from the region of impact. For heavy slabs, as considered in references [4, 5, 6], the resilient part is due to the floor covering. Lindblad's major interest, however, was in the non-linear behaviour of coverings that interact with the hammer. Vér [6] derived a complete and accurate description of the force spectrum and the impact noise level a tapping machine produces on hard surfaces, including the rebound. The improvement in insulation achieved by use of an elastic surface layer (floor covering) or of floating floors with surfaces of high impedance is also considered.

A lightweight floor structure can usually not be regarded as a homogenous structure of high impedance. It consists of thin plates of wood, chipboard, gypsum, or whatever, and is reinforced by joist stiffeners. Thus, it cannot be assumed that the force spectrum in [4, 5, 6] is applicable generally. Nevertheless, in more recent papers on impact-sound insulation, such as Gerretsen [7], the

momentum model of Cremer and Heckl [4] has continued to be used, also for non-homogenous or lightweight floors. Thus, it is common to assume the force spectrum to be invariant with respect to the excitation system (i.e. of its being a linear source with infinite source mobility). In the present paper no such assumption is made. In another recent paper, by Scholl et al. [8], the interaction between the source, the floor covering and the floor structure is considered. However, the floor structure is represented by the mass of the structure, not taking into account that the driving-point impedance of a plate on average has the characteristics of a resistance (i.e. $8\sqrt{m''B}$), and in general is complex. Thus, no energy (or momentum) consuming part is included in the model used by Scholl.

Measurements, such as those of Hall's [9], indicates there to be a 6 dB gap at low frequencies between the force (or acceleration) spectrum of a hammer impacting on a high impedance surface such as concrete and its impacting on a low impedance surface such as an mdf-board. This can easily be explained in terms of simple momentum consideration in a manner comparable with the case to which Cremer's [4] calculations but letting the hammer be stuck to the plate, as will be taken up in section 2.

The organisation of the paper is as follows: In order to obtain a force spectrum of a form suitable for the solution technique applied to the system described in [2], the findings reported in [4, 5, 6] are integrated and re-analysed in sections 2 and 3, several numerical examples being provided there. A system of arbitrary frequency-dependent driving-point mobilities is then added in section 4, in which different causes for the frequency-dependent driving-point mobilities are discussed. The procedure for evaluating these mobilities numerically is described in section 5. The numerical results are presented in section 6, the conclusions being summarized, finally, in section 7.

The present analysis is based on linear theory implying that the contact area during impact is constant, as discussed in section 3.2. The displacement of the receiver structure is in addition small, and therefore assumed to be within the linear range. It should be noted, however, that a direct linear-system analysis is not applicable since the system is changed when the object producing the impact leaves the structure with which it has had contact. Thus, the boundary condition between the object and the structure is rather being an inequality than an equation, and the situation is not time-invariant.

2. The hammer impact force in the time and the frequency domain

The ISO standard tapping machine [1] consists of five hammers spaced equally along a line 40 cm in length. As an approximation, it is assumed here, however, that all hammer impacts act on the same position. Each hammer has a mass of $M = 0.5$ kg and it is dropped from a height h of 4 cm. The hammers strike the floor with a rate of $f_r = 10$ times per second, giving a repetition time of $T_r = $

$1/f_r = 0.1$ s. Consider initially, however, a single hammer impact with the force time history $f_1(t)$. The Fourier spectrum of this force pulse is $F_1(f) = \mathcal{F}_t\{f_1(t)\}$, $\mathcal{F}_t\{\cdot\}$ being the Fourier transform operator (time to frequency). In the present paper, the word spectrum is used to denote a function in the (Fourier) frequency domain. The excitation caused by the tapping machine can be regarded as an array of separate force pulses $f_1(t)$. The time history of the repeated force $f_R(t)$ is thus

$$f_R(t) = \sum_{n=-\infty}^{\infty} f_1(t - nT_r). \tag{1}$$

This time history is a periodic signal. Accordingly, it can be represented by a Fourier series, e.g. by the two-sided complex Fourier series

$$f_R(t) = \sum_{n=-\infty}^{\infty} F_n e^{i2\pi nt/T_r}. \tag{2}$$

The signal is represented by a Fourier series consisting of an infinite number of discrete frequency components of amplitude F_n. The Fourier spectrum for the signal is the tonal spectrum

$$F_R(f) = \mathcal{F}_t\{f_R(t)\} = \sum_{n=-\infty}^{\infty} F_n \delta(f - nf_r) \tag{3}$$

where $F_R(f)$ denotes the spectrum of the repeated signal. It was used in [2] as the excitation force of the system, whereas δ denotes the Dirac delta function. Each amplitude is given by

$$F_n = \frac{1}{T_r} \int_0^{T_r} f_1(t) e^{-i2\pi nt/T_r} dt \tag{4}$$

where, as indicated above, $f_1(t)$ is the force time history of a single hammer impact. This integral is identical with the Fourier transform of the individual force pulse except for the factor $1/T_r$. Thus, for the tapping machine the repeated force components F_n is 10 s^{-1} times the force spectrum for a single impact. If a trigonometric Fourier series is used instead, each sine or cosine component is twice that in (4). This is due to the two-sided representation described in (2), which is the most suitable representation in the present situation, since the force spectrum is used in a two-sided model, i.e. one in which there is assumed to be an e^{iwt} dependence. Cremer [4] and Vér [6] used a one-sided representation, together with a RMS and a (third) octave band procedure.

For low-frequency components the force pulse is usually short compared with the period of interest. Accordingly, the Fourier amplitude of the force pulse train during the effective interval of the force pulse, $\exp(-i2\pi nt/T_r) \approx 1$, can be approximated by

$$F_n|_{f\to 0} = \frac{1}{T_r} \int_0^{T_r} f_1(t) dt \tag{5}$$
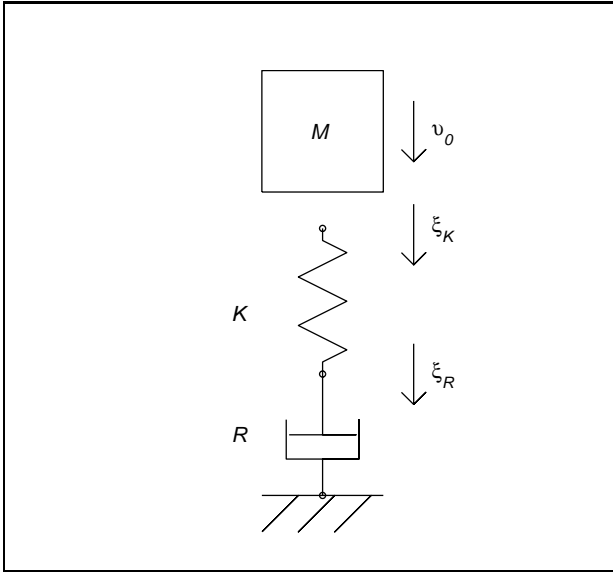
Figure 1. Model of hammer impact

which is the mechanical impulse divided by T_r, the mechanical impulse being equal to the change in momentum. The hammer hits the slab with a velocity $v_0 = (2gh)^{1/2} = 0.886$ m/s. If the impact is purely elastic, the momentum of the hammer after impact is equal in magnitude to that prior to impact but is of the opposite sign, the hammer lifting from the slab with the velocity v_0. Thus, $F_n|_{f\to 0} = 2Mv_0/T_r = 8.859$ N (where for a single force pulse the corresponding low-frequency asymptote is $F_1|_{f\to 0} = 2Mv_0$). Since this is the highest possible low-frequency asymptote of the impact spectrum, it is the maximum value for the magnitude of the spectrum. At the other extreme, if the impact is so damped that the entire momentum is dissipated during impact, the hammer does not rebound. The mechanical impulse is then $F_n|_{f\to 0} = Mv_0/T_r = 4.430$ N ($F_1|_{f\to 0} = Mv_0$). This is the lowest possible low-frequency asymptote of the impact spectrum. Thus, these two cases constitute the upper and lower bounds of the low-frequency asymptote of the force spectrum, which represents a span of 4.429 N, or 6 dB. As indicated above, this span can be clearly seen in measurements that have been made [9].

3. Impact force and lumped system

In order to include cases between the two extremes just referred to, a lumped model can be employed, one that provides a somewhat more realistic description than that of momentum consideration does. The model and the solution arrived at are taken from Lindblad [5], whereas the physical situation and the analysis are new. A treatment of general frequency-dependent impedances is found in section 4.

3.1. A single slab, interaction between hammer and floor

A lumped model of the impact of the hammer on a single slab floor is shown in Figure 1. The floor consists of a resilient part and an energy consuming part, represented by a spring with stiffness K and by a dashpot with resistance R, respectively. The physical meaning of the two components is discussed in section 3.2.

When the hammer has reached the slab, the differential equation for the system assumed is

$$M\partial^2\xi_K/\partial t^2 = K(\xi_K - \xi_R)$$
$$K(\xi_R - \xi_K) = R\partial\xi_R/\partial t \qquad (6)$$

where ξ_K and ξ_R are displacements. Under the initial condition v_0, and assuming frequency independent K and R, the solution is found to be [5]

$$f_1(t) = \begin{cases} v_0 K \frac{\sinh(\Omega_{oc}t)}{\Omega_{oc}} e^{-Kt/2R}, & KM \geq 4R^2 \\ v_0 K \frac{\sin(\Omega_{uc}t)}{\Omega_{uc}} e^{-Kt/2R}, & KM < 4R^2 \end{cases} \qquad (7)$$

which of these applies depending on whether the oscillation is overcritical or not, where

$$\Omega_{oc} = \sqrt{(K/2R)^2 - K/M}$$
$$\Omega_{uc} = \sqrt{K/M - (K/2R)^2}$$

are the overcritical and the undercritical angular frequency, respectively. In Lindblad [5] the first of these is denoted as the 'stuck to the floor' case and the latter as the 'rebound' case. If an overcritical oscillation is present, a numerically more appropriate form would be to write the expression in terms of exponential functions instead of hyperbolics combined with exponentials. For $R \to \infty$, or if $\xi_R = 0$, equation (7) is replaced by

$$f_1(t) = v_0 K \sin(\sqrt{K/M}\,t)/\sqrt{K/M} \qquad (8)$$

which is an undamped oscillation in which $f_{cut}^{ud} = 1/(2\pi)(K/M)^{1/2}$ is the undamped natural frequency (and cutoff frequency). The force starts at zero at the moment the hammer hits the slab, and increases to a maximum, at which point the hammer reaches its maximum depth, the hammer then starting to return and the force decreasing. As the force reaches the zero crossing at $t_{cut} = 1/(2f_{cut})$, the hammer rebounds, takes off from the slab and is picked up by a catching mechanism (an eccentric cam). Thus, the force is zero after this moment,

$$f_1(t) = \begin{cases} \frac{v_0 K}{\sqrt{K/M}} \sin(\sqrt{K/M}\,t), & 0 < t < \frac{1}{2f_{cut}} \\ 0, & \text{else.} \end{cases}$$

The same conditions hold for the damped oscillations described in (7). In the overcritical case the force will never completely be zero. However, the force still decreases rapidly after reaching the maximum and is approximately zero at T_r. Each amplitude in the tonal spectrum of the ISO tapping machine is given then by

$$F_n = \frac{1}{T_r} \int_0^{T_r \approx \infty} f_1(t) e^{-i2\pi nt/T_r} dt \qquad (9)$$

in the case of overcritical damping, and by

$$F_n = \frac{1}{T_r} \int_0^{t_{cut}} f_1(t) e^{-i2\pi nt/T_r} dt \qquad (10)$$

in the case of undercritical damping. These integrals can be expressed in closed form, but are likewise well suited for numerical integration. The Fourier transforms of a single impact are given below, where the cutoff frequencies are also determined. For the over-critical case, the inequality $K/2R > \Omega_{oc}$ holds, giving a Fourier transform over time to angular frequency $\omega = 2\pi f$ of equation (7),

$$\begin{aligned} F_{1,oc} &= \mathcal{F}_t\{f_1(t)|_{oc}\theta(t)\} \\ &= \frac{v_0 KM}{K - \omega^2 M + i\omega KM/R} \end{aligned} \qquad (11)$$

where $\theta(t)$ is the unit step function. The low-frequency asymptote of (11) is

$$F_{1,oc}|_{f\to 0} = v_0 M$$

as expected. In the undercritical case, a Fourier transform over time of equation (7) yields, taking into account the time interval of interest

$$\begin{aligned} F_{1,uc} &= \mathcal{F}_t\{f_1(t)|_{uc}\left(\theta(t) - \theta(t - t_{cut})\right)\} \\ &= \frac{v_0 KM\left(1 + e^{-t_{cut}(i\omega + K/2R)}\right)}{K - \omega^2 M + i\omega KM/R} \end{aligned} \qquad (12)$$

where

$$t_{cut} = \pi/\Omega_{uc} = 1/2f_{cut}$$

is the time of zero-crossing. The low-frequency asymptote is

$$F_{1,uc}|_{f\to 0} = v_0 M\left(1 + e^{-Kt_{cut}/2R}\right)$$

which has two extremes depending on the resistance R,

$$F_{1,uc} = \begin{cases} 2v_0 M, & f \to 0 \text{ and } R \to \infty \\ v_0 M, & f \to 0 \text{ and } R \to \frac{1}{2}\sqrt{KM} \end{cases}$$

which agrees with the asymptotes schematically derived in section 2 on the basis of the mechanical impulse and the change in momentum.

In both the overcritical and the undercritical case, the Fourier series components are then found to be $F_n = F_1(nf_r)f_r$, and the complex cutoff angular frequency (i.e. the poles) is

$$\omega_{cut} = iK/2R \pm \sqrt{K/M - K^2/(2R)^2} \qquad (13)$$

If the negative sign is chosen, the absolute value of the complex cutoff angular frequency yields the point of interest on the real axis,

$$|\omega_{cut}| = \begin{cases} \frac{K}{2R} - \sqrt{\frac{K^2}{(2R)^2} - \frac{K}{M}}, & KM \ge 4R^2 \\ \sqrt{\frac{K}{M}}, & KM < 4R^2 \end{cases} \qquad (14)$$

The cutoff frequency then is

$$f_{cut} = |\omega_{cut}|/2\pi, \qquad (15a)$$

whereas in the undercritical case the undamped cutoff frequency,

$$f_{cut}^{ud} = 1/(2\pi)\sqrt{K/M} \qquad (15b)$$

is employed, this being the frequency at which the phase equals $-\pi/2$.

3.2.   Choice of the frequency independent stiffness and resistance

In Figure 1 the impedance at the position where the hammer hits the floor is represented by a spring and a dashpot in series. Thus, a suitable stiffness K and a resistance R need to be found in order to achieve an adequate approximation of what occurs at impact. The resilient part is often the result of there being an elastic surface layer on an otherwise bending stiff slab. The stiffness of the elastic layer is then $K = EA_h/d$, c.f. Vér [6], where E is Young's modulus, d is the thickness of the elastic layer, and A_h is the area of the hammer. The resistance is then related to the local dissipation, $R = \eta(KM)^{1/2}$, η being the loss factor for the material. In the lightweight floor structures considered in this paper, however, the hammer hits a rather thin plate made of gypsum or of wooden material. It can thus be assumed that the resilient part is due to local deformation of the plate, and the resistive part to energy transportation within the plate. As a first approximation, the stiffness of the local deformation can be found, as in [10, 11], by

$$K = 2GD_h/(1 - \nu) = ED_h/(1 - \nu^2) \qquad (16)$$

where G is the shear modulus, ν is Poisson's ratio and $D_h = 2(A_h/\pi)^{1/2}$ is the diameter of the hammer. The local stiffness here is found for a static deformation caused by a rigid stamp on a semi-infinite elastic solid, the so-called Bossinesq deformation. If the area of contact between the hammer and the floor can be regarded as involving contact between two elastic bodies of different radii, a geometric non-linearity will occur, a so-called Hertz deformation [10]. The hammers of the tapping machine are actually not entirely flat, but since after a few impacts the material in the impact zone becomes somewhat plastically deformed by the hammer it is assumed that the Hertz deformation effect will not be dominant in the steady-state vibrational phase.

The resistance is taken to be the real driving-point impedance of a thin plate,

$$R = 8\sqrt{m''B}, \qquad (17)$$

its being taken into account that energy is transported away from the excitation point by bending wave motion. Here m'' is the mass per unit area and $B = EI'$ is the bending stiffness of the plate.
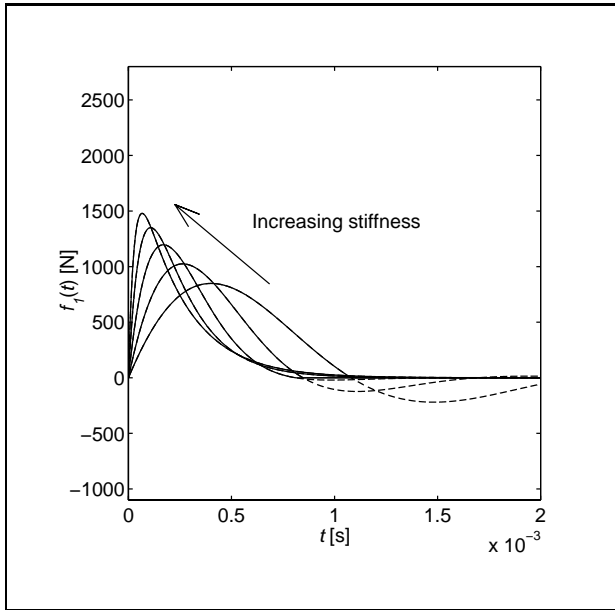
Figure 2. Time history of hammer impact. Solid line (—) denotes the interrupted force, dashed line (- - -) denotes the oscillating force. The parameters are $K = \{5\ 10\ 20\ 40\ 80\} \cdot 10^6$ N/m, $R = 2 \cdot 10^3$ Ns/m .
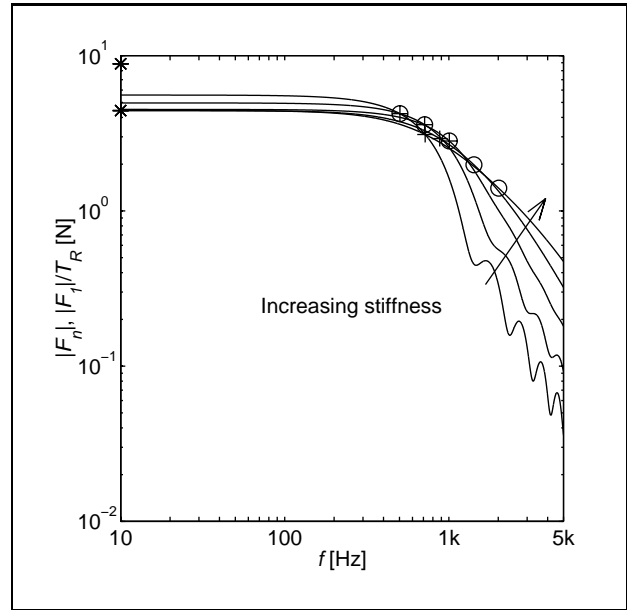
Figure 3. Hammer impact spectrum, showing magnitudes. The parameters are $K = \{5\ 10\ 20\ 40\ 80\} \cdot 10^6$ N/m and $R = 2 \cdot 10^3$ Ns/m.

Both of these lumped parameters are frequency independent, a necessary condition for the solution technique described in section 3.1.

3.3. Numerical examples

Various numerical examples will be presented now to illustrate certain features of the lumped two-parameter description of the impact force of the tapping machine. The examples will come from a specific combination of R and K, where $R = 2 \cdot 10^3$ Ns/m and $K = 4 \cdot 10^6$ N/m. These values correspond roughly to an infinite 22 mm thick wooden plate, use being made of equations (16) and (17), respectively. The parameters are varied one at the time.

In Figures 2 to 4 the stiffness is varied as $K = \{5\ 10\ 20\ 40\ 80\} \cdot 10^6$ N/m. Figure 2 shows the time history of the impact force. The first three impact forces are undercritical, as indicated by the dashed line (- - -), since they should oscillate if uninterrupted. The increase in stiffness results in a narrower pulse, and thus a somewhat broader frequency range, as can be seen in Figure 3.

Figure 3 shows the magnitude of the force spectrum, as derived from equation (11) or (12). The undamped cutoff frequency (15b) is indicated by circles (o) and the actual cutoff frequency (15a) by pluses (+). The extremes of the low-frequency asymptotes are indicated by two stars on the ordinata (∗). The undercritical behaviour of the first three pulses manifests itself as oscillation in the high-frequency range. The overcritical force pulses are close to the lower extreme of the low-frequency asymptotes.

The behaviour of the cutoff frequency when the stiffness increases can be described as follows: The cutoff
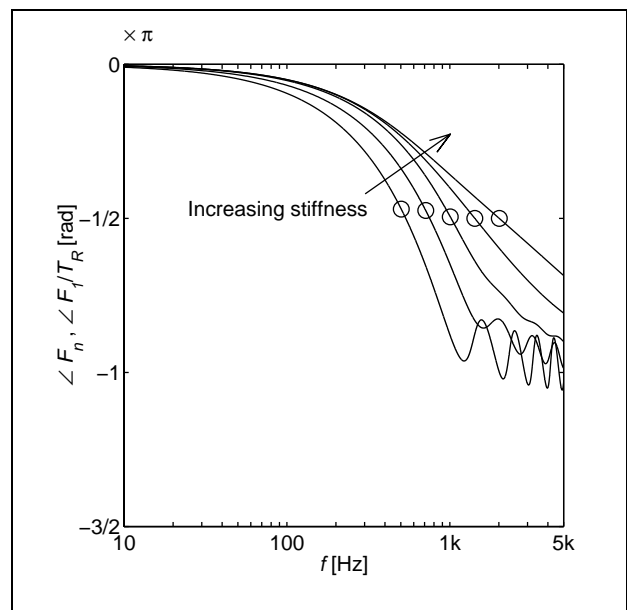
Figure 4. Hammer impact spectrum, showing the phases. The parameters are $K = \{5\ 10\ 20\ 40\ 80\} \cdot 10^6$ N/m and $R = 2 \cdot 10^3$ Ns/m.

frequency increases with increasing stiffness up to the point where critical damping occurs, where $K = 4R^2/M$. Thereafter the cutoff frequency decreases as the stiffness increases further. The undamped cutoff frequency always increases with increasing stiffness.

Figure 4 shows the phase of the force spectrum. The undamped cutoff frequency (15b) is marked by circles (o). As a reference to the phases, the time of impact is taken, giving a low-frequency asymptote of zero.
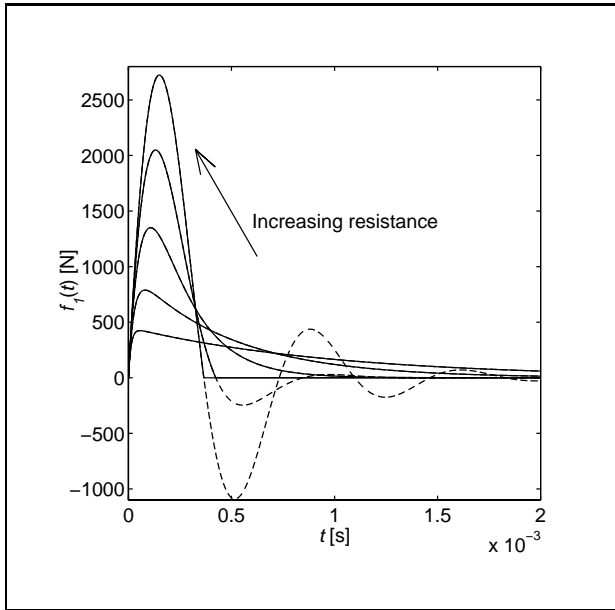
Figure 5. Hammer impact time history. Solid line (—) denotes the interrupted force, dashed line (- - -) denotes the oscillating force. The parameters are $R = \{0.5\ 1\ 2\ 4\ 8\} \cdot 10^3$ Ns/m and $K = 40 \cdot 10^6$ N/m .
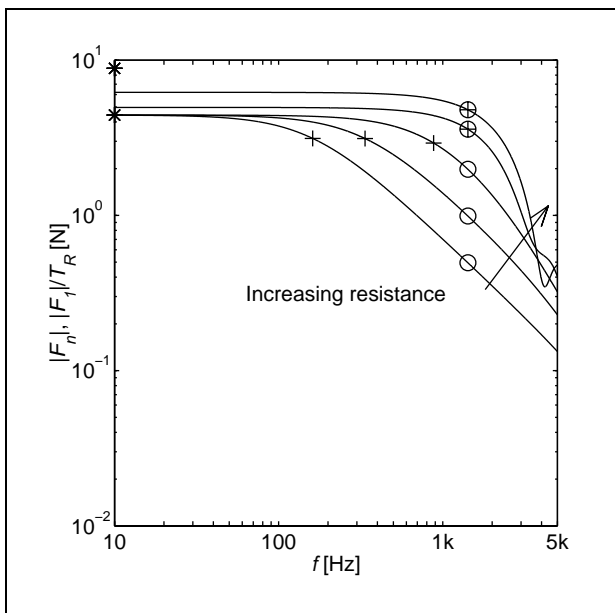
Figure 6. Hammer impact spectrum: magnitudes. The parameters are $R = \{0.5\ 1\ 2\ 4\ 8\} \cdot 10^3$ Ns/m and $K = 40 \cdot 10^6$ N/m.

In Figure 5 to 7 the resistance is varied as $R = \{0.5\ 1\ 2\ 4\ 8\} \cdot 10^3$ Ns/m. Figure 5 shows the time history of the impact force. The two final impact forces are undercritical. The dashed line (- - -) indicates how they would have continued if uninterrupted. An increase in resistance results in the pulse becoming narrower, and thus in the frequency range becoming somewhat broader, as can be seen in Figure 6. The undamped cutoff frequency remains unchanged, however.
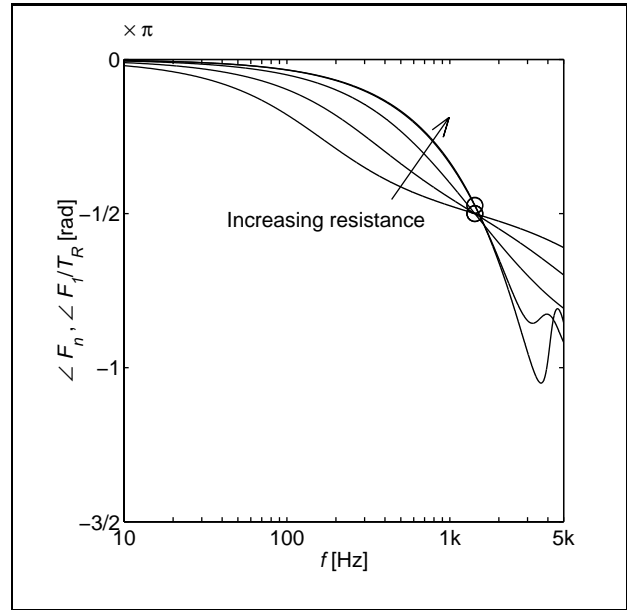
Figure 7. Hammer impact spectrum: phases. The parameters are $R = \{0.5\ 1\ 2\ 4\ 8\} \cdot 10^3$ Ns/m and $K = 40 \cdot 10^6$ N/m.

Figure 6 displays the magnitude of the force spectrum, as derived from equation (11) or (12). The undamped cutoff frequency (15b) is indicated by circles (o) and the actual cutoff frequency (15a) by pluses (+). The extremes of the low-frequency asymptote are indicated by two stars on the ordinata (∗). The last spectrum ($R = 8 \cdot 10^3$ Ns/m) is not much affected by dissipation, the low-frequency asymptote consequently having increased. For the overcritical pulses, the spectrum starts to decrease at the actual (lower) cutoff frequency, not at the undamped one.

Figure 7 shows the phase of the force spectrum involved. The reference to the phases is taken at the time of impact, giving a low-frequency asymptote of zero. The undamped cutoff frequency (15b) is indicated by circles (o).

To conclude: increasing the stiffness gives a lower low-frequency asymptote and a higher cutoff frequency, whereas increasing the resistance gives a higher low-frequency asymptote and an unchanged undamped cutoff frequency (15b) and a lower actual cutoff frequency (15a).

3.4. Floating floors, a discussion

A floating floor can be described with two infinite plates connected by a resilient layer [4, 12]. To simplify the situation, it can be assumed that the plates are thin and that the resilient layer is point-reacting and massless. To simplify the situation still further, two different cases can be distinguished such that in the first case the impedance of the excited plate is so high that the impact situation is the same as described in section 3.1–3.2, whereas in the second case the impedance of the excited plate is so low that the secondary (non-excited) plate can be regarded as rigid. In this second case the plate system can be simplified to
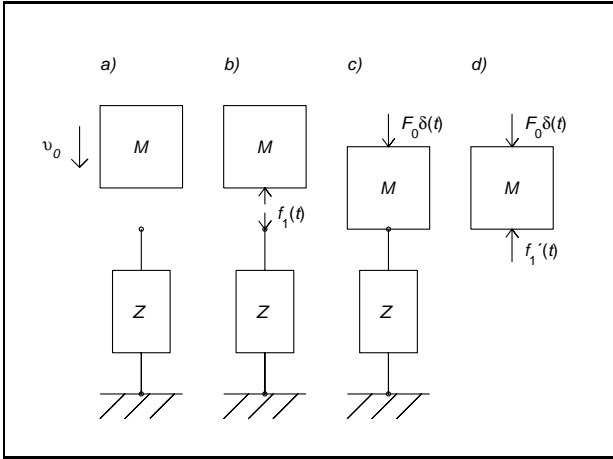
Figure 8. Modified impact description, impedance $Z = 1/Y$.

a Winkler foundation, involving a plate resting on a lo-cally reacting resilient layer. The bending wave-number is $k_B^4 = (m''\omega^2 - K)/B$, where m'' is the mass per unit area of the plate, K is the stiffness of the foundation and B is the bending stiffness of the plate. The driving-point mobility then is

$$Y = \frac{\omega}{-8B^{1/2}\mathrm{i}\sqrt{K - m''\omega^2}},$$

where the square-root in the denominator yield as a con-sequence that no lumped model can be used, even for this simple case. Thus, a more general description is needed.

4. Impact force and the general system

In section 3 the impact force spectrum was derived for frequency-independent parameters K and R in a me-chanical series. The spectrum was given explicit expres-sions (11–12). However, the floor system cannot gener-ally be described in terms of frequency-independent pa-rameters. The lumped description of the driving-point impedance/mobility is basically an ad hoc approximation of the actual situation. A more accurate description would be to calculate the driving-point mobility from the system description. The driving-point mobility is defined as the complex ratio of velocity to applied force, where the ve-locity is measured at the point of application of the force, c.f. [13].

Since the methods employed in section 3 cannot be used for frequency-dependent mobility, however, an approach to finding the force spectrum for an arbitrary driving-point mobility needs to be found. A suitable approach is to solve the differential equations in the frequency domain, inverse transform the result obtained in order to find the time of rebound, and to then transform the remaining force into the frequency range.

4.1. The interaction between the hammer and the floor

Figure 8 shows the generalised impact situation and the procedure employed. Figure 8 a) presents a general model of the impact. The hammer, of mass M, strikes the floor with the velocity v_0. The floor can be described in terms of the general driving-point mobility Y (or impedance $Z = 1/Y$). The desired force, $f_1(t)$, is shown in Figure 8 b).

The mobility is frequency-dependent, implying that the equations of motion can easily be solved in the frequency domain. On the other hand, the impact history is inter-rupted after the first zero crossing of the force. Thus the system is not time-invariant and therefore is best treated in the time domain. To deal with this problem, consider Figure 8 c), in which the mass M is now fixed on top of the impedance Z. The entire system is driven by a force $F_0\delta(t)$. This modified form of the problem is both linear and time-invariant. The equation of motion and the floor reaction force, if taken in the frequency domain, are

$$F_0 - F_1' = \mathrm{i}\omega M v, \quad F_1' = v/Y, \tag{18}$$

where $v = \mathcal{F}_t\{v(t)\}$ is the velocity spectrum of the floor and F_1' is the spectrum of the continuing impact force, i.e. the floor reaction force between the mass and the impedance, as shown in Figure 8 c-d), $F_1' = \mathcal{F}_t\{f_1'(t)\}$. One solves then for F_1' and v,

$$F_1' = F_0/(1 + \mathrm{i}\omega M Y), \tag{19a}$$
$$v = Y F_1'. \tag{19b}$$

The magnitude of the force F_0 needs to be selected so that the velocity at $t = 0_+$ equals the velocity of the falling hammer. At $t = 0_-$ the velocity should be zero,

$$v(0_+) = v_0, \quad v(0_-) = 0. \tag{20}$$

In evaluating $v(0)$, however, account needs to be taken of the fact that the Dirac $\delta(t)$ that excites the floor at time $t = 0$ is only at half inside the infinitesimal region from $t = 0$ to $t = 0_+$. This is compensated for if a value halfway between $v(0_+)$ and $v(0_-)$ is employed,

$$v(0)|_{Dirac} = v_0/2. \tag{21}$$

The velocity of the floor at $t = 0$ is evaluated as the inte-gral over all the frequencies,

$$v(0) = \frac{1}{2\pi}\int_{-\infty}^{\infty} v(\omega)\mathrm{d}\omega$$
$$= \frac{F_0}{2\pi}\int_{-\infty}^{\infty}\frac{\mathrm{d}\omega}{\mathrm{i}\omega M + 1/Y(\omega)} \equiv F_0 I_0, \tag{22}$$

where equation (19b) is used in next-to-the-last equality, and the last equality is the definition of the integral I_0. One then inserts (21) in (22) to obtain the magnitude of the driving force in the modified system,

$$F_0 = v_0/2I_0, \tag{23}$$

where the integral I_0 (mostly) needs to be calculated numerically. Equation (19a) then becomes

$$F_1' = \frac{v_0/2I_0}{1 + i\omega MY(\omega)}. \tag{24}$$

The time history of this force can be found by means of the inverse Fourier transform, $f_1'(t) = \mathcal{F}_t^{-1}\{F_1'\}$, implemented numerically as a fast digital inverse transform. The moment in time of the first zero crossing of the force is obtained then as

$$t_{cut} = \min\{t | t > 0,\ f_1'(t) = 0\}. \tag{25}$$

The actual, interrupted, excitation impact force then is

$$f_1(t) = f_1'(t)\theta(t_{cut} - t), \tag{26}$$

the corresponding force spectrum being found by means of a Fourier transform $F_1 = \mathcal{F}_t\{f_1(t)\}$, implemented numerically as a fast digital transform. The Fourier series components of (4) are $F_n = F_1(nf_r)f_r$, where $f_r = 1/T_r$ is the repetition frequency of the tapping machine.

4.2. The driving-point mobility

In the lumped system description presented in section 3, which made use of frequency-independent components, both the stiffness and the resistance were important for the solution. For a general mobility, this implies that both the real and the imaginary part of the mobility are important.

For an infinite homogenous plate, the imaginary part of the mobility, or the finite stiffness, can only be due to local effects. In section 3, the stiffness was chosen to be the stiffness due to deformation near the impact zone on a semi-infinite elastic solid, the Bossinesq expression (16). It would be more realistic to determine the local stiffness of a plate of finite thickness, i.e. to treat the plate as an elastic continuum. The force excites the plate asymmetrically on its upper surface. Thus, the excitation force produces a complicated displacement field under and near the point of excitation.

However, the description of the elastic continuum has too high a level of complexity to be appropriate for the entire system, including the reinforcing beams, for example. To this end, it is better to use thin plate theory, assuming plane sections to remain plane in the plate, which implies the excitation force to be constrained to produce a uniform displacement field in the thickness direction. Thus, no local deformation can be attained in terms of thin plate theory.

A heuristic description of the driving-point mobility could be to combine the mobility as determined for the global system, Y_G, with the mobility as determined for the detailed description near the excitation point, Y_L. Note that both Y_G and Y_L are in general complex. The parts of the mobilities that overlap need to be subtracted, i.e. the mobility of an infinitely thin plate. The total mobility is expressed as a correction of the global mobility,

$$Y = Y_G + \triangle Y,\ \ \triangle Y = Y_L - 1/8\sqrt{m''B}, \tag{27}$$

where m'' is the mass per unit area and B is the bending stiffness of the excited plate. This is quite an elaborate description of the driving-point mobility. The mobilities Y_L and Y_G need to be determined then.

One can also use measured mobilities as an alternative to the theoretically derived mobilities, provided the frequency resolution is sufficiently high.

4.3. Local effects on the mobility

The mobility Y_L due to local effects needs to be determined, the global parts of the system being excluded. The mobility of a plate of finite thickness and infinite extent excited on its upper surface by an indenter, is described in the literature. The indenter is assumed to be circular, weightless and stiff as compared with the plate, and to be small as compared with the wavelengths of the bending and quasilongitudinal waves of the plate. A rigid indenter, such as the case of a metal hammer acting on a wooden or a gypsum plate, can be assumed to provide a better approximation of the actual situation than a soft indenter would. Use of a rigid indenter is also more reasonable than use of a soft one (assuming the pressure distribution to be uniform), since it allows the pressure distribution under the indenter to change as the frequency increases.

In all analyses describing the motion of 'thin' structures, such as in the Kirchoff and the Mindlin theories, it is assumed that the two sides of the structure have exactly the same displacement at each point. This is an approximation, and both additional weakness and inertia effects can occur. Thus, simplified 'thin' theories are not sufficient for the case at hand.

More detailed three-dimensional analyses have been carried out, such as by Ljunggren [14] for a rigid indenter and by Heckl [15] for a soft indenter. Petersson and Heckl [11] have investigated the influence of different choices of pressure distribution. The boundary value problem is simpler mathematically in the case of a soft indenter than of a rigid one. Therefore, by assuming a pressure distribution under the indenter, Ljunggren [14], and Petersson and Heckl [11] (when dealing with a rigid indenter) avoided the problems a rigid indenter involves. The pressure distribution taken was that of a rigid indenter statically loading an elastic semi-infinity. Since there is no guarantee that this assumption actually results in a uniform displacement under the indenter, such a case can be designated as quasirigid.

In a paper by the authors [16], the pressure distribution at the interface between the indenter and the plate was determined by use of a variational formulation. The expressions obtained are approximations, although the choice of these is an optimal one. The mobility described in [16] is written as

$$Y_L = \frac{1}{2\pi R^2}\frac{I_a I_c - I_b^2}{I_c - I_b + I_a/4} \tag{28}$$

where

$$I_a = \int_0^\infty \frac{\sin^2(Rk_r)}{k_r} A(k_r)\mathrm{d}k_r, \qquad (29)$$

$$I_b = \int_0^\infty \frac{\mathrm{J}_1(k_r R)\sin(Rk_r)}{k_r} A(k_r)\mathrm{d}k_r, \qquad (30)$$

$$I_c = \int_0^\infty \frac{\mathrm{J}_1^2(k_r R)}{k_r} A(k_r)\mathrm{d}k_r, \qquad (31)$$

and where $A(k_r)$ is the admittance, used in all the references [11, 14, 15, 16].

It should be pointed out that only the imaginary part of Y_L can be said to be due to local deformation, the real part being due to the rest of the system as well, and it is in a broad frequency range close to $1/8\sqrt{m''B}$.

4.4. Global effects on the mobility

The mobility Y_G due to global considerations needs to be determined, local effects near the excitation zone being excluded. Both the real and the imaginary parts of the driving-point mobility of the floor structure may be due to global effects. An infinite thin plate has a real mobility, whereas in a finite plate, if no damping is included, the mobility is entirely imaginary. Thus, an infinite plate has only a resistance part in the mobility, whereas a finite plate has only stiffness and mass parts in the mobility. In lightweight floors consisting of plates reinforced by beams, the mobility has an imaginary part, also in the case of infinite systems. In [2], a typical lightweight floor system is described by use of a spatial Fourier transform method. The driving-point mobility due to global effects can be derived using the same strategy.

Assume that the transformed displacement field is found in a way similar to that presented in [2]. The driving-point displacement can be found then by means of a double inverse Fourier transform in spatial coordinates,

$$w(x_0, y_0) = \frac{1}{4\pi} \iint_{-\infty}^\infty \tilde{w}(\alpha, \beta)\mathrm{e}^{-\mathrm{i}(x_0\alpha + y_0\beta)}\mathrm{d}\alpha\mathrm{d}\beta, \quad (32)$$

where w is the displacement field of the excited plate, $\tilde{w}$ is the spatially transformed displacement field, x_0 and y_0 are the coordinates of excitation, and α and β are the transform wavenumbers. An account of how to simplify and reduce the integrals in (32) to be suited for numerical integration is presented in the Appendix. A simplified floor system is also described there.

The driving-point mobility due to global considerations is defined as

$$Y_G = v(x_0, y_0)/F_1 = \mathrm{i}\omega w(x_0, y_0)/F_1 \qquad (33)$$

How the driving-point mobility is determined is not crucial, however, for the methods in section 4.1. One can use modal sums, FEM or any other deterministic method, as long as the frequency resolution is sufficiently high.
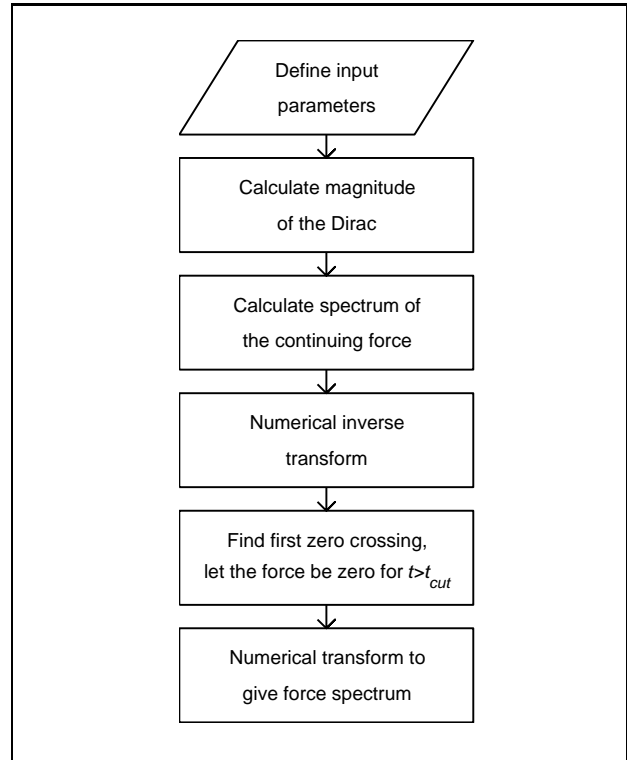
Figure 9. Flow chart for calculation of the force spectrum.

5. Numerical evaluation and programming

Since the impact force description of the general driving-point mobility is not given in the form of a closed expression, program coding is an important part of describing the excitation. Certain important aspects of the program developed will be taken up and be shown in a flowchart (Figure 9).

The program starts by defining the input parameters, including that the driving-point mobility Y is to be determined. Equations (28–31) are used for the local part of the mobility. The global part of the mobility can be integrated from equations (32–33), see also the Appendix. In the numerical example to be taken up, an adaptive and recursive Newton-Cotes eight-panel integration scheme, the Matlab function `quad8` [17], was used in the numerical evaluation. In order to speed up the calculations, a frequency resolution of 10 Hz was employed, and the frequency range being 10 Hz to 6000 Hz. The numerical 'signal theoretic' methods described in section 4.1 are in need of a better frequency resolution and of a broader frequency range, as will soon be evident. The narrower frequency range is achieved using a spline interpolation, and the extended frequency range is achieved by using the asymptotic mobilities of an infinite plate for excitation positions between beams, and of an infinite beam for excitation positions at the beams.

The magnitude of the Dirac shown in Figure 8 c needs to be calculated then, by use of (22) and (23). The spectrum of the continuing force is calculated then from (24) and numerically inverse transformed by use of the IFFT

algorithm. It is important that the frequency resolution is sufficient to describe the pulse peak and detect the first zero-crossing correctly.

As an example, consider the lumped model with $R = 2 \cdot 10^3$; and $K = 2 \cdot 10^7$, use of (14) showing that $t_{cut} = 8.112 \cdot 10^{-4}$ s. An appropriate time resolution might then be > 20 points for describing the force pulse. Thus, the time resolution should be $\triangle t < 4.06 \cdot 10^{-5}$ s, giving an upper frequency limit of $f_{nyq} > 12.3 \cdot 10^3$ Hz (the Nyquist frequency). If a frequency resolution of $\triangle f = 2$ Hz is employed, an FFT/IFFT of 16384 points is needed.

In the numerical example to be presented, the resolution data chosen were; $\triangle t = 8.33 \cdot 10^{-6}$ s, $\triangle f = 3.66$ Hz and $f_{nyq} = 60 \cdot 10^3$ Hz, a 16384-points FFT/IFFT being employed. Since the impact noise is often only of interest up to 5000 Hz a low-pass filter of $10 \cdot 10^3$ Hz was used, to prevent high-frequency terms from influencing the force spectrum.

The first zero-crossing needs to be found then, so that the actual, interrupted impact force was determined from (26). The zero-crossing was found by examining the change of sign. The exact position could not be determined since the time resolution is fixed. The force spectrum was calculated then by use of the fast digital Fourier transform FFT, the same resolution data as before being employed.

Due to the material models and numerical procedures there will be some causality problems in the procedure. If the force is non-zero before and at the time of impact $t = 0$ it clearly violating the causality rules. This not only produces a wrong result, but also complicates the numerical treatment since sometimes more than one zero crossing may need to be found. However, when the time and frequency resolution are good and the damping is slight, problems of this sort are held to a minimum, its being assumed in such cases that the errors involved can be disregarded.

6. Numerical results and discussion

A numerical example will be given to illustrate the excitation force description when a frequency dependent driving-point mobility is employed. One plate reinforced by one set of periodically spaced beams, as described in the Appendix, is used instead of the complete floor structure, so as to simplify the calculations.

The following data were used in the numerical calculations: distance between beams $l = 0.6$ m, modulus of the plates $E_p/(1 - \mu^2) = 7.2 \cdot 10^9$ Pa, Young's modulus for the framing beams $E_f = 9.8 \cdot 10^9$ Pa, density of the beams and plates $\rho_p = \rho_f = 500 \text{ kg/m}^3$, thickness of the plates $h = 22 \cdot 10^{-3}$ m, and material damping $\eta = 0.03$. The beams are 0.220 m in height and 0.067 m in width.

The magnitude of the driving-point mobility is shown in Figure 10, calculated there for 15 positions. These are the global mobilities. The excitation co-ordinates are $x_0 = \{0 \ 0.012 \ 0.053 \ 0.084 \ 0.101 \ 0.122 \ 0.150 \ 0.175 \ 0.205 \ 0.213 \ 0.220 \ 0.232 \ 0.255 \ 0.291 \ 0.3\}$ m (chosen randomly) and $y_0 = 0$ m. These mobilities are used as input
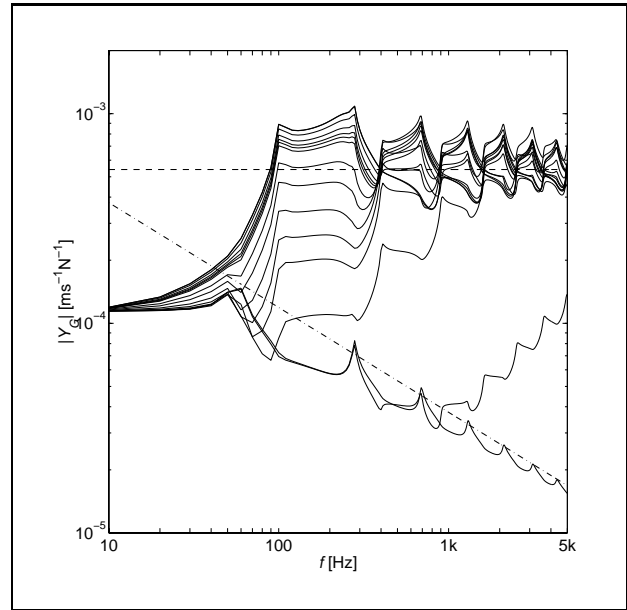
Figure 10. Global driving-point mobility at 15 positions, solid line (—). Driving-point mobility for an infinite plane, dashed line (- - -). Driving-point mobility for an infinite beam, dashed-dotted line (- · -).
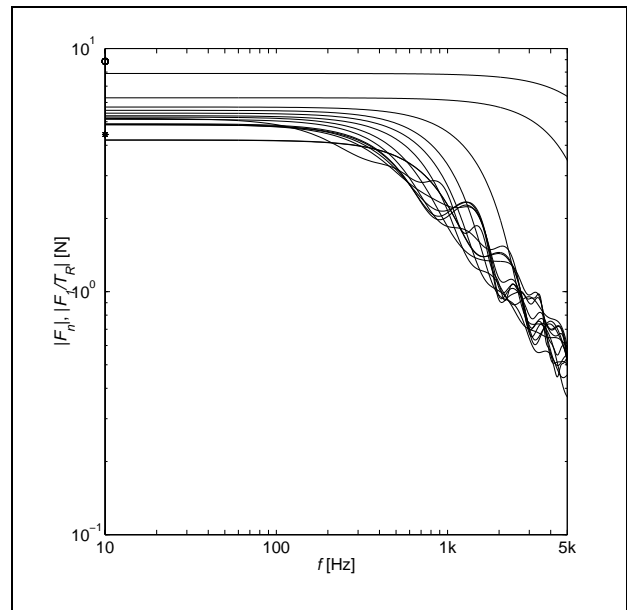
Figure 11. Force spectrum, calculated according to sections 4 and 5. Mobility is taken as the global one, see section 4.4, no local weakness are present.

data in calculating the impact force. The asymptotic mobilities for an infinite plate ($\cdots$) and for an infinite beam ($-\cdot-$) are also shown in the figure.

The force spectrum resulting from the mobilities contained in Figure 10, without consideration of local effects, is shown in Figure 11. The points of excitation are clearly important, since these differ both in the low-frequency asymptote and at the cutoff frequency. The extremes of
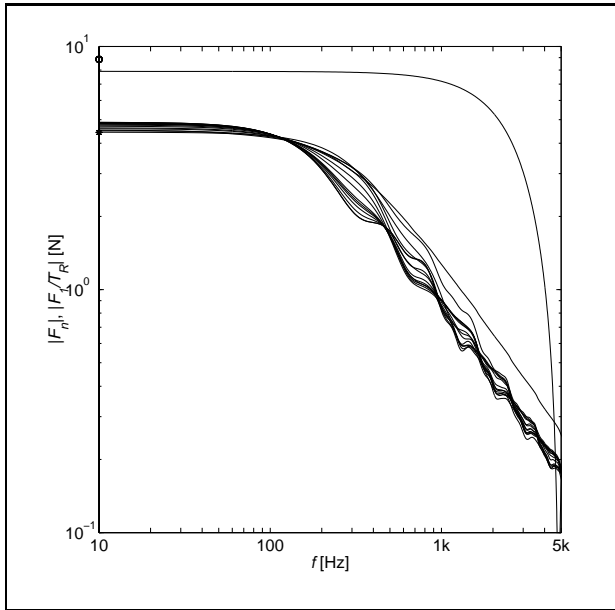
Figure 12. Force spectrum, calculated according to 4 and 5. Mobility taken as the global one in section 4.4, but with local weakness added in accordance with section 4.3.

the low-frequency asymptotes are indicated by one star ($*$) and one circle ($\circ$) on the ordinata. One of the curves fall outside the extremes, implying the numerical procedures to not be perfect. The errors, however, are minor, the important features being clearly illustrated. It should be pointed out that for this case there are no problems concerning causality.

In Figure 12 the local mobility has been added to the global mobility, in accordance with equation (27), the force spectrum being calculated then. Local effects are also important; the corresponding excitation points in Figures 11 and 12 differ both in the asymptote and in the cutoff frequency. The cutoff frequency and the low-frequency asymptote are consisting less in Figure 12.

7.   Summary and conclusions

Findings concerning the excitation force achieved by the ISO tapping machine, as reported in the literature, have been summarised and reconsidered. A two-parameter lumped model of impact developed by Lindblad [5], was analysed. The model can only deal with frequency-independent parameters. Low-frequency asymptotes and cutoff frequencies were derived. The low-frequency asymptotes were found to have a span of 6 dB. The lumped parameters were taken as the local stiffness and the driving-point mobility of an infinite plate. On the basis of a numerical parametric study, it was concluded that increasing the stiffness gives a lower low-frequency asymptote and a higher cutoff frequency, and that increasing the resistance gives a higher low-frequency asymptote, as well as an unchanged undamped cutoff frequency and a lower actual cutoff frequency.

A description of impact force applicable to general, frequency-dependent impedances and mobilities was derived. The general force description was implemented by means of numerical integration and FFT. The mobilities may be due to local effects, to the use of thick plate theory, and/or global effects, obtained using spatial Fourier transform methods and numerical integration. From a numerical example it was concluded that both the local and the global effects are important in determining the excitation force of the ISO tapping machine on a non-homogenous lightweight floor. In order to adequately describe what occurs, the global and the local driving-point mobility has to be used and combined. The results also indicate how important it is to use an accurate and detailed system description in order to predict the impact force spectrum appropriate. The force spectrum needs to be determined on the basis of the entire driving-point mobility, that is both the real and the imaginary parts.

Acknowledgement

Appendix

The driving-point mobility is needed for determining the force spectrum of the tapping machine. A simplified system for performing the calculations is considered, one taking account of the upper plate and the beams. Moreover, the fluid reaction is not taken into account. The simplification and the reductions of the number of integrals to be evaluated are inspired by Mace [18, 19]. The transformed displacement used in this system, discussed by Evseev [20] and Mace [21] and also in [2], can be written as

$$\tilde{w}(\alpha, \beta) = \frac{F_R e^{i(\alpha x_0 + \beta y_0)}}{S(\alpha, \beta)}$$
$$- \frac{P_a(\alpha, \beta)G(\beta)/l}{S(\alpha, \beta)(1 + P_b(\alpha, \beta)G(\beta)/l)}, \quad (A1)$$

where

$$S(\alpha, \beta) = D\big((\alpha^2 + \beta^2)^2 - \kappa^4\big), \qquad (A2)$$
$$G(\beta) = E_f I_f \beta^4 - \rho_f A_f \omega^2, \qquad (A3)$$

are the transformed plate and beam operators, respectively, D is the bending stiffness of the plate, κ the bending wave number, $E_f I_f$ the bending stiffness of the beam and $\rho_f A_f$

the mass per unit length of the beam. The two help functions P_a and P_b are

$$P_a(\alpha, \beta) = \frac{F_R e^{i\beta y_0}}{D} \sum_{n=-\infty}^{\infty} \frac{e^{i(\alpha - en)x_0}}{\left((\alpha - en)^2 + \beta^2\right)^2 - \kappa^4}, \quad (A4)$$

$$P_b(\alpha, \beta) = \frac{1}{D} \sum_{n=-\infty}^{\infty} \frac{1}{\left((\alpha - en)^2 + \beta^2\right)^2 - \kappa^4}, \quad (A5)$$

where, as before, $e = 2\pi/l$ and κ is the bending wave number. The fluid reaction is not included in equations (A2–A5).

The inverse transform $w(x, y) = \mathcal{F}_{x,y}^{-1}\{\tilde{w}(\alpha, \beta)\}$ is defined in [2], equation (2 b). The half-way transform, transformed in the $y - \beta$ direction or inverse transformed in the $x - \alpha$ direction, is denoted $\breve{w}(x, \beta) = \mathcal{F}_x^{-1}\{\tilde{w}(\alpha, \beta)\} = \mathcal{F}_y\{w(x, y)\}$.

Define a function Λ for the sums in (A4–A5),

$$\Lambda(\alpha, \beta; x_0) = \sum_{n=-\infty}^{\infty} \frac{e^{i(\alpha - en)x_0}}{\left((\alpha - en)^2 + \beta^2\right)^2 - \kappa^4}. \quad (A6)$$

Thus, equations (A4) and (A5) can be expressed in terms of Λ,

$$P_a(\alpha, \beta) = F_R e^{i\beta y_0} \Lambda(\alpha, \beta; x_0)/D,$$
$$P_b(\alpha, \beta) = \Lambda(\alpha, \beta; 0)/D.$$

The function Λ can be given explicitly using the Poisson's sum formula, contour integration and a geometric series expression, a method described in Mace [18, 19]. After considerable manipulations, equation (A6) can be expressed as

$$
\begin{aligned}
&-\frac{4\kappa^2}{l}\Lambda(\alpha, \beta; x_0) \\
&= \frac{i e^{-ix_0 q_-}/q_-}{1 - e^{-il(\alpha + q_-)}} - \frac{i e^{ix_0 q_-}/q_-}{1 - e^{-il(\alpha - q_-)}} \\
&+ \frac{e^{-x_0 q_+}/q_+}{1 - e^{-l(i\alpha + q_+)}} - \frac{e^{x_0 q_+}/q_+}{1 - e^{-l(i\alpha - q_+)}}
\end{aligned} \quad (A7)
$$

for $0 < x_0 < l$, and where $q_+ = \sqrt{\kappa^2 + \beta^2}$ and $q_- = \sqrt{\kappa^2 - \beta^2}$. For other positions of x_0, the periodicity of the structure can be used to translate the co-ordinates so that the inequality is fulfilled. However, the sum in (A6) converges rapidly (due to the fourth-order expression in the nominator) making it possible to use a truncated sum instead of the explicit expression (A7). When the fluid reaction is included, a truncated sum needs to be employed.

The integrals in the inverse transform is now to be evaluated,

$$
\begin{aligned}
\breve{w}(x, \beta) &= \frac{1}{2\pi} \int_{-\infty}^{\infty} \frac{F_R e^{i(\alpha x_0 + \beta y_0)}}{S(\alpha, \beta)} e^{-i\alpha x} d\alpha \\
&- \frac{1}{2\pi} \int_{-\infty}^{\infty} \frac{P_a(\alpha, \beta) G(\beta) l^{-1} e^{-i\alpha x}}{S(\alpha, \beta)\left(1 + P_b(\alpha, \beta) G(\beta)/l\right)} d\alpha \\
&= I_1 - I_2, \quad (A8)
\end{aligned}
$$

where the integrals I_1 and I_2 are defined. The second integral in (A8) is

$$
\begin{aligned}
I_2 &= \frac{G(\beta) F_R e^{i\beta y_0}}{2\pi l D} \\
&\times \int_{-\infty}^{\infty} \frac{\Lambda(\alpha, \beta; x_0) e^{-i\alpha x} d\alpha}{S(\alpha, \beta)\left(1 + \Lambda(\alpha, \beta; 0) G(\beta)/lD\right)} \quad (A9)
\end{aligned}
$$

In order to simplify the integration, subdivide the infinite integral I_2 into an infinite sum of finite integrals,

$$\int_{-\infty}^{\infty} \cdot \; d\alpha = \sum_{n=-\infty}^{\infty} \int_{(2n-1)\pi/l}^{(2n+1)\pi/l} \cdot \; d\alpha \quad (A10)$$

Making use of the periodic behaviour of the infinite sums yields

$$\Lambda(\alpha, \beta; x_0) = \Lambda(\alpha + 2n\pi/l, \beta; x_0).$$

A variable substitution $\alpha' = \alpha - 2n\pi/l$ and a change of order between the sum and the integral, allow (A9) to be written as

$$
\begin{aligned}
I_2 &= \frac{G(\beta) F_R e^{i\beta y_0}}{2\pi l D} \\
&\times \int_{-\pi/l}^{\pi/l} \frac{\sum_{n=-\infty}^{\infty} \frac{e^{-i(\alpha + en)x}}{S(\alpha' + en, \beta)} \Lambda(\alpha', \beta; x_0) d\alpha'}{1 + \Lambda(\alpha', \beta; 0) G(\beta)/lD} \quad (A11)
\end{aligned}
$$

The sum in (A11) is identified as

$$\sum_{n=-\infty}^{\infty} \frac{e^{-i(\alpha + en)x}}{S(\alpha' + en, \beta)} = \Lambda(-\alpha', \beta; x)/D.$$

Thus, I_2 becomes a finite integral,

$$
\begin{aligned}
I_2 &= \frac{G(\beta) F_R e^{i\beta y_0}}{2\pi l D} \\
&\times \int_{-\pi/l}^{\pi/l} \frac{\Lambda(-\alpha', \beta; x) \Lambda(\alpha', \beta; x_0) d\alpha'}{1 + \Lambda(\alpha', \beta; 0) G(\beta)/lD} \quad (A12)
\end{aligned}
$$

Since the driving-point mobility is to be evaluated, $x = x_0$. Utilising this and the fact that Λ is symmetric in a if $x = 0$, $\Lambda(\alpha, \beta; 0) = \Lambda(-\alpha, \beta; 0)$, can be used to reduce the integral to

$$
\begin{aligned}
I_2 &= \frac{G(\beta) F_R e^{i\beta y_0}}{\pi l D} \\
&\times \int_0^{\pi/l} \frac{\Lambda(-\alpha', \beta; x) \Lambda(\alpha', \beta; x_0) d\alpha'}{1 + \Lambda(\alpha', \beta; 0) G(\beta)/lD} \quad (A13)
\end{aligned}
$$

The first integral in (A8) is

$$I_1 = \frac{F_R e^{i\beta y_0}}{2\pi} \int_{-\infty}^{\infty} \frac{d\alpha}{S(\alpha, \beta)} \quad (A14)$$

After use of (A10), variable substitution and change of order between the sum and the integral and identifying Λ, I_1

can be written as a finite integral. The negative side can be reduced using the symmetry of Λ in α, yielding

$$I_1 = \frac{F_R e^{i\beta y_0}}{\pi} \int_0^{\pi/l} \Lambda(\alpha', \beta, 0) d\alpha' \qquad (A15)$$

The integral in the β-direction is now to be evaluated. The complete inverse transform is written as

$$w(x_0, y_0) = \frac{1}{2\pi} \int_{-\infty}^{\infty} I_1(\beta) e^{-i\beta y_0} d\beta$$
$$- \frac{1}{2\pi} \int_{-\infty}^{\infty} I_2(\beta) e^{-i\beta y_0} d\beta = J_1 - J_2. \quad (A16)$$

where the integrals J_1 and J_2 are defined. The second term is

$$J_2 = \frac{F_R}{2\pi^2 l D}$$
$$\times \int_{-\infty}^{\infty} G(\beta) \int_0^{\pi/l} \frac{\Lambda(-\alpha, \beta; x)\Lambda(\alpha, \beta; x_0) d\alpha d\beta}{1 + \Lambda(\alpha, \beta; 0)G(\beta)/lD}. \quad (A17)$$

The symmetry of the functions $\Lambda(\alpha, -\beta; x_0) = \Lambda(\alpha, \beta; x_0)$ and $G(-\beta) = G(\beta)$ can be used to reduce the integral to

$$J_2 = \frac{F_R}{\pi^2 l D}$$
$$\times \int_0^{\infty} G(\beta) \int_0^{\pi/l} \frac{\Lambda(-\alpha, \beta; x)\Lambda(\alpha, \beta; x_0) d\alpha d\beta}{1 + \Lambda(\alpha, \beta; 0)G(\beta)/lD}. \quad (A18)$$

The first integral J_1 can be shown to be

$$J_1 = \frac{F_R}{4\pi^2} \iint_{-\infty}^{\infty} S^{-1} d\alpha d\beta = \frac{F_R}{i\omega 8\sqrt{m''D}}.$$

It is better numerically, however, to evaluate this integral in the same way as J_2. Thus, if the symmetry is used

$$J_1 = \frac{F_R}{\pi^2} \int_0^{\infty} \int_0^{\pi/l} \Lambda(\alpha, \beta; 0) d\alpha d\beta. \qquad (A19)$$

Summing up (A18) and (A19), the inverse transform (A16) can now be written as

$$w(x_0, y_0) = \frac{F_R}{\pi^2} \int_0^{\infty} \int_0^{\pi/l} \Lambda(\alpha, \beta; 0)$$
$$- \frac{\Lambda(\alpha, \beta; x_0)\Lambda(-\alpha, \beta; x_0)G(\beta)}{lD + \Lambda(\alpha, \beta; 0)G(\beta)} d\alpha d\beta, (A20)$$

where (A20) is to be evaluated numerically. The driving-point mobility is found by using the results presented in sections 4.2 to 4.4.

References

[1] ISO 140-6: – Acoustics – Measurement of sound insulation in buildings and building elements – part 6: Laboratory measurments of impact sound insulation of floors.

[2] J. Brunskog, P. Hammer: Prediction model for the impact sound level of lightweight floors. Acustica / acta acustica **accepted**.

[3] J. Brunskog, P. Hammer: Prediction models of impact sound insulation on timber floor structures; a literature survay. Journal of Building Acoustics **7** (2000) 89–112.

[4] L. Cremer, M. Heckl, E. E. Ungar: Structure-borne sound. Springer-Verlag, Berlin, 1988.

[5] S. Lindblad: Impact sound characteristics of resilient floor coverings. a study on linear and nonlinear dissipative compliance. Dissertation. Division of Building Technology, Lund Institute of Technology, Lund, Sweden, 1968.

[6] Vér: Impact noise isolation of composite floors. Journal of the Acoustical Society of America **50** (1971) 1043–1050.

[7] E. Gerretsen: Calculation of airborne and impact sound insulation between dwellings. Applied Acoustics **19** (1986) 245–264.

[8] W. Scholl, W. Maysenhölder: Impact sound insulation of timber floors: Interaction between source, floor coverings and load bearing floor. J. Building Acoustics **6** (1999) 43–61.

[9] R. Hall: The standard impact test and thin floating floor constructions. Institute of Acoustics. Proceedings, Volume 22 Pt 2, 77A St Peters's Street, St Albans, Herts AL1 3BN, UK, 2000. 43–50.

[10] S. Timoshenko: Theory of elasticity. McGraw-Hill Book Company, New York and London, 1939.

[11] B. A. T. Petersson, M. Heckl: Concentrated excitaion of structures. Journal of Sound and Vibration **196** (1996) 295–321.

[12] S. Gudmundsson: Sound insulation improvment of floating floors. A study of parameters. TVBA–3017. Dissertation. Building Acoustics, LTH, Lund University, Lund, Sweden, 1984.

[13] C. L. Morfey: Dictionary of acoustics. Academic press, 2001.

[14] S. Ljunggren: Generation of waves in an elastic plate by a vertical force and by a moment in the vertical plane. Journal of Sound and Vibration **90** (1983) 559–584.

[15] M. Heckl: Körperschallübertragung bei homogenen platten beliebiger dicke. Acustica **49** (1981) 183–191.

[16] J. Brunskog, P. Hammer: Rigid indenter excitation of plates. Acustica / acta acustica **submitted**.

[17] MATLAB Reference guide. The MathWorks, Inc., 1992.

[18] B. R. Mace: Periodically stiffened fluid-loaded plates, I: Response to convected harmonic pressure and free wave propagation. Journal of Sound and Vibration **73** (1980) 473–486.

[19] B. R. Mace: Periodically stiffened fluid-loaded plates, II: Response to line and point forces. Journal of Sound and Vibration **73** (1980) 487–504.

[20] V. N. Evseev: Sound radiaton from an infinite plate with periodic inhomogeneities. Soviet physics – Acoustics **19** (1973) 345–351.

[21] B. R. Mace: Sound radiate from a plate reinforecd by two sets of parallel stiffeners. Journal of Sound and Vibration **71** (1980) 435–441.

Prediction model for the impact sound level of lightweight floors

Jonas Brunskog and Per Hammer

Division of Engineering Acoustics, LTH, Lund University, P.O. Box 118, SE-221 00 Lund, Sweden
E-mail: jonas.brunskog@acoustics.lth.se, per.hammer@acoustics.lth.se

Summary

Lightweight floors are often troubled by poor impact-sound insulation. In order to develop and explain structures with acceptable insulation, a deterministic prediction model was developed. The paper considers transmission through the system and the response of the model. Excitation (as caused by the ISO-tapping machine) is considered in a separate paper [1]. The system description employs a spatial transform technique, making use of the periodicity of the floor structure with the aid of Poisson's sum rule. The radiated power is calculated using numerical integration in the wavenumber domain, the radiated power enabling the impact sound level to be calculated. Comparisons are made between measurements found in the literature and the proposed prediction model, the effects of different excitation models being discussed. A relatively close agreement is achieved, especially if an elaborate excitation model is employed.

PACS no. 43.55.Rg, 43.40.Kd, 43.40.Dx

1. Introduction

Interest in lightweight building techniques has increased in recent years, partly because of the possibility this provides of lowering house production costs. However, it is also well-known that structures of this type have poor impact-sound insulation. The demand for more adequate sound insulation has led to the development of lightweight floor structures with better impact-sound-insulation characteristics [2], although the production cost involved are still rather high. A prediction model sensitive to changes in system details is an important tool for developing and analysing structures with an acceptable degree of sound insulation. Such a model can consist of a chain of three parts: excitation – system – response. Point impact excitation, which can be achieved by use of the standard tapping machine, is dealt with in [1], including interaction between the hammer and the floor. The present paper focus instead on the latter two parts in the chain: the system and the response. The system is the actual floor structure, assumed to be linear, with the possible exception of its interaction with the hammer [3]. Thus, linear theory will be used in the theoretical model of the system. The response is the sound pressure in the receiver room, which is related to the radiated power.

1.1. The excitation

The ISO standard tapping machine [4] is used as an excitation source in rating the impact sound level of a floor structure. Although the machine does not simulate a real footstep, the test results provide valuable information on the dynamic behaviour of the floor. The impact noise level caused by a tapping machine, together with expressions for the force-spectrum, have been derived for high-impedance homogenous structures by Cremer et al. [5], and Vér [6]. The improvement obtained by use of an elastic surface layer (floor covering) and floating floors on high impedance surfaces has been the main focus of studies in this area, such as that of Lindblad [3], which deals specifically with the force- and velocity-spectrum of the impacting hammer. In the present paper, in contrast, the floor generally functions as a low-impedance system. The force spectrum of such a system and of systems with arbitrary frequency-dependent driving-point mobilities is dealt with in [1], the results of which are used in the present paper.

1.2. The floor system

In designing lightweight floor structures with respect to impact noise, various system parameters can be important. The structure consists of different construction elements differing in weight, stiffness and damping. A suitable mathematical model is needed to take these parameters into account. A mathematical model for point-excited sound transmission through an ordinary lightweight floor structure has been presented by the authors in [7, 8], and will also be described in a forthcoming paper. The present paper concerns a somewhat simplified situation, in which two infinite plates are connected rigidly in the transverse direction but are free to rotate (lack moment coupling, viz. pin joints) on the framing beams. Thus, no resilient device is employed. In the present case, the system is entirely infinite, no type of boundary conditions being present (except the plate frame coupling).

The main structure to be studied consists of two parallel plates, reinforced by Euler beams, which aslo connects them. The beams are spaced at equal distances, a method utilising this periodicity being employed. The coupling between the plates has two main paths: via the cavity and via the rigid connections at the points of contact between the beams and the plates. A similar solution is given by Lin and Garrelick [9], for a case in which the excitation

is a convected harmonic pressure and the beams are rigid bodies. An extension of the present paper in contrast to [9] is thus the use of reinforcing Euler beams and of point excitation. A further extension in the present paper is the inclusion of a Delaney-Bazely porous material in the cavity, which can be either full or partly filled.

The prediction models for impact noise found in the literature are based on power flow, SEA and/or semi-empirical theory. The idea of utilising energy average to develop details of the floor structure is likely to fail, however, due to the omission of crucial parameters. There is a lack of detailed information due to the fact that the averaging process is occurring at an early stage – within SEA theory itself, before the model is fixed. At low frequencies when few modes are present, SEA also provides too rough an estimate of the acoustic response, and is thus likely to fail within the low-frequency region that is important in impact sound insulation. In addition, an SEA model fails to predict certain important details such as global resonance and the effects of periodicity. Although simplified models for impact noise isolation exist, these have been developed for heavy floors, e.g. of concrete, and make use of average energy assumptions. Vér [6] employes such an approach, using a force description of the tapping machine on a hard surface, together with the energy balances, to obtain the impact sound level for bare concrete floors. Through taking account of the effects of an elastic layer (linear theory) and of isolation by floating floors, the model is improved then. In the last section of his paper, formulas are provided that can be applied to simple cases of lightweight floor structures. Gerretsen [10] also deals with impact noise isolation, using a general model including airborne and flanking transmission, an approach similar to [6] in the sense that reciprocal relations and energy averaging are used. In [10], theory pertinent to homogenous, single leaf structures has been applied to describe the input mobility and impact isolation for periodical floor systems.

In the present paper a spatial Fourier transform approach is employed rather than any of the methods just refereed to, since such an approach has certain advantages. The theoretical model to be used needs to be able to readily handle sound radiation, as well as point forces in a two-dimensional sense, and non-homogenous 'system floors'. Lightweight floor structures consist of plates reinforced by beam stiffeners spaced at equal intervals. If this periodicity is taken into account, the reduction in redundant information makes the solution simpler. All these matters can be handled by the spatial Fourier transform technique.

This technique has been applied to the problem of sound radiation from periodically stiffened plates, and its use there has been developed over a long period of time. Evseev [11] utilises the periodicity in an infinite plate with periodic reinforcements of beams through use of spatial Fourier transforms in two dimensions, the plate in question being subjected to the action of a time-harmonic driving force. The boundary conditions between the plate and the supports are applied in wavenumber space, the stiffeners responding to the plate with only normal forces. The

solution was derived with the aid of Poisson's sum and other sum-operations – involving the fact that adding an integer to the argument of a function that is being summed from minus infinity to infinity does not contribute to the sum. Rumerman [12] dealt with a similar problem, but included the effects of the line moments produced by the beams. The approach taken was not the same as Evseev, as the boundary conditions between the plate and the supports was applied after the inverse transform were applied, and making use of the Floquéts principle. Lin and Garrelick [9] investigated the transmission of a plane wave through two infinite parallel plates connected by periodical frames that behaved as rigid bodies. A fluid coupling in the cavity between the plates was also taken into account. The two systems were solved simultaneously by use of Fourier transform techniques and a matrix notation, following Evseevs approach. Mace [13] considered a plate reinforced by two sets of stiffernes and loaded on one side by a fluid. He used the same approach as Evseev and derived expressions for the far-field pressure that results from a point excitation. The far-field pressure was determined by a stationary-phase approximation. In [14, 15, 16, 17] Mace instead made use of the approach used by Rumerman. In [14] Mace obtained an expression for the plate displacement in the space-harmonic form caused by a convected harmonic pressure. In [15] Mace investigated the sound radiated by a stiffened plate excited by either a sinusoidal line force parallel to the stiffeners or a point force at an arbitrary location. The result in [14] was used as a starting point, integrating the responses caused by spatially harmonic sources. The work with periodical structures whas continued in [16, 17], deling with periodicity in two orthogonal directions. Although the Rumerman approach – applying boundary conditions when the inverse transform is taken and using Floquéts principle – has its advantages, the Evseevs approach – that of taking the boundary conditions in the transformed space – fulfills the present purposes to the extent that the far-field pressure and the radiated power can be derived in the transformed space, making an inverse transform unnecessary. Takahashi [18] considered noise control in buildings with double-plate walls. Each structure examined consisted of two parallel plates of infinite extent with various connectors. The connectors were either point connectors or rib-stiffeners. The structures were driven by point forces, the resulting sound radiation being studied. Takahashi follows the Evseev approach, using a Fourier transform model and dealing with the periodicity by means of Poisson's sum formula. More resent contributions on the topic of periodic double plate systems are presented by Skelton [19] and Urusovskii [20].

An extended survey of the literature on the theoretical models available is to be found in [21].

1.3. The response and the possibility of comparison

The radiated power can be found by integral methods in the transformed (wave number) domain [5, pp. 526–537]. The response of the receiver room can be found on the

basis of the radiated power, a diffuse sound field being assumed, a power balance then being applied. This is an ordinary room-acoustic approach as employed by Cremer and Heckl [5, pp. 551–554], Vér [6] and Gerretsen [10], and also used in this paper. A method of predicting the impact sound level for a specific type of floor structure can be found by combining the expressions arrived at for the excitation and for the system as this relate to of the response. Comparisons with measured data can then indicate whether the prediction model is sufficiently accurate. Measurement of the type of floor structure considered can be found in the literature. Bodlund [22] investigated the sound insulation in old wooden floor constructions, including impact noise. In the report, laboratory measurements of very simple wooden floor structures are included, measurements that are suitable for comparison with result of the present prediction model.

1.4. Summary of the approach and conclusion of the introduction

The approach to be taken will be summarised here. The excitation force caused by the ISO-tapping machine when applied to lightweight floors was derived in [1]. The floor structure examined, consisting of two plates – rigidly connected and stiffened by beams – is described by its governing equations. A periodical description of the structure is used. The coupled plate equations obtained are Fourier transformed and solved for the transformed deformation. The radiated power is obtained by use of integral methods, using the transformed displacement. The impact sound level is calculated from the radiated power, there being assumed to be a diffuse sound field in the receiver room. The paper is organised as follows: first, the theoretical model of the floor structure is derived in two sections, followed by a short section on sound radiation and the response. The results obtained then are presented as numerical calculations, which are compared with measured results, the findings obtained being discussed in the section thereafter, the paper concluding with a summary and final remarks.

2. The system; a theoretical model of the floor

2.1. Description

Consider a system of two coupled parallel plates infinite in their extent, separated by a cavity of depth d, through which they are coupled. The plates are also coupled by rigid mechanical connections consisting of an infinite periodic array of connection lines of beams. The plates are modelled as classic thin plates (Kirchhoff theory). An excitation pressure acts on the upper plate, plate 1. Later on, the general pressure is specified as a point force. Reaction forces from two periodic arrays of discontinuities in the form of beam stiffeners, and also from the surroundings and from fluids in the cavity are present. The fluids satisfy the ordinary acoustic wave equation. The structural configuration that is modelled is shown in Figure 1. The
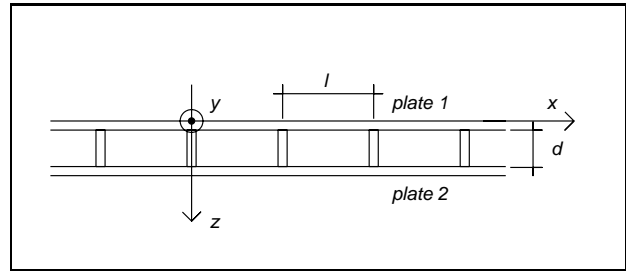
Figure 1. Floor system and co-ordinates.
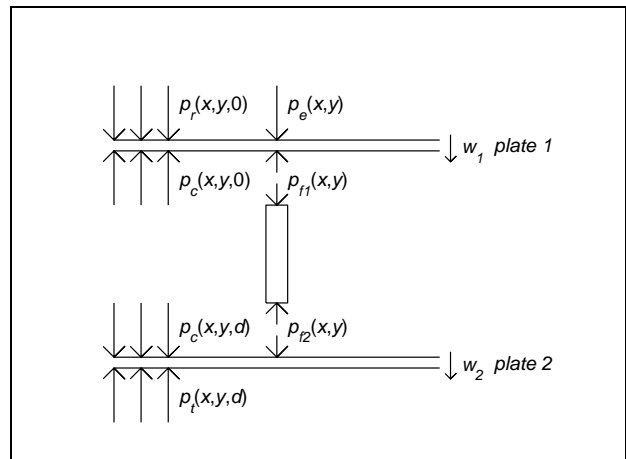
Figure 2. Model for the equation of motion.

formulation employed is mainly due to Lin and Garrelick [9], but also to Mace [13]. Lin and Garrelick is providing the matrix formulation of the coupled problem, but the description of the beams and certain of the notations are the same as Mace uses. A similar formulation can be found in Takahashi [18]. The use of operator notations and the presence of mineral wool in the cavity is novel for the present approach, as well as the use of an elaborate description of the excitation force.

Not every parameter of possible importance in the real floor structure can be taken into account in a theoretical model, in the present model such parameters as moment coupling, orthotropic plates, boundaries, plate bending in the beams and structural waves in the porous material being ignored. The plates and the beams are assumed to be infinitesimally thin in terms of the geometry involved. Also, only radiation from an infinite area is considered.

2.2. The governing equations

As shown in Figure 2, the first plate is excited by the pressure $p_e(x, y)\mathrm{e}^{\mathrm{i}\omega t}$ and is reinforced by parallel beams at a spacing of l. The time variation $\mathrm{e}^{\mathrm{i}\omega t}$ will henceforth be suppressed throughout. The cartesian coordinates and the beam spacing are defined in Figure 1.

The equations to be solved can be written as

$$D_1\left(\frac{\partial^2}{\partial x^2}+\frac{\partial^2}{\partial y^2}\right)^2 w_1 - m_1''\omega^2 w_1 = p_e + p_r - p_{f1} - p_c \quad (1)$$

$$D_2\left(\frac{\partial^2}{\partial x^2}+\frac{\partial^2}{\partial y^2}\right)^2 w_2 - m_2''\omega^2 w_2 = p_c - p_t + p_{f2} \quad (2)$$

The displacement of the plates in the positive z-direction, $w_1(x,y)$ and $w_2(x,y)$, satisfies equations (1) and (2) respectively. Both equations are solved simultaneously. The excitation pressure is p_e, the remaining reaction pressures being due to: interaction of the fluid with the surrounding medium (transmission p_t and radiation p_r), to the framing beams p_f, and to the coupling between the plates governed by the cavity p_c. The mass densities of the plates per unit area are denoted as m_1'' and m_2'' respectively, the flexural rigidities being denoted as D_1 and D_2 respectively. The effects of moments and boundaries are of no concern. Small passive linear pressures and deformations are assumed.

2.3.   Fourier transform of the governing equations

The Fourier transform of the displacement w_i, $i = \{1,2\}$, with respect to the co-ordinates x and y is defined as

$$\tilde{w}_i(\alpha,\beta) = \iint_{-\infty}^{\infty} w_i(x,y) e^{i(\alpha x + \beta y)} dx dy \quad (3)$$

where $i = 1,2$. The corresponding inverse transform is then defined as

$$w_i(x,y) = \frac{1}{4\pi^2} \iint_{-\infty}^{\infty} \tilde{w}_i(\alpha,\beta) e^{-i(\alpha x + \beta y)} d\alpha d\beta \quad (4)$$

where α and β are the transform wavenumbers in the plate in the x- and y-directions, respectively.

Since (1) and (2) are differential equations, it can be postulated that the reaction pressures are related to the displacements by linear operators, including constants and x- and y-derivatives of arbitrary order. This implies the spatial Fourier transform of each operator to be an algebraic expression. The operators and the corresponding Fourier transforms are given in section 3. Calligraphic font typed symbols, such as $\mathcal{R}$ and $\mathcal{T}$, denote the operators. Thus, the reaction pressures can be written as

$$p_r(x,y) = \mathcal{R}w_1(x,y), \quad (5)$$

$$p_t(x,y) = \mathcal{T}w_2(x,y), \quad (6)$$

and the coupling via the cavity can be written as the matrix

$$\begin{bmatrix} p_c(x,y,0) \\ p_c(x,y,d) \end{bmatrix} = \begin{bmatrix} \mathcal{J}_{11} & \mathcal{J}_{12} \\ \mathcal{J}_{21} & \mathcal{J}_{22} \end{bmatrix} \begin{bmatrix} w_1(x,y) \\ -w_2(x,y) \end{bmatrix}, \quad (7)$$

where the matrix operator components $\mathcal{J}_{ij}$ can be regarded as components in a stiffness two-port.

The connection between each plate-frame joint is assumed to be rigid, the continuity equation taking the following form

$$w_1(nl,y) = w_2(nl,y), \; n = -\infty, \cdots, \infty \quad (8)$$

$$F_{1,n} - F_{2,n} = \mathcal{G}w_1(nl,y), \; n = -\infty, \cdots, \infty \quad (9)$$

where $\mathcal{G}$ is a linear beam operator, and $F_{1,n}$ and $F_{2,n}$ are the reaction forces acting on the first and second plate, respectively. The reaction pressures due to the frames are thus

$$p_{f1}(x,y) = \sum_{n=-\infty}^{\infty} F_{1,n}(y)\delta(x-nl), \quad (10)$$

$$p_{f2}(x,y) = \sum_{n=-\infty}^{\infty} F_{2,n}(y)\delta(x-nl). \quad (11)$$

The transform of the sums in (10–11) can be written as

$$\mathcal{F}_{x,y}\left\{ \sum_{n=-\infty}^{\infty} F_{i,n}(y)\delta(x-nl) \right\} = \sum_{n=-\infty}^{\infty} \breve{F}_{i,n}(\beta)e^{i\alpha nl} \quad (12)$$

where $\mathcal{F}_{x,y}$ indicates the double Fourier transform operator in the x-y-directions (3), $i = \{1,2\}$, and the force field is only transformed in the y-direction. Lin and Garrelick [9] assume that under such conditions the force function is two-dimensional, their using the same form of expression here as for the sum of the displacement field derived below. Although their result appears to be accurate, it will become evident that there is no need of introducing this assumption.

In order to connect the force field to the displacement field, sums over the displacement field are also obtained. First, a transformation in the y-direction of the displacement field is performed

$$\mathcal{F}_y w(nl,y) = \breve{w}(nl,\beta)$$
$$= \frac{1}{2\pi} \int_{-\infty}^{\infty} \tilde{w}(\alpha',\beta)e^{-i\alpha' nl} d\alpha' \quad (13)$$

where $\mathcal{F}_y$ indicates the partial Fourier transform in the y-direction. The full xy-transform is

$$\mathcal{F}_{x,y}\left\{ \sum_{n=-\infty}^{\infty} w(nl,y)\delta(x-nl) \right\} = \sum_{n=-\infty}^{\infty} \breve{w}(nl,\beta)e^{i\alpha nl}$$
$$= \frac{1}{2\pi} \int_{-\infty}^{\infty} \sum_{n=-\infty}^{\infty} \tilde{w}(\alpha',\beta)e^{i(\alpha-\alpha')nl} d\alpha' \quad (14)$$

The Poisson's sum can be derived by contour integration and Fourier transformation, c.f. Morse Feshbach [23], and can be used to show that

$$\sum_{n=-\infty}^{\infty} e^{i\alpha nl} = 2\pi \sum_{n=-\infty}^{\infty} \delta(\alpha l - 2n\pi) \quad (15)$$

The total transform (14) can then be written as

$$\sum_{n=-\infty}^{\infty} \breve{w}(nl, \beta) e^{i\alpha nl}$$

$$= \int_{-\infty}^{\infty} \sum_{n=-\infty}^{\infty} \tilde{w}(\alpha', \beta) \delta(\alpha l - \alpha' l - 2n\pi) d\alpha' \quad (16)$$

Following this, the variable change of $(\alpha - \alpha')l \to \alpha$ is made. After some manipulations, the transform of the sum over the displacement points, (14), using (16), can then be written as

$$\mathcal{F}_{x,y} \left\{ \sum_{n=-\infty}^{\infty} w(nl, y) \delta(x - nl) \right\}$$

$$= \frac{1}{l} \sum_{n=-\infty}^{\infty} \tilde{w}(\alpha - 2n\pi/l, \beta) \quad (17)$$

Transforming the pressures (5–7) and (10–11) gives algebraic expressions for the reaction pressures, which can be written as

$$\tilde{p}_r(\alpha, \beta) = R\tilde{w}_1(\alpha, \beta), \quad (18)$$

$$\tilde{p}_t(\alpha, \beta) = T\tilde{w}_2(\alpha, \beta), \quad (19)$$

where R and T are the transformed versions of the linear operators $\mathcal{R}$ and $\mathcal{T}$. The transformed version of the linear operators will be denoted as coefficients. For the matrix relation (7), the transformed version is

$$\begin{bmatrix} \tilde{p}_c(\alpha, \beta, 0) \\ \tilde{p}_c(\alpha, \beta, d) \end{bmatrix} = \begin{bmatrix} J_{11} & J_{12} \\ J_{21} & J_{22} \end{bmatrix} \begin{bmatrix} \tilde{w}_1(\alpha, \beta) \\ -\tilde{w}_2(\alpha, \beta) \end{bmatrix}. \quad (20)$$

and for the frame reactions it is

$$\tilde{p}_{f1}(\alpha, \beta) = \sum_{n=-\infty}^{\infty} \breve{F}_{1,n}(\beta) e^{i\alpha nl}, \quad (21)$$

$$\tilde{p}_{f2}(\alpha, \beta) = \sum_{n=-\infty}^{\infty} \breve{F}_{2,n}(\beta) e^{i\alpha nl}. \quad (22)$$

where (12) has been made use of in (21–22). The continuity equation at each plate-frame boundary implies that

$$\sum_{n=-\infty}^{\infty} \tilde{w}_1(\alpha - 2\pi n/l, \beta) = \sum_{n=-\infty}^{\infty} \tilde{w}_2(\alpha - 2\pi n/l, \beta), \quad (23)$$

$$\sum_{n=-\infty}^{\infty} \breve{F}_{1,n}(\beta) - \sum_{n=-\infty}^{\infty} \breve{F}_{2,n}(\beta)$$

$$= \frac{G}{l} \sum_{n=-\infty}^{\infty} \tilde{w}_1(\alpha - 2\pi n/l, \beta) \quad (24)$$

In formal terms, applying the Fourier transform (3) to equation (1–2) yields

$$\left(D_1 \left(\alpha^2 + \beta^2 \right)^2 - m_1'' \omega^2 \right) \tilde{w}_1 = \tilde{p}_e + \tilde{p}_r - \tilde{p}_{f1} - \tilde{p}_c \quad (25)$$

$$\left(D_2 \left(\alpha^2 + \beta^2 \right)^2 - m_2'' \omega^2 \right) \tilde{w}_2 = \tilde{p}_c - \tilde{p}_t + \tilde{p}_{f2} \quad (26)$$

Introducing two spatial dynamic stiffnesses (transformed plate operators) gives

$$S_1(\alpha, \beta) = D_1 \left(\alpha^2 + \beta^2 \right)^2 - m_1'' \omega^2 \quad (27)$$

$$S_2(\alpha, \beta) = D_2 \left(\alpha^2 + \beta^2 \right)^2 - m_2'' \omega^2 \quad (28)$$

Equation (25–26) can then be rewritten, using (21–24) and suppressing the α and β dependence where they are obvious, as

$$S_1 \tilde{w}_1 = \tilde{p}_e + R\tilde{w}_1 - \sum_{n=-\infty}^{\infty} \breve{F}_{1,n} e^{i\alpha nl}$$

$$- J_{11} \tilde{w}_1 + J_{12} \tilde{w}_2 \quad (29)$$

$$S_2 \tilde{w}_2 = J_{21} \tilde{w}_1 - J_{22} \tilde{w}_2 - T\tilde{w}_2$$

$$+ \sum_{n=-\infty}^{\infty} \breve{F}_{2,n} e^{i\alpha nl} \quad (30)$$

2.4. Solution of the transformed equations

It in now easy to rewrite (29–30) in matrix form as

$$\begin{bmatrix} S_1 - R + J_{11} & -J_{12} \\ -J_{21} & S_2 + T + J_{22} \end{bmatrix} \begin{bmatrix} \tilde{w}_1 \\ \tilde{w}_2 \end{bmatrix}$$

$$= \begin{bmatrix} \tilde{p}_e \\ 0 \end{bmatrix} - \begin{bmatrix} \sum_{n=-\infty}^{\infty} \breve{F}_{1,n} e^{i\alpha nl} \\ -\sum_{n=-\infty}^{\infty} \breve{F}_{2,n} e^{i\alpha nl} \end{bmatrix} \quad (31)$$

where the β-dependency of $\breve{F}_{i,n}$ is suppressed for reasons of clarity. Denote the first matrix from the left as $\mathbf{S}$,

$$\mathbf{S} = \begin{bmatrix} S_{11} & S_{12} \\ S_{21} & S_{22} \end{bmatrix} \equiv \begin{bmatrix} S_1 - R + J_{11} & -J_{12} \\ -J_{21} & S_2 + T + J_{22} \end{bmatrix}.$$

Inverting $\mathbf{S}$ and multiplying from the left yields

$$\begin{bmatrix} \tilde{w}_1 \\ \tilde{w}_2 \end{bmatrix} = \frac{1}{\det \mathbf{S}} \begin{bmatrix} S_{22} & -S_{12} \\ -S_{21} & S_{11} \end{bmatrix} \quad (32)$$

$$\times \left(\begin{bmatrix} \tilde{p}_e \\ 0 \end{bmatrix} - \begin{bmatrix} \sum_{n=-\infty}^{\infty} \breve{F}_{1,n} e^{i\alpha nl} \\ -\sum_{n=-\infty}^{\infty} \breve{F}_{2,n} e^{i\alpha nl} \end{bmatrix} \right)$$

which in formal terms is the solution to the transformed displacement, although the relations between the displacement and the force field in the beams need to be applied. The calculations needed can be found in the Appendix, where closed expressions for the summed forces are found in equation (A7–A8). The solution is thus found to be given by equation (32), where the first term is the solution to the problem without beams, and the second term is the correction needed because of the beams.

If the sums over the reaction forces are put to zero, the solution describes two plates coupled through a fluid field and driven on the first plate by a point force. If the couplings between the plates are put to zero, that is if $S_{21} = S_{12} = 0$ and $F_{2,n} = 0, \forall\, n = 0, \pm 1, \pm 2, \cdots$, the

equation for the displacement of the first plate becomes

$$\tilde{w}_1 = \frac{\tilde{p}_e}{S_{11}} - \frac{P_1 G/l}{S_{11}\left(1 + Y_{11}G/l\right)} \qquad (33)$$

where the notation P_1 and Y_{11} is defined in the appendix. This result, equation (33), is equivalent to the results obtained in [11] and [13] (if the second periodicity of beams is not taken into account), and describes the displacement of a single plate periodically reinforced by beams.

3. The system; the excitation and reaction forces

In order to obtain a complete solution, the forces and pressures involved need to be specified.

3.1. The excitation force

The excitation force is assumed to be a point force in the position x_0, y_0.

$$p_e(x, y) = F_R \delta\left(x - x_0, y - y_0\right) \qquad (34)$$

where F_R is the time-frequency Fourier transform of the excitation force of the impact under consideration, and the subscript R stands for repeated signals. The corresponding spatial Fourier transform is

$$\tilde{p}_e(\alpha, \beta) = F_R \mathrm{e}^{\mathrm{i}(\alpha x_0 + \beta y_0)} \qquad (35)$$

F_R being specified in [1], and some further considerations being found in section 4.3.

3.2. The frame reactions

For the n'th frame, the equation of motion, modelled as a Euler beam and excited by a linear force $Q_n(y)$ along the line $x = nl$,

$$E_f I_f \frac{d^4 u_n}{dy^4} - \rho_f A_f \omega^2 u_n = Q_n \qquad (36)$$

where $E_f I_f$ is the bending rigidity and $\rho_f A_f$ is mass per unit length of the frame. The difference between the plates frame reaction pressure is

$$p_{f1}(x, y) - p_{f2}(x, y) \qquad (37)$$
$$= \sum_{n=-\infty}^{\infty} \left(E_f I_f \frac{d^4 u_n}{dy^4} - \rho_f A_f \omega^2 u_n \right) \delta(x - nl)$$

From equation (36), the operator $\mathcal{G}$ in equation (9) can now be identified. The algebraic expression for G in (24) is found by transforming (36) as follows:

$$G = E_f I_f \beta^4 - \rho_f A_f \omega^2 \qquad (38)$$

and equation (24) can be found then by transforming (36), making use of (12).
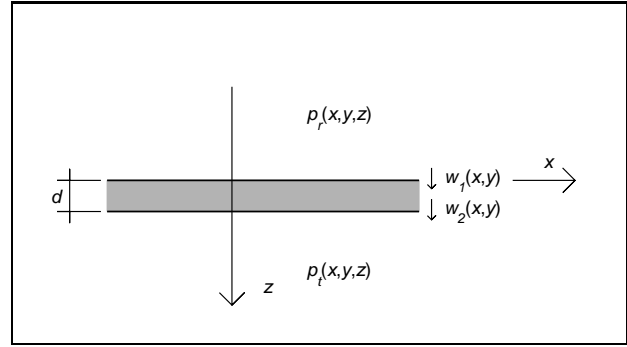
Figure 3. The acoustic pressure in the outer fields.

3.3. The fluid reactions

Consider Figure 3, in which a fluid occupies the upper and lower half spaces. The two fields are assumed to have the same sound speed c_0, density ρ_0 and wavenumber $k = \omega/c_0$. Two moving surfaces occupy the x-y-plane in $z = 0$ and $z = d$, vibrating with displacements $w_1(x, y)$ and $w_2(x, y)$. The acoustic pressure satisfies the Helmholtz equation

$$\left(\frac{\partial^2}{\partial x^2} + \frac{\partial^2}{\partial y^2} + \frac{\partial^2}{\partial z^2} \right) p_{r,t} + \frac{\omega^2}{c_0^2} p_{r,t} = 0, \qquad (39)$$

together with the boundary conditions

$$\left[\frac{\partial p_r}{\partial z} \right]_{z=0} = \omega^2 \rho_0 w_1 \,, \quad \left[\frac{\partial p_t}{\partial z} \right]_{z=d} = \omega^2 \rho_0 w_2 \qquad (40)$$

which ensures both the equality of the fluid velocity at the plate surface and the plate velocity. The relation between displacement and pressure can be found in e.g. [5, pp. 502–505], and can for the radiated pressure be written,

$$\tilde{p}_r(\alpha, \beta, 0) = \frac{\omega^2 \rho \tilde{w}_1(\alpha, \beta)}{\sqrt{\alpha^2 + \beta^2 - k^2}}, \qquad (41)$$

where the branch of $\gamma = \sqrt{\alpha^2 + \beta^2 - k^2}$ is taken so that $\Re\gamma \geq 0$, $\Im\gamma \geq 0$ if $\Re\gamma = 0$, in order that the condition for outgoing waves be met.

In the same way, if $z = d$,

$$\tilde{p}_t(\alpha, \beta, d) = -\frac{\omega^2 \rho \tilde{w}_2(\alpha, \beta)}{\sqrt{\alpha^2 + \beta^2 - k^2}} \qquad (42)$$

Accordingly, one can identify the coefficients in (18–19) as

$$R = -T = \frac{\omega^2 \rho}{\sqrt{\alpha^2 + \beta^2 - k^2}} \qquad (43)$$

3.4. The reaction of the fluid-filled cavities

Following the procedure described in the last section, consider Figure 4, in which a fluid occupyies the space $0 < z < d$. An acoustic pressure $p_c(x, y, z)$ is present.

Note that, as an approximation, in this description the frames do not effect the cavity field. A more elaborate account of this will be presented in a forthcoming paper.
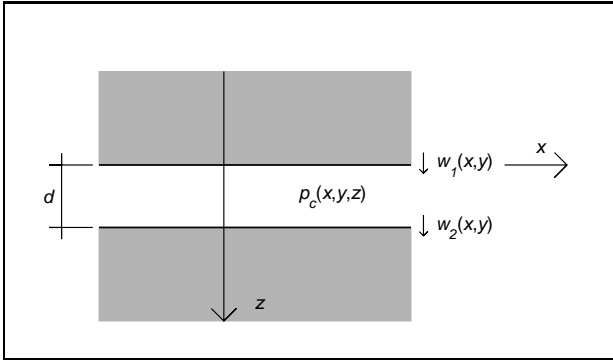
Figure 4. The acoustic pressure in the cavity field.

The acoustic pressure satisfies the Helmholtz equation that corresponds to (39), where c_c is the speed of sound in the medium and ρ_c is the density. The acoustic pressure also satisfies the boundary conditions

$$\left[\frac{\partial p_c}{\partial z}\right]_{z=0} = \omega^2 \rho_c w_1, \quad \left[\frac{\partial p_c}{\partial z}\right]_{z=d} = \omega^2 \rho_c w_2, \quad (44)$$

which ensures the equality of the fluid velocity at the plate surface and the plate velocity. The Helmholtz equation is now transformed, a solution being found by assuming there to be one wave in the positive z-direction and one in the negative z-direction,

$$\tilde{p}_c(\alpha, \beta, z) = \hat{p}_{c+} e^{-i\sqrt{k_c^2 - \alpha^2 - \beta^2} z} \qquad (45)$$
$$+ \hat{p}_{c-} e^{i\sqrt{k_c^2 - \alpha^2 - \beta^2} z}$$

where $k_c = \omega/c_c$ is the wavenumber for the fluid in the cavity, and c_c is the speed of sound in the cavity. One derivation with respect to z gives an expression suited to the boundary condition. The amplitudes of the components in the standing wave are then obtained, using (44) and (45). After some manipulations, setting $z = 0$ and $z = d$ the result, written in a matrix form, reads

$$\begin{bmatrix} \tilde{p}_c(\alpha, \beta, 0) \\ \tilde{p}_c(\alpha, \beta, d) \end{bmatrix} = \frac{\omega^2 \rho_c}{k_d}$$
$$\times \begin{bmatrix} \cot(k_d d) & \csc(k_d d) \\ \csc(k_d d) & \cot(k_d d) \end{bmatrix} \begin{bmatrix} \tilde{w}_1(\alpha, \beta) \\ -\tilde{w}_2(\alpha, \beta) \end{bmatrix}, \quad (46)$$

where J_{11}, J_{12}, J_{21} and J_{22} in equation (20) can be identified, and $k_d \equiv \sqrt{k_c^2 - \alpha^2 - \beta^2}$ and where the branch of $k_d = i\gamma_d$ is so taken that $\Re\gamma_d \geq 0$, $\Im\gamma_d \geq 0$ if $\Re\gamma_d = 0$. Moreover, $\cot x = \cos x / \sin x$ and $\csc x = 1/\sin x$.

If the cavity is filled with mineral wool, a semi-empirical model of an equivalent fluid, as formulated by Delaney and Bazley [24] and later also investigated by Mechel [25], can be used to derive both the wavenumber k_{min} and the impedance z_{min} to be used,

$$k_{\min} = k \left(-i\, 0.189 C^{0.618} + 1 + 0.0978 C^{0.693}\right), \quad (47)$$
$$z_{\min} = \rho_0 c_0 \left(1 + 0.0489 C^{0.754} - i\, 0.087 C^{0.731}\right), \quad (48)$$

where

$$C \equiv R_{\min} / (\rho_0 f),$$

R_{min} being the flow resistance of the mineral wool, which is the only material parameter of the mineral wool included in the model, and where $R_{min} = \Delta p / hu$, Δp being the pressure difference over a sample of depth h under a flow velocity u. Equation (46) is then replaced by the corresponding equation for mineral wool, where $k_{d,\min} \equiv \sqrt{k_{\min}^2 - \alpha^2 - \beta^2}$ is used instead of k_d and ρ_c is replaced by z_{min}/c_0. For a partly filled cavity, a combination of the expressions (46) and the corresponding mineral wool equation need to be used, which is described in the appendix, equations (A9–A14).

4. The response; radiation, impact noise level and tonal spectrum

In measuring the impact noise level, the response quantity is the sound pressure level in the receiver room. In the prediction model, this quantity needs to be simulated.

4.1. Radiated power from an infinite area

In order to compare the calculations with measured values, the radiated power is now focused upon. The finite area of radiation, although it probably affects the result, is not considered here. Instead the expression for power radiation found in Cremer and Heckl [5, pp. 534] will be employed:

$$\Pi_{Rad} = \frac{k\rho c}{8\pi^2} \iint\limits_{\alpha^2 + \beta^2 \leq 1} \frac{\omega^2 |\tilde{w}(\alpha, \beta)|^2}{\sqrt{k^2 - \alpha^2 - \beta^2}} \, d\alpha d\beta \qquad (49)$$

(This expression was derived for a finite radiation situation, but it is also suited for point excitation, as is the case here.) In order to simplify the integration, use $\alpha = k_r \sin(\varphi)$ and $\beta = k_r \cos(\varphi)$ so that $d\alpha d\beta = k_r dk_r d\varphi$

$$\Pi_{Rad} = \frac{k\rho c}{8\pi^2} \qquad (50)$$
$$\times \int_0^k \int_0^{2\pi} \frac{\omega^2 |\tilde{w}(k_r \sin(\varphi), k_r \cos(\varphi))|^2}{\sqrt{k^2 - k_r^2}} k_r dk_r d\varphi.$$

In [7, 8, 18], use was made of an equivalent expression, emanating from the far-field pressure. Equation (50) is integrated numerically, see section 5.1.

4.2. Power balance for standard impact noise

The impact noise level is defined as [4]

$$L_n = L_p + 10 \log \frac{A}{A_0} \text{ dB} \qquad (51)$$

where L_p is the measured sound pressure level, A is the absorption area and $A_0 = 10 \text{ m}^2$ is a reference. Written with an antilogarithm applied, the expression is instead

$$p_n^2 = \left\langle |p|^2 \right\rangle \frac{A}{A_0} \qquad (52)$$

where $\langle |p|^2 \rangle$ is the mean square pressure and p_n^2 denotes the 'equivalent impact noise pressure' (rms). A power balance reads

$$\Pi_{Rad} = \Pi_{Out} = \frac{\left\langle |p|^2 \right\rangle}{\rho c} \frac{A}{4} \qquad (53)$$

Combing (52) and (53) gives

$$p_n^2 = \Pi_{Rad} \frac{4\rho c}{A_0}, \qquad (54)$$

and therefore

$$L_n = 10 \log \left(\frac{\Pi_{Rad}}{p_{ref}^2} \frac{4\rho c}{A_0} \right) \text{ dB.} \qquad (55)$$

4.3. Tonal spectrum, transfer functions and third octave band values

The theoretical model of the system is derived, a $\exp(\mathrm{i}\omega t)$ dependence being assumed, which is equivalent to applying a time-frequency Fourier transform to the system. The driving force caused by the tapping machine can be regarded as an array of periodic force pulses, as described in reference [1], equation (1). The time-frequency Fourier transform of this signal is a tonal spectrum, see reference [1] equation (3). A two-sided description of the driving force is achieved by applying a complex Fourier series. Non-zero values are then only present at discrete frequency points, nf_r, the positions of the Dirac's in the sum. In standard impact noise level measurements, third octave bands are employed. The third octave band levels are found by adding the responses calculated in frequency points mf_r, where the integer $m \in \Delta f_t / f$, where Δf_t is the third octave band in question.

5. Results and discussion; numerical computations and comparison with measurements

Comparisons of the measured data with the computations need to be performed so as to judge whether the proposed prediction model is sufficiently accurate enough.

A possible disagreement between the model and the measurements could be due to details in the real structure that are ignored in the model, e.g. moment coupling or orthotropic behaviour in the upper and lower plates.

The excitation position is an important aspect of the problem, most of the calculations presented being means over different positions (15 positions) in order to simulate the measurements, which are also means over different positions.

The present chapter is disposed as follows: the calculation program is discussed, measurements found in the literature are presented, the material data is defined, a comparison is made with conditions of no mineral wool in the cavity (the mean value and the values at different positions), a comparison is made with mineral wool in the cavity, and a comparison is made with an orthotropic plate.
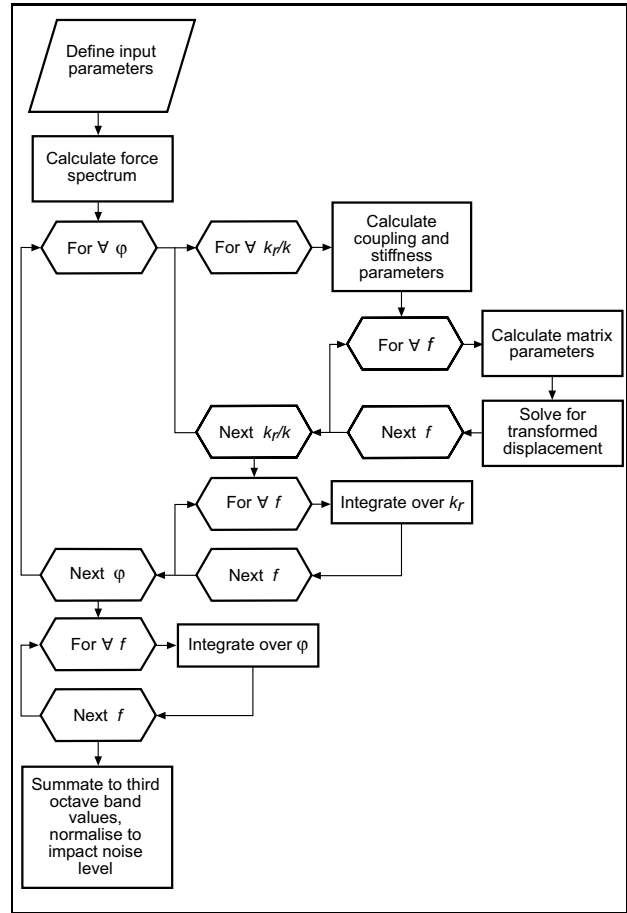
Figure 5. Flow chart for the calculation program.

5.1. Programming

Since the theoretical model proposed in the paper is not a closed expression, equation (50) containing integrals that are intended to be solved numerically, program coding is an important part of the prediction model. Certain important aspects of the program will be presented both in text and in flow-chart form (Figure 5). The program is written in MATLAB [26].

The program starts by defining the material properties, together with the range and resolution present in the frequency and wave number parameters φ and k_r. The materials are described in section 5.3. The frequency range includes the third octave bands from 50 Hz to 5000 Hz, the resolution being the same as for the tapping machine, $\Delta f = f_r = 10$ Hz. The wavenumber parameters have the ranges $\varphi \in \{-\pi + \epsilon, \pi + \epsilon\}$ and $k_r / k \in \{0 + \epsilon, 1 + \epsilon\}$, so as to include the radiating wavenumbers, where the small number $\epsilon = 10^{-8}$ is used in order to avoid problems of singularity. The resolution for the wavenumber parameters is $\Delta\varphi = 2\pi/25$ and $\Delta k_r / k = 1/100$.

Convergence is checked by means of visual inspection as the resolution is increased. Only small changes in the results where noted in the range $\Delta k_r / k = 1/30 - 1/200$ and $\Delta\varphi = 2\pi/7.5 - 2\pi/50$. The convergence was also checked by comparison with an adaptive Gaussian quadrature (in the low frequencies); only minor discrepancies be-
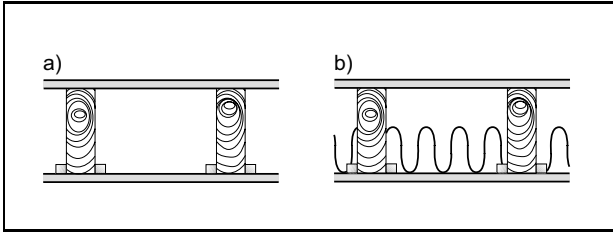
Figure 6. Two floor structures considered in [22]. a) 67×220 mm beams, 600 mm spacing, 22 mm matched boards in floor and ceiling. b) The same plus 120 mm mineral wool (density 20 kg/m^3).

Figure 7. The 15 calculation positions. A beam is located at x=0 m (- - -) and the line halfway between the beams is located at x=0.3 m (– · –).

ing noted. Note that this convergence reasoning is only valid, however, for a third octave-band integrated spectrum. If a narrow-band spectrum is calculated, the adaptive Gaussian quadrature is probably needed.

The force spectrum is then calculated, using the results reported in [1], yielding a complex F_n for each frequency point.

The different parameters required are then calculated in the for-loops according to Figure 5. The for-loops runs over the wavenumber parameters φ and k_r/k, and over the frequency f. The infinite sums are calculated in subroutines, truncated to an appropriate number of terms on each side of zero. At the end the trapezoid rule is used to integrate over the k_r/k and the the φ points. The third octave band values is then being calculated and the impact noise level is being found by means of equation (55). The program then stops, producing various plots and saving routines.

5.2. Bodlund's measurements

The floor structure studied in the present paper has very poor impact noise insulation and is thus not commonly used for insulation between dwellings. However, it can sometimes be found as a structure separating rooms in the same dwelling, such as in two-story villas. Since building codes are mainly concerned with disturbances between neighboring dwellings, it is difficult to find laboratory measurements concerning this type of floor structure.

In [22] Bodlund studied airborne and impact-noise insulation in buildings with wooden floor structures built in the 1930s or earlier. The report contains both laboratory and field measurements of wooden floor structures according to the ISO standard [4]. Some of the laboratory measurements are made on the very simple floor structures shown in Figure 6. These measurements are suitable for comparison with result of the present prediction model.

The measurements were made at SP, the Swedish National Testing and Research Institute. The dimensions of the laboratory were $3.70 \times 6.66 \times 5.38$ m, giving a volume of 138.2 m^3. The dimensions of the specimen opening were 3×4 m.

5.3. Material data

Since finding the proper material data is a difficult task when comparisons are made with measurements con-

ducted by others, one can achieve little more than a good guess regarding the actual material data. This is similar, however, to the situation when designing a floor.
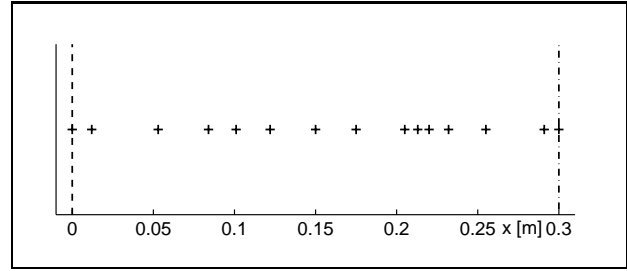
The following data have been used in the numerical calculations: distance between beams $l = 0.6$ m, modulus in the plates $E_p/(1 - \mu^2) = 7.2 \cdot 10^9$ Pa, Young's modulus in the framing beams $E_f = 9.8 \cdot 10^9$ Pa, Young's modulus for the local stiffness $E_{local} = 1.42 \cdot 10^9$ Pa. The local Young's modulus is taken as the geometric mean of the modulus in the three directions. The density of the beams and plates is $\rho_p = \rho_f = 500$ kg/m^3, the thickness of the plates $h = 22 \cdot 10^{-3}$ m, the material damping $\eta = 0.03$, the density of the air $\rho_0 = 1.29$ kg/m^3, and the speed of sound in air $c_0 = 340$ m/s, with a damping of $\eta_{air} = 1 \cdot 10^{-8}$ in the surrounding air and $\eta_c = 1 \cdot 10^{-3}$ for the air trapped in the cavity. The damping is added to the modulus. The beams are 0.220 m in height and 0.067 m in width. Thus, the distance between the plates is also $d = 0.220$ m. In the first and second examples (sections 5.4–5.5), no mineral wool was used. In the third example (section 5.6), mineral wool with a flow resistance of $R_{min} = 11770$ Ns/m^4 and a depth of $d_{min} = 0.12$ m was employed.

The local stiffness is defined as the apparent stiffness for a local indentation, and is for the so-called Bossinesq deformation (which is the deformation caused by a rigid indenter statically acting on a semi-infinite elastic half-sphere) $K = E_{local}D_h/(1 - \nu^2)$, where D_h is the diameter of the indenter, se [1]. A more elaborate description of the local stiffness (or more correctly local mobility) is also employed, taken from [27] where three-dimensional elastic plate theory is used.

The 15 calculation positions are $x_0 = \{0\ 0.012\ 0.053\ 0.084\ 0.101\ 0.122\ 0.150\ 0.175\ 0.205\ 0.213\ 0.220\ 0.232\ 0.255\ 0.291\ 0.3\}$ m and $y_0 = 0$ m, chosen randomly (except for the start and the end point). The positions are shown in Figure 7.

5.4. Comparison with a simple floor structure without mineral wool.

The floor structure described in Figure 6 a) will be considered first, see Figure 8. The cavity of this structure contains no mineral wool. Four different descriptions of the excitation, increasing in their degree of elaboration, were tested. The excitation/mobility models, described in
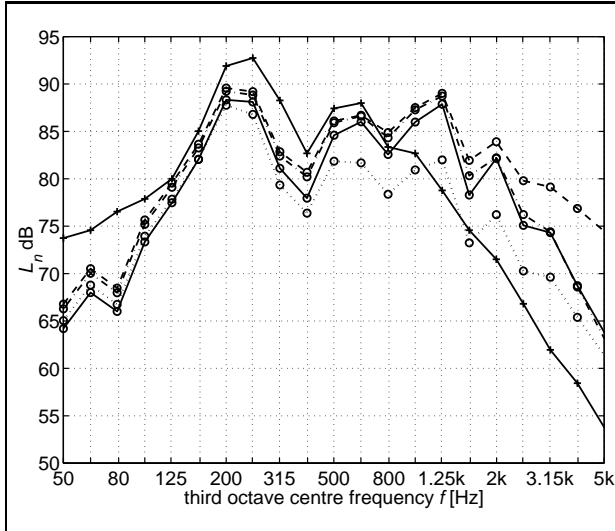
Figure 8. Floor a). Mean over 15 excitation positions in the calculations, where 'o' denotes the mean of the calculated values and '+' denotes measured values [22]. Case I) (—), case II) (- - -), case III) (− · −) and case IV) (· · ·).

[1], are I) the lumped model, in which the frequency-independent stiffness K and resistance R are employed, is represented by a solid line (—); II) the 'global' driving-point mobility Y_G expression, is denoted by the dashed line (- - -); III) the expression $Y_G + i\omega/K$, in which K is frequency independent according to (16) in [1], is denoted by a dashed-dotted line (− · −); and finally IV) the mobility expression $Y_G + Y_L - 1/(8\sqrt{MD})$, the 'local' mobility Y_L being calculated according to [27], is described by the dotted line (· · ·).

For all the excitation situations, the agreement between the measurements and the computations, as shown in Figure 8, is quite good in the frequency range of 100-800 Hz. Although all the peaks and troughs are there, a systematic disagreement of approximately 5-3 dB is found, the calculations underestimating the results. This is probably due to the lack of moment coupling in the model, as will be discussed in the context of the orthotropic model, section 5.7. Other possible explanations for the disagreement are found below. The best agreement for the higher frequencies is with the most elaborate mobility model IV) (however, for frequencies below 800 Hz this case is the worst). The I) and III) models are almost the same in the agreement achieved. If no local weakness is employed in the mobility description, as in model II), high-frequency behaviour cannot be predicted. It can be concluded that the choice of excitation/mobility description is crucial to the prediction model, the local stiffness (or mobility) is being especially important.

The room dimensions influence the measured results in the frequency region below the cut-on frequency for the diffuse-field assumption. This lower frequency limit, at which a statistical treatment of the superimposed normal modes in a room is possible, can be shown to be approximately as in [28, 29],

$$f_g \approx 2000\sqrt{\frac{T_{60}}{V}} \qquad (56)$$

where Schroeder [29] uses a constant of 4000 instead of 2000. The volume of the room employed is $V=138.2$ m^3, the reverberation time being assumed to be $T_{60} \approx 2$ s. Although the frequency limit then is $f_g \approx 240$ Hz, the agreement is quite good even below this frequency.

Another explanation of the disagreement found in the three lowest third octave bands is that the tonal spectrum is not narrow enough to be evenly spread over the lowest third octave bands. The first band, 50 Hz, has only one tone. The next, 63 Hz, has two tones. The 80 Hz third octave band has again only one tone, whereas the 100 Hz third octave band, the 125 Hz third octave band and the 160 Hz third octave band have three tones, and so on. In obtaining the measurements, the periodicity of the hammer signal is not perfect, resulting in a less than distinct tonal spectrum, making the problem not particularly evident in the measurements. Yet another explanation is that the disagreement at low frequencies could come from the radiation effect associated with the finite size of the floor not taken into account for in the model.

A possible explanation of parts of the disagreement found in the middle to higher frequencies is that the influence of the segmentation of the air cavity by the beams can not be completely neglected, in particular when the cavity is without mineral wool.

In the higher frequency region, above approximately 800 Hz, the disagreement between measurements and the calculations is approximately 5 dB, as can be seen in curve IV). The slope, however, is almost the same in all the curves except II). A possible explanation of this behaviour is that the Young's modulus for the local stiffness is overestimated, giving too high a cut-off frequency f_{cut} for the driving force spectrum given in reference [1] equation (15). When the material data is so defined in section 5.3 and in mobility model II), the local stiffness is $K = 4.66 \cdot 10^7$ N/m and the resistance $R = 2.12 \cdot 10^3$ Ns/m, and the mass of the hammer is $M = 0.5$ kg, giving a cut-off frequency of $f_{cut} \approx 1540$ Hz. The measurements are assumed to have a lower cut-off frequency. By visual inspection, the cut-off frequency was estimated to be approximately $f_{cut,measure} \approx 800$ Hz, giving a local stiffness of $K = 1.26 \cdot 10^7$ N/m, the resistance being assumed to be constant.

In [22] another structure that was almost as simple as the one above was studied, with the difference that the ceiling plate was replaced by a chipboard of thickness $h = 12 \cdot 10^{-3}$ m, density $\rho_p = 700$ kg/m^3, and modulus $E_p/(1 - \mu^2) = 3 \cdot 10^9$ Pa.

The agreement in Figure 9 is not as good as in Figure 8, the differences at around 200 Hz exceeding 10 dB. For higher frequencies, the agreement is better. The disagreement is possible due to the lack of moment coupling in the theoretical model.
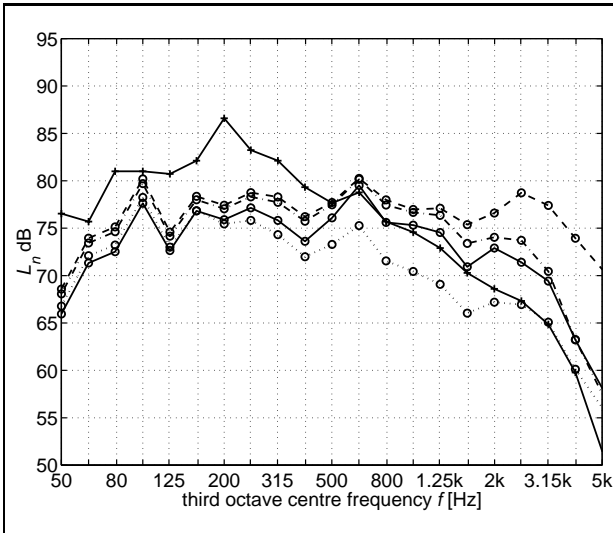
Figure 9. Floor a), but the ceiling plate exchanged for a chipboard. Means of 15 excitation positions are shown in the calculations, 'o' denoting the mean of the calculated values and '+' denotes the measured values [22]. Case I (—), case II (- - -), case III ($- \cdot -$) and case IV) ($\cdots$).
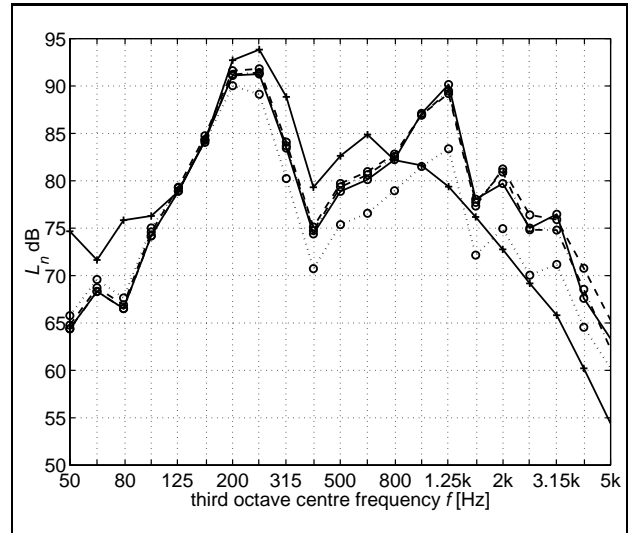
Figure 11. Floor a). Positions between beams, x0=0.3 m and $y_0 = 0$ m, where 'o' denotes the calculated values and '+' denotes measured values [22]. Case I (—), case II (- - -), case III ($- \cdot -$) and case IV) ($\cdots$).
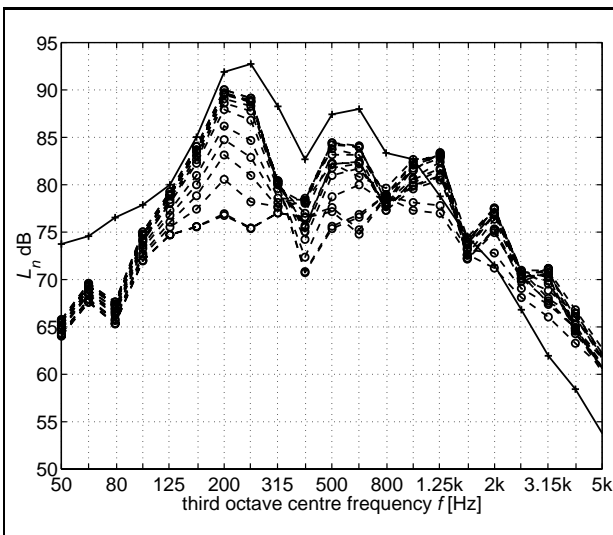
Figure 10. Floor a). Calculations made 15 excitation positions, 'o' denoting the calculated values for the different positions and the excitation according to case IV), and '+' denoting measured mean values [22].
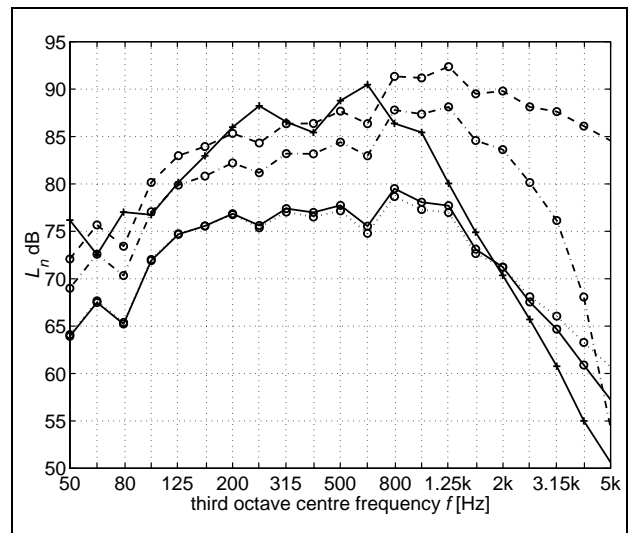
Figure 12. Floor a). Positions at a beam, $x_0 = 0$ m and $y_0 = 0$ m, where 'o' denotes the mean of the calculated values and '+' denotes measured values [22]. Case I (—), case II (- - -), case III ($- \cdot -$) and case IV) ($\cdots$).

5.5. Comparison between different positions

The position of excitation is an important aspect of the problem. In order to obtain data for simulating the measurements presented in the previous section, a mean over 15 positions was calculated. Each of these computations is shown in Figure 10 for the same floor as in Figure 8, floor a) in Figure 6.

The influence of the excitation position was also studied in [22]. For the same floor structure, Figure 6 a), measurements in which the tapping machine was placed at 10 different positions coinciding with the beam positions and

at 10 different positions between two beams (the same distance as to the beams) are presented. These measurements can be used to investigate how well the present model can take position into account.

As the first example of the influence of position, consider the excitation as being located between two beams. The comparison this results in is shown in Figure 11. The agreement is relatively good within the entire frequency range. The slopes, peaks and troughs in the theoretical model follow satisfactorily those found in the experiments. However, one can note a 10 dB discrepancy in the frequency range 300-600 Hz for case IV).
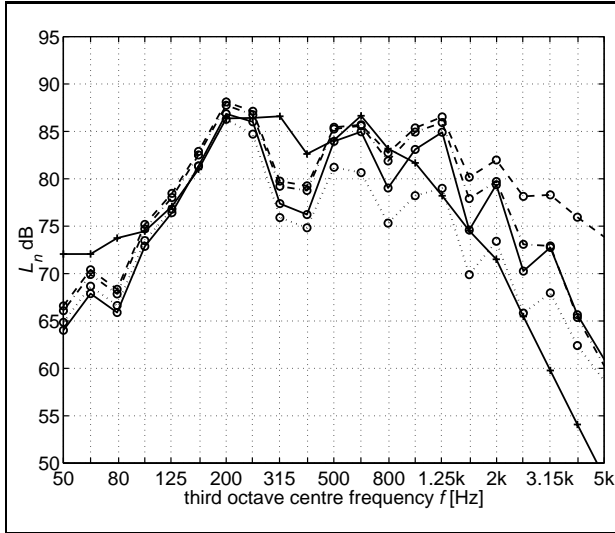
Figure 13. Floor b), with mineral wool in cavity. Mean are obtained over 15 excitation positions in the calculations, where 'o' denotes the mean of the calculated values and '+' denotes measured values [22]. Case I) (—), case II) (- - -), case III) (— · —) and case IV) (· · ·).

In Figure 12 the comparison involves the excitation being located directly at a beam. For cases II) and III), excitation describes the situation up to about 1000 Hz well. Thereafter, cases I) and IV) are closer to the measured curve, indicating a too high local stiffness. The local stiffness of the beam is probably closer to the Bossinesq stiffness, c.f. reference [1] equation (16), since the depth of the deformed material is much greater than when no beam supports the plate, which is the fact in cases I) and III). The real part of the mobility is close to that of a beam, which is true for cases II), III) and IV). Thus, case III) should have the best fit here, which the results indicates.

Another explanation of the disagreement could be that the excitation caused by the ISO tapping machine includes the excitation both of the beam and the plate due to the finite area of the hammer and to the fact that five hammers at different position are employed, whereas in the calculation the excitation point is given exactly and is infinitely small.

The structure behaves more like an orthotropic structure if driven at the beams, the vibration will be almost the same on both sides. Comparing the results of the calculations in Figure 12 with those of the orthotropic calculations in Figure 14, indicates the two cases to be quite similar.

5.6.   Comparison when mineral wool is present.

In the floor shown in Figure 6 b) the cavity is partly filled with mineral wool. The agreement is close for this floor too, as can be seen in Figure 13. For a discussion of the excitation cases, see section 5.4.

5.7.   Comparison with an orthotropic plate

When the bending wavelength is considerably greater than the beam spacing, the structure can be regarded as an or-

thotropic plate [5, pp. 301–304].

$$
\left(D_x \frac{\partial^4}{\partial x^4} + 2 \left(D_\mu + 2D_G \right) \frac{\partial^4}{\partial x^2 \partial y^2} + D_y \frac{\partial^4}{\partial y^4} \right) w
$$
$$
- m''_{orth} \omega^2 w = p_e - p_a \tag{57}
$$

The stiffnesses can be defined as

$$
D_x = \frac{E}{1-\mu^2} I'_x, \; D_y = \frac{E}{1-\mu^2} I'_y,
$$
$$
D_{xy} \equiv D_\mu + 2D_G \approx \sqrt{D_x D_y}.
$$

where

$$
I'_x = \frac{h^3}{6} + 2h \left(d/2 + h \right)^2,
$$
$$
I'_y = \frac{h^3}{6} + 2h \left(d/2 + h \right)^2 + \frac{bd^3}{12l},
$$

and where b is the width of the beam, d is the distance between the plates, h is the thickness of the plates and l is the spacing between the beams. As before, a small amount of damping can be added to the stiffness. The moments of inertia is calculated using the configuration shown in Figure 6 a), and assuming the ceiling plate and the floor plate to be equal and to interact fully with the beams (including the moment coupling). The total mass per unit area is $m''_{orth} = m''_1 + m''_2 + bd\rho_f/l$. Applying the Fourier transform (3) to equation (57) gives an algebraic expression that can be solved for the transformed displacements

$$
\tilde{w}\left(\alpha, \beta \right) = \frac{\tilde{p}_e\left(\alpha, \beta \right)}{S_{orth}\left(\alpha, \beta \right)} \tag{58}
$$

where, if radiation damping is included, S_{orth} is the spatial stiffness,

$$
S_{orth}\left(\alpha, \beta \right) = D_x \alpha^4 + 2D_{xy} \alpha^2 \beta^2 + D_y \beta^4
$$
$$
- m''_{orth} \omega^2 - \frac{2\omega^2 \rho}{\sqrt{\alpha^2 + \beta^2 - k^2}}, \tag{59}
$$

The same procedures as described above can be used to obtain the impact noise level.

In Figure 14 results for the experiment and for equation (58) as inserted into the power expression described in sections 4.2–4.3 are compared. The excitation is taken as case I); the frequency being independent of the stiffness and the resistance. The low-frequency asymptote appears to coincide well. This is probably due to the moment coupling being present. In the mid- and high-frequency regions, however, discrepancies can be noted. In the frequency region of 100 – 700 Hz, peaks and troughs are found in the experimental results that are not present in the orthotropic model. If the point mobility of the orthotropic model had been used in the excitation model, the model would have overestimated the results above approximately 700 Hz, probably due to use of the excitation model and to the orthotropic model being too stiff.

6.   Summary and concluding remarks

A theoretical model for simple point-excited lightweight floors is presented. The model is used to predict the im-
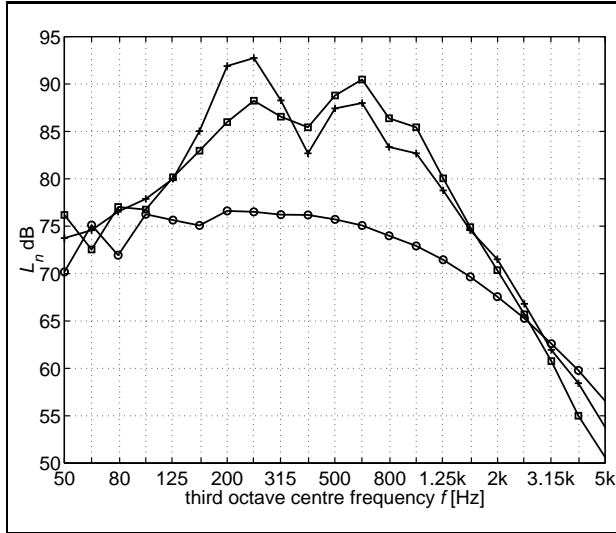
Figure 14. Orthotropic plate, where 'o' denotes calculated values, '+' denotes measured values (just as in Figure 8), excitation case I) and '□' denotes measured values with excitation on the beams.

pact noise level. Comparisons of numerical computations with measurements found in the literature are made. The agreement between the measurements and the calculations is relatively close, especially since the peaks and troughs found in the experimental results can also be seen in the predictions, although there is a systematic underestimation of the impact noise level of about 5-3 dB.

An orthotropic plate model was also studied. The results achieved for the orthotropic plate indicate the lack of moment coupling in the model to probably be the main reason for the underestimation of the impact noise level in the full prediction model.

Quite an accurate description of the force spectrum was achieved by use of a lumped frequency-independent K and R impedance description. However, in order to achieve a satisfactory description here, the global and local driving-point mobilities need to be used and in combination in determining the impact force.

Finally, it can be concluded that it is important to use an accurate and detailed model of both the system and the excitation force, in order to predict the impact noise level of a lightweight floor structure.

Acknowledgement

Appendix

Define two help matrices $\mathbf{P}$, of size 2×1, and $\mathbf{Y}$, of size 2×2,

$$\begin{bmatrix} P_1 \\ P_2 \end{bmatrix} = \sum_{n=-\infty}^{\infty} \frac{1}{\det \mathbf{S}(\alpha - n2\pi/l)} \tag{A1}$$

$$\times \begin{bmatrix} S_{22}(\alpha - n2\pi/l) \\ -S_{21}(\alpha - n2\pi/l) \end{bmatrix} \tilde{p}_e(\alpha - n2\pi/l)$$

$$\begin{bmatrix} Y_{11} & Y_{12} \\ Y_{21} & Y_{22} \end{bmatrix} = \sum_{n=-\infty}^{\infty} \frac{1}{\det \mathbf{S}(\alpha - n2\pi/l)} \tag{A2}$$

$$\times \begin{bmatrix} S_{22}(\alpha - n2\pi/l) & -S_{12}(\alpha - n2\pi/l) \\ -S_{21}(\alpha - n2\pi/l) & S_{11}(\alpha - n2\pi/l) \end{bmatrix}.$$

Equation (32) is now to be summed at the position $\alpha = n2\pi/l$. In the first step, the variables need to be changed to $\alpha - em$, where m is an integer,

$$\begin{bmatrix} \tilde{w}_1(\alpha - m2\pi/l) \\ \tilde{w}_2(\alpha - m2\pi/l) \end{bmatrix} = \frac{1}{\det \mathbf{S}(\alpha - n2\pi/l)} \tag{A3}$$

$$\times \begin{bmatrix} S_{22}(\alpha - n2\pi/l) & -S_{12}(\alpha - n2\pi/l) \\ -S_{21}(\alpha - n2\pi/l) & S_{11}(\alpha - n2\pi/l) \end{bmatrix}$$

$$\times \left(\begin{bmatrix} \tilde{p}_e(\alpha - m2\pi/l) \\ 0 \end{bmatrix} - \begin{bmatrix} \sum_{n=-\infty}^{\infty} \breve{F}_{n,1} e^{i(\alpha - m2\pi/l)nl} \\ -\sum_{n=-\infty}^{\infty} \breve{F}_{n,2} e^{i(\alpha - m2\pi/l)nl} \end{bmatrix} \right).$$

The statement $\exp(i\alpha nl + i2\pi mn) = \exp(i\alpha nl)$ can be used to suppress the m-dependence of the sum. In the second step, sum over all m's and then let $m = n$,

$$\begin{bmatrix} \sum_{n=-\infty}^{\infty} \tilde{w}_1(\alpha - n2\pi/l) \\ \sum_{n=-\infty}^{\infty} \tilde{w}_2(\alpha - n2\pi/l) \end{bmatrix} = \begin{bmatrix} P_1 \\ P_2 \end{bmatrix}$$

$$- \begin{bmatrix} Y_{11} & Y_{12} \\ Y_{21} & Y_{22} \end{bmatrix} \begin{bmatrix} \sum_{n=-\infty}^{\infty} \breve{F}_{n,1} e^{i\alpha nl} \\ -\sum_{n=-\infty}^{\infty} \breve{F}_{n,2} e^{i\alpha nl} \end{bmatrix} \tag{A4}$$

where the matrixes of (A1–A2) are used. Solve for two of the infinite sums using (23–24) in (A4), which yields four unknowns and four equations. The summed displacement is solved for, giving two remaining equations for the summed forces

$$\left(1 + Y_{11} \frac{G}{l} \right) \sum_{n=-\infty}^{\infty} \breve{F}_{n,1} e^{i\alpha nl}$$

$$= \frac{G}{l} P_1 + \left(Y_{12} \frac{G}{l} + 1 \right) \sum_{n=-\infty}^{\infty} \breve{F}_{n,2} e^{i\alpha nl} \tag{A5}$$

$$\left(1 + Y_{21} \frac{G}{l} \right) \sum_{n=-\infty}^{\infty} \breve{F}_{n,1} e^{i\alpha nl}$$

$$= \frac{G}{l} P_2 + \left(Y_{22} \frac{G}{l} + 1 \right) \sum_{n=-\infty}^{\infty} \breve{F}_{n,2} e^{i\alpha nl} \tag{A6}$$

Solving for the summed forces yields

$$\sum_{n=-\infty}^{\infty} \breve{F}_{n,2} e^{i\alpha nl} = \left(\frac{GP_2}{l + Y_{21}G} - \frac{GP_1}{l + Y_{11}G} \right)$$

$$\times \left(\frac{Y_{12}G + l}{l + Y_{11}G} - \frac{Y_{22}G + l}{l + Y_{21}G} \right)^{-1} \quad \text{(A7)}$$

$$\sum_{n=-\infty}^{\infty} \breve{F}_{n,1} e^{i\alpha nl} = \left(\frac{GP_1}{l + Y_{12}G} - \frac{GP_2}{l + Y_{22}G} \right)$$

$$\times \left(\frac{Y_{11}G + l}{l + Y_{12}G} - \frac{Y_{21}G + l}{l + Y_{22}G} \right)^{-1} \quad \text{(A8)}$$

The expressions to be used for a partly filled cavity, discussed in section 3.4, is now to be found. The relation between the plates can be expressed in transfer matrix form as

$$\begin{bmatrix} \tilde{p}_c(\alpha, \beta, 0) \\ \tilde{w}_1(\alpha, \beta) \end{bmatrix} = \begin{bmatrix} T_{11} & T_{12} \\ T_{21} & T_{22} \end{bmatrix} \begin{bmatrix} \tilde{p}_c(\alpha, \beta, d) \\ \tilde{w}_2(\alpha, \beta) \end{bmatrix} \quad \text{(A9)}$$

The total transfer matrix $\mathbf{T}$ is found by multiplying the transfer matrices of the two parts. The result reads

$$T_{11} = \cos(kd_{air}) \cos(k_{\min} d_{\min})$$
$$\qquad - \sin(kd_{air}) \sin(k_{\min} d_{\min}) \rho c / z_{\min}, \quad \text{(A10)}$$

$$T_{12} = - \cos(kd_{air}) \sin(k_{\min} d_{\min}) \omega z_{\min}$$
$$\qquad - \sin(kd_{air}) \cos(k_{\min} d_{\min}) \rho c \omega, \quad \text{(A11)}$$

$$T_{21} = \sin(kd_{air}) \cos(k_{\min} d_{\min}) / (\rho c \omega)$$
$$\qquad - \cos(kd_{air}) \sin(k_{\min} d_{\min}) / (z_{\min} \omega), \quad \text{(A12)}$$

$$T_{22} = - \sin(kd_{air}) \sin(k_{\min} d_{\min}) z_{\min} / (\rho c)$$
$$\qquad + \cos(kd_{air}) \cos(k_{\min} d_{\min}), \quad \text{(A13)}$$

where J_{11}, J_{12}, J_{21} and J_{22} in equation (20) can be identified respectively, as

$$J_{11} = \frac{T_{11}}{T_{21}}, \ J_{12} = \frac{1}{T_{21}}, \ J_{21} = \frac{1}{T_{21}}, \ J_{22} = \frac{T_{22}}{T_{21}}. \quad \text{(A14)}$$

References

[1] J. Brunskog, P. Hammer: The interaction between the ISO tapping machine and lightweight floors. Acustica / acta acustica **accepted**.

[2] P. Hammer: Impact sound transmission of wooden-joist floor. TVBA 3077, Engineering Acoustics, LTH, Lund University, Box 118, SE-221 00 Lund, Sweden, 1994.

[3] S. Lindblad: Impact sound characteristics of resilient floor coverings. a study on linear and nonlinear dissipative compliance. Dissertation. Division of Building Technology, Lund Institute of Technology, Lund, Sweden, 1968.

[4] ISO 140-6: – Acoustics – Measurement of sound insulation in buildings and building elements – part 6: Laboratory measurments of impact sound insulation of floors.

[5] L. Cremer, M. Heckl, E. E. Ungar: Structure-borne sound. Springer-Verlag, Berlin, 1988.

[6] I. L. Vér: Impact noise isolation of composite floors. J. Acoust. Soc. Am. **50** (1971) 1043–1050.

[7] J. Brunskog, P. Hammer: Prediction of impact sound on light weight floor structures. Proceedings of Inter-Noise 97, Budapest, Hungary, 1997. 751–754.

[8] J. Brunskog, P. Hammer: On sound transmission trough point excited light weight periodic structures. Proceedings of Inter-Noise 98, Christchurch, New Zealand, 1998.

[9] G. F. Lin, J. M. Garrelick: Sound transmission through periodically framed parallel plates. J. Acoust. Soc. Am. **61** (1977) 1014–1018.

[10] E. Gerretsen: Calculation of airborne and impact sound insulation between dwellings. Applied Acoustics **19** (1986) 245–264.

[11] V. N. Evseev: Sound radiaton from an infinite plate with periodic inhomogeneities. Soviet physics – Acoustics **19** (1973) 345–351.

[12] M. L. Rumerman: Vibration and wave propagation in ribbed plates. J. Acoust. Soc. Am. **57** (1975) 370–373.

[13] B. R. Mace: Sound radiate from a plate reinforecd by two sets of parallel stiffeners. J. of Sound and Vibration **71** (1980) 435–441.

[14] B. R. Mace: Periodically stiffened fluid-loaded plates, I: Responce to convected harmonic pressure and free wave propagation. J. of Sound and Vibration **73** (1980) 473–486.

[15] B. R. Mace: Periodically stiffened fluid-loaded plates, II: Responce to line and point forces. J. of Sound and Vibration **73** (1980) 487–504.

[16] B. R. Mace: Sound radiation from fluid loaded orthogonally stiffened plates. J. of Sound and Vibration **79** (1981) 439–452.

[17] B. R. Mace: The vibration of plates on two-dimensionally periodic point supports. J. of Sound and Vibration **192** (1995) 629–643.

[18] D. Takahashi: Sound radiated from periodically connected double-plate structures. J. of Sound and Vibration **90** (1983) 541–557.

[19] E. A. Skelton: Acoustic scattering by parallel plates with periodic connectors. Proc. R. Soc. Lond. A **427** (1990) 419–444.

[20] I. A. Urusovskii: Sound transmission through two periodically framed parallel plates. Sov. Phys. Acoust. **38** (1992) 411–413.

[21] J. Brunskog, P. Hammer: Prediction models of impact sound insulation on timber floor structures; a literature survay. J. of Building Acoustics **7** (2000) 89–112.

[22] K. Bodlund: Ljudisolering i ombyggnadsprojekt med träbjälklag. BFR R54:1987, Byggforskningsrådet, Sweden, 1987.

[23] P. M. Morse, H. Feshbach: Methods of theoretical physics, part I. McGraw-Hill Book Company, Inc., New York, 1953.

[24] M. E. Delaney, E. N. Bazely: Acoustical properties of fibrous absorbent materials. Applied Acoustics **3** (1970) 105–116.

[25] F. P. Mechel: Ausweitung der Absorberformel von Delaney und Bazley zu tiefen Frequenzen. Acustica **35** (1976) 210–213.

[26] MATLAB Reference guide. The MathWorks, Inc., 1992.

[27] J. Brunskog, P. Hammer: Rigid indenter excitation of plates. Acustica / acta acustica **submitted**.

[28] H. Kuttruff: Room acoustics. Elsevier applied science, London, 1973, Third edition 1991.

[29] M. R. Schroeder: Statistical parameters of the frequency response curves of large rooms. Journal of the Audio Engineering Society (Originally published in Acustica, 4, pp 594–600, 1954) **35** (1987) 299–305.

The influence of finite cavities in sound insulation of double-plate structures

Jonas Brunskog

Division of Engineering Acoustics, LTH, Lund University, P.O. Box 118, SE-221 00 Lund, Sweden
E-mail: jonas.brunskog@acoustics.lth.se

Summary

Lightweight walls are often designed as frameworks of studs with plates on each side – a double-plate structure. The studs constitute boundaries for the cavities, thereby both affecting the sound transmission directly by short-cutting the plates, and indirectly by disturbing the sound field between the plates. The paper presents a deterministic prediction model for airborne sound insulation including both effects of the studs. A spatial transform technique is used, taking advantage of the periodicity. The acoustic field inside the cavities is expanded by means of cosine-series. The transmission coefficient (angle-dependent and diffuse) and transmission loss are studied. Numerical examples are presented and comparisons with measurement are performed. The result indicates that a reasonably good agreement between theory and measurement can be achieved.

PACS no. 43.40.Dx, 43.55.Ti, 43.20.Tb

1. Introduction

New building systems are often designed as lightweight systems. One advantage of these systems is the possibility they provide of lowering house production costs. The interest in such lightweight building techniques is therefore large. Acoustically there are both advantages and disadvantages with such structures. One of the advantages is that a wall consisting of two plates – a double-plate structure – provides good insulation against airborne noise in relation to its weight. There is, however, no theoretical prediction model for sound-insulation that takes into account all important aspects of such a wall system.

If a double-plate structure consists of a framework of studs, the studs will not only influence the vibration field directly, i.e., short-cutting the plates as sound bridges [1, pp. 462–474], but also affect the acoustic field in the cavities. The studs can be seen as walls in the cavities, thus introducing finiteness, which leads to resonance. Consider therefore a double-leaf structure excited by an incoming wave on the source side. The plate on the source side is excited and will radiate to the cavities and excite the framing beams. The plate on the receiver side is then excited by the acoustic field in the cavities and by the vibration of the beams, and will radiate to the surrounding acoustic fields.

In building acoustics it is common to use Statistical Energy Analysis (SEA), different power-flow methods such as those associated with the new European standard for computing building acoustics (EN 12354 [2]), or various semi-empirical methods to find prediction models. Such approaches are often preferable when details of a standard type of construction are considered, for example, when well-known elements are combined in EN 12354, or when large variations in the material or geometric data affect the results very little. An approach of this type is basically pragmatic, emphasis being placed on achieving reason-

able results quickly. The amount of information used to account for the physics involved is minimal, each building element being described by a number (for each frequency); the mean of the sound energy being obtained for each part or component of the structure separately. The fact that only a minimal amount of information is utilized here represents both an advantage and a disadvantage. These approaches are particularly appropriate for dealing with homogeneous and clearly distinguishable building elements, such as in traditional building construction systems in which the elements are heavy and homogeneous. Such approaches are not likely to be successful, however, if one's interest is in discovering new types of solutions, since the lack of the information needed makes it impossible to describe the physics of the situation adequately. Moreover, wood frame building elements (or other stud-plate building elements) may not be considered as homogeneous and isotropic. Hence, they do not meet the basic requirements for simplified prediction models (such as EN and basic SEA models) where it is assumed that all building elements can be considered to be a single subsystem. This has also been observed in measurements [3]. For studies of SEA applied to sound insulation with double wall systems, Craik [4] and Craik and Smith [5] are examples. As an example of semi-empirical prediction models, the model described by Sharp [6] should be mentioned.

Instead, an analytical/deterministic approach is used in the present paper. The approach is largely based on the following papers. The classical work on double-leaf walls is made by London [7]. This work, however, does not take into account the studs or the finiteness of the cavities. Cremer et al. [1, pp. 450–462] describe two parallel plates connected via a locally reacting stiffness layer. A resent similar study by Kropp and Rebillard [8], treats airborne sound insulation of double-wall constructions without studs. The focus is on the possibility of optimizing the sound insulation. Lin and Garrelick [9] investigated

the transmission of a plane wave through two infinite parallel plates connected by periodical studs that behave as rigid bodies. A fluid coupling in the cavities between the plates was also present, which let the waves pass unaffected through the beams. The two systems were solved simultaneously by means of Fourier transforms and periodic considerations. Recent measurements on wood stud walls, made by Bradley and Birta [10], show that the Lin and Garrelick theory explains the most important low-frequency features of sound transmission through these wood stud walls. Rumerman [11] and Mace [12] treated a single infinite plate reinforced by beams and excited by a convected pressure (that could be a incoming plane wave) using Fourier transforms. Takahashi [13] considered noise control in buildings having double-plate walls. Each structure considered consisted of two parallel plates of infinite extent connected by various connectors. The connectors were point connectors or rib-stiffeners, and the sound field in the cavity passed unaffected through them. The structures were driven by point forces, and the resulting sound radiation was studied. The problem of acoustic reflection of a double-plate system with periodic connectors were studied by Skelton [14], who also assumed the connectors to be invisible to the fluid in the cavity. The connectors were applied in form of longitudinal plate waveguides. The related problem of acoustic reflection of a plate with periodic ribs and a back cavity was studied by Sakagami et al. [15]. Also here the ribs were acoustically transparent so that the sound field in the back cavity was not influenced by them. The only paper found that takes account of the influence of ribs or connectors on the cavity field is Skelton [16], who considered the effect of a single connector, rigid with respect to the fluid, using the Wiener-Hopf technique. Also Urusovskii [17] studied a periodic double plate system, but used a space-harmonic assumption and truncated the infinite system of equation that arose. The cavity field was unaffected by the beams. The present author and Hammer have studied impact sound transmissions in lightweight floors using transform technique [18], including the beams and a cavity, but letting the waves go unaffected through the beams (as in [9, 13, 14, 17, 15]). A literature survey of available deterministic prediction methods that takes periodicity into account can be found in [19] (with focus on point excitation).

The approach in the present paper is similar to the one introduced by Rumerman [11] and Mace [12], but the treatment of the cavities is original for the present paper. An expansion in a suitable orthogonal series is made for the cavity field in order to take into account the finiteness of the cavities. The paper is comprised as follows: Following the introduction, the problem under consideration is formulated. In section 3, the cavity reactions and field are studied, and the remaining reaction forces are collected in the section 4. In section 5, the solution is described. Sound radiation and sound insulation are considered in section 6. The numerical results are presented and discussed in section 7, and the paper ends with some concluding remarks.
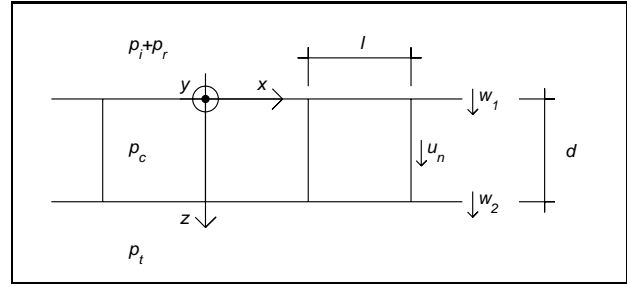
Figure 1. A double leaf structure.

2.   Formulation of the problem

Consider a double-leaf wall stiffened with studs, as in Figure 1. The studs are assumed to be infinitely stiff in bending round the z-axis and of zero thickness. However, they are allowed to bend round the x-axis. The structure is infinite in both the x- and y-direction. The studs are located periodically with equal distance l between them. The studs are assumed to not cause any moment reactions or coupling; the connection plate-stud is assumed to be in form of a pin-joint. The displacement of the plates are denoted w_1 and w_2, and the displacement of the n'th beam is denoted u_n.

In the field in front of the first plate a pressure p_i due to an incident wave, and a reaction pressure p_r due to radiated waves is present. In the field backing the second plate a reaction pressure p_t is present due to transmitted waves. The incident pressure is of the form

$$p_i = \hat{p}_i \mathrm{e}^{-\mathrm{i}(k_x x + k_y y + k_z z - \omega t)} \tag{1}$$

where a possible choice of the wave numbers are

$$k_x = k \sin\theta \cos\varphi, \ \ k_z = k \sin\theta \sin\varphi, \ \ k_y = k \cos\theta$$

i.e., an incoming wave with wavenumber $k = \omega/c$. The time dependence and the z-dependence, $\exp(\mathrm{i}wt - \mathrm{i}k_z z)$, will henceforth be suppressed throughout. Further, since the structure is periodic in x the response satisfies the periodicity relation, see e.g. [12] or [19],

$$w_i(x + l) = w_i(x)\mathrm{e}^{-\mathrm{i}k_x l} \tag{2}$$

usually denoted as Floquet's principle.

2.1.   Governing equations

The system of governing equations that is to be solved can be written as

$$D_1' \nabla^4 w_1 - m_1'' \omega^2 w_1 = p_i|_{y=0} - p_c|_{y=0} + p_r|_{y=0} - p_{f1} \tag{3}$$
$$D_2' \nabla^4 w_2 - m_2'' \omega^2 w_2 = p_c|_{y=d} - p_t|_{y=d} + p_{f2} \tag{4}$$

for the first and the second plate respectively, where

$$\nabla^4 = \frac{\partial^4}{\partial x^4} - 2k_z^2 \frac{\partial^2}{\partial x^2} + k_z^4$$
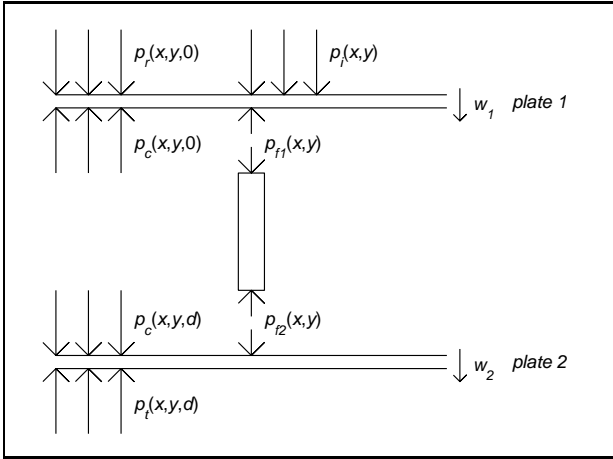
Figure 2. Model for the equation of motion.

and D_i' and m_i'' are the flexural rigidity and mass per unit area of plate number i respectively, $\omega = 2\pi f$ is the angular frequency and d the distance between the plates. It is convenient to decompose the reflected pressure into two components, $p_r = p_g + p_s$, where p_g is the reflected pressure generated by a rigid reflector (geometrical reflection), so that

$$p_g|_{y=0} = p_i|_{y=0}, \tag{5}$$

and p_s is the scattered part due to the elastic motion of the structure. Figure 2 shows the different reaction fields. The reaction pressures from the surrounding fluid can be assumed to be coupled to the displacements field by operators,

$$p_s|_{y=0} = \mathcal{R} w_1 \tag{6}$$

$$p_t|_{y=0} = \mathcal{T} w_2 \tag{7}$$

where $\mathcal{R}$ and $\mathcal{T}$ are linear operators that will be determined in section 4. The cavity pressure p_c and frame pressure p_f are treated in separate sections, due to their complexity.

2.2. Transformed equations

The Fourier transform of the displacement w_i with respect to the co-ordinate x and the corresponding inverse transform is defined as

$$\tilde{w}_i(\alpha) = \int_{-\infty}^{\infty} w_i(x) e^{i\alpha x} dx \tag{8}$$

$$w_i(x) = \frac{1}{2\pi} \int_{-\infty}^{\infty} \tilde{w}_i(\alpha) e^{-i\alpha x} d\alpha \tag{9}$$

Thus, the Fourier transform over x of the incoming wave yields a Dirac function, $\tilde{p}_i = 2\pi \hat{p}_i \delta(\alpha - k_x)$. For the re-

action pressure, the transform yields algebraic expressions instead of operators. Thus, the transformed pressures are

$$(\tilde{p}_i + \tilde{p}_g)|_{y=0} = 4\pi \hat{p}_i \delta(\alpha - k_x) e^{-ik_z y},$$
$$\tilde{p}_s|_{y=0} = R\tilde{w}_1,$$
$$\tilde{p}_t|_{y=0} = T\tilde{w}_2,$$

where R and T are the transformed version of the operators $\mathcal{R}$ and $\mathcal{T}$. Applying the Fourier transform with respect to x to equations (3–4), taking into account (6–7), gives

$$\begin{bmatrix} S_1 & 0 \\ 0 & S_2 \end{bmatrix} \begin{bmatrix} \tilde{w}_1 \\ -\tilde{w}_2 \end{bmatrix} \tag{10}$$

$$= 4\pi \begin{bmatrix} \hat{p}_i \\ 0 \end{bmatrix} \delta(\alpha - k_x) - \begin{bmatrix} \tilde{p}_{f1} \\ \tilde{p}_{f2} \end{bmatrix} - \begin{bmatrix} \tilde{p}_c|_o \\ \tilde{p}_c|_d \end{bmatrix}$$

where

$$S_1(\alpha) = D_1' \left(\alpha^2 + k_z^2\right)^2 - m_1'' \omega^2 - R(\alpha), \tag{11}$$

$$S_2(\alpha) = D_2' \left(\alpha^2 + k_z^2\right)^2 - m_2'' \omega^2 + T(\alpha), \tag{12}$$

are spatial stiffnesses. The solution of equation (10) and its inverse transform is given in section 5. It is, however, first necessary to give expressions for the reaction pressures.

3. The cavity

The reaction pressures due to the cavity field are examined in this section.

3.1. The cavity, a parallelepipedic space

Consider ones more Figure 1, where a fluid is occupying the space $0 < y < d$, divided into subspaces $nl \leq x \leq (n+1)l$. An acoustic pressure $p_c(x,y,z)$ is present in the fluid. The acoustic pressure satisfies the Helmholtz equation

$$\left(\frac{\partial^2}{\partial x^2} + \frac{\partial^2}{\partial y^2}\right) p_c + \left(k_c^2 - k_z^2\right) p_c = 0 \tag{13}$$

where $k_c = \omega/c_c$ is the wavenumber in the cavity (possibly different from k, the wave number in the surrounding fluid) and c_c is the speed of sound in the medium. The acoustic pressure also satisfies the boundary conditions

$$\left[\frac{\partial p_c}{\partial y}\right]_{z=0} = \omega^2 \rho_c w_1, \tag{14}$$

$$\left[\frac{\partial p_c}{\partial y}\right]_{z=d} = \omega^2 \rho_c w_2 \tag{15}$$

where ρ_c is the density of the fluid. Equation (14) ensures equality of the fluid velocity at the plate surface and the plate velocity. These boundary conditions are the ones that are fulfilled in the papers [9, 13, 16, 17, 18]. In the present paper a new set of boundary conditions is also to be fulfilled, namely

$$\left[\frac{\partial p_c}{\partial x}\right]_{x=nl} = 0, \tag{16}$$

$$n = 0, \pm 1, \pm 2, \cdots, \pm\infty$$

ensuring absence of displacement at the rigid walls at $x = nl$. Divide the field into subfields corresponding to the cavities

$$p_c(x, y) = \sum_{m=-\infty}^{\infty} p_c^{(m)}(x, y)\Theta(x, ml, ml + l) \quad (17)$$

where

$$\Theta(x, ml, ml + l) \equiv \theta(x - ml) - \theta(x - (m+1)l)$$

and where $\theta(x)$ is Heaviside's step function and $\Theta(x, a, b)$ is the 'hat' function that equals unity between a and b and are zero otherwise. Assume that the pressure field in the m'th cavity can be written as an orthogonal sum of cosine functions in the x-direction. Define ε_n,

$$\varepsilon_n \equiv \begin{cases} \frac{1}{2} & \text{if } n = 0 \\ 1 & \text{if } n \neq 0 \end{cases}$$

Thus, the cosine expansion can be written

$$p_c^{(m)}(x, y) = \sum_{n=0}^{\infty} \varepsilon_n p_{c,n}^{(m)}(y) \, \cos(n\pi x/l) \qquad (18)$$

where $ml \leq x \leq (m+1)l$. It is easily shown that this assumption fulfils the boundary conditions (14–15) and (16), as well as the Helmholtz equation (13). The periodicity , expressed in (2), is now to be taken into account. This implies that the pressure acting on two neighbouring bays is related to each other though a phase difference

$$p_c^{(m+1)} = p_c^{(m)} \mathrm{e}^{-ik_x l}$$

and especially

$$p_c^{(m)} = p_c^{(0)} \mathrm{e}^{-ik_x ml}$$

Hence, equation (17) reduces to

$$p_c(x, y) = p_c^{(0)}(x, y) \sum_{m=-\infty}^{\infty} \Theta(x, ml, ml + l)\mathrm{e}^{-ik_x ml} \quad (19)$$

Thus, the total field in the cavities is determined by the field in the 0'th cavity. Expressing this field in terms of a cosine series, equation (18), and inserting in (19), yields

$$p_c(x, y) = \sum_{n=0}^{\infty} \varepsilon_n p_{c,n}^{(0)}(y) \cos(n\pi x/l) \qquad (20)$$
$$\times \sum_{m=-\infty}^{\infty} \Theta(x, ml, ml + l)\mathrm{e}^{-ik_x ml}$$

Hence, the two sums are separated. The spatial Fourier transform of the cavity reaction pressure formally is

$$\tilde{p}_c(\alpha, y) = \int_{-\infty}^{\infty} \sum_{n=0}^{\infty} \varepsilon_n p_{c,n}^{(0)} \cos(n\pi x/l) \qquad (21)$$

$$\times \sum_{m=-\infty}^{\infty} \Theta(x, ml, ml + l) \, \mathrm{e}^{-ik_x ml}\mathrm{e}^{i\alpha x}\mathrm{d}x$$

and will be further treated in section 3.4.

3.2. The field in the 0'th cavity

The cosine expansion (18) is inserted into the Helmholtz equation (13). It can be shown that this expression reduces to

$$\frac{\partial^2 p_{c,n}^{(0)}(y)}{\partial y^2} + \left(k_c^2 - \left(\frac{n\pi}{l}\right)^2 - k_z^2\right)p_{c,0}^{(0)}(y) = 0,$$
$$n = 0, \, 1, \, 2, \, \cdots \qquad (22)$$

Define a propagation number for the n'th component

$$\gamma_n^2 \equiv \left(\frac{n\pi}{l}\right)^2 + k_z^2 - k_c^2$$

The solution can be written as one wave in the positive z-direction and one in the negative z-direction,

$$p_{c,n}^{(0)}(y) = \hat{p}_{c,n+}\mathrm{e}^{-\gamma_n y} + \hat{p}_{c,n-}\mathrm{e}^{\gamma_n y} \qquad (23)$$

and one derivation with respect of y gives

$$\frac{\partial p_{c,n}^{(0)}(y)}{\partial y} = \gamma_n\left(-\hat{p}_{c,n+}\mathrm{e}^{-\gamma_n y} + \hat{p}_{c,n-}\mathrm{e}^{\gamma_n y}\right) \quad (24)$$

The remaining boundaries are now expanded into cosine series

$$w_i(x) = \sum_{n=0}^{\infty} \varepsilon_n w_{i,n} \cos(n\pi x/l), \qquad (25)$$

where

$$w_{i,n} = \frac{2}{l}\int_0^l w_i(x)\cos(n\pi x/l)\mathrm{d}x. \qquad (26)$$

The boundary conditions (14–15) have to be fulfilled by every Fourier component, connecting $p_{c,n}^{(0)}$ to $w_{i,n}$,

$$\left.\frac{\partial p_{c,n}^{(0)}}{\partial y}\right|_{y=0} = \omega^2\rho_c w_{1,n}, \quad \left.\frac{\partial p_{c,n}^{(0)}}{\partial y}\right|_{y=d} = \omega^2\rho_c w_{2,n}$$

Taking into account the standing wave and its derivatives (23–24) gives a system of equations, which yields the following amplitudes of the components in the standing wave,

$$\hat{p}_{c+} = \frac{\omega^2\rho_c}{\gamma_n}\frac{\left(w_{2,n} - w_{1,n}e^{\gamma_n d}\right)}{2\sinh(\gamma_n d)}, \qquad (27)$$

$$\hat{p}_{c-} = \frac{\omega^2\rho_c}{\gamma_n}\frac{\left(w_{2,n} - w_{1,n}e^{-\gamma_n d}\right)}{2\sinh(\gamma_n d)} \qquad (28)$$

Insert (27–28) in (23)

$$p_{c,n}^{(0)}(y) = \frac{\omega^2\rho_c}{\sinh(\gamma_n d)\gamma_n} \qquad (29)$$

$$\times \; (w_{2,n} \cosh(\gamma_n y) - w_{1,n} \cosh(\gamma_n (d-y)))$$

Putting $y = 0$ and $y = d$ respectively, and rewriting in a matrix form yields

$$\begin{bmatrix} p_{c,n}^{(0)}(0) \\ p_{c,n}^{(0)}(d) \end{bmatrix} = \frac{\omega^2 \rho_c}{\gamma_n \sinh \gamma_n d} \quad (30)$$

$$\times \; \begin{bmatrix} \cosh(\gamma_n d) & 1 \\ 1 & \cosh(\gamma_n d) \end{bmatrix} \begin{bmatrix} w_{1,n} \\ -w_{2,n} \end{bmatrix}.$$

3.3. Solution of the cavity pressure field

The cavity reaction pressures used in (3–4) can then be expressed as, if (30) is inserted in (20),

$$\begin{bmatrix} p_c(x,0) \\ p_c(x,d) \end{bmatrix} = \left(\sum_{n=0}^{\infty} \varepsilon_n \mathbf{J}_n \begin{bmatrix} w_{1,n} \\ -w_{2,n} \end{bmatrix} \cos(n\pi x/l) \right) \quad (31)$$

$$\times \; \sum_{m=-\infty}^{\infty} \Theta(x, ml, ml+l) \, e^{-ik_x ml}$$

where the following definition $\mathbf{J}_n$ of the matrix in equation (30) has been introduced,

$$\mathbf{J}_n \equiv \frac{\omega^2 \rho_c}{\gamma_n \sinh(\gamma_n d)} \begin{bmatrix} \cosh(\gamma_n d) & 1 \\ 1 & \cosh(\gamma_n d) \end{bmatrix}.$$

The displacement field in the plates is unknown, and needs to be solved for. The components $w_{i,n}$ are expressed as integrals in equation (26).

3.4. Fourier transform of the cavity pressure

The spatial Fourier transform of the cavity reaction pressure is formally given in equation (21). Define a help function

$$\Phi_n(\alpha) \quad (32)$$

$$\equiv \mathcal{F}_x \left\{ \cos\left(\frac{n\pi x}{l}\right) \sum_{m=-\infty}^{\infty} \Theta(x, ml, ml+l) e^{-ik_x ml} \right\}$$

Then, the transformed cavity pressures at the boundaries are

$$\begin{bmatrix} \tilde{p}_c(\alpha,0) \\ \tilde{p}_c(\alpha,d) \end{bmatrix} = \sum_{n=0}^{\infty} \begin{bmatrix} J_{11,n} & J_{12,n} \\ J_{21,n} & J_{22,n} \end{bmatrix} \begin{bmatrix} w_{1,n} \\ -w_{2,n} \end{bmatrix} \varepsilon_n \Phi_n(\alpha) \quad (33)$$

where $J_{11,n}$ et cetera are the components of $\mathbf{J}_n$. A more suitable form of the function $\Phi_n(\alpha)$ is needed. Some manipulations, including use of the Poisson sum formula, yields

$$\Phi_n(\alpha) = \frac{i\pi}{l} \frac{1 - e^{i\alpha l} e^{-in\pi}}{\alpha - n\pi/l} \sum_{m=-\infty}^{\infty} \delta(\alpha - k_x + (n-2m)\pi/l)$$

$$+ \frac{i\pi}{l} \frac{1 - e^{i\alpha l} e^{in\pi}}{\alpha + n\pi/l} \sum_{m=-\infty}^{\infty} \delta(\alpha - k_x - (n+2m)\pi/l). \quad (34)$$

For details see the appendix. Moreover, due to the infinite sums, we have

$$\sum_{m=-\infty}^{\infty} \delta(\alpha - k_x + (\pm n - 2m)\pi/l)$$

$$= \sum_{m=-\infty}^{\infty} \delta(\alpha - k_x - 2m\pi/l).$$

Thus, we can rewrite (34)

$$\Phi_n(\alpha) = \frac{2\pi}{l} \varsigma_n(\alpha) \sum_{m=-\infty}^{\infty} \delta(\alpha - k_x - 2m\pi/l) \quad (35)$$

where

$$\varsigma_n(\alpha) \equiv i\alpha \frac{1 - e^{i\alpha l}(-1)^n}{\alpha^2 - (n\pi/l)^2} \quad (36)$$

Combining equations (33) and (35) yields the transformed cavity reaction pressures

$$\begin{bmatrix} \tilde{p}_c(\alpha,0) \\ \tilde{p}_c(\alpha,d) \end{bmatrix} = \frac{2\pi}{l} \sum_{n=0}^{\infty} \begin{bmatrix} J_{11,n} & J_{12,n} \\ J_{21,n} & J_{22,n} \end{bmatrix} \begin{bmatrix} w_{1,n} \\ -w_{2,n} \end{bmatrix} \varepsilon_n \varsigma_n(\alpha)$$

$$\times \; \sum_{m=-\infty}^{\infty} \delta(\alpha - k_x - 2m\pi/l). \quad (37)$$

3.5. Pressure and displacement field in the cavity

The field inside a cavity is of interest. It is only necessary to consider the 0'th cavity due to the periodic relation (2). The pressure field in the 0'th cavity is given in (18) where index $m = 0$ is to be used, and $p_{c,n}^{(0)}$ is given in equation (29). The corresponding displacement field in the cavity is

$$w_{c,x}^{(0)} = \frac{1}{\rho \omega^2} \frac{\partial p_c^{(0)}}{\partial x}, \quad w_{c,y}^{(0)} = \frac{1}{\rho \omega^2} \frac{\partial p_c^{(0)}}{\partial y}$$

for displacement in the x- and y-direction respectively. Derivation of equation (18) yields

$$w_{c,x}^{(0)} = - \sum_{n=0}^{\infty} \varepsilon_n \frac{n\pi}{l\gamma_n} \frac{\omega^2 \rho_c}{\sinh(\gamma_n d)} \sin(n\pi x/l) \quad (38)$$

$$\times \; (w_{2,n} \cosh(\gamma_n y) - w_{1,n} \cosh(\gamma_n (d-y)))$$

$$w_{c,y}^{(0)} = \sum_{n=0}^{\infty} \varepsilon_n \frac{\omega^2 \rho_c}{\sinh(\gamma_n d)} \cos(n\pi x/l) \quad (39)$$

$$\times \; (w_{2,n} \sinh(\gamma_n y) + w_{1,n} \sinh(\gamma_n (d-y)))$$

for the x- and y-direction respectively.

4. The remaining reaction forces

In order to get a complete solution, the forces and pressures involved must be specified.
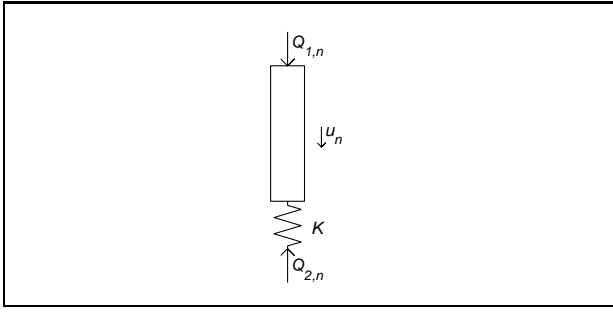
Figure 3. The n'th beam.
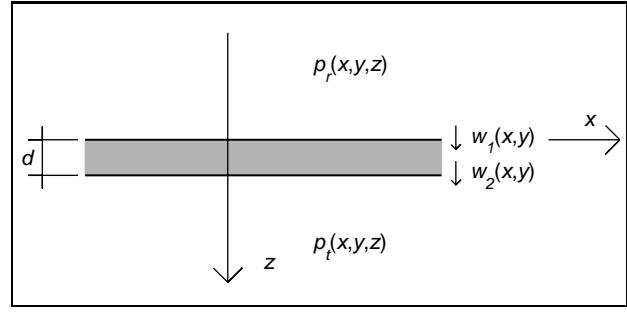
Figure 4. The acoustic pressure.

4.1.   The frame reactions

The continuity equation at each plate-beam connection point is assumed to be spring-like and takes the following form, if the displacement of the n'th beam equals the displacement of the first plate, $u_n(z) = w_1(nl, 0, z)$, and

$$Q_{1,n}(z) - Q_{2,n}(z) = \mathcal{G} w_1(nl, 0, z) \qquad (40)$$

$$Q_{2,n}(z) = K(w_1(nl, 0, z) - w_2(nl, 0, z)) \quad (41)$$

where $n = -\infty, \cdots, \infty$, and where $\mathcal{G}$ is a linear operator, K is a stiffness and $Q_{i,n}$ are line forces. For the n'th beam,

$$\begin{bmatrix} Q_{1,n}(z) \\ Q_{2,n}(z) \end{bmatrix} = \begin{bmatrix} \mathcal{G} + K & K \\ K & K \end{bmatrix} \begin{bmatrix} w_1(nl, 0, z) \\ -w_2(nl, 0, z) \end{bmatrix} (42)$$

The linear operator corresponding to a Euler beam is

$$\mathcal{G} = E_f I_f \frac{d^4}{dz^4} - \rho_f A_f \omega^2 \qquad (43)$$

where $E_f I_f$ is the bending rigidity and $\rho_f A_f$ is mass per unit length of the frame. The y-deviates will be replaced by k_y^4 due to the assumed $e^{-ik_y y}$ dependency in (1). Thus, the algebraic expression for transformed operator G is found,

$$G = E_f I_f k_z^4 - \rho_f A_f \omega^2 \qquad (44)$$

The frame reaction pressure is

$$p_{fi} = \sum_{m=-\infty}^{\infty} Q_{i,n} \delta(x - ml), \qquad (45)$$

for $i = 1, 2$. The displacement fields w_1 and w_2 satisfy the periodicity relation (2) since the structure and driving are periodic. Therefore

$$w_i(nl) = w_i(0) e^{-ink_x l}, \qquad (46)$$

for $i = 1, 2$. Therefore, using (40–41) and (46), the reaction fields caused by the beams, used in (3–4), can be written

$$\begin{bmatrix} p_{f1} \\ p_{f2} \end{bmatrix} = \begin{bmatrix} G + K & K \\ K & K \end{bmatrix} \begin{bmatrix} w_1(0, 0, z) \\ -w_2(0, d, z) \end{bmatrix} \qquad (47)$$
$$\times \sum_{m=-\infty}^{\infty} e^{-imk_x l} \delta(x - ml)$$

Fourier transform equation (47), and make use of the Poisson sum formula (A7–A8),

$$\begin{bmatrix} \tilde{p}_{f1} \\ \tilde{p}_{f2} \end{bmatrix} = \frac{2\pi}{l} \begin{bmatrix} G + K & K \\ K & K \end{bmatrix} \begin{bmatrix} w_1(0, 0, z) \\ -w_2(0, d, z) \end{bmatrix} \quad (48)$$
$$\times \sum_{m=-\infty}^{\infty} \delta(\alpha - 2m\pi/l - k_x)$$

4.2.   The reactions from the transmitted and reflected fields

The transformed versions of the operators $\mathcal{R}$ and $\mathcal{T}$ in equations (6–7), denoted R and T respectively, is to be determined. Consider Figure 4, where a fluid is occupying the upper half space with an acoustic pressure $p_s(x, y, z)$, $z \leq 0$, and the lower half space is occupied by a fluid with an acoustic pressure $p_t(x, y, z)$, $z \geq d$. The total pressure field in the incident side is $p_i + p_g + p_s$, as was discussed more closely in section 2. It is assumed that the two fields have the same sound speed c_0 and density ρ_0. Two moving surfaces occupy the x-y-plane in $z = 0$ and $z = d$, vibrating with displacements $w_1(x, y)$ and $w_2(x, y)$. The total acoustic pressure field can be expressed as

$$p(x, y, z) = \begin{cases} p_s(x, y, z) & z \leq 0 \\ p_t(x, y, z) & z \geq d \end{cases} \qquad (49)$$

The acoustic pressure satisfies the Helmholtz equation

$$\left(\frac{\partial^2}{\partial x^2} + \frac{\partial^2}{\partial y^2} - k_z^2 \right) p + \frac{\omega^2}{c_0^2} p = 0 \qquad (50)$$

where c_0 is the speed of sound and ω is the radian frequency, together with the boundary conditions, the same as in (14–15) but with p_s in the former equation and p_t in the latter, ensuring equality of the fluid velocity at the plate surface and the plate velocity. The Helmholtz equation (50) is now transformed, indicating a wave in the z-direction. The solution can be written

$$\tilde{p}(\alpha, y) = \begin{cases} \hat{p}_r e^{\gamma y}, & y < 0 \\ \hat{p}_t e^{-\gamma(y-d)}, & y > d \end{cases} \qquad (51)$$

assuming only outgoing waves, and where

$$\gamma^2 \equiv \alpha^2 + k_z^2 - k_c^2$$

where γ has to be evaluated so that $\Re\{\gamma\} \geq 0$, $\Im\{\gamma\} \geq 0$ if $\Re\{\gamma\} = 0$. Therefore, using the boundary conditions (14–15) together with the derivative of (51), for $z = 0$ and $z = d$, yields the identification of the coefficients,

$$R = -T = \frac{\omega^2 \rho}{\gamma(\alpha)}.$$

5. The inverse transform and the solution of the problem

The solution to the problem can now be found by means of applying the inverse Fourier transform on equation (10), making use of equation (37) and (48). The Dirac functions ensure that the inverse transform can be easily performed, and the displacement field can thus be determined. The displacements are

$$w_1(x) = \frac{2\hat{p}_i e^{-ik_x x}}{S_1(k_x)} \tag{52}$$

$$- \frac{1}{l}((G+K)w_1(0) - Kw_2(0))T_1^{(f)}(x)$$

$$- \frac{1}{l}\sum_{n=0}^{\infty}(J_{11,n}w_{1,n} - J_{12,n}w_{2,n})\varepsilon_n T_{1,n}^{(c)}(x)$$

and

$$w_2(x) = \frac{1}{l}(Kw_1(0) - Kw_2(0))T_2^{(f)}(x) \tag{53}$$

$$+ \frac{1}{l}\sum_{n=0}^{\infty}(J_{21,n}w_{1,n} - J_{22,n}w_{2,n})\varepsilon_n T_{2,n}^{(c)}(x)$$

where the following abbreviations have been used

$$T_j^{(f)}(x) \equiv \sum_{m=-\infty}^{\infty}\frac{e^{-i\alpha_m x}}{S_j(\alpha_m)} \tag{54}$$

$$T_{j,n}^{(c)}(x) \equiv \sum_{m=-\infty}^{\infty}\frac{\varsigma_n(\alpha_m)e^{-i\alpha_m x}}{S_j(\alpha_m)} \tag{55}$$

where $\alpha_m = k_x + 2m\pi/l$ and where $j = 1, 2$. The $w_1(0)$, $w_2(0)$ and the Fourier components are still unknown. To determine them, let $x \to 0$ in (52), for the first plate

$$w_1(0) = \frac{2\hat{p}_i}{S_1(k_x)} - \frac{(G+K)}{l}T_1^{(f)}(0)w_1(0) \tag{56}$$

$$+ \frac{K}{l}T_1^{(f)}(0)w_2(0) - \frac{1}{l}\sum_{n=0}^{\infty}J_{11,n}\varepsilon_n T_{1,n}^{(c)}(0)\,w_{1,n}$$

$$+ \frac{1}{l}\sum_{n=0}^{\infty}J_{12,n}\varepsilon_n T_{1,n}^{(c)}(0)\,w_{2,n}$$

and (53) for the second plate

$$w_2(0) = \frac{KT_2^{(f)}(0)}{l}w_1(0) \tag{57}$$

$$- \frac{KT_2^{(f)}(0)}{l}w_2(0) + \frac{1}{l}\sum_{n=0}^{\infty}J_{21,n}\varepsilon_n T_{2,n}^{(c)}(0)\,w_{1,n}$$

$$- \frac{1}{l}\sum_{n=0}^{\infty}J_{22,n}\varepsilon_n T_{2,n}^{(c)}(0)\,w_{2,n}.$$

Multiply (52–53) by $2/l\cos(s\pi x/l)$ and integrate from 0 to l, s being an integer, in order to identify the Fourier components, for the first plate

$$w_{1,s} = \frac{2}{l}\int_0^l \frac{2\hat{p}_i e^{-ik_x x}\cos(s\pi x/l)\,\mathrm{d}x}{S_1(k_x)} \tag{58}$$

$$- \frac{2(G+K)}{l^2}I_{1,s}^{(f)}w_1(0) + \frac{2K}{l^2}I_{1,s}^{(f)}w_2(0)$$

$$- \frac{2}{l^2}\sum_{n=0}^{\infty}J_{11,n}\varepsilon_n I_{1,s,n}^{(c)}w_{1,n} + \frac{2}{l^2}\sum_{n=0}^{\infty}J_{12,n}\varepsilon_n I_{1,s,n}^{(c)}w_{2,n}$$

and for the second plate

$$w_{2,s} = \frac{2K}{l^2}I_{2,s}^{(f)}w_1(0) - \frac{2K}{l^2}I_{2,s}^{(f)}w_2(0) \tag{59}$$

$$+ \frac{2}{l^2}\sum_{n=0}^{\infty}J_{21,n}\varepsilon_n I_{2,s,n}^{(c)}w_{1,n} - \frac{2}{l^2}\sum_{n=0}^{\infty}J_{22,n}\varepsilon_n I_{2,s,n}^{(c)}w_{2,n}$$

where the following abbreviations have been used,

$$I_{j,s}^{(f)} \equiv \int_0^l \cos(s\pi x/l)T_j^{(f)}(x)\mathrm{d}x \tag{60}$$

$$I_{j,s,n}^{(c)} \equiv \int_0^l \cos(s\pi x/l)T_{j,n}^{(c)}(x)\mathrm{d}x \tag{61}$$

where $i = 1, 2$. The integrals are calculated in the appendix, as well as the integral in the first term in (58). A system of equations can now be set and solved for $w_1(0)$, $w_2(0)$ and the Fourier components, if truncating the cosine expansion to N components. The displacement components to be solved for are arranged in a row vector

$$\mathbf{w} = \begin{bmatrix} w_1(0) & w_2(0) & w_{1,0} & w_{2,0} & ... & w_{1,N} & w_{2,N} \end{bmatrix}^T$$

Defining a matrix $\mathbf{A}$ and a row vector $\mathbf{P}$, se the appendix (A9–A13), and solving for the displacement components $\mathbf{w}$ yields

$$\mathbf{w} = \mathbf{A}^{-1}\mathbf{P} \tag{62}$$

Inserting these components in equation (52–53) gives the displacement of the plates.

The solution can alternatively be written in a space harmonic form,

$$w_2 = \sum_{m=-\infty}^{\infty}W_m e^{-i\alpha_m x} \tag{63}$$

for the second plate (which is of interest in connection to sound transmission), where

$$W_m = \frac{-1}{lS_2(\alpha_m)} \left(Kw_1(0) - Kw_2(0) \right. \tag{64}$$
$$\left. + \sum_{n=0}^{\infty} \left(J_{21,n}w_{1,n} - J_{22,n}w_{2,n} \right) \varepsilon_n \varsigma_n(\alpha_m) \right)$$

6. Exterior fluid fields and radiation

We have so far found expressions for the displacement field of the plates. However, expressions for the reflected and transmitted pressure fields are also needed, as well as the radiated power per unit area and expressions for the sound transmission.

6.1. Transmission and radiation

Transmission is now to be determined. The transmission coefficient is defined as transmitted power divided by incident power, or in the present infinite case as the transmitted intensity divided by incident intensity,

$$\tau \equiv \frac{I_t}{I_i}$$

The total sound intensity radiated per unit area of the plate, that is the sound intensity I_t in the direction normal to the plate, is

$$I_t = \frac{1}{2} \Re \{ p_t v^* \} \tag{65}$$

which can be expressed as the sum of the sound intensity radiated normal to the plate by each harmonic (v being the velocity). Thus, if using the fact that $v^* = -\mathrm{i}\omega w^*$ and that the radiated pressure can be written as a space harmonic series, the transmitted sound intensity can be calculated. Using the radiated pressure written as a space harmonic series, similar to equation (63–64), Mace [12] derives the radiated sound intensity as

$$I_t = \frac{1}{2} \omega^3 \rho \sum_{n \in radiators} \frac{|W_n|^2}{|\beta_n|}, \tag{66}$$

where the sum is to be preformed over all the radiating harmonics where $\beta_n \in \mathbb{I}$, where $\mathbb{I}$ being the imaginary numbers.

The incidence sound intensity normal to the plate is,

$$I_i = \frac{1}{2} \Re \{ p_i v_i^* \} \tag{67}$$

where v_i is the velocity in the normal direction of the incident wave,

$$v_i = \frac{-1}{\mathrm{i}\omega\rho} \frac{\partial p_i}{\partial y} = \frac{k_y}{\omega\rho} p_i.$$

and thus for the incidence sound intensity

$$I_i = \frac{1}{2} \frac{\Re \{ k_y^* \}}{\omega\rho} |p_i|^2 = \frac{1}{2} \frac{k_y}{\omega\rho} |p_i|^2. \tag{68}$$

where the last step is only correct if the incident exciting wave is a travelling wave.

From the relations (65–68) one may determine the transmission efficiency $\tau(\theta, \varphi)$ for each incidence angle θ and φ; the transmission efficiency is the ratio of the transmitted/radiated sound intensity $I_{n,Rad}$ to the incident sound intensity $I_{n,In}$,

$$\tau(\theta, \varphi) = I_t(\theta, \varphi) / I_i(\theta, \varphi). \tag{69}$$

using equation (66) and (68), together with $k_y = k \cos\theta$, yields

$$\tau(\theta, \varphi) = \frac{\omega^4 \rho^2}{k \cos\theta |p_i|^2} \sum_{n \in radiators} \frac{|W_n|^2}{|\beta_n|}, \tag{70}$$

The statistical transmission coefficient τ_s is found as

$$\tau_s = \langle I_t(\theta, \varphi) \rangle / \langle I_i(\theta, \varphi) \rangle$$

where $\langle \cdot \rangle$ denotes the mean. The statistical transmission coefficient therefore becomes

$$\tau_s = \frac{1}{\pi} \int\limits_0^{2\pi} \int\limits_0^{\pi/2} \tau_n(\theta, \varphi) \sin\theta \cos\theta \, \mathrm{d}\theta \, \mathrm{d}\varphi \tag{71}$$

and the transmission loss R dB is,

$$R = 10 \log 1/\tau_s \text{ dB}. \tag{72}$$

However, as the transmission loss is defined for all angles of incidence, the integral over all possible angles are needed, (71). This is a very time-consuming operation. The angle of incidence is therefore chosen randomly in order to approximate the integral over the incidence angles, i.e., a Monte Carlo approach. The calculation is ended when the maximum error (as compared to the last estimate of τ_s) falls below a given number.

7. Numerical results and discussion

7.1. Data for the numerical examples

Consider a wall with 13 mm thick gypsum plates and wooden studs (45×95 mm) and let the cavity not be filled with mineral wool. The studs are separated with a distance of $l = 0.6$ m. The bending stiffness of the gypsum plates is taken to be $D_1 = D_2 = 520$ Nm, and the mass per unit area $m_1'' = M_1'' = 10.9$ kg/m². Young's modulus for the beams is $E_f = 9.8 \cdot 10^9$ Pa and the density for the beams $\rho_f = 500$ kg/m³. The speed of sound is $c_0 = 340$ m/s and density for air $\rho_0 = 1.29$ kg/m³. Material damping in the beams and plates are taken to be $\eta = 0.03$ added to the Young's modulus. Material damping in the air is $\eta_{air} = 1 \cdot 10^{-5}$. The stiffness in the frame coupling is
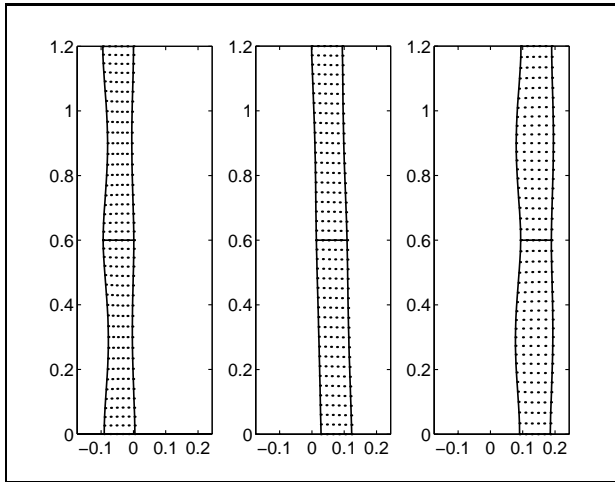
Figure 5. Displacement of cavity field at $f = 30$ Hz . Snapshots from the left: at $t = 0$ s, $t = T/4$ and $t = T/2$ s, T being the period.
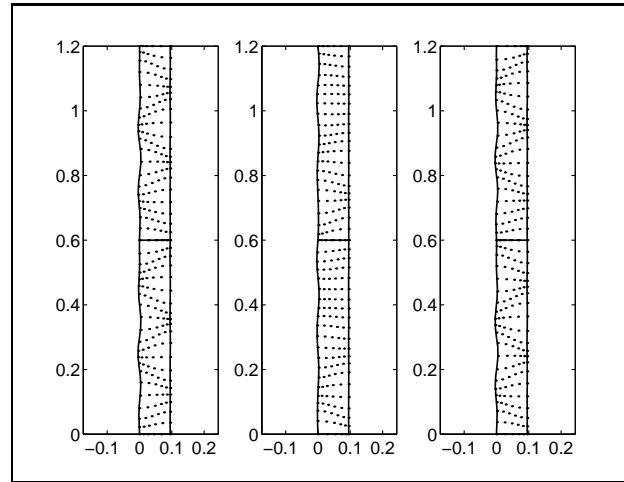
Figure 7. Displacement of cavity field at $f = 3$ kHz. Snapshots from the left: at $t = 0$ s, $t = T/4$ and $t = T/2$ s, T being the period.
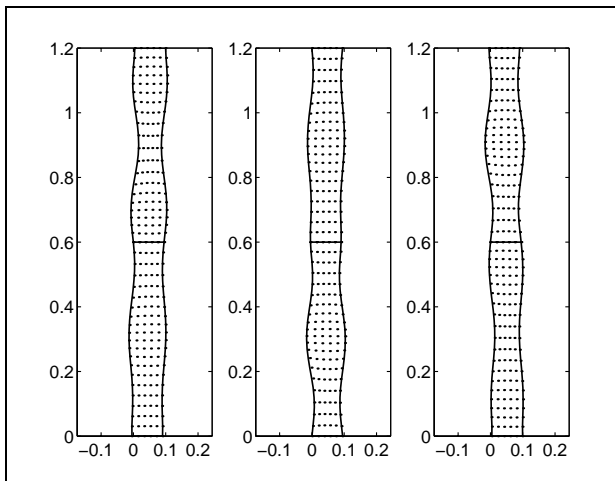
Figure 6. Displacement of cavity field at $f = 300$ Hz. Snapshots from the left: at $t = 0$ s, $t = T/4$ and $t = T/2$ s, T being the period.

chosen to $1 \cdot 10^{10}$ N/m^2 as to have a rigid connection in the frequency range of interest.

7.2. Displacement

The displacement of a grid of particles in the cavities is magnified and shown in Figures 5–7. The system is excited by a incoming pressure wave with the wave numbers $k_x = k \sin(55°)$, $k_z = 0$. In Figure 5 the frequency is $f = 30$ Hz. Two bays are shown and the solid lines represent the plates. Snapshots are shown, from the left representing the displacement at time $t = 0$ s, $t = T/4$ and $t = T/2$ s, T being the period. In this low frequency example it can be noticed that the cavity is symmetrically deformed even though the frequency is below the first resonance. This observation appears contradictious to the result in Cremer and Heckl [1, pp. 450–462], where

a double plate system without mechanical point connectors first moves in phase which each other, and then – for frequencies above the first mass-spring-mass resonance – moves out of phase. The explanation is that the reaction fields caused by the beams are of opposite sign for the two plates, as can be seen in equations (52–53). This fact can also be seen in the next section in [1, pp. 462–474], where the reaction field caused by a point connector is of opposite sign in the second plate compared to the first plate. And moreover, the total displacement is in-phase as overall displacement of the wall (the rigid body motion) is larger than the more local deformation of the plates relative to the beams. In Figure 6 is the same situation studied at $f = 300$ Hz, and in Figure 7 at $f = 3$ kHz. In Figure 6 the displacement of the two plates is truly out of phase, as the frequency is above the first resonance. The plate displacement is continuous over the stud, but the cavity field has a discontinuity, as clearly seen in the high frequency example Figure 7. In the same figure the standing wave motion in the x-direction is also noticeable.

7.3. Transmission loss

The transmission loss is now to be calculated for the configuration described above. The transmission loss is calculated according to section 6.1. The result is shown in Figure 8, where also experimental results are shown for the same wall (as taken from a measurement report from the 1970's found in the division archive). The agreement is satisfactory if the rough material models, the infinite description and the lack of moment coupling are taken into account. For the calculated transmission loss curve the troughs and peaks between 160 to 1600 Hz correspond well with those found in the experimental curve.

In Figure 9 some variations from the base configuration are shown (relative to the base configuration, as being the one described in section 7.1). The effect of letting the stiffness be zero, $K = 0$, is shown with circles (–∘–). The two
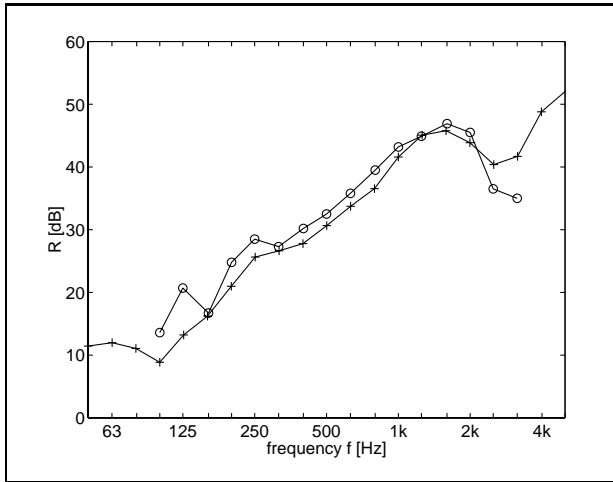
Figure 8. Transmission loss, $-\circ-$ measurements and $-+-$ calculations.
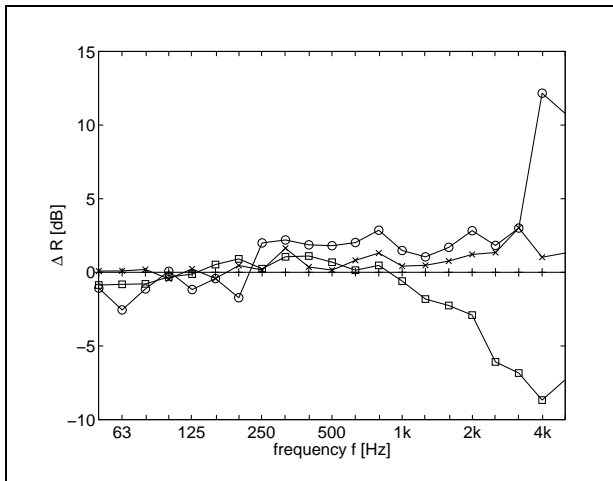
Figure 9. Transmission loss difference relative the base configuration, $R - R_{base}$ dB. Base configuration ($-+-$), zero stiffness $K = 0$ ($-\circ-$), only the zero term present in cavity expansion $N = 0$ ($-\times-$), no bending stiffness and mass in beams ($-\square-$).

plates are then mechanically uncoupled. No large effects are seen (a little surprisingly), only about 2 dB are gained in the frequency interval 250–3160 Hz. It should however be noted that the airspace between the plates is quite thin and undamped. The effect of only including the zero term in the expansion of the cavity is also shown ($-\times-$), which is similar to having a locally reacting air cavity. Nor in this case any large effects are seen; only an increase of about 1 dB above 250 Hz. Thus, the calculation time can be reduced without to much errors if reducing the number of terms in the expansion. Moreover, the error of letting the cavity field passing through the beams is probably minor (at least for thin constructions and for third octave band filtrated transmission losses). The effect of ignoring the mass and bending stiffness of the beams is also shown ($-\square-$). A small decrease at low frequencies (below 125 Hz) and a larger decrease for frequencies above 1000 Hz is seen.

8. Concluding remarks

The paper has shown that it is possible to use a periodic assumption and transform technique to include the effects of finiteness when treating a double-plate wall with studs.

At frequencies below the first resonance, the displacements of the plates are out of phase, if the displacement relative to the beams is considered (that is if the rigid body motion is subtracted). This is due to the reaction field caused by the beams.

Comparison between measured and calculated results shows satisfactory agreement, the troughs and peaks between 160 to 1600 Hz comparing well with those being found in the experimental curve.

No large effects are noticed (for the present configuration) if the mechanical coupling between the plates is removed or if only the zero term in the cavity expansion is used. The latter fact means that the calculation time can be reduced without to much errors if reducing the number of terms in the expansion and that the error of letting the cavity field passing through the beams probably is minor.

Acknowledgement

Appendix

We have the following help function from equation (32),

$$\Phi_n = \mathcal{F}_x \Bigg\{ \cos\left(n\pi x/l\right) \sum_{m=-\infty}^{\infty} e^{-ik_x ml}$$
$$\times \left(\theta(x - ml) - \theta(x - (m+1)l) \right) \Bigg\}$$

Define a new function

$$\Theta_m = \mathcal{F}_x \big\{ \cos\left(n\pi x/l\right) e^{-ik_x ml} \qquad \text{(A1)}$$
$$\times \left(\theta\left(x - ml\right) - \theta\left(x - (m+1)l\right) \right) \big\}$$

so that

$$\Phi_n = \sum_{m=-\infty}^{\infty} \Theta_m \qquad \text{(A2)}$$

Use the following identities

$$\mathcal{F}_x \left\{ \theta\left(x - a\right) \right\} = e^{i\alpha a} \left(\pi \delta\left(\alpha\right) - \frac{1}{i\varepsilon} \right) \qquad \text{(A3)}$$

$$\mathcal{F}_x \left\{ \theta\left(x - a\right) e^{ibx} \right\} = e^{i(\alpha - b)a} \qquad \text{(A4)}$$
$$\times \left(\pi \delta\left(\alpha - b\right) - \frac{1}{i\left(\alpha - b\right)} \right)$$

to rewrite Θ_m

$$
\begin{aligned}
\Theta_m &= \frac{e^{-ik_x ml}}{2} \mathcal{F}_x \Big\{ \theta(x - ml) e^{in\pi x/l} \\
&- \theta(x - (m+1)l) e^{in\pi x/l} + \theta(x - ml) e^{-in\pi x/l} \\
&- \theta(x - (m+1)l) e^{-in\pi x/l} \Big\} \\
&= \frac{e^{-ik_x ml}}{2} \Big(e^{i(\alpha - n\pi/l)ml} \Big(\pi\delta(\alpha - n\pi/l) + \frac{i}{\alpha - n\pi/l} \Big) \\
&- e^{i(\alpha - n\pi/l)(m+1)l} \Big(\pi\delta(\alpha - n\pi/l) + \frac{i}{\alpha - n\pi/l} \Big) \Big) \\
&+ \frac{e^{-ik_x ml}}{2} \Big(e^{i(\alpha + n\pi/l)ml} \Big(\pi\delta(\alpha + n\pi/l) + \frac{i}{\alpha + n\pi/l} \Big) \\
&- e^{i(\alpha + n\pi/l)(m+1)l} \Big(\pi\delta(\alpha + n\pi/l) + \frac{i}{\alpha + n\pi/l} \Big) \Big)
\end{aligned}
$$

Taking the limit $\alpha \to \pm n\pi/l$ it can be shown that the amplitude of Dirac's function equals zero. Thus, after some rearrangement

$$
\begin{aligned}
\Theta_m &= -\frac{e^{-ik_x ml} e^{i\alpha ml}}{2} \Big(\big(1 - e^{i\alpha l} e^{-in\pi}\big) \frac{e^{-inm\pi}}{i(\alpha - n\pi/l)} \\
&+ \big(1 - e^{i\alpha l} e^{in\pi}\big) \frac{e^{inm\pi}}{i(\alpha + n\pi/l)} \Big)
\end{aligned}
\tag{A5}
$$

Therefore, using (A2) and (A5)

$$
\begin{aligned}
\Phi_n &= -\frac{1}{2i} \Big(\frac{1 - e^{i\alpha l} e^{-in\pi}}{\alpha - n\pi/l} \sum_{m=-\infty}^{\infty} e^{-inm\pi} e^{i(\alpha - k_x)ml} \\
&+ \frac{1 - e^{i\alpha l} e^{in\pi}}{\alpha + n\pi/l} \sum_{m=-\infty}^{\infty} e^{inm\pi} e^{i(\alpha - k_x)ml} \Big)
\end{aligned}
\tag{A6}
$$

The Poisson sum formula can be used to show that

$$
\sum_{m=-\infty}^{\infty} f(am) = \frac{1}{a} \sum_{q=-\infty}^{\infty} F\Big(\frac{2q\pi}{a} \Big)
\tag{A7}
$$

which together with the rules for the Dirac function $\delta(\alpha l) = \delta(\alpha)/l$ implies that

$$
\begin{aligned}
&\sum_{m=-\infty}^{\infty} e^{i(\alpha - k_x)ml} e^{\pm in\pi m} \\
&= \frac{2\pi}{l} \sum_{m=-\infty}^{\infty} \delta(\alpha - k_x + (n \pm 2m)\pi/l)
\end{aligned}
\tag{A8}
$$

The matrix components in (62) are

$$
A_{11} = 1 + \frac{(G+K)}{l} T_1^{(f)}(0)
$$

$$
A_{12} = -\frac{K}{l} T_1^{(f)}(0)
$$

$$
A_{1n} = \begin{cases} \frac{J_{11,n}\varepsilon_n}{l} T_{1,n}^{(c)}(0), & n \text{ odd} \\ \frac{-J_{12,n}\varepsilon_n}{l} T_{1,n}^{(c)}(0), & n \text{ even} \end{cases}
\tag{A9}
$$

and

$$
A_{21} = -\frac{K}{l} T_2^{(f)}(0)
$$

$$
A_{22} = 1 + \frac{K}{l} T_2^{(f)}(0)
$$

$$
A_{2n} = \begin{cases} -\frac{J_{21,n}\varepsilon_n}{l} T_{2,n}^{(c)}(0), & n \text{ odd} \\ \frac{J_{22,n}\varepsilon_n}{l} T_{2,n}^{(c)}(0), & n \text{ even} \end{cases}
\tag{A10}
$$

and for odd s

$$
A_{s1} = \frac{2(G+K)}{l^2} I_{1,s}^{(f)}
$$

$$
A_{s2} = -\frac{2K}{l^2} I_{1,s}^{(f)}
$$

$$
A_{sn} = \delta_{sn} + \begin{cases} \frac{2}{l^2} J_{11,n}\varepsilon_n I_{1,s,n}^{(c)}, & n \text{ odd} \\ -\frac{2}{l^2} J_{12,n}\varepsilon_n I_{1,s,n}^{(c)}, & n \text{ even} \end{cases}
\tag{A11}
$$

and for even s

$$
A_{s1} = -\frac{2K}{l^2} I_{2,s}^{(f)}
$$

$$
A_{s2} = \frac{2K}{l^2} I_{2,s}^{(f)}
$$

$$
A_{sn} = \delta_{sn} + \begin{cases} -\frac{2}{l^2} J_{21,n}\varepsilon_n I_{2,s,n}^{(c)}, & n \text{ odd} \\ \frac{2}{l^2} J_{22,n}\varepsilon_n I_{2,s,n}^{(c)}, & n \text{ even} \end{cases}
\tag{A12}
$$

The vector components in (62) are

$$
\begin{aligned}
P_1 &= \frac{2\hat{p}_i}{S_1(k_x)}, \\
P_2 &= 0, \\
P_s &= \begin{cases} \frac{2 \cdot 2\hat{p}_i}{lS_1(k_x)} \int_0^l e^{-ik_x x} \cos(s\pi x/l)dx & , s \text{ odd} \\ 0 & , s \text{ even} \end{cases}
\end{aligned}
\tag{A13}
$$

where the last expression is valid for $s > 2$, and where the integral is

$$
\int_0^l e^{-ik_x x} \cos(s\pi x/l)dx = ik_x \frac{1 - (-1)^s e^{-ik_x l}}{(s\pi/l)^2 - k_x^2}
$$

The integral in equation (60) is, using (54) and interchanging the integral and the sum

$$
I_{i,s}^{(f)} = \sum_{m=-\infty}^{\infty} \frac{I_s(\alpha_m)}{S_i(\alpha_m)}
\tag{A14}
$$

where

$$
\begin{aligned}
I_s(\alpha_m) &= \int_0^l \cos(s\pi x/l) e^{-i\alpha_m x}dx \\
&= i\alpha_m \frac{1 - (-1)^s e^{-i\alpha_m l}}{(s\pi/l)^2 - \alpha_m^2}.
\end{aligned}
\tag{A15}
$$

The integral in equation (61) is, using (55) and interchanging the integral and the sum

$$I_{i,s,n}^{(c)} = \sum_{m=-\infty}^{\infty} \varsigma_n(\alpha_m) \frac{I_s(\alpha_m)}{S_i(\alpha_m)} \qquad (A16)$$

where $I_s(\alpha_m)$ is evaluated according to (A15).

References

[1] L. Cremer, M. Heckl, E. E. Ungar: Structure-borne sound. Springer-Verlag, Berlin, 1988.

[2] EN 12354: Building acoustics – estimation of acoustic performance of buildings from the performace of products. part I: Airborne sound insulation between rooms. EN 12354-1. part II: Impact sound insulation between rooms. EN 12354-2. European Standard, 1996.

[3] T. R. T. Nightingale, I. Bosmans: Vibration response of lightweight wood frame building elements. J. Building Acoustics **6** (1999) 269–288.

[4] R. J. M. Craik: Sound transmission through buildings. Gower, Aldershot, Hampshire GU11 3HR, England, 1996.

[5] R. J. M. Craik, R. S. Smith: Sound transmission through double leaf lightweigth partitions part I: airborn sound. Applied Acoustics **61** (2000) 223–245.

[6] B. H. Sharp: Prediction methods for the sound transmission of building elements. Noise Control Engineering **11** (1978) 53–63.

[7] A. London: Transmission of reverberant sound through double walls. J. Acoust. Soc. Am. **22** (1950) 270–279.

[8] W. Kropp, E. Rebillard: On the air-borne sound insulation of double wall constructions. Acustica / acta acustica **85** (1999) 707–720.

[9] G. F. Lin, J. M. Garrelick: Sound transmission through periodically framed parallel plates. J. Acoust. Soc. Am. **61** (1977) 1014–1018.

[10] J. S. Bradley, J. A. Birta: On the sound insulation of wood stud exterior walls. J. Acoust. Soc. Am. **110** (2001) 3086–3096.

[11] M. L. Rumerman: Vibration and wave propagation in ribbed plates. J. Acoust. Soc. Am. **57** (1975) 370–373.

[12] B. R. Mace: Periodically stiffened fluid-loaded plates, I: Response to convected harmonic pressure and free wave propagation. J. Sound and Vibration **73** (1980) 473–486.

[13] D. Takahashi: Sound radiated from periodically connected double-plate structures. J. Sound and Vibration **90** (1983) 541–557.

[14] E. A. Skelton: Acoustic scattering by parallel plates with periodic connectors. Proc. R. Soc. Lond. A **427** (1990) 419–444.

[15] K. Sakagami, H. Gen, M. Morimoto, D. Takahashi: Acoustic reflection of an elastic plate with periodic ribs and a back cavity. Acustica / acta acustica **85** (1999) 1–11.

[16] E. A. Skelton: Acoustic scattering by a rigid berrier between two fluid-loaded parallel plates. Proc. R. Soc. Lond. A **435** (1991) 217–232.

[17] I. A. Urusovskii: Sound transmission through two periodically framed parallel plates. Sov. Phys. Acoust. **38** (1992) 411–413.

[18] J. Brunskog, P. Hammer: Prediction model for the impact sound level of lightweight floors. Acustica / acta acustica **accepted**.

[19] J. Brunskog, P. Hammer: Prediction models of impact sound insulation on timber floor structures; A literature survey. J. Building Acoustics **7** (2000) 89–112.

Near-periodicity in acoustically excited stiffened plates and its influence on vibration, radiation and sound insulation

Jonas Brunskog

Division of Engineering Acoustics, LTH, Lund University, P.O. Box 118, SE-221 00, Sweden

Summary
Due to variabilities in the material, the geometrical configuration, or the manufacturing properties, a structure that is designed to be spatially periodic cannot be exactly periodic. The presence of small irregularities in a nearly periodic structure may influence the propagation of the vibration field, the field being localised. A number of papers have addressed such localisation phenomena. This paper will instead focus on the mean vibration field and its influence on sound radiation and sound insulation in a plate stiffened by supports or beams. The approach is to seek a formal solution with the aid of spatial transform technique (similar to the perfect periodic case) and then apply the expected value operator to the solution. Two assumptions must then be introduced: I) The reaction forces are statistically independent of a phase-term that is due to the irregularity, and II) the mean field is periodic. The approach is presented in general terms, the specific configuration (a stiffened plate) being presented as an example. Numerical results are presented and discussed, and it can be seen that the small irregularities cause an increase in stiffness and damping (when material damping is present).

PACS no. 43.40.Dx, 43.55.Ti

1. Introduction

A structure designed to be spatially periodic in its configuration cannot be exactly periodic due to material, geometrical, and manufacturing variabilities. The presence of small irregularities in a nearly periodic structure may influence the propagation of vibration strongly and localise the vibration field.

Anderson [1] described localisation phenomena for nearly periodic systems in solid state physics, concerning the transport of electrons in an atomic lattice (leading to a Nobel Prize). Obviously, localisation also occurs in disordered periodic structural systems, but its theoretical investigation is more difficult than that of a one-dimensional atomic lattice, since governing equations for structural systems are generally more complex. However, a number of papers have been addressed to localisation phenomena in such structures.

Hodges and Woodhouse [2] describe the theory and some simple experiments carried out to demonstrate the phenomenon of Anderson localisation in an acoustic/mechanical context. A simple chain of pendula coupled by springs and a string with nearly equally spaced point masses was studied. A perturbation method was used in the statistical treatment and a localisation factor was calculated in the form of an exponential decay constant. Pierre and Dowell [3] investigated the localisation of modes of free vibration in discrete disordered structural systems consisting of coupled subsystems. The degree of localisation is dependent upon two parameters: the coupling between and the mistuning among the component systems. Perturbation methods are used for slightly disordered systems because they are cost effective. At the same time, they lead to very accurate results for small perturbations. Cai and Lin [4] treated a one-dimensional, nearly periodic

system using transfer matrixes. The localisation factor was defined as the limit of the logarithm of the transmission part in the random matrixes. Thus, transmitted waves have an average exponential decaying rate. Other papers on the subject of localisation of free wave propagation in nearly periodic structures can be found in reference [5], containing a survey of periodic and nearly periodic solution techniques.

In problems concerning sound-insulation in dwellings, for example, the excitation of the system can be seen as a superposition of spatially harmonic pressure fields. The system will then vibrate and radiate sound in the receiver room.

None of the foregoing papers concerning nearly periodic systems deal with the questions of acoustical excitation or radiation. Whether the localisation phenomena influence these problems is still an open question. Moreover, the analysis methods described are not suited for this type of problem; they consider free wave propagation or excitation in one bay and propagation in the rest of the system. Another problem with the analysis methods described is that they are only suited for one-dimensional problems and therefore not suited, for example, for systems built up by plates [5].

This paper will instead focus on the mean vibration field caused by spatial harmonic excitation and its influence on sound radiation in a plate stiffened by supports. The localisation factor found in the cited literature can be seen as a virtual damping. The aim of this paper is to investigate if additional damping, in an average sense, also is found for spatially harmonic driven systems, and if this can be noted in the sound insulation. This problem is important in the fields of structural and building acoustics. However, the approach is also suited for evaluation of the free waves, so this will also be studied (briefly). The paper is comprised

as follows: First, the general equations formulated and the considerations needed are stated. Then the solution technique for the perfectly periodic case is presented. Thereafter, the solution technique for the nearly periodic case – the main issue of the paper – is stated, including statistical considerations. The radiated sound and sound-insulation are then investigated. The numerical results are presented and analysed. The paper ends with summary and conclusions.

2. General considerations and formulations

The main idea of the solution technique in the present paper is to use a method similar to the one used in the perfectly periodic case, but to solve for the mean displacement field. This is achieved by applying the expected value operator $E[\cdot]$ to the formal version of the solution. There are two main assumptions in this approach that the reader should be aware of: I) It is assumed that the reaction forces are statistically independent of the harmonic term $e^{i\alpha\varphi_n}$, where φ_n is the divergence from perfect periodicity and α is the transform wavenumber and II) It is assumed that the mean field (displacement and force) is periodic. The assumptions are recognized to be reasonable, but they are not proven. However, as can be seen in the simulations in section 6.3, the result is not exactly the same as the ensemble average; there is a discrepancy between the nearly-periodic estimation of the expected value and the mean of the Monte Carlo simulations.

The theory will be presented in general terms, the specific examples involving plate systems being presented in examples in separate subsections. It is hoped that the generality of the approach can be seen in this way.

2.1. Introduction to the solution technique

This section will introduce the spatial Fourier transform technique and the concept of general linear differential operators. Consider a linear differential operator $\mathcal{S}[\cdot]$. An inhomogeneous differential equation can then be written

$$\mathcal{S}[w(x)]e^{i\omega t} = p(x)e^{i\omega t} \tag{1}$$

for a time harmonic displacement, where the time harmonic term $e^{i\omega t}$ is henceforth suppressed. In equation (1) w can be a displacement and p a pressure field. The Fourier transform pair – with the transform variable α – for an arbitrary function $g(x)$ is defined as

$$g(x) = \frac{1}{2\pi}\int_{-\infty}^{\infty}\tilde{g}(\alpha)\,e^{-i\alpha x}d\alpha, \tag{2}$$

$$\tilde{g}(\alpha) = \int_{-\infty}^{\infty}g(x)\,e^{i\alpha x}dx, \tag{3}$$

where $\tilde{\ }$ is used to denote transformed field variables. Fourier transform the equation (1)

$$S(\alpha)\tilde{w}(\alpha) = \tilde{p}(\alpha) \Leftrightarrow \tilde{w}(\alpha) = \tilde{p}(\alpha)/S(\alpha)$$

where S is the transformed version of the operator in (1). The inverse Fourier transform is

$$w(x) = \frac{1}{2\pi}\int_{-\infty}^{\infty}\frac{\tilde{p}(\alpha)}{S(\alpha)}e^{-i\alpha x}d\alpha. \tag{4}$$

If a z-dependency also is present, an extra transform-pair in this direction is superimposed on the expressions in (2–4) (except when a dependency of the form $e^{-ik_z z}$ is present, which directly can be suppressed).

2.2. Examples

As an example to be used in this report, take the linear differential operator in (1) to be that of a thin plate in bending,

$$\mathcal{S}[w] = D'\Delta\Delta w - \omega^2 m'' w\,, \tag{5}$$

$$S = D'\left(\alpha^2 + k_z^2\right)^2 - m''\omega^2 \tag{6}$$

where

$$\Delta\Delta = \left(\frac{\partial^2}{\partial x^2} + \frac{\partial^2}{\partial z^2}\right)^2$$

and where k_z is the excitation wavenumber in the z-direction, w is the displacement, D' is the bending stiffness and m'' is the mass per unit area. The influence of fluid loading is neglected, except in case of sound-insulation, see section 5. In order to simplify, set $k_z = 0$ (where not said differently).

Another example could be the Helmholtz equation for an acoustic fluid together with an excitation or incident pressure (and boundary conditions), in one, two or three dimensions.

3. Exact periodicity

When the periodicity is perfect, the solution can be found with methods similar to Mace [6]. This approach is described in the present section, so that a similar theory can be used for the nearly periodic case in section 4.

3.1. Formulation

First, let the system be exactly periodic in the co-ordinate x (the other co-ordinates are assumed to be in the form $e^{-\beta y - ik_z z}$ and suppressed),

$$\mathcal{S}[w(x)] = p_d(x) - \sum_{n=-\infty}^{\infty} F_n\delta(x - nl) \tag{7}$$

The driving part of the equation is due to a driving periodic pressure p_d,

$$p_d = \hat{p}_d e^{-ik_x x},\ \tilde{p}_d = 2\pi\hat{p}_d\delta(\alpha - k_x)$$

and a periodic set of reaction forces F_n. These reaction forces are due to a periodic set of boundary conditions located at the positions $x = nl$. Thus, the reaction forces F_n are to be chosen so that the boundary condition at the periodic boundaries is fulfilled. The periodicity implies that Floquet's principle is valid, which in the present case can be written:

$$w(x + nl) = w(x)\mathrm{e}^{-\mathrm{i}k_x nl} \Rightarrow F_n = F_0\mathrm{e}^{-\mathrm{i}k_x nl} \quad (8)$$

where k_x is given from the driving force p_d. Thus equation (7) is written, if using equation (8) and then applying the Fourier transform

$$S\tilde{w}(\alpha) = \tilde{p}_d(\alpha) - F_0 \sum_{n=-\infty}^{\infty} \mathrm{e}^{-\mathrm{i}k_x nl}\mathrm{e}^{\mathrm{i}\alpha nl}. \quad (9)$$

Poissons sum formula [7] states that

$$\sqrt{a} \sum_{n=-\infty}^{\infty} g(na) = \sqrt{\frac{b}{2\pi}} \sum_{n=-\infty}^{\infty} \tilde{g}(nb) \quad (10)$$

where $ab = 2\pi$ and $\tilde{g}(k)$ is the Fourier transform of the arbitrary function $g(x)$. This relation gives for the reaction part of equation (9), if using the rules for the Dirac's delta function,

$$\sum_{n=-\infty}^{\infty} \mathrm{e}^{-\mathrm{i}k_x nl}\mathrm{e}^{\mathrm{i}\alpha nl} = \frac{2\pi}{l} \sum_{n=-\infty}^{\infty} \delta(\alpha - k_x - 2n\pi/l) \quad (11)$$

which simplifies the inverse transformation.

3.2. Solution

The solution is then found by means of inserting (11) and $\tilde{p}_d$ in (4), and then evaluating the integrals, yielding the displacement

$$w(x) = w_\infty(x) - F_0 T(x), \quad (12)$$

where

$$w_\infty(x) \equiv \frac{\hat{p}_d}{S(k_x)}\mathrm{e}^{-\mathrm{i}k_x x}, \quad (13)$$

$$T(x) \equiv \frac{1}{l} \sum_{n=-\infty}^{\infty} \frac{\mathrm{e}^{-\mathrm{i}\left(k_x + \frac{2n\pi}{l}\right)x}}{S(k_x + 2n\pi/l)}. \quad (14)$$

This formulation is similar to Mace [6]. The sum coverage rapidly due to $S(\alpha) \propto \alpha^q$ as $\alpha \to \infty$, q being the order of the operator ($q = 4$ in case of a plate), and is therefore suited for truncation. However, the sum can in many cases be given in a closed form.

The displacement can also be regarded as a series of space harmonic type,

$$w(x) = \sum_{n=-\infty}^{\infty} W_n\mathrm{e}^{-\mathrm{i}(k_x + 2n\pi/l)x} \quad (15)$$

where the coefficients can be identified as

$$W_n = \frac{\hat{p}_d}{S(k_x)}\delta_{0n} - \frac{F_0(k_x)}{lS(k_x + 2n\pi/l)}, \quad (16)$$

where δ_{0n} is the Kronecker delta; $\delta_{0n} = 1$ if $n = 0$, else $\delta_{0n} = 0$.

3.3. Reaction forces

The reaction force is determined by the boundary condition: For Dirichlet conditions $w(nl) = w_{bc}$, which inserted in (12) gives

$$F_0 = \frac{w_{bc} - w_\infty(0)}{T(0)}. \quad (17)$$

For Neumann conditions $F_n = F_{bc}$, which directly gives

$$F_0 = F_{bc}. \quad (18)$$

For Robin (mixed) conditions

$$w(nl) + K_{bc}F_n = w_{bc}$$

which inserted in (12) gives

$$F_0 = \frac{w_{bc} - w_\infty(0)}{T(0) - K_{bc}}. \quad (19)$$

Boundary conditions of higher degree (e.g., dipoles, moments) can be introduced in a similar way [8, 6].

If the plate is reinforced by beam, the reaction force is determined as [9, 6, 10] $F_0 = \mathcal{G}w(0)$ which inserted in (12) gives

$$F_0 = \frac{\mathcal{G}w_\infty(0)}{1 + \mathcal{G}T(0)}, \quad (20)$$

where the differential operator $\mathcal{G}$ describes the deflection of a Euler beam due to a line force,

$$\mathcal{G} = EI\partial^4/\partial z^4 - m'\omega^2$$

Where not said differently, a homogeneous Dirichlet condition $w(nl) = 0$ is henceforth assumed.

3.4. Free wave propagation

As the excitation pressure p_d tends to zero, the solution (12) reduces to

$$w(x) = -F_0 T(x), \quad (21)$$

the boundary condition (homogeneous Dirichlet condition assumed) reduces to $w(0) = 0 = -F_0 T(0)$, and thus the plate displacement is nonzero only if

$$T(0) = 0, \quad (22)$$

as also F_0 is nonzero. This relation yields the proper wavenumber $\kappa \leftrightarrow k_x$, that is being purely real for travelling waves – corresponding to pass-bands – and purely imaginary for decaying waves – corresponding to stop-bands.
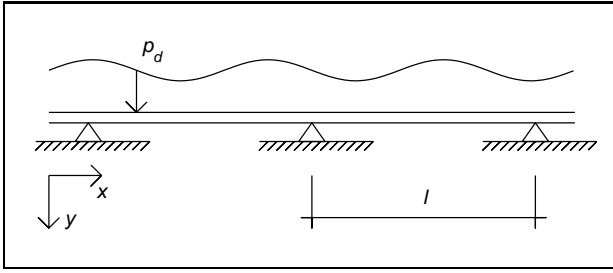
Figure 1. The structure under consideration, a supported plate, p_d being the driving pressure and l being the spacing.

Figure 2. The location of the reaction force is assumed to be stochastic, φ_n being the divergence from the periodic position nl, the arrow representing the reaction force in terms of a Dirac delta, and the curve indicating a probability density function for φ_n.

3.5. A supported plate, part I

Consider a plate resting on equally spaced simple supports, Figure 1. Take the linear differential operator in (1) to be that of a thin plate in bending, equation (5). Let the driving pressure be a space harmonic force,

$$p_d = \mathrm{e}^{-\mathrm{i}k_x x}, \quad \tilde{p}_d = 2\pi\delta\left(\alpha - k_x\right).$$

Moreover, let the boundary condition be the homogenous Dirichlet condition, $w(nl) = 0$, i.e., simply supported. Material damping can be introduced as a complex bending stiffness $D' \cdot (1 + \mathrm{i}\eta)$, η being the damping. Thus, the solution is found to be

$$w_\infty(x) = \frac{\mathrm{e}^{-\mathrm{i}k_x x}}{D'k_x^4 - m''\omega^2}, \tag{23}$$

and

$$T(x) = \frac{1}{l}\sum_{n=-\infty}^{\infty}\frac{\mathrm{e}^{-\mathrm{i}(k_x + 2n\pi/l)}}{D'\left(k_x + 2n\pi/l\right)^4 - m''\omega^2}. \tag{24}$$

An explicit expression for this sum is given in [6]. The boundary condition $w(nl) = 0$ yields according to equation (17)

$$F_0 = w_\infty(0)/T(0). \tag{25}$$

The free wave propagation is examined by means of equation (22). Thus

$$T(0) = \frac{1}{l}\sum_{n=-\infty}^{\infty}\frac{1}{D'\left(\kappa + 2n\pi/l\right)^4 - m''\omega^2} = 0. \tag{26}$$

where κ fulfilling (26) is solved for.

4. Near-periodicity

Consider a small divergence φ_n from the exact periodic formulation, Figure 2, the divergence being assumed to be associated with the location of the reaction forces. It is assumed that the divergence can be described as a stochastic variable with a given statistical distribution.

4.1. Formulation

In terms of the differential equation (1), the nearly periodic version can be written

$$\mathcal{S}[w(x)] = p_d(x) - \sum_{n=-\infty}^{\infty}F_n\delta\left(x - nl - \varphi_n\right) \tag{27}$$

where φ_n is the stochastic number (in a given distribution). Assume the standard deviation σ_φ to be small compared to the average spacing, $\sigma_\varphi \ll l$. Each φ_n is assumed to be statistically independent of the other φ_m, $m \neq n$. In this case we have no general periodic description. However, it can be assumed that the field is close to the field in the periodic case. Thus, proceed in the same way as in section 3. The Fourier transform of the driving part is

$$\tilde{p}_d(\alpha) - \sum_{n=-\infty}^{\infty}F_n\mathrm{e}^{\mathrm{i}\alpha\varphi_n}\mathrm{e}^{\mathrm{i}\alpha nl}, \tag{28}$$

the stochastic divergence from periodic spacing being found as a phase disturbance.

4.2. Approaching the solution

Insert (28) in (4)

$$w(x) = \frac{1}{2\pi}\int_{-\infty}^{\infty}\frac{\tilde{p}_d(\alpha)}{S(\alpha)}\mathrm{e}^{-\mathrm{i}\alpha x}\mathrm{d}\alpha \tag{29}$$

$$-\frac{1}{2\pi}\int_{-\infty}^{\infty}\sum_{n=-\infty}^{\infty}F_n\frac{\mathrm{e}^{-\mathrm{i}\alpha(x - nl - \varphi_n)}}{S(\alpha)}\mathrm{d}\alpha$$

The yet unknown parameters F_n can be found by the boundary conditions at $x = ml + \varphi_m$, leading to an infinite set of equations (if the φ_m's are explicitly chosen),

$$w(ml + \varphi_m) = w_\infty(ml + \varphi_m) - \sum_{n=-\infty}^{\infty}F_nC_{nm} \tag{30}$$

(combined with the boundary conditions in section 3.3) where

$$C_{nm} = \frac{1}{2\pi} \int\limits_{-\infty}^{\infty} \frac{e^{-i\alpha((m-n)l+\varphi_m-\varphi_n)}}{S(\alpha)} d\alpha. \qquad (31)$$

This infinite set of equations has to be truncated in order to be solved. However, this approach is not the main approach in the present paper, it is only to be used for comparison purposes in section 6.3.

4.3. Statistical considerations

Instead of solving the problem exactly for a given configuration, we try to take the expected value of the nearly periodic displacement. The expected displacement field, $\bar{w}(x) = E[w(x)]$, is

$$\bar{w}(x) = \frac{1}{2\pi} \int\limits_{-\infty}^{\infty} \frac{\tilde{p}_d(\alpha)}{S(\alpha)} e^{-i\alpha x} d\alpha \qquad (32)$$

$$- \frac{1}{2\pi} \int\limits_{-\infty}^{\infty} E\left[\sum_{n=-\infty}^{\infty} \frac{F_n e^{i\alpha\varphi_n} e^{i\alpha nl}}{S(\alpha)} \right] e^{-i\alpha x} d\alpha$$

Thus, the expected value is taken on a sum of functions of independent stochastic variables. The rules for the expected value operator can be used to show that

$$E\left[\sum_{n=-\infty}^{\infty} Y_n(\phi_n) \right] = \sum_{n=-\infty}^{\infty} E[Y_n(\phi_n)]$$

where $Y_n(\phi_n)$ is a function of a stochastic variable ϕ_n and correspond to the terms in the sum, and ϕ_n is the n-th independent stochastic variable. Thus, the expected value can be taken at each term using

$$E[Y_n(\phi_n)] = \int\limits_{\Omega} f_{\phi_n} Y_n(\phi_n) d\phi_n \qquad (33)$$

where f_ϕ is the distribution density function and Ω is the domain of the given distribution. Thus, in the present case

$$E\left[\sum_{n=-\infty}^{\infty} \frac{F_n e^{i\alpha\varphi_n} e^{i\alpha nl}}{S(\alpha)} \right] = \sum_{n=-\infty}^{\infty} \frac{E[F_n e^{i\alpha\varphi_n}] e^{i\alpha nl}}{S(\alpha)}.$$

The reaction force is a function of all stochastic variables $\varphi = \{\varphi_n\}$,

$$F_n = F_n(\varphi).$$

However, if the reaction force is statistically independent of the harmonic term $e^{i\alpha\varphi_n}$, the expectation of the reaction force can be separated from the harmonic term. It is hereby assumed that this is the case, and thus

$$E[F_n e^{i\alpha\varphi_n}] \approx \bar{F}_n E[e^{i\alpha\varphi_n}] \qquad (34)$$

It can now also be assumed that the expected displacement and force field is periodic, and therefore, using (8)

$$\bar{F}_n = \bar{F}_0 e^{-ik_x nl}. \qquad (35)$$

4.4. Continuing the solution

Equation (32) can now be written

$$\bar{w}(x) = w_\infty(x) - \bar{F}_0 \bar{T}(x) \qquad (36)$$

where the notation

$$\bar{T}(x) = \frac{1}{2\pi} \int\limits_{-\infty}^{\infty} \frac{\mu(\alpha)}{S(\alpha)} e^{-i\alpha x} \sum_{n=-\infty}^{\infty} e^{i(\alpha-k_x)nl} d\alpha \quad (37)$$

$$\mu(\alpha) = E[e^{i\alpha\varphi_n}], \qquad (38)$$

has been introduced.

As before, the sum in (37) is replaced by means of Poisson's relation (10), so that the integration is easily performed, yielding

$$\bar{T}(x) = \frac{1}{l} \sum_{n=-\infty}^{\infty} \frac{\mu(k_x + 2n\pi/l) e^{-i(k_x+2n\pi/l)x}}{S(k_x + 2n\pi/l)} \qquad (39)$$

The mean displacement can also be regarded as a series of space harmonic type,

$$\bar{w}(x) = \sum_{n=-\infty}^{\infty} \bar{W}_n e^{-i(k_x+2n\pi/l)x} \qquad (40)$$

where the coefficients can be identified as

$$\bar{W}_n = \frac{\hat{p}_d}{S(k_x)} \delta_{0n} - \frac{\bar{F}_0(k_x)\mu(k_x + 2n\pi/l)}{lS(k_x + 2n\pi/l)}, \quad (41)$$

where δ_{0n} is the Kronecker delta.

4.5. Boundary conditions and reaction forces

The yet unknown parameter $\bar{F}_0$ can be found by boundary conditions at $n = 0$ in agreement with section 3.3. However, in order to avoid the assumption that the boundary condition also applies to the mean field, equation (36) is not used as a basis to determine $\bar{F}_0$. Instead, from (29–31) we have for the 0'th support,

$$w(0+\varphi_0) = w_{bc} = w_\infty(0+\varphi_0) - \sum_{n=-\infty}^{\infty} F_n C_{n0}. (42)$$

where it should be noted that the boundary condition w_{bc} is a given value not affected by the stochastic numbers. Apply the expected value operator to equation (42),

$$w_{bc} = E[w_\infty(\varphi_0)] - \sum_{n=-\infty}^{\infty} E[F_n C_{n0}]. \qquad (43)$$

The first term is, if we use the notation $E[\mathrm{e}^{-\mathrm{i}\alpha\varphi_0}] = E[\mathrm{e}^{\mathrm{i}\alpha\varphi_n}] = \mu(\alpha)$,

$$E[w_\infty(\varphi_0)] = \bar{w}_\infty = \frac{1}{2\pi}\int\limits_{-\infty}^{\infty}\frac{\tilde{p}_d(\alpha)}{S(\alpha)}E[\mathrm{e}^{-\mathrm{i}\alpha\varphi_0}]\mathrm{d}\alpha$$

$$= \frac{1}{2\pi}\int\limits_{-\infty}^{\infty}\frac{\tilde{p}_d(\alpha)}{S(\alpha)}\mu(\alpha)\mathrm{d}\alpha. \qquad (44)$$

The term in the sum is, if it is assumed that F_n is statistically independent of the harmonic term $\mathrm{e}^{\mathrm{i}\alpha\varphi_n}$, and thereby also of C_{n0},

$$E[F_nC_{n0}] \approx \bar{F}_n E[C_{n0}] = \bar{F}_0 \mathrm{e}^{-\mathrm{i}k_x nl}E[C_{n0}],$$

where

$$E[C_{n0}] = \bar{C}_{n0} = \frac{1}{2\pi}\int\limits_{-\infty}^{\infty}\frac{E\left[\mathrm{e}^{\mathrm{i}\alpha(\varphi_n-\varphi_0)}\right]\mathrm{e}^{\mathrm{i}\alpha nl}}{S(\alpha)}\mathrm{d}\alpha. \quad (45)$$

The statistical independency implies then

$$E\left[\mathrm{e}^{\mathrm{i}\alpha(\varphi_n-\varphi_0)}\right] = E\left[\mathrm{e}^{\mathrm{i}\alpha\varphi_n}\right]E\left[\mathrm{e}^{-\mathrm{i}\alpha\varphi_0}\right] = \mu^2(\alpha), \quad (46)$$

the last equality being due to the fact that all the φ_n have a zero mean and equal spread. Thus

$$\bar{C}_{n0} = \frac{1}{2\pi}\int\limits_{-\infty}^{\infty}\frac{\mu^2(\alpha)\mathrm{e}^{\mathrm{i}\alpha nl}}{S(\alpha)}\mathrm{d}\alpha, \qquad (47)$$

and the mean reaction

$$w_{bc} = \bar{w}_\infty(0) - \bar{F}_0\sum_{n=-\infty}^{\infty}\mathrm{e}^{-\mathrm{i}k_x nl}\bar{C}_{n0} \qquad (48)$$

$$= \bar{w}_\infty(0) - \frac{\bar{F}_0}{2\pi}\int\limits_{-\infty}^{\infty}\frac{\mu^2(\alpha)}{S(\alpha)}\sum_{n=-\infty}^{\infty}\mathrm{e}^{\mathrm{i}(\alpha-k_x)nl}\mathrm{d}\alpha$$

As before, the sum is replaced by means of the Poisson's relation in (11), yielding

$$\bar{F}_0 = \frac{w_{bc} - \bar{w}_\infty(0)}{\bar{T}_0}, \qquad (49)$$

$$\bar{T}_0 = \frac{1}{l}\sum_{n=-\infty}^{\infty}\frac{\mu^2(k_x + 2n\pi/l)}{S(k_x + 2n\pi/l)} \qquad (50)$$

where it should be noted that $\bar{T}_0 \neq \bar{T}(0)$.

4.6. Uniformly distributed locations

The mean of the harmonic term, $\mu(\alpha)$, is now to be found. Take φ_n to be a stochastic number, uniformly distributed in the range $\varphi_n \in \{-a, a\}$. The corresponding probability density function f_φ is given as

$$f_\varphi(x) = \begin{cases} \frac{1}{2a} & \text{if } x \in \{-a, a\} \\ 0 & \text{otherwise} \end{cases} \qquad (51)$$

Thus, the expected value of the harmonic term (38) is

$$\mu(\alpha) = E\left[\mathrm{e}^{\mathrm{i}\alpha\varphi_n}\right] = \frac{1}{2a}\int\limits_{-a}^{a}\mathrm{e}^{\mathrm{i}\alpha\varphi_n}\mathrm{d}\varphi_n \qquad (52)$$

$$= \frac{\sin(\alpha a)}{\alpha a} \equiv \mathrm{sinc}\,(\alpha a)$$

where the last step is the definition of the sinc-function.

4.7. Gaussian distributed locations

Take φ_n to be a stochastic number, this time Gaussian distributed in the range $\varphi_n \in \{-\infty, \infty\}$, and with a zero mean value and a standard deviation σ. The corresponding probability density function f_φ is given as

$$f_\varphi(x) = \frac{1}{\sigma\sqrt{2\pi}}e^{-\frac{x^2}{2\sigma^2}} \qquad (53)$$

Thus, the expected value of the harmonic term (38) in this case is

$$\mu(\alpha) = E\left[\mathrm{e}^{\mathrm{i}\alpha\varphi_n}\right] \qquad (54)$$

$$= \frac{1}{\sigma\sqrt{2\pi}}\int\limits_{-\infty}^{\infty}\mathrm{e}^{-\frac{\varphi_n^2}{2\sigma^2}}\mathrm{e}^{\mathrm{i}\alpha\varphi_n}\mathrm{d}\varphi_n = \mathrm{e}^{-\frac{(\alpha\sigma)^2}{2}}$$

4.8. A supported plate, part II

Consider the same example as in the previous section. Therefore, from (23)

$$\bar{w}(x) = w_\infty(x) - \bar{F}_0\bar{T}(x),$$

$$w_\infty(x) = \frac{\mathrm{e}^{-\mathrm{i}k_x x}}{D'k_x^4 - m''\omega^2} .$$

Consider first the uniformly distributed case. The sum is calculated from (24) and (52),

$$\bar{T}(x) = \frac{1}{l}\sum_{n=-\infty}^{\infty}\mathrm{sinc}\left(k_x a + \frac{2n\pi a}{l}\right) \qquad (55)$$

$$\times \frac{\mathrm{e}^{-i\left(k_x + \frac{2n\pi}{l}\right)x}}{D'\left(k_x + 2n\pi/l\right)^4 - m''\omega^2}$$

and then the Gaussian distributed case. The sum is calculated from (24) and (54),

$$\bar{T}(x) = \frac{1}{l}\sum_{n=-\infty}^{\infty}\mathrm{e}^{-\frac{(k_x l+2n\pi)^2\sigma^2}{2l^2}} \qquad (56)$$

$$\times \frac{\mathrm{e}^{-\mathrm{i}\left(k_x + \frac{2n\pi}{l}\right)x}}{D'\left(k_x + 2n\pi/l\right)^4 - m''\omega^2}.$$

These expressions will be evaluated in a numerical example in section 6.

The correctness of the solution technique described will be checked by means of solving the infinite system of

equation (30) for a specific choice of φ. Thus, the matrix components (31) are in the present example

$$C_{nm} = \frac{1}{2\pi} \int_{-\infty}^{\infty} \frac{e^{i\alpha(\varphi_n - \varphi_m)}}{D'\alpha^4 - m''\omega^2} e^{-i\alpha(m-n)l} d\alpha, \quad (57)$$

an explicit expression being given in equation (A8) in the Appendix.

The free wave propagation is examined by means of equation (22), which in the present case reduces to $\bar{T}_0 = 0$, as F_0 is non-zero. Thus, by means of (52),

$$\bar{T}_0 = \frac{1}{l} \sum_{n=-\infty}^{\infty} \frac{\operatorname{sinc}^2\left(\kappa a + \frac{2n\pi a}{l}\right)}{D'\left(\kappa + 2n\pi/l\right)^4 - m''\omega^2} = 0. \quad (58)$$

for the uniformly distributed case, the corresponding equation for the Gaussian distributed case is found by means of (54), and where κ is solved for in both cases.

5. The radiated field and sound insulation of the supported plate

Consider once again the example in the previous sections, a plate resting on simple supports. The vibration of the plate will cause acoustic radiation on the side opposite to the excitation, denoted transmitted pressure field. If equations (15–16) and (40–41) for the periodic and the nearly periodic case respectively are taken as an standpoint, the transmitted pressure component for each space harmonic is

$$P_n^{(t)} = -\frac{\omega^2 \rho}{\beta_n} W_n, \quad \bar{P}_n^{(t)} = -\frac{\omega^2 \rho}{\beta_n} \bar{W}_n \quad (59)$$

where as before $\mu(\alpha) = E\left[e^{i\alpha\varphi_n}\right]$ is present in $\bar{W}_n$, and where

$$\beta_n^2 = (k_x + 2n\pi/l)^2 + k_z^2 - k^2$$

where $k = \omega/c_0$ is the wavenumber in the fluid, and where β_n has to be evaluated so that

$$\Re\{\beta_n\} \geq 0, \ \Im\{\beta_n\} \geq 0 \text{ if } \Re\{\beta_n\} = 0.$$

and further, the incident wavenumbers are

$$\begin{aligned}
k_x &= k\sin\theta\cos\varphi, \\
k_z &= k\sin\theta\sin\varphi, \\
k_y &= k\cos\theta.
\end{aligned} \quad (60)$$

The angle falls in the regions $0 \leq \theta < 2\pi$ and $0 \leq \varphi < \pi/2$.

It is important here that the radiation load is present in the space-harmonic terms W_n and $\bar{W}_n$. Thus, for the case of supported plate, the spatial stiffness (6) to be used is

$$S(\alpha) = D'(\alpha^2 + k_z^2)^2 - m''\omega^2 \quad (61)$$
$$- 2\rho_0\omega^2/\sqrt{\alpha^2 + k_z^2 - k^2},$$

where the last term is due to the radiation load, c.i. [6, 9, 10] and also [11, pp. 544–545].

The transmitted pressure is then given by the series

$$\bar{p}_t(x,y,z) = \sum_{n=-\infty}^{\infty} \bar{P}_n^{(t)} e^{-i(k_x + 2n\pi/l)x - ik_z z} e^{-\beta_n y}. \quad (62)$$

in the nearly periodic case (and in the periodic case the corresponding equation with p_t and P_n).

The total sound power radiated per unit area of the plate, that is the sound intensity $I_{n,Rad}$ in the direction normal to the plate (index n stands for normal), is

$$I_{n,Rad} = \frac{1}{2}\Re\{\bar{p}_t\bar{v}^*\} \quad (63)$$

which can be expressed as the sum of the sound intensity radiated normal to the plate by each harmonic. Thus, if using equations (15–16) and (40–41) for the periodic and the nearly periodic case respectively, together with (59) and $v^* = -i\omega w^*$,

$$I_{n,Rad} = \frac{1}{2}\omega^3\rho \sum_{n\in radiators} \frac{|\bar{W}_n|^2}{|\beta_n|}, \quad (64)$$

where the sum is to be performed over all the radiating harmonics $\beta_n \in \mathbb{I}$, where $\mathbb{I}$ being the imaginary numbers (and in the periodic case the corresponding equations with p_t and W_n are to be used).

The incidence sound intensity normal to the plate is

$$I_{n,In} = \frac{1}{2}\Re\{p_i v_i^*\} \quad (65)$$

where $p_i|_{y=0} = p_d|_{y=0}/2$ is the incident pressure and v_i is the velocity in the normal direction of the incident wave, if assuming a incidence wave of the form $p_i = \hat{p}_i e^{-i(k_x x + k_y y + k_z z)}$,

$$v_i = \frac{-1}{i\omega\rho}\frac{\partial p_i}{\partial y} = \frac{k_y}{\omega\rho}p_i.$$

and thus for the incidence sound intensity

$$I_{n,In} = \frac{1}{2}\frac{\Re\{k_y^*\}}{\omega\rho}|p_i|^2 = \frac{1}{2}\frac{k_y}{\omega\rho}|p_i|^2. \quad (66)$$

where the last step is only correct if the incident exciting wave is a travelling wave.

From the relations (63–66) one may determine the transmission efficiency $\tau(\theta, \varphi)$ for each incidence angle θ and φ; the transmission efficiency is the ratio of the transmitted/radiated sound intensity $I_{n,Rad}$ to the incident sound intensity $I_{n,In}$,

$$\tau(\theta, \varphi) = I_{n,Rad}(\theta, \varphi)/I_{n,In}(\theta, \varphi). \quad (67)$$

using equation (64) and (66), together with $k_y = k\cos\theta$, yields

$$\tau(\theta, \varphi) = \frac{\omega^4\rho^2}{k\cos\theta|p_i|^2} \sum_{n\in radiators} \frac{|\bar{W}_n|^2}{|\beta_n|}, \quad (68)$$
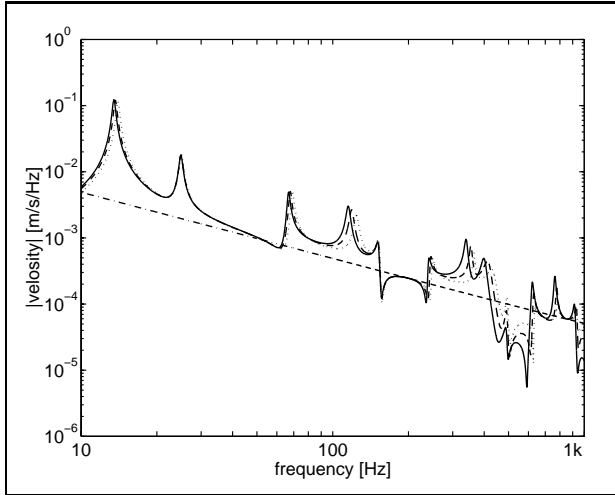
Figure 3. Magnitude of velocity due to pressure excitation, $x = 2l/3$ m and $l = 1$ m, low frequencies. Periodic (—), unsupported plate (- · -) and nearly periodic: uniformly distributed (- - -) and gaussian distributed (· · ·).
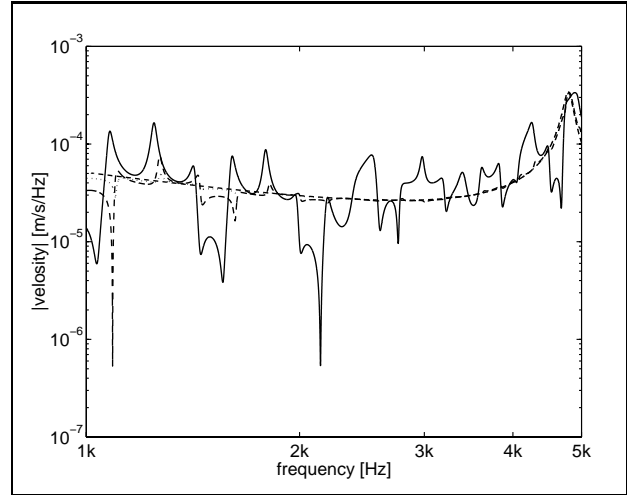
Figure 4. Magnitude of velocity due to pressure excitation, $x = 2l/3$ m and $l = 1$ m, high frequencies. Periodic (—), unsupported plate (- · -) and nearly periodic: uniformly distributed (- - -) and gaussian distributed (· · ·).

The statistical transmission coefficient τ_s is found as

$$\tau_s = \langle I_{n,Rad}(\theta, \varphi) \rangle / \langle I_{n,In}(\theta, \varphi) \rangle$$

where $\langle \cdot \rangle$ denotes the mean. The statistical transmission coefficient therefore becomes

$$\tau_s = \frac{1}{\pi} \int_0^{2\pi} \int_0^{\pi/2} \tau_n(\theta, \varphi) \sin\theta \cos\theta \, d\theta \, d\varphi \qquad (69)$$

and the transmission loss R dB is,

$$R = 10 \log 1/\tau_s \text{ dB}. \qquad (70)$$

6. Results: numerical examples

6.1. Numerical data

As a numerical example, consider the plate to be a chipboard plate whit Young's modulus $E = 4.6 \cdot 10^9$ N/m^2, density $\rho = 650$ kg/m^3, damping $\eta = 0.03$ and thickness 5 mm. The periodic length is $l = 1$ m. For the excitation field gracing incidence is assumed, that is $\theta = \pi/2$ and $k_x = k \sin\theta$.

6.2. Vibration response of acoustic excitation

The magnitude of the vibration velocity is plotted in Figures 3 and 4. Four different cases are studied; periodic, nearly periodic with uniform distribution, nearly periodic with Gaussian distribution and the same plate without the supports. The numbers of spread is set to $a = \sigma = 0.05 \cdot l$. The calculations is performed for the position $x = 2l/3$. Also the positions $x = l/4$ and $l/2$ were studied with similar result (but not presented here). In Figure 3 the frequency region is taken from 10 to 1000 Hz, with a frequency resolution of 0.1 Hz, whereas in Figure 4 the fre-
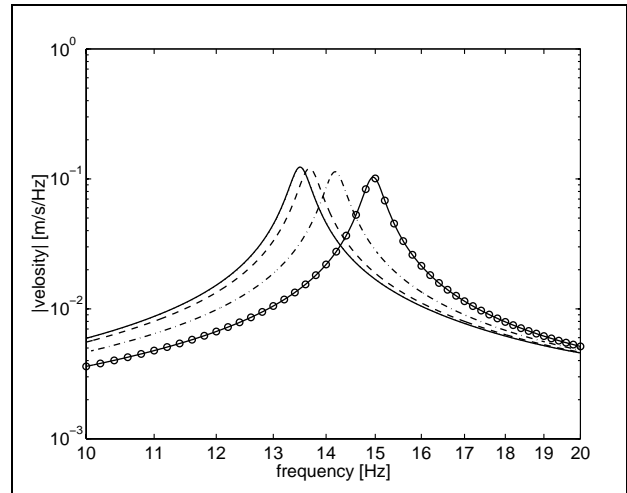
Figure 5. Magnitude of velocity due to pressure excitation, x=0.67 m. First peak in Figure 3. Uniform distribution in case of nearly periodicity. Periodic (—), nearly periodic: $a = 0.01l$ (· · ·), $a = 0.05l$ (- - -), $a = 0.1l$ (-··-), $a = 0.15l$ (-o-).

quency region taken from 1000 to 5000 Hz, with the same frequency resolution.

In Figure 5 the first peak in Figure 3 is studied more closely. The frequency region is taken from 10 to 20 Hz, with a frequency resolution of 0.01 Hz. The position is $x = 2l/3$ m. Five different cases are studied: the periodic case and four cases with uniform distribution with increasing spread. The number of spread is taken to be $a = \{0.01l \ 0.05l \ 0.1l \ 0.15l\}$.

In Figure 6 and 7 another peak in Figure 3 (the fourth peak from the left) is studied. The frequency region is taken from 90 to 150 Hz, with a frequency resolution of 0.01 Hz. The position is $x = 2l/3$ m. In Figure 7 the damping is set to zero, $\eta = 0$. The number of spread is taken to be $a = \{0.01l \ 0.05l \ 0.1l \ 0.15l\}$.
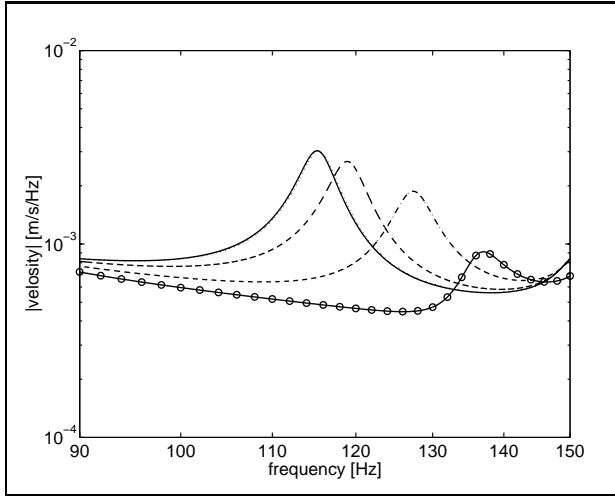
Figure 6. Magnitude of velocity due to pressure excitation, x=0.67 m. Fourth peak in Figure 3. Uniform distribution in case of nearly periodicity. Periodic (——), nearly periodic: $a = 0.01l$ ($\cdots$), $a = 0.05l$ (- - -), $a = 0.1l$ (-··-), $a = 0.15l$ (-o-).

Figure 8. Force F_0. Correctness check by means of Monte Carlo simulations. Solid line (——) nearly periodic case $\bar{F}_0$ using equation (49), dashed line (- - -) ensemble mean of the simulations using equations (30–31), dotted line ($\cdots$) is the perfectly periodic case using equation (17).

Figure 7. Magnitude of velocity due to pressure excitation, x=0.67 m, no damping. Fourth peak in Figure 3. Uniform distribution in case of nearly periodicity. Periodic (——), nearly periodic: $a = 0.01l$ ($\cdots$), $a = 0.05l$ (- - -), $a = 0.1l$ (-··-), $a = 0.15l$ (-o-).

sample function, and belongs to the solution space of the problem.

This procedure is then repeated a large number of times, so that the ensemble average converges (3200 sample functions was used in the examples). The result for the 0'th reaction force F_0 is shown in Figure 8.

As there is a disagreement between the nearly periodic case and the ensemble mean of the simulations, another approach is also used: That is to determine which of the sample functions determined by the simulations is most 'similar' to the other sample functions. This is determined by means of the least squares method. Thus, a least-square integral is defined as

$$Q_{nm} = \int_0^{f_{max}} \left| |F_0^{mc}(f)|_n - F_0^{mc}(f)|_m \right|^2 \, df. \quad (71)$$

The sample function that has the minimum least square sum are then sorted out,

$$\min \sum_{m=0}^{N} Q_{nm} \quad (72)$$

where N is the number of simulations ($N = 3200$ in the present example), and the resulting sample functions will be denoted the 'median' sample functions. It should be noted that this function belongs to the function space of the problem but the ensemble average do not belong to the function space. The comparison between the nearly periodic case, the perfectly periodic case, the 'median' case using equations (71–72) and the ensemble average of the 'median' from 50 simulations is shown in Figure 9.

6.3. Correctness check by means of Monte Carlo simulations

The correctness of the present formulation is checked by means of Monte Carlo simulations. For each simulation a specific set of φ_n is chosen randomly according to the uniform distribution. The reaction forces is then determined from the system of equations (30), which is truncated with an equal number of support present on both sides of the 0'th support. (The truncation is checked by means of comparing with the perfect periodic case, and 50 supports on each side are sufficient for this use). The resulting system of equation is solved, yielding the reaction forces F_n, including F_0. The result of one simulation is denoted a

6.4. Free wave propagation

Free wave propagation is examined by means of solving the dispersion relations (26) and (58) for the periodic and
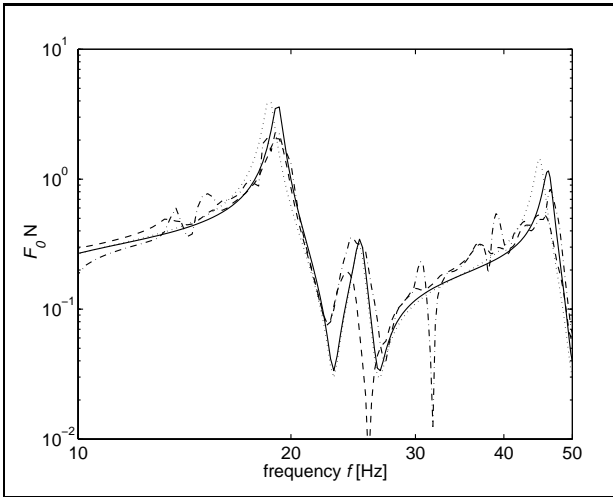
Figure 9. Force F_0. Correctness check by means of Monte Carlo simulations. Solid line (—) nearly periodic case $\bar{F}_0$ using equation (49), dash-dotted line (- · -) is the 'median' case using equations (71–72), dashed line (- - -) ensemble mean of the 'median' from 50 simulation, dotted line (· · ·) is the perfectly periodic case using equation (17)
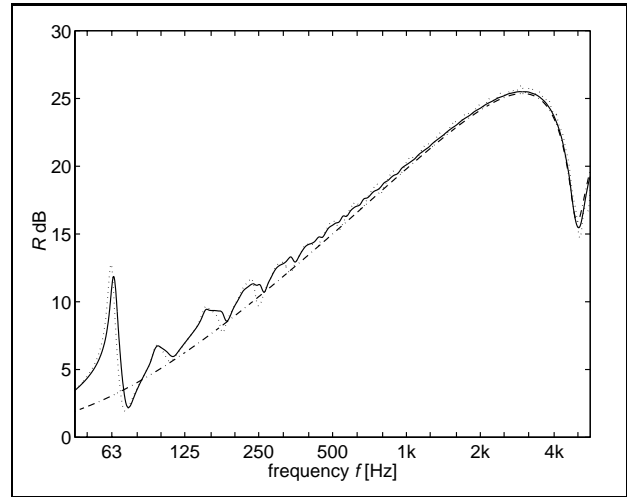
Figure 11. Transmission loss $R = 10 \log 1/\tau_s$ dB for the periodic case (· · ·), the nearly periodic case (—) and the unsupported plate case (- - -).
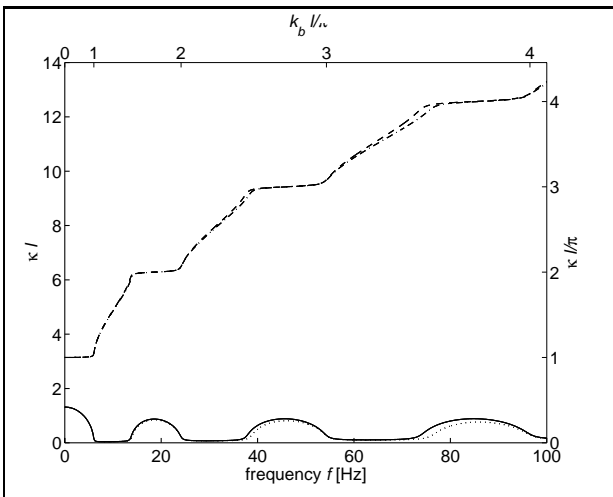
Figure 10. Frequency variation of propagation number κ, periodic $\Re\kappa$ (—), periodic $\Im\kappa$ (- - -), nearly periodic $\Re\kappa$ (· · ·), nearly periodic $\Im\kappa$ (- · -)

Figure 12. Increase in transmission loss $\Delta R = R - R_\infty$ dB for the periodic case (· · ·) and the nearly periodic case (—).

nearly periodic case respectively, by means of a simplex optimization routine; the minimal value of $|\bar{T}_0|$ and $|T(0)|$ is searched for in the complex κ-plane. The result is examined in Figure 10 for the case with no wave-motion in the z-direction, that is for $k_z = 0$, which is equivalent to a beam on supports. This figure can be compared with [11, pp. 419], Figure V/27.

When wave-propagation also is present in the z-direction, k_z is nonzero. Then each pair of f and k_z will yield a κ. This will however not be presented here, as no further insight will be gained.

6.5. Radiation and sound-insulation

The effects that near-periodicity in the supported plate have on sound-radiation and especially on sound-insulation are investigated by means of the results presented in section 5. The result is shown in Figure 11, where the transmission loss $R = 10 \log 1/\tau_s$ dB is presented for the periodic case, the nearly periodic case, and the unsupported plate case. In Figure 12 the same data are shown normalized with respect to the unsupported case (denoted R_∞ dB). It should be noted that in both figures a spline interpolation has been applied between calculation points in order to save calculation time.

7. Analysis

The effects of near-periodicity are analysed and compared to the perfect periodic case in this section. The general observation is: The nearly periodic case follows the perfectly periodic case but with peaks and dips slightly shifted to higher frequencies and more damped, the effect of the near-periodicity being increased with increasing frequency.

The tendency in the numerical examples shown in Figures 6–7 is that increasing the amount of irregularity shifts the peaks to increasing frequencies and in most cases decreases the height of the peaks. It can therefore be concluded that the irregularities increase the stiffness and damping in the expected vibration field if material damping is present. If material damping is not present, the irregularities increases only the stiffness, as shown in Figure 7. For increasing frequencies the nearly periodic velocity versus frequency curves tend to be more damped and closer to the unsupported plate, as shown in Figures 3 and 4.

In Figure 8 the ensemble mean of a large (3200) number of simulations for the 0'th support force is compared to the nearly periodic and the periodic results. There is a disagreement between the results; the ensemble mean is more damped and has more peaks than the nearly periodic result. However, the tendency is the same and the ensemble mean result is clearly closer to the nearly periodic result than to the periodic result. (This was also investigated by means of the least squares method using an integral similar to (71), and the result was that the sample functions were always closer to the nearly periodic curve than to the perfect periodic curve.) The disagreement is due to the assumptions stated in the beginning of section 2. The first assumption, that the reaction forces are statistically independent of the harmonic term $e^{i\alpha\varphi_n}$ is most likely to be the cause to the disagreement. To make the proposed approach better, there must be a better assumption here.

In Figure 10 the possible choices of wave-number κ for free wave propagation is presented. The same tendency as before can be noted: in the nearly periodic case has κ slightly shifted towards higher stiffness and higher damping.

In Figures 11 and 12 the sound-insulation transmission loss is shown. The same tendency as before is also noted in these examples; the stiffness and damping has increased in the nearly periodic case in relation to the perfect periodic case, and the tendency is more predominant for increasing frequencies; the nearly periodic case tends to the unsupported plate case. However, no conclusion can be drawn from these examples as to whether the nearly periodic case provides better sound insulation than the perfect periodic case.

8. Summary and concluding remarks

The effects of small irregularities in a nearly periodic spatially excited structure have been studied with a new statistical approach. The method used is suited for sound insulation problems. Also the acoustic radiation has been considered.

The irregularities cause extra damping and stiffness in the mean vibration field if material damping is present. If no material damping is present, only an increase in the stiffness can be seen. A conclusion addressed to shipyards and the building industry is that it may be a good idea to maintain and increase the amount of irregularities and imperfections in built-up structures such as walls and floors.

Monte-Carlo simulations shows that the nearly periodic solution is not identical to the ensemble average. However, the tendency is the same and the sample functions are always closer to the nearly periodic solution than to the perfect periodic solution.

The proposed method is also shown to be suited for evaluation of the free wave propagation.

Sound radiation and sound-insulation transmission loss has also been studied. The method is well suited to handle this situation (unlike the methods used in the past, such as [2, 3, 4]). The same tendency as before can be noticed in this case.

Acknowledgement

Appendix

Calculation of the matrix components C_{nm} in section 4.8, equation (57). Consider the integral

$$I(x,\theta) = \frac{1}{2\pi} \int_{-\infty}^{\infty} \frac{e^{i\alpha\theta}}{D'\alpha^4 - m''\omega^2} e^{-i\alpha x} d\alpha. \quad (A1)$$

The integral is calculated by means of contour integration.

$$D'\alpha^4 - m''\omega^2 = 0 \Rightarrow \alpha_i^4 = m''\omega^2/D' \quad (A2)$$

Thus, if using the notation $k_B = \sqrt[4]{m''\omega^2/D'}$,

$$\begin{aligned} \alpha_1 &= k_B, \quad \alpha_2 = -k_B, \\ \alpha_3 &= ik_B, \quad \alpha_4 = -ik_B. \end{aligned} \quad (A3)$$

The residues are found to be

$$\operatorname*{Res}_{\alpha \to \alpha_i} \left\{ \frac{e^{-i\alpha(x-\theta)}}{D'\alpha^4 - m''\omega^2} \right\} = \frac{e^{-i\alpha_i(x-\theta)}}{4D'\alpha_i^3} \quad (A4)$$

If $x - \theta < 0$ is the upper half space to be used, and (after considering the effect of damping) the poles α_2 and α_3 fall

inside the contour,

$$I(x,\theta) = \frac{1}{2\pi} 2\pi \mathrm{i} \sum_{n=2,3} \operatorname*{Res}_{\alpha=\alpha_n} \tag{A5}$$

$$= \frac{-1}{4D'k_B^3} \left(\mathrm{i} e^{\mathrm{i}k_B(x-\theta)} + e^{k_B(x-\theta)} \right),\ x-\theta < 0.$$

If $x - \theta > 0$ is the lower half space to be used, and the poles α_1 and α_2 fall inside the contour,

$$I(x,\theta) = -\frac{1}{2\pi} 2\pi \mathrm{i} \sum_{n=1,4} \operatorname*{Res}_{\alpha=\alpha_n} \tag{A6}$$

$$= \frac{-1}{4D'k_B^3} \left(\mathrm{i} e^{-\mathrm{i}k_B(x-\theta)} + e^{-k_B(x-\theta)} \right),\ x-\theta > 0.$$

Thus, if combining (A5) and (A6)

$$I(x,\theta) = \frac{-1}{4D'k_B^3} \left(\mathrm{i} e^{-\mathrm{i}k_B|x-\theta|} + e^{-k_B|x-\theta|} \right) \tag{A7}$$

and matrix components are found to be

$$C_{nm} = I(m-n, \varphi_n - \varphi_m) \tag{A8}$$

$$= \frac{-1}{4D'k_B^3} \left(\mathrm{i} e^{-\mathrm{i}k_B|ml+\varphi_m-nl-\varphi_n|} + e^{-k_B|ml+\varphi_m-nl-\varphi_n|} \right).$$

References

[1] P. W. Andersson: Absence of diffusion in certain random lattices. Physical Review **109** (1958) 1492–1505.

[2] C. H. Hodges, J. Woodhouse: Vibration isolation from irregularity in a nearly periodic structure: Theory and measurements. J. Acoustical Society of America **74** (1983) 894–905.

[3] C. Pierre, E. H. Dowell: Localization of vibrations by structural irregularity. J. Sound and Vibration **114** (1987) 549–564.

[4] G. Q. Cai, Y. K. Lin: Localization of wave propagation in disordered periodic structures. American Institute of Aeronautics and Astronautics Journal **29** (1990) 450–456.

[5] J. Brunskog, P. Hammer: Prediction models of impact sound insulation on timber floor structures; a literature survey. J. Building Acoustics **7** (2000) 89–112.

[6] B. R. Mace: Periodically stiffened fluid-loaded plates, I: Response to convected harmonic pressure and free wave propagation. J. Sound and Vibration **73** (1980) 473–486.

[7] P. M. Morse, H. Feshbach: Methods of theoretical physics, part I. McGraw-Hill Book Company, Inc., New York, 1953.

[8] M. L. Rumerman: Vibration and wave propagation in ribbed plates. J. Acoustical Society of America **57** (1975) 370–373.

[9] B. R. Mace: Sound radiate from a plate reinforeced by two sets of parallel stiffeners. J. Sound and Vibration **71** (1980) 435–441.

[10] J. Brunskog, P. Hammer: Prediction model for the impact sound level of lightweight floors. Acustica / acta acustica **accepted**.

[11] L. Cremer, M. Heckl, E. E. Ungar: Structure-borne sound. Springer-Verlag, Berlin, 1988.